

A study of amorphous materials: Surface dynamics, surface modification, and polyamorphism

By
Yuhui Li

A dissertation submitted in partial fulfilment of
the requirements for the degree of

Doctor of Philosophy
(Pharmaceutical Sciences)

at the
UNIVERSITY OF WISCONSIN-MADISON
2022

Date of final oral examination: 05/18/2022

The dissertation is approved by the following members of the Final Oral Committee:

Lian Yu, Professor, Pharmaceutical Sciences

Mark D. Ediger, Professor, Chemistry

Ronald Burnette, Professor, Pharmaceutical Sciences

Sandro Mecozzi, Professor, Pharmaceutical Sciences

To my parents and my wife

Acknowledgement

During the past five years, I have read dissertations of different people and thought many times about how I would start my thesis. Finally, it is time to write mine. These five years is a wonderful journey. Through it, I am becoming a better me, not only with a new Dr. title. I am ready to step into any unknown area with my trained self-teaching and invoked curiosity, and I am ready to overcome any adversity with my strengthened mind. I appreciate the people I have met during the journey. They make me feel supported and loved in a foreign land.

First of all, I would like to appreciate my advisor Dr. Lian Yu. It is now I realize why the graduates thank their advisors first in the acknowledgement. 80 % of this thesis was edited by Dr. Yu word by word and sentence by sentence. It is he who leads me to the field of physical chemistry and supports me whenever I need help. He shows me how to be an exceptional scientist: being curious, enthusiastic and rigorous. Every time an interesting observation is found, he would dive into it and find the scientific explanation; Every time a new member joins the group or the school, he would offer help; Every time a new set of important data is collected, or a new manuscript is written, he would go through all the details again and again. Outside the lab, he is a good friend, sharing with us the vegetables he grew, treating us with big festival meals and introducing us nice places to visit. All these colors my life in Madison.

I would also like to appreciate my committee members: Dr. Mark Ediger, Dr. Sandro Mecozzi and Dr. Ronald Burnette. Mark is a great mentor with a sharp mind. A lot of good ideas in my projects nucleated from the discussions with him, and his course on polymer physical is one of the most informative that I have ever taken. Sandro and Ron provide valuable advice and feedback from the viewpoints out of my research area, which usually lead to comprehensive overviews of my projects.

I appreciate the help from my mentors outside the lab. Dr. Ed Elder and Dr. Mark Sacchetti supervised me when I interned at the Zeeh Pharmaceutical Experiment Station, during which a lot of pharmaceutical-related knowledge and techniques were learned. (Luckily, one of the formulations we participated in was approved by FDA recently. Another item checked on my wish list!) Dr. Pallavi Pawar mentored me during the internship at GlaxoSmithKline plc. Her style of working and communicating is a great example of what a good researcher should be like in the industry.

I would also like to thank the members of Yu group. Chengbin is the one who recruited me into Yu lab five years ago and is a great “consultant” in research and in life. I appreciate his help over the years. M taught me all the techniques in the lab and is a great friend to hang out with. Zhenxuan has been a big brother to me. I admire his kindness, perseverance, and eagerness to help others. Yue is an outstanding researcher and a good collaborator. Xin and I joined the group in the same year and he has been a nice friend to talk about science, life and politics. Junguang is a great lab mate, who is always willing to help and give suggestions. I would also like to thank the other group members, Changlin, Hao, Chengyu, Kennedy, Amy and Caroline, for the good memories we had in the lab during the years. I also thank the alumina, who don't have overlap with me, for their help on experiment set-up and job hunting: Men, Wei, Shigang, Yinshan, Lei, Hanmi and Junshu. Last but not least, I would like to thank my parents and my wife for their consistent support and love during the years. I am looking forward to working with you in the same company, Dr. Du! I also appreciate my friends for their accompany in Madison: Bo, Lim, Chenyu, Lu, Linqun, Jiatong, Qijun, Kai, Yuchuan and Rong, thank you!

Table of Contents

Abstract.....	ix
Chapter 1 Introduction.....	1
1.1 Overview.....	2
1.2 Bulk dynamics of glasses and fragility	5
1.3 Dynamics at the glass surface.....	9
1.3.1 Importance of surface dynamic study	9
1.3.2 The measurements of surface dynamics	12
1.3.3 Theories on surface-enhanced dynamics	16
1.4 Immobilizing surfaces with surface coating	19
1.5 Polyamorphism	22
1.6 Contribution of this thesis.....	24
1.7 References.....	29
Chapter 2 Surface diffusion in glasses of rod-like molecules posaconazole and itraconazole: Effect of interfacial molecular alignment and bulk penetration	36
2.1 Abstract.....	37
2.2 Introduction.....	38
2.3 Experimental Section	39
2.4 Mullins' Theory of Surface Evolution.....	41
2.5 Results.....	42
2.5.1 Posaconazole (POS).....	43
2.5.2 Itraconazole (ITZ)	48
2.6 Discussion.....	50
2.6.1 Correlation between Surface Diffusion and molecular surface penetration depth.	50
2.6.2 Correlation between Surface Diffusion and Bulk Fragility.	56
2.7 Conclusion	59

2.8 Acknowledgements.....	61
2.9 Supporting Information.....	61
2.9.1 Viscosity and structural relaxation time for GSF.....	61
2.9.2 Viscosity and structural relaxation time for POS and ITZ.....	62
2.10 References.....	63
Chapter 3 Surface diffusion of a glassy discotic organic semiconductor and the surface mobility gradient of molecular glasses.....	67
3.1 Abstract.....	68
3.2 Introduction.....	68
3.3 Experimental Section.....	71
3.4 Results.....	73
3.5 Discussion.....	78
3.6 Conclusions.....	90
3.7 Acknowledgements.....	92
3.8 References.....	92
Chapter 4 Surface diffusion is controlled by bulk fragility across all glass types	95
4.1 Abstract.....	96
4.2 Results and Discussion	96
4.3 Conclusion	106
4.4 Acknowledgement	106
4.5 Supporting Information.....	106
4.5.1 Surface and bulk diffusion of OTP by simulations.....	106
4.5.2 Surface and bulk diffusion of silica by simulations.....	108
4.5.3 Extrapolation of Surface Diffusivity from Simulations to Laboratory T_g	111
4.5.4 Viscosity of silicon	112
4.6 References.....	113

Chapter 5 Surface mobility of amorphous indomethacin containing moisture and surfactant: A concentration-temperature superposition principle	120
5.1 Abstract.....	121
5.2 Introduction.....	121
5.3 Experimental Section	123
5.4 Results.....	126
5.4.1 Effect of Moisture on IMC Surface Mobility.	127
5.4.2 Effect of Surfactant Tween 20 on IMC Surface Mobility.	134
5.5 Conclusion	142
5.6 References.....	143
Chapter 6 Polymer nanocoating of amorphous drugs for improving stability, dissolution, powder flow, and tableability: The case of chitosan-coated indomethacin.....	146
6.1 Abstract.....	147
6.2 Introduction.....	147
6.3 Materials and methods	150
6.4 Results and discussions.....	155
6.4.1 Stability Test in Film Geometry.	155
6.4.2 Stability of Coated Amorphous Particles.....	156
6.4.3 Comparison of Particle Formation Methods.....	159
6.4.4 Dissolution Rate.....	160
6.4.5 Powder Flow.	162
6.4.6 Tableability.	164
6.5 Conclusion.	165
6.6 Supporting Information.....	166
6.7 References.....	167

Chapter 7 A low-density second amorphous phase of D-mannitol with novel 3 nm mesoscopic order	169
7.1 Abstract	170
7.2 Introduction.....	170
7.3 Experimental Section	172
7.4 Results.....	177
7.4.1 X-Ray Scattering.....	177
7.4.2 Kinetics of Transformation.....	181
7.4.3 ssNMR.....	185
7.5 Discussion.....	188
7.5.1 Structure Associated with the Main Peak: C...C Correlation.....	188
7.5.2 Hydrogen Bond Network.....	191
7.6 Conclusions.....	198
7.7 Acknowledgements.....	199
7.8 References.....	199
Chapter 8 Future work.....	203
8.1 New method for surface diffusion measurements.....	204
8.2 Growth of single-layer smectic structure.....	208
8.3 Drastic enhancement of crystal nucleation by polyamorphic transition.....	210

Abstract

The glass is a unique solid state with liquid-like spatial uniformity and crystal-like mechanical strength. Different materials have been prepared into the glassy state for applications in various situations. Nevertheless, glasses are unequilibrated and tend to crystallize. During this process, the dynamics and the structure inside the glasses play a vital role. This thesis is concerned with these two properties, especially the dynamics at the free surface of glasses and the structural change during the polyamorphic transition.

Molecular diffusion rate was determined by the method of surface grating decay at the free surface of three glasses, posaconazole, itraconazole, and MTDATA. The results are analyzed along with other molecular glasses without extensive hydrogen bonds. In total, these systems cover a wide range of molecular geometries from rod-like to quasi-spherical to discotic and their surface diffusion coefficients vary by 9 orders of magnitude. This variation can be well explained by the existence of a steep surface mobility gradient and the anchoring of surface molecules at different depths. The survey of surface diffusion was then extended to other glass types. A strong correlation between surface diffusion and the fragility of bulk dynamics was discovered. This trend extends through glasses of all kinds: molecular, polymeric, chalcogenide, silicon, metallic, and oxide. The correlation is attributed to the robustness of covalent network bonds present in strong liquids, making them more resistant to environmental excitation from bulk to surface. The findings help understand and predict surface mobility to develop amorphous materials with high stability for their diverse applications.

In real applications, amorphous materials are usually developed by doping multiple components but the effect of composition on surface dynamics remains poorly understood. The surface

mobility of amorphous indomethacin was measured using the method of surface grating decay in the presence of moisture and the surfactant Tween 20. It is found that both components significantly enhance the surface mobility, and their effects are well described by the principle of *concentration-temperature superposition* (CTS); that is, the same surface dynamics is observed at the same T_g -normalized temperature, where T_g the composition-dependent glass transition temperature. The CTS principle allows the prediction of the surface dynamics of multi-component amorphous materials.

Due to the fast surface mobility, amorphous drugs can grow crystals much more rapidly at the surface than in the bulk, causing poor stability and slow dissolution of drug products. We show that a nano-coating of chitosan (a pharmaceutically acceptable polymer) can be deposited on the surface of amorphous indomethacin by electrostatic deposition, leading to significant improvement of physical stability, wetting by aqueous media, dissolution rate, powder flow, and tabletability. The coating condition was chosen so that the positively charged polymer deposits on the negatively charged drug. This electrostatic deposition can be used as a general method to manufacture stable amorphous formulations.

Other than the surface dynamics, this thesis is also concerned with the bulk structures of amorphous materials. X-ray scattering and solid-state NMR (ssNMR) were used to investigate the structural change during the polyamorphic transition of D-mannitol. We find that the non-polar hydrocarbon groups in D-mannitol changes with density during the conversion, while the structure constructed by hydrogen-bonding is significantly reorganized. The reorganization occurs by rearranging the second coordination shells and beyond, resulting in supramolecular aggregates that give rise to low-angle prepeaks in the scattering pattern. This study provides the structural basis for the phenomenon of polyamorphism.

Chapter 1

Introduction

Yuhui Li

1.1 Overview

A same composition could have different physical states. On the phase diagram, the material is gaseous at a high enough temperature; it will then condense into liquid when the system is cooled down; with further cooling, the liquid could either solidify into a crystalline phase through crystallization, or into a glassy phase through vitrification. The biggest difference between these two solid phases is their microscopic packing: crystals have both short-range and long-range order, while glasses have only some degrees of short-range but no long-range order. And this difference enables glassy material several advantages over its crystalline counterpart: better macroscopic homogeneity, higher compositional flexibility, easy processing, and higher solubility.

The history of manufacturing glassy materials dates back to at least 3600 years: the ancient glassmaker made containers and windows with glassy materials for their better transparency. In modern society, glasses have been applied widely for their unique physical properties in different fields: Molecular glasses have been developed as drug formulations and new-generation display material^{1,2}; Chalcogenide were used as data storage media and optical imaging^{3,4}; Metallic glasses have commercial applications such as transformer cores and biomedical implants. Despite these industrial applications, glasses are also scientifically important for their unique structure and dynamics.

There are multiple ways to prepare glasses and most of them rely on fast *kinetic freezing*, including melt-quenching, solvent evaporation, and vapor deposition. Melt-quenching is the most traditional way. Figure 1.1 shows the change of volume or enthalpy during the melt-quenching process. At high temperatures above the melting point T_m , the material is a liquid. By cooling to temperatures below T_m , the material has a strong tendency to crystallize and lower the energy. If the quenching

rate is fast enough, the atoms/molecules inside the system would not have enough time to rearrange themselves to form a crystalline structure. Instead, the material remains amorphous and transits into a “super-cooled liquid” state, which is an equilibrated but metastable state. By further cooling, the dynamics inside the material keeps decreasing, and at a specific temperature, the dynamics would not be fast enough to respond to the temperature change. Finally, the system falls out of equilibrium and enters the glassy state. This temperature is called glass transition temperature T_g and it is one of the most important characteristics of glassy properties.

The glassy state is an unstable and unequilibrated state. The slow-enough dynamics of the glassy state persists its amorphous nature. This is also the reason why we need to study the dynamics of

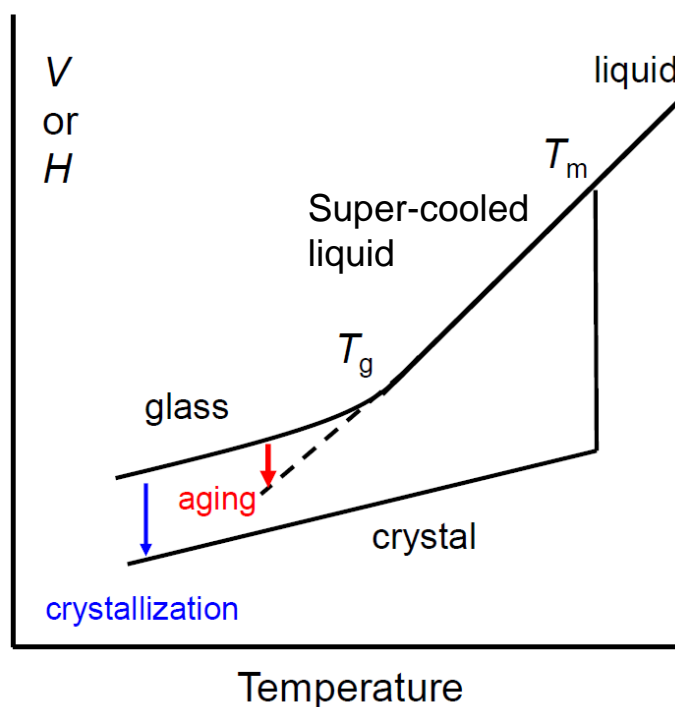


Figure 1.1. Temperature dependence of volume (V) or enthalpy (H). T_m and T_g are melting point and glass transition temperature, respectively. During annealing, glass tends to equilibrate into “ideal glass” through glass aging, which is labelled by red arrow. At the same time, it would also crystallize to further lower the free energy, which is labeled by blue arrow.

glasses. A thorough understanding of glass dynamics enables us to predict the stability of the glassy material, to screen the right receipt for development, to fabricate “stable glasses” and to construct glasses even with anisotropic structures. To build this understanding, one direction is to study it “intrinsically”, which includes studying the structure-dynamic correlation,⁵ the dynamic heterogeneity,⁶ and the different dynamic motions.⁷ Another direction is to study the response of the dynamics to external perturbation, such as, temperature change and *free surface exposure*.

When exposed to vapor interface, the atoms/molecules would have faster dynamics, as they have fewer neighbors to hinder their movement. However, this surface-enhanced dynamics is not well-understood. At the same time, this fast surface dynamics plays a vital role in the stability, fabrication, and manufacturing of glassy materials. Based on these, the following questions are concerned in this thesis: 1) is there a predictive model for surface diffusion rates of glasses? 2) how will the surface dynamics be influenced by a secondary dopant? 3) how to eliminate the fast surface dynamics and prolong the shelf life of amorphous pharmaceuticals?

Except for the dynamics, the structure of glasses is also of strong interest for its coherence with different properties. Though there is no long-range order in glasses, a certain degree of short-range order exists and can be used to describe the structure of glasses. Polyamorphism is a phenomenon that rises from the subtle change of this short-range order. Polyamorphism refers to the existence of two amorphous phases of the same substance separated by a first-order transition. It is analogous to polymorphism in crystals, but is far more rare and often controversial.⁸ The structural change of D-mannitol during the polyamorphic transition will be discussed later in this thesis.

Overall, we consider the surface dynamics and bulk structure of glasses. In Chapter 2 and 3, we consider the relationship between the surface molecular penetration depth and surface diffusion of

molecular glasses. In Chapter 4, we survey the relationship between fragility and surface diffusion of glasses of all kinds. In Chapter 5, we quantify the influence of plasticizers on surface dynamics. In Chapter 6, we apply a surface-modification method to stabilize amorphous drugs. In Chapter 7, we study the structural change during the polyamorphic transition of D-mannitol. In the rest of this Chapter 1, I will introduce the bulk and surface dynamics of glassy materials, the recent process on surface polyelectrolyte coating to stabilize amorphous pharmaceuticals and polyamorphism.

1.2 Bulk dynamics of glasses and fragility

T_g is the temperature at which the dynamics starts to fail to respond to the temperature change. It is, thus, not a fixed value but cooling-rate-dependent. There are multiple ways to define T_g for a system: in Differential scanning calorimetry (DSC), T_g is commonly defined as the onset temperature of glass transition with a 10 K/min heating rate; in dielectric relaxation measurement or rheology measurement, T_g is defined as the temperature where α relaxation time $\tau_\alpha = 100$ s or viscosity $\eta = 10^{12}$ Pa·s, respectively. Glasses, regardless of the composition, have similar dynamics around their T_g . As a result, T_g can be used as a universal ruler to scale and compare the dynamics of glasses of all kinds. This is the basis of the famous “Angell plot” (Figure 1.2).

Another important contribution of the Angell plot is the introduction of fragility to classify different systems. Fragility is a qualitative concept that describes the deviations of dynamics from Arrhenius behavior. Atoms in a strong system, like SiO_2 , are bonded with covalent interaction, which is strong and directional. With increasing temperature, the bond is largely intact, leading to a mild change of volume, structure, and dynamics. On the contrary, the weak and nondirectional interaction (e.g. van der Waals interaction) in fragile systems can be dramatically unraveled upon heating. This is the reason of the fast gain of mobility when the fragile glass is heated to become

a liquid and of the super-Arrhenius temperature dependence of dynamics in fragile liquid. Molecular or ionic liquids are usually in the fragile end. Between the strong and fragile ends, we found materials with intermediate fragility: silicates, chalcogenides and metals.

Fragility was first introduced as a qualitative concept⁹ and up to now, there are various ways to quantify it. In Figure 1.2, three common methods are included:

1. The steepness index, m , is defined as

$$m = \lim_{T \rightarrow T_g} \frac{d \log \langle \eta \rangle}{d(T_g/T)}$$

m measures temperature dependence of viscosity around T_g and is also the most commonly used method to quantify fragility. While m is often used, there are several concerns. Firstly, as Richert and Angell pointed out, “it is disconcertingly unreliable due to author subjectivity in slope-taking at T_g as well as experimental subtleties in this slowly equilibrating regime”¹⁰ Secondly, m was expanded too extensively that the value can be obtained from measuring various parameters, including viscosity, shear relaxation, dielectric relaxation and calorimetry response, which are sometimes used without distinguishment. Both concerns could lead to a big fluctuation of the value and mislead the comparison when using m as the fragility measure. For example, the m value for indomethacin ranges from 60 to 90.^{11,12,13,14}

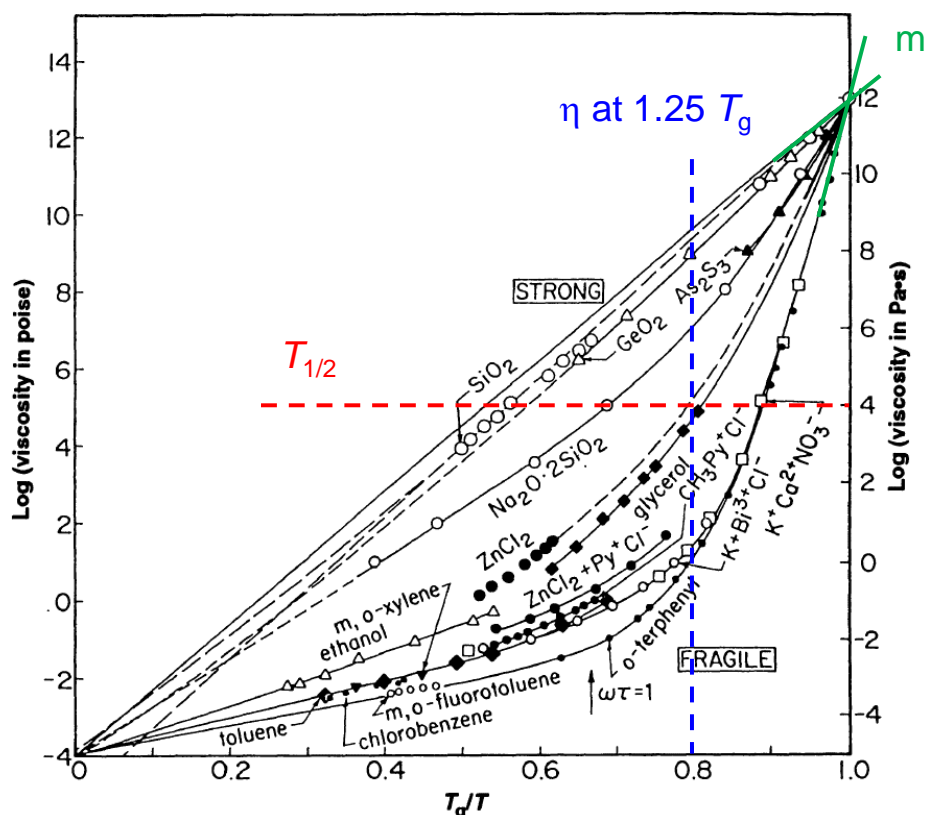


Figure 1.2. Angell plot: the temperature dependence of viscosity, where the temperature is scaled by the glass transition temperature. Here, T_g is defined as the temperature where viscosity is 10^{12} Pa·s. The viscosities of different systems converge at the two ends: T_g and the infinitely high temperature. In the middle region, dynamics in glasses with different compositions shows various temperature dependence. Strong glasses, like SiO_2 , show Arrhenius temperature dependence, while fragile glasses quickly gain mobility (viscosity decrease) when heated from T_g and show super-Arrhenius dependence. To quantify fragility, there are several measuring methods, including m , η at $1.25 T_g$, and $F_{1/2}$. They are introduced in the main text. Reproduced with the permission from Angell, *Science*, **1995**, 267, 1924-1935. Copyright 1995 American Association for the Advancement of Science.

2. To address the issue of using m , Richert and Angell proposed another fragility measure, defined as:

$$F_{1/2} = 2 \frac{T_g}{T_{1/2}} - 1$$

Where $T_{1/2}$ can be identified by the horizontal dashed line in Figure 1.2. $F_{1/2}$ was originally proposed using dielectric relaxation data and $T_{1/2}$ is the temperature where $\tau_\alpha = 10^{-6}$ s. In terms of viscosity, $T_{1/2}$ is the temperature where $\eta = 10^4$ Pa·s. The more fragile systems deviate more from the Arrhenius dependence and have bigger $F_{1/2}$ values.

3. The third way of quantifying fragility is by comparing the value of viscosity (or relaxation time) at $1.25 T_g$, which can be determined by the vertical dashed line in Figure 1.2. This method compares the displacement from the Arrhenius behavior when it is the largest and has the advantage of better distinction of the systems.

Even though the concept of fragility is firmly rooted in glass science, its quantitative measure, using a single parameter, has not been standardized. All the measures mentioned above are valid and it is usually the author's choice to use the "right" measure. As the difference in the fragility of similar materials is usually small, it is recommended to choose the measure with bigger displacement and better distinction to analyze materials within the same category. For instance, Tylinski et al. found that the stability of vapor deposited glasses has a strong correlation with the fragility of the material. They systematically compared different fragility measures, m , $F_{1/2}$, and $\log \tau_\alpha$ at $1.25 T_g$, and the correlation is the clearest when using $\log \tau_\alpha$ at $1.25 T_g$.¹⁵

1.3 Dynamics at the glass surface.

1.3.1 Importance of surface dynamic study

Atoms or molecules have fewer nearest neighbors at the free surface and are less hindered during their dynamic motions, leading to significant surface dynamic enhancement. While the portion of surface material is small compared to the bulk, this fast surface dynamics usually induces problematic material failure and, on the other hand, enables new fabrication methods: 1) As the glassy state is thermodynamically unstable, the glasses tend to crystallize, and this process can be dramatically accelerated by the fast dynamics at the free surface. Figure 1.3a shows the cross-section image of a γ crystal grown at the surface of a molecular glass, indomethacin (IMC), under scanning electron microscopy (SEM).¹⁶ The crystal tends to grow laterally at the free surface, while the growth into the interior is much slower. This surface-enhanced crystallization has been found in various glass types, including molecular,^{17, 18, 19, 20, 21} chalcogenide,^{22, 23} silicon²⁴, metal,^{25, 26} and polymer.²⁷ 2) In the lithography industry, photoresist polymers are manufactured into fine structures for device etching. These nanostructures with a big surface-to-volume ratio expose more material to the vapor interface. As a result, the surface plays a bigger role in dynamics, and the fabricated structure could collapse due to the fast surface mobility even below the freezing temperature of the bulk material.²⁸ 3) Since the first report on using physical vapor deposition (PVD) to prepare “ultra-stable” glasses,²⁹ it has seen a great process in tuning the structure³⁰ and stability³¹ of glasses by PVD. Figure 1.3c introduces the process of PVD schematically. The source material is heated to evaporate, and the gaseous material will eventually condense at the substrate surface. After landing, the atom or molecule has the fast surface dynamics to equilibrate into low-energy states before burial by the coming material. This surface-equilibrating mechanism produces not only the glasses with higher density, higher stability, and bigger modulus, but also the glasses

with anisotropic structures.^{32,33} While the product can be modified by substrate temperature and deposition rate, the intrinsic surface mobility of the source material is also vital. As shown by Chen et al., the stability of PVD molecular glasses has a positive correlation with its surface diffusion rate.³⁴ So far, there is a big collection of PVD stable glasses and the materials expand from organic (molecule and polymer³⁵), to inorganic^{36,37} and metallic.³⁸ 4) As the fast crystallization at high temperature is one of the biggest challenges of metallic glasses, it is preferred to fabricate them at relatively low temperatures, where the crystallization rate is slow. Ma et al developed a cold-welding technique, taking advantage of the fast surface dynamics of the metallic glass even at temperature way below T_g .³⁹ The same principle has also been adopted to sinter the polymer nanoparticles at room temperature,⁴⁰ and it is also the underlying mechanism of additive manufacturing. Overall, even though the surface layer only represents a small portion of the glassy material, its fast dynamics plays a vital role in its stability and manufacture. Because of this central role, understanding and predicting surface mobility is of strong interest.

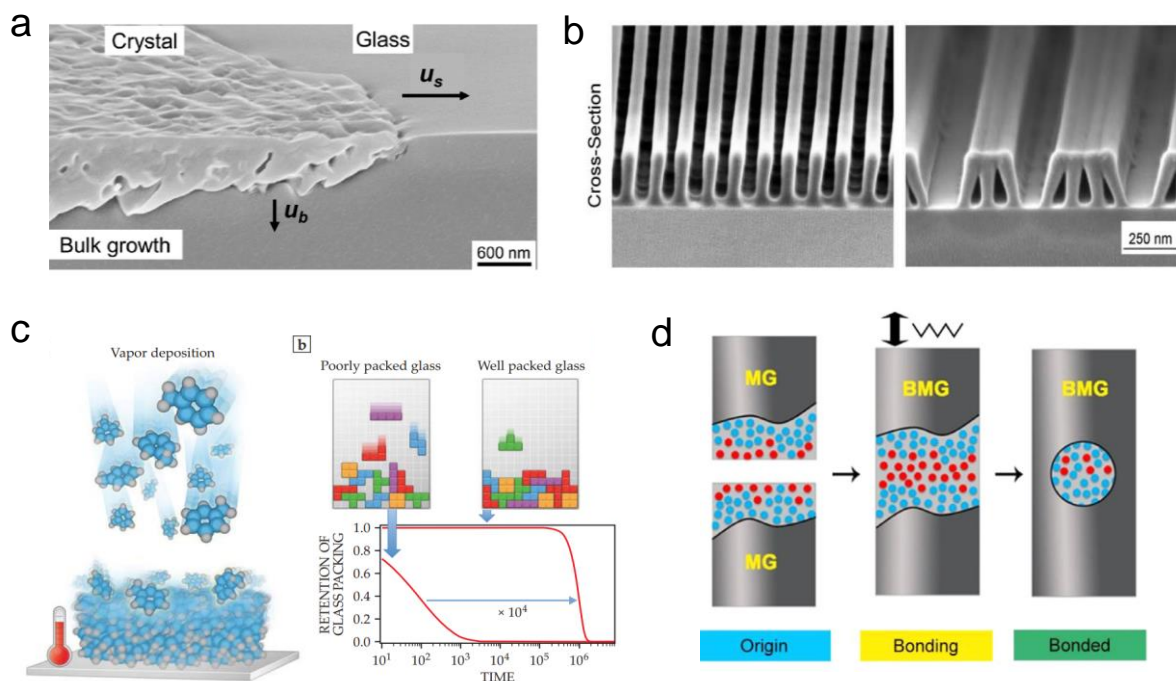


Figure 1.3. (a) Crystal of γ IMC grown at the free surface of IMC glass. The image is a cross-section of the sample under SEM. Reproduced with permission from Hasebe *et al.*, *J. Phys. Chem. B* **2015**, *119*, 3304–3311. Copyright 2015 American Chemical Society. (b) Cross-sectional SEM image of stable and collapsed PMMA nanostructures. Reproduced with permission from *Soft Matter*, **2010**, *6*, 2475–2483. Copyright 2010 Royal Society of Chemistry. (c) Left: schematic presentation of the process of PVD. Gaseous molecules condense on the substrate and equilibrate with fast surface mobility before burial. Right: deposition rate influences the stability of PVD glasses. Reproduced with permission from *Phys. Today*, **2016**, *69*, 40. Copyright 2016 American Institute of Physics. (d) The cold joining mechanism of metallic glass during the ultrasonic bonding. Reproduced with permission from *Scripta Materialia*, **2020**, *185*, 100-104. Copyright 2020 Acta Materialia Inc. Published by Elsevier Ltd.

1.3.2 The measurements of surface dynamics

There are multiple measures to quantify the dynamics at the free surface. Structural relaxation time is an inclusive concept and can be characterized by different methods: Paeng et al. used the method of photo-bleaching to quantify the reorientation relaxation time of the dopant molecule in the surface layers;⁴¹ Bishop et al. analyzed the anisotropic structure of PVD glasses to quantify the relaxation time of surface molecular rotation;⁴² Mckenzie et al. used implanted $^8\text{Li}^+$ and β -detected nuclear magnetic resonance (NMR) to quantify the γ -relaxation time of polystyrene at the free surface;⁴³ Hao et al. measured the evolution of wetting ridge to quantify the Rouse relaxation and reptation relaxation at the entangled polystyrene surface;⁴⁴ Zhang et al. adopted electron correlation microscopy (ECM) to quantify the surface structural relaxation in an autocorrelated manner for metallic nanowires;⁴⁵ This idea of autocorrelation is also prevalent in using simulations to quantify the relaxation time at the free surface of polymers.⁴⁶ When the material is prepared into nanometer-scale films, the film property is dominated by its surface region. In this case, the change of properties, such as T_g or dewetting rate, can be also used to quantify the enhanced surface mobility.^{47,48}

Apart from the above-mentioned measures, the translational diffusion rate is another important characterization of mobility, and its surface value has been reported by different methods in various glass types. The surface diffusivity of glasses can be quantified by monitoring the evolution of surface contours driven by the surface tension. Different types of surface contours are collected in Figure 1.4, including surface gratings, nano-holes, nano steps, and depletion zones at the edge of surface crystals.

- 1) Zhu et al. first reported using surface sinusoidal wave to measure the diffusion coefficient of IMC, as shown in Figure 1.4a. The surface gratings were thermally embossed by masters

and the evolution was monitored by either atomic force microscope (AFM) or light/laser diffraction. The surface diffusivity can be calculated from the decay kinetics of the gratings when the surface diffusion is confirmed to be the decay mechanism. The theoretical basis for these studies was mathematically described by Mullins in 1959.⁴⁹ Later, Cao et al. adopted a similar method to measure the diffusivity of Pd-based and Au-based metallic glasses.^{50,51} In Figure 1.4b, the decay kinetics of the surface grating of an Au-based glass was shown. Because of the fast surface crystallization, only the initial decay can be captured and used for diffusivity calculations. In this case, the surface gratings are fabricated by AFM scratching and the wavelength can be as small as 150 nanometers. Except for molecular and metallic glasses, the method of surface grating decay has also been applied to measure the surface diffusivity of polymer⁵² and chalcogenide.⁵³

- 2) The method of the capillary level of nanoholes was first developed by Ruan et al. to measure the surface diffusion of molecular glass,⁵⁴ and was recently applied to measure the diffusion of Selenium, as shown in Figure 1.4c.⁵⁵ The healing process is self-similar, meaning the evolving profiles of a nanohole will collapse by scaling its dimension with time.
- 3) The method of surface nano-steps has been developed to measure the surface mobility of polymers (Figure 1.4d).^{56,57} With its good malleability and hydrophobicity, polystyrene can be prepared into thin films with tens or hundreds of nanometer thickness, and floated at the water surface. Then, these films can be picked up by another substrate-supported polystyrene film. Surface tension drives the coarsening of the sharp steps, and the evolution of the profiles is simply self-similar, providing the rate of surface diffusion.⁵⁸

- 4) As the surrounding molecules supply the upward growth of the surface crystals, there are usually depressed grooves or depletion zones around the crystals on the initially flat amorphous surface. Similar to the capillary leveling of nano-holes and nano-steps, the profiles of the depletion zone are self-similar. Sallese et al. analyzed the depletion zone at the surface of amorphous silicon and the surface diffusion rate of silicon atom was obtained by fitting the evolution.⁵⁹ Similarly, Hasebe et al. followed the depletion zone at the surface of amorphous IMC and the obtained diffusion rate of IMC molecule agrees with that of Zhu et al. using the method of surface grating decay.
- 5) Surface diffusion rate can be also obtained by following the mean-square-displacement (MSD) of atoms in the Fickian regime (MSD changes linearly with time) in simulations. In Figure 1.4f, the MSD of o-terphenyl (OTP) over time is shown. It is found that the MSD of molecules in the surface layer is much larger than that in the bulk, suggesting a higher surface diffusivity. Such a method has also been adopted to study the surface diffusion of metals,^{60,61} silica,^{62,63} and silicates.⁶⁴

Through decades of study by multiple research groups, there accumulates a big database of surface diffusion coefficients for various amorphous materials. With this database, it is of interest to compare the diffusivity of different systems systematically and try to build up a predictive model on the surface diffusivity. In Chapter 2 and Chapter 3 of this thesis, a prediction model based on surface molecular penetration depth is developed for molecular glasses without extensive hydrogen bonding. In Chapter 4, a prediction model based on bulk fragility is developed for glasses of all kinds.

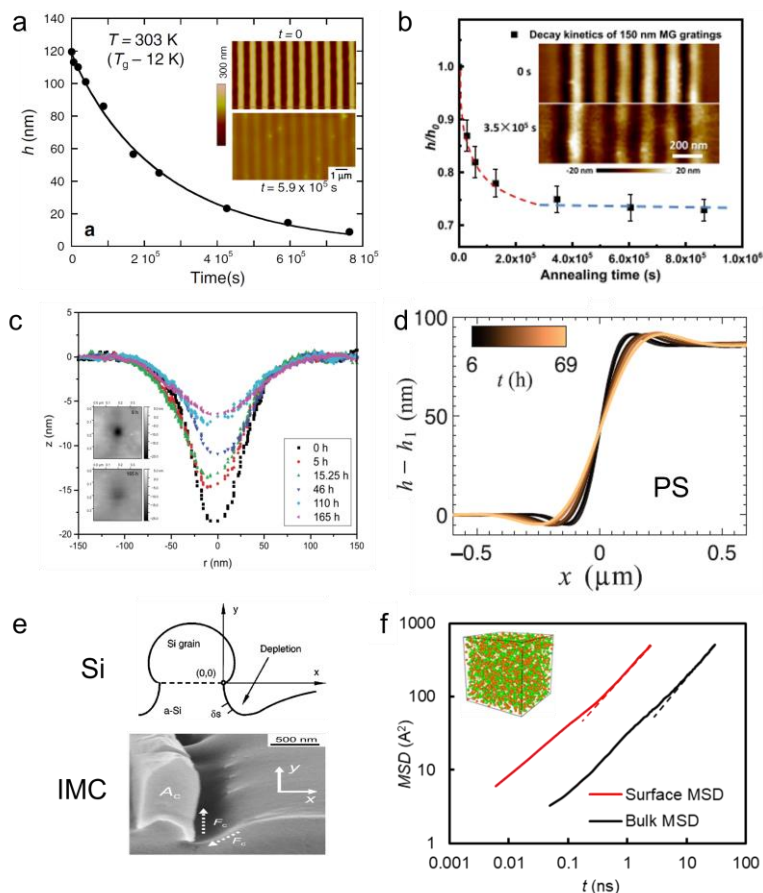


Figure 1.4. (a) The decay kinetics of the sinusoidal grating at amorphous IMC surface. Inset: AFM images of 1000 nm gratings at 0 and 5.9×10^5 s. Reproduced with permission from Zhu *et al.*, *Phys. Rev. Lett.* **2011**, *106*, 256103. Copyright 2011 American Physical Society. (b) The decay kinetics of the surface sinusoidal grating of the Au-based metallic glass. Inset: AFM images of 150 nm gratings at 0 and 3.5×10^5 s. Reproduced with permission from *Appl. Phys. Lett.* **2020**, *116*, 231601. Copyright 2020 American Institute of Physics. (c) Healing of a surface nano-hole of amorphous selenium. Inset: AFM images at 0 and 165 hours. Reproduced with permission from *J. Chem. Phys.* **2021**, *154*, 074703. Copyright 2016 American Institute of Physics. (d) Coarsening of a surface nano-step of polystyrene. Reproduced with permission from *Science*, **2014**, *343*, 994. Copyright 2014 American Association for the Advancement of Science. (e) Up: scheme of the depletion zone around a Si surface crystal. Bottom: SEM image of the depletion zone around an IMC surface crystal. Reproduced with permission from Hasebe *et al.*, *J. Phys. Chem. B* **2015**, *119*, 3304–3311. (f) MSD profiles of bulk and surface OTP glasses in simulation.

1.3.3 Theories on surface-enhanced dynamics

The theories of dynamics of amorphous materials are usually developed based on their bulk mobility, and several theories have been expanded to explain the origin of the enhanced surface dynamics.

1) Coupling Model (CM) theory

CM is based on the assumption that a primitive relaxation process (τ_0) exists and is unaffected by the interaction between molecules.⁶⁵ At a high enough temperature, the α relaxation is dominated by this primitive relaxation. Upon cooling, the strength of the intermolecular coupling starts influencing the dynamics and the α relaxation decouples from the primitive relaxation. The decoupling starts from t_c , which is about 2 ps for fragile molecular glasses, and is written as

$$\tau_\alpha = (t_c^{-n} \tau_0)^{1/(1-n)} \quad (1.3.1)$$

where n is the coupling factor and varies with systems by their intermolecular forces. Its value can be obtained by fitting the bulk relaxation kinetics using Kohlrausch–Williams–Watt (KWW).

To extend this to surfaces, it is assumed that the surface molecules are less influenced by the intermolecular interactions as they have fewer nearest neighbors, and the surface relaxation time is the primitive relaxation time, $\tau_{\text{surf}} = \tau_0$.⁶⁶ In this case, eq. 1.3.1 can be rewritten as

$$\tau_\alpha / \tau_{\text{surf}} = (\tau_\alpha / t_c)^n \quad (1.3.2)$$

2) Radom First-Order Transition (RFOT) theory

RFOT divides the amorphous glass into mosaic regions and assumes each region presents a specific metastable amorphous state, separated by the dynamic barriers in the free energy landscape.⁶⁷ These barriers, written as F^* , determine the glass transition and are a sum of the reconfiguration entropy and the interfacial free energy. The α relaxation time, τ_a , of the glasses can be then calculated by

$$\tau_\alpha = \tau_0 e^{F^*/kT} \quad (1.3.3)$$

where $\tau_0 = 1$ ps for molecular glasses.

To extend this to surfaces, Stevenson and Wolynes simply assumed the surface energetic barrier is half of the bulk one.⁶⁸ In this way, the surface relaxation time τ_{surf} can be obtained from eq. 1.3.3 as:

$$\tau_\alpha / \tau_{\text{surf}} = (\tau_\alpha / \tau_0)^{0.5} \quad (1.3.4)$$

Similarities can be observed between eq. 1.3.2 and eq. 1.3.4. Firstly, both suggest that there is a power-law relationship between bulk and surface relaxation time, with n being the exponent for CM and 0.5 for RFOT. Secondly, both equations suggest the surface relaxation starts to decouple from the bulk relaxation at a specific physical state, when the bulk relaxation time is 2 ps in CM and 1 ps in RFOT. Given that the two theories have different origins, these similarities are intriguing and will be discussed more in Chapter 3 and Chapter 4.

3) Elastically Collective Nonlinear Langevin Equation (ECNLE) theory

In contrast to considering the glasses “mosaicly” in ROFT, ECNLE considers the microscopic jumping process of individual molecules or atoms. During the movement, two energy barriers are counted: local cage constraint F_B , which is dictated by the effective force due to the nearest

neighbors, and long-range elastic penalty F_{elastic} , which is due to the reconfiguration of the particles outside the cage. By knowing the energetic barrier, Mirigian and Schweizer calculated the mean alpha relaxation time using Kramers theory⁶⁹:

$$\tau_{\alpha} = \tau_s \left[1 + \frac{2\pi k_B T}{d^2 \sqrt{K_0 K_B}} e^{\frac{F_B + F_{\text{elastic}}}{k_B T}} \right] \quad (1.3.5)$$

Where k_B is the Boltzman constant, K_0 the local stiffness, K_B the barrier curvature and τ_s the nonactive short relaxation time.

To extend the theory to surfaces, Mirigian and Schweizer modified the energy barriers of local cage constraint and elastic penalty at the surface by considering fewer nearest neighbors and less extended out-cage displacement.⁷⁰ With this surface modification, ECNLE is able to predict not only the relaxation time at the top surface but also local relaxation time changing with the penetration depth into the bulk. By further modifying the local-cage barrier into a step-wise geometry with penetration into the bulk, ECNLE is able to reproduce the double-exponential mobility gradient beneath the surface⁷¹, which has been observed by simulations⁷² and experiments⁷³.

As might be noticed, none of the above-mentioned theories considers the structural or density change of the surfaces from their bulk contour. The question then goes to “will the local surface structure strongly influence the local dynamics?” This is an interesting question and is only possible to be resolved in simulations. So far, there are multiple simulation results supporting that the structural change is not the major reason of the enhanced dynamics at the free surface. The arguments include: 1) the surface-induced mobility gradient extends much deeper into the bulk than the density gradient, and mobility enhancement still exists even when the local structure is confined to the bulk structure by soft interfaces.⁷⁴ 2) the effort by machine learning on the

correlation between local structure and surface diffusion indicates that the largely enhanced surface mobility cannot be easily explained by the surface structural changes.⁷⁵

1.4 Immobilizing surfaces with surface coating

As discussed previously, the fast surface dynamics usually induce a fast surface crystallization rate and eventual material failure. And the situation gets worse when the material is prepared into the geometries with a high surface-to-volume ratio, such as particles or thin films.⁷⁶ To suppress the fast surface crystallization, an effective method would be immobilizing the surface molecules. Wu et al. coated the surface of amorphous IMC with a thin layer of gold and observed a significant delay in the surface crystallization.⁷⁷ Furthermore, they developed the method of using polyelectrolytes to coat amorphous drugs. The basic assumption is that the surface of an ionizable drug can be coated by a polymer, which bears opposite charges, when the amorphous drug is immersed into the polymer solution. So far, this method has been tested in various drug molecules with different polyelectrolyte counterions^{78,79,80} and they are summarized in Figure 1.5.

It was confirmed that the crystallization rate of amorphous drugs is dramatically suppressed by this thin layer of polymer coating both in dry and humid conditions. For instance, chitosan-coated IMC particles remain amorphous after 15 days at 303 K/75 % RH, when the uncoated particles have already been fully crystallized. It is surprising that the prolonged physical stability is not the only benefit of polymer coating. The following pharmaceutically interesting properties are also proven to be improved: 1) particle flowability: as the polymer coatings modify the physical and chemical environment at the free surfaces, it could smoothen the particle surface⁸¹ and reduces the cohesion between particles. 2) particle tabletability: it was proposed that two factors dominate the tabletability, bonding area and bonding strength.⁸² The former is determined by the elastic deformation during compaction and the latter by the interaction between the compacted interfaces.

Since the coating is achieved by electrostatic deposition, only one layer of the polymer would be coated at the surface. The thin coating layer will not strongly change the mechanical strength of drug particles but could strengthen the interfacial attraction, e.g., inducing more hydrogen bonds.⁸³

3) particle wetting: as the introduction of the hydroxyl group strengthens the interaction between the particle and water, the polymer coating could improve the wettability and there are reports of using hydrophilic polymer coating to improve the wetting of medical devices.⁸⁴ 4) elongated supersaturation: the amorphous drugs have a higher solubility than their crystalline counter, while, at the same time, their crystallization during dissolving will eliminate this supersaturation. This is observed as spring-parachute phenomenon. The surface coating could delay the crystallization during dissolving and thus, maintain the supersaturation, leading to a higher area-under-curve (AUC) and better bioavailability.

We will discuss in detail about this polyelectrolyte coating method in Chapter 6, including the detailed sample-preparation methods, improved physical stability and other pharmaceutically interesting properties. Because of the robust electrostatic interaction and fast coating process (usually 10 s is good enough to form coating), we anticipate this coating process can be achieved simultaneously by different process units during manufacture, including homogenization, milling and granulation.

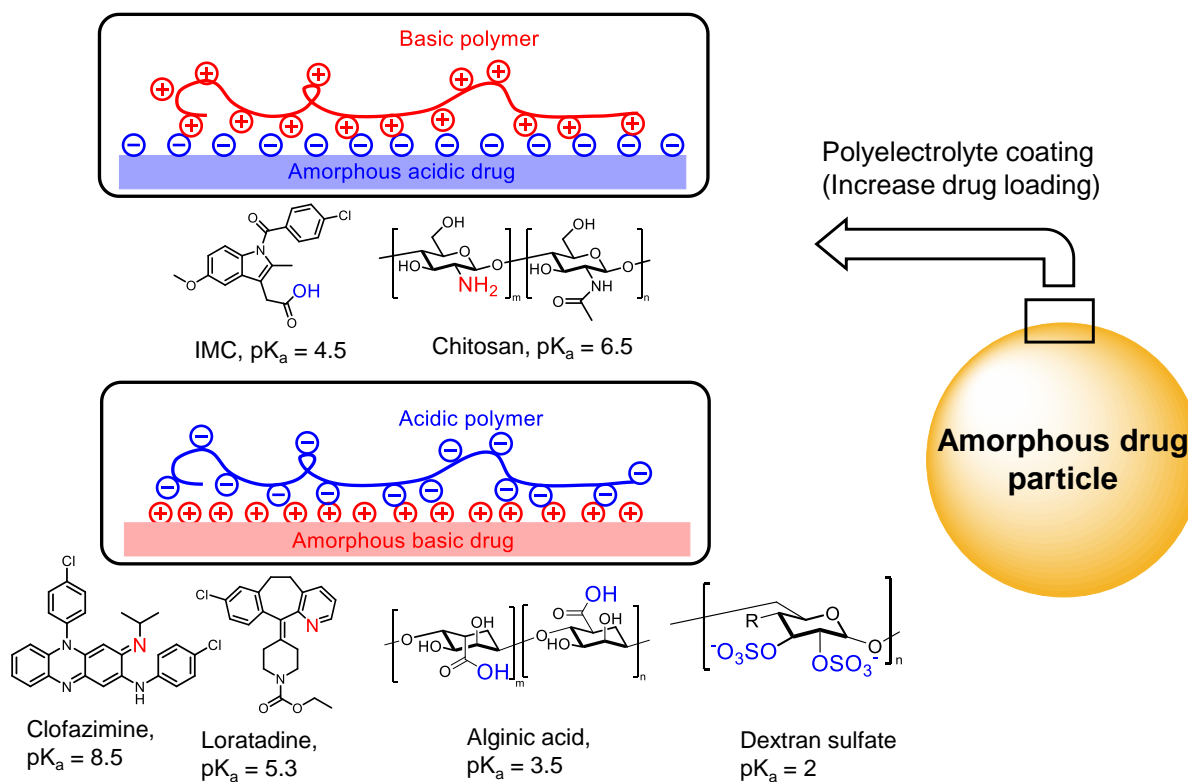


Figure 1.5. Polyelectrolyte coating for amorphous drug particles. To achieve the coating, amorphous drugs are immersed into the aqueous polymer solution, where the pH was adjusted between the pK_a s of drug and polymer. The strategy can be applied to an acidic drug (IMC) with a basic polymer (chitosan) or to a basic drug (CFZ or LRT) with an acidic polymer (Alginic acid or Dextran sulfate).

1.5 Polyamorphism

As amorphous phase is a physical state where atoms/molecules are randomly packed, it is counterintuitive that there are distinguishable amorphous structures of the same substance connected by first order transition. Though much rarer than the polymorphism in crystals, polyamorphism attracts recent attention in the field of glass science and is found existent in various systems, including elemental liquids (S,⁸⁵ Si⁸⁶, P⁸⁷, possibly C⁸⁸), oxides⁸⁹ and molecular liquids (water,⁹⁰ triphenyl phosphite,⁹¹ n-butanol⁹² and D-mannitol⁹³). Recent attention has also been attracted to the observed polyamorphism in metallic systems.⁹⁴ Overall, there is accumulated evidence to show that such polyamorphism exists in multiple glass types.

The liquid phases of a polyamorphic material differ in various physical properties, including density, short-range atom/molecular ordering, dynamics, relative free energy, and interfacial tension.⁹⁵ To distinguish these changes, various techniques have been adopted:

1. Calorimetry: as the transition between the two amorphous phases is first-order, an exothermal or endothermal signal is expected during the transition. The enthalpy of the transitions has been determined by calorimetry as 0.54, 7.0 and 12 kJ/mol for water, TPP and D-mannitol, respectively.^{96,97,93} Furthermore, the reversibility of the polyamorphic transition is an important piece of evidence to argue against the theory of nanocrystals. This reversible transition has been observed in the calorimetry experiments during isothermal annealing for TPP and D-mannitol. Except for thermodynamics, well-designed calorimetry studies could also provide information on kinetics. Zhu et al. found the LDA phase has a higher T_g than the normal liquid phase, HDA, suggesting a slower kinetics of LDA.⁹³ The same was observed by Kobayashi et al. in TPP.⁹⁸

2. Microscopy and light scattering: though both phases are transparent and non-birefringent due to their amorphous nature, the 2 % density change is expected to induce an

obvious interface between the two amorphous domains. In this case, the evolution of the second phase can be observed under either the phase-contrast microscope or light scattering.^{99,100} It should be noted that this is only achievable when the domain size of the new phase is bigger than the wavelength of visible light. For instance, the microscopy image of D-mannitol stays the same during the transition, suggesting the LDA domains are much smaller.

3. Vibration spectroscopy: Infrared and Raman spectrum respond to the vibrational and rotational motions of molecules, elucidating the molecular interaction and packing. Mishima et al. studied the polyamorphic transition of water using Raman microscopy and the OH stretching band ($3000 - 3500 \text{ cm}^{-1}$) was used to characterize hydrogen bonding (HB) change.¹⁰¹ It was shown that the hydrogen bonding strengthens during the transition from HDA to LDA. Similar observations have been observed by Murata et al. and Zhu et al during the polyamorphic transition of water-glycerol mixture¹⁰² and D-mannitol⁹³, respectively.

4. X-ray diffraction: X-ray scattering experiment has been the gold standard for determining the structure of crystalline materials. To characterize the structure of amorphous phases, the method of pair distribution functions (PDFs) is developed. PDF describes the density modulation relative to bulk density as a function of distance r , with which the short- mid-range order of amorphous material can be extracted. By analyzing the PDF of HDA and LDA phases of water, Bizid et al. observed a significant difference in the region $r = 3.5 - 4.5 \text{ \AA}$, corresponding to the neighboring distance between unbound water molecules in the second coordination shell.¹⁰³ This suggests HB changes during the transition, consistent with the change in Raman spectrometry. Other than PDF, small angle x-ray diffraction (SAXS) has also been used to characterize the structural change. Murata et al. observed a continuously-increasing peak at $q = 0.8 \text{ nm}^{-1}$ with SAXS during the polyamorphic transition of TPP, which was attributed to the domain size of the locally

avored structure in the second amorphous phase. A similar observation by us in D-mannitol will be discussed in detail in Chapter 7.

1.6 Contribution of this thesis

This thesis focuses on the surface dynamics, surface modification and bulk structure of amorphous materials. Chapter 2 and Chapter 3 show that the surface molecular penetration depth determines the surface diffusion of molecular glasses. Chapter 4 extends the survey to all types of glasses and finds the strong correlation between bulk fragility and surface diffusion, providing a valuable empirical model to predict surface diffusion. Chapter 5 considers the dopant effect on the surface dynamics of amorphous drugs and finds a principle of concentration-temperature superposition to predict the plasticizer effect from water and surfactant. Chapter 6 applies surface coating to amorphous drugs with significant improvement of physical stability, wetting by aqueous media, dissolution rate, powder flow, and tabletability. Chapter 7 studies the structural change during the polyamorphic transition of D-mannitol. Overall, this thesis is organized by the following questions: how surface dynamics is tuned by intrinsic molecular properties, how it responds to a secondary additive, how to apply the knowledge of surface dynamics to stable amorphous pharmaceuticals and what structures are changed between the two amorphous phase of D-mannitol.

While the molecular/atomic diffusion at the free surface is usually faster than that in the bulk, it was recently noticed that the degree of enhancement varies in different systems. Chapter 2 and Chapter 3 consider this variation in molecular glasses. Figure 1.6 compares the surface diffusion rate, D_s , and bulk diffusion rate, D_v , of different molecular glasses: ortho-terphenyl (OTP), tris-naphthyl benzene (TNB), indomethacin (IMC), polystyrene (PS) oligomers (1110 and 1700 g/mole), posaconazole (POS) and 4,4',4''-Tris[(3-methylphenyl)phenylamino]triphenylamine

(MTDATA). The temperature has been scaled by T_g and in this format, the D_v values cluster together, while the D_s values are widely different. Figure 1.6 suggests that the surface diffusivity of different organic glasses could vary by 5 orders of magnitude while their bulk diffusivity shares the same value. As will be discussed in Chapter 2 and Chapter 3, this arises from the different penetration depths of surface molecules into the bulk glass.

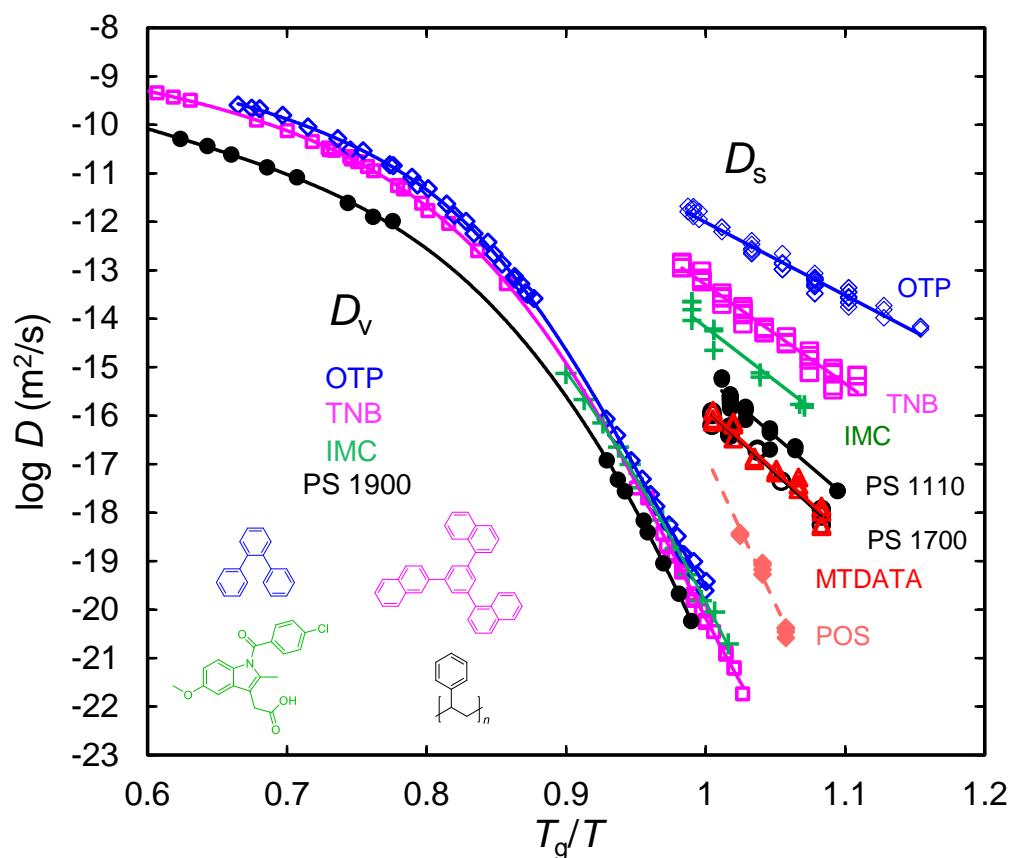


Figure 1.6. Diffusivity plotted against temperature, scaled by the glass transition temperature T_g . Bulk diffusivity D_v of different systems clusters together, especially around T_g . However, surface diffusivity D_s shows a big system-to-system variation. Inset: molecular structures of OTP, TNB, IMC and PS oligomers.

Chapter 2 initiates this study with two rod-like molecules POS and itraconazole (ITZ). The two molecules have been proven to show preferred surface orientation at the free surface. Together with their elongated molecular shape, the two would have much bigger penetration depth into the bulk than quasi-spherical molecules of similar volume. By using the method of surface grating decay, it is found that surface diffusion in these two molecules is significantly slower than in the glasses of quasi-spherical molecules. Between the two systems, ITZ shows slow surface diffusion. This results from the fact that ITZ forms liquid-crystalline (LC) structure and surface molecules would orientate more vertically at the free surface. All of these observations suggest a strong correlation between surface diffusion and surface molecular penetration depth.

Chapter 3 further test this correlation by measuring the surface diffusion of MTDATA, which has a new molecular geometry, discotic shape. The surface diffusivity of MTDATA is analyzed along with the results on other molecular glasses without extensive hydrogen bonds. These systems cover a wide range of molecular geometries from rod-like to quasi-spherical to discotic and their surface diffusion coefficients vary by 9 orders of magnitude. We find that the variation is well explained by the existence of a steep surface mobility gradient and the anchoring of surface molecules at different depths. Quantitative analysis of these results supports a recently proposed double-exponential form for the mobility gradient: $\log D(T, z) = \log D_v(T) + [\log D_0 - \log D_v(T)] \exp(-z / \xi)$, where $D(T, z)$ is the depth-dependent diffusion coefficient, $D_v(T)$ is the bulk diffusion coefficient, $D_0 \approx 10^{-8} \text{ m}^2/\text{s}$, and $\xi \approx 1.5 \text{ nm}$. Assuming a representative bulk diffusion coefficient for fragile glass formers, it reproduces the presently known surface diffusion rates within 0.6 decade. Our result is relevant for predicting the surface diffusion rates in molecular glasses.

Chapter 4 extends the survey to all types of glasses. However, the interactions between diffusion units vary significantly across different glasses, from van der Waals interaction in several kJ/mole

to metallic or covalent bonds in hundreds of kJ/mol. At the same time, the diffusion units also vary from molecules on nanometer scale to atoms on angstrom scale. These lead to the fact that the finding in Chapter 2 and Chapter 3 cannot be directly extended to other glasses types. Nevertheless, it is found that the variation of surface diffusivity is even bigger when compared across glass types. In fragile molecular glasses, surface diffusion can be a factor of 10^8 faster than bulk diffusion at the glass transition temperature, while in the strong system SiO₂, the enhancement is only a factor of 10. Between these two extremes lie systems of intermediate fragility, including metallic glasses and amorphous selenium and silicon. This indicates that stronger liquids have greater resistance to dynamic excitation from bulk to surface and enables the prediction of surface diffusion using the value of bulk fragility.

Chapter 5 concerns the dopant effect on the surface dynamics of amorphous drugs, particularly the plasticizing effect from moisture absorption and surfactant doping. Both components are of pharmaceutical interest and prevailed in the developed drug formulations. In this study, the surface mobility of amorphous indomethacin was measured using the method of surface grating decay in the presence of moisture and the surfactant Tween 20. It is found that both components significantly enhance the surface mobility, and their effects are well described by the principle of *concentration-temperature superposition* (CTS); that is, the same surface dynamics is observed at the same T/T_g , where T is temperature and T_g the composition-dependent glass transition temperature. For the surfactant-doped system, the T_g used is the value for the surface layer to account for the surface enrichment of the surfactant (determined by X-ray Photoelectron Spectroscopy). The CTS principle allows the prediction of the surface dynamics and surface-mediated transformation of multi-component amorphous materials.

Chapter 6 applies the surface coating to stabilize amorphous drugs. The fast surface dynamics accelerates the crystallization process at the free surface and eventually induces fast material failure. To inhibit the fast surface crystallization, Chapter 6 develops the method of polymer coating to immobilize surface molecules. We show that a nanolayer of chitosan can be deposited at the free surface of amorphous IMC. Chitosan is a linear polysaccharide derived from chitin, whose chain segments are randomly distributed D-glucosamine and N-acetyl-D-glucosamine. The glucosamine group is weakly basic and protonated below $\text{pH} \approx 6.5$ (the pK_a of chitosan), making chitosan a polycation at low pH. From the pK_a values of chitosan (6.5) and IMC (4.5), we expect that in the pH range of 4.5–6.5, IMC is negatively charged, and chitosan is positively charged. The charge-charge interaction between opposite ions attracts chitosan to the surface of IMC to form a layer of coating. Because of the mechanism of electrostatic interaction, the coating layer is only several nanometers, enabling the potential for new formulations with high drug loading.

Chapter 7 studies the structural change during the polyamorphic transition of D-mannitol. Polyamorphism, the existence of two amorphous phases of the same substance separated by a first-order transition, is an important and often controversial phenomenon. The polyamorphism of D-mannitol has been described as “the most recent (and perhaps the cleanest) example”. We show that the normal liquid of D-mannitol transforms near its glass transition temperature to a low-density amorphous phase (LDA) with new mesoscopic order, notably a 3 nm density modulation. In the LDA, the non-polar hydrocarbon groups are farther apart from each other, while the hydrogen-bonded (HB) structure is more ordered. The reorganization of the HB network occurs by rearranging the second coordination shells and beyond, leading to the prepeaks in the scattering pattern. The LDA has enhanced smectic-like order as seen in the crystalline structures but the new

3 nm density modulation is completely devoid of any crystalline counterpart. This new length scale is attributed to the densely nucleated LDA domains in the normal liquid.

In summary, this thesis considers the surface dynamics of amorphous materials from three different aspects: intrinsic determining factors, the response to secondary dopants, and the application for stable amorphous materials. The bulk structures of two polyamorphic phases of D-mannitol are also studied. The theoretical understanding and applicable ideas would be helpful to improve the quality of amorphous materials and be used as a guide for the synthesis of new-generation glasses.

1.7 References

¹ Yu, L. Amorphous Pharmaceuticals – Preparation, Characterization and Stabilization. *Drug Delivery Rev.* **2001**, *48*, 27-42.

² Zou, S.-J.; Shen, Y.; Xie, F.-M.; Chen, J.-D.; Li, Y.-Q.; Tang, J.-X. Recent Advances in Organic Light-Emitting Diodes: Toward Smart Lighting and Displays. *Mater. Chem. Front.* **2020**, *4*, 788–820.

³ Raoux, S.; Welnic, W.; Ielmini, D. Phase Change Materials and Their Application to Nonvolatile Memories. *Chem. Rev.* **2010**, *110* (1), 240-267.

⁴ Granzow, N.; Schmidt, M. A.; Chang, W.; Wang, L.; Coulombier, Q.; Troles, J.; Toupin, P.; Hartl, I.; Lee, K. F.; Fermann, M. E.; Wondraczek, L.; Russell, P. S. Mid-infrared supercontinuum generation in As₂S₃-silica "nano-spike" step-index waveguide. *Opt. Express* **2013**, *21* (9), 10969-10977.

⁵ Teerakapibal, R.; Huang, C.; Gujral, A.; Ediger, M. D.; Yu, L. Organic glasses with tunable liquid-crystalline order. *Phys. Rev. Lett.* **2018**, *120* (5), 055502.

⁶ Ediger, M. D. Spatially heterogeneous dynamics in supercooled liquids. *Annu. Rev. Phys. Chem.* **2000**, *51*(1), 99-128.

⁷ Hansen, C.; Stickel, F.; Berger, T.; Richert, R.; Fischer, E. W. Dynamics of glass-forming liquids. III. Comparing the dielectric α - and β -relaxation of 1-propanol and o-terphenyl. *J. Chem. Phys.* **1997**, *107*(4), 1086-1093.

⁸ Tanaka, H. Liquid–liquid transition and polyamorphism. *J. Chem. Phys.* **2020**, *153*(13), 130901.

-
- ⁹ Angell, C. A. Strong and fragile liquids. *Relaxations in complex systems* **1985**, 3-11.
- ¹⁰ R. Richert and C. A. Angell, Dynamics of glass-forming liquids. V. On the link between molecular dynamics and configurational entropy. *J. Chem. Phys.* **1998**, *108*, 9016.
- ¹¹ Pogna, E. A. A., Rodríguez-Tinoco, C., Krisch, M., Rodríguez-Viejo, J., Scopigno, T. Acoustic-like dynamics of amorphous drugs in the THz regime. *Sci. Rep.* **2013**, *3*(1), 1-6.
- ¹² Andronis, V., Zografí, G. The molecular mobility of supercooled amorphous indomethacin as a function of temperature and relative humidity. *Pharm. Res.* **1998**, *15*(6), 835-842.
- ¹³ Swallen, S. F., Ediger, M. D. Self-diffusion of the amorphous pharmaceutical indomethacin near T_g. *Soft Matter*, **2011**, *7*(21), 10339-10344.
- ¹⁴ Moura Ramos, J. J., Correia, N. T., Taveira-Marques, R., & Collins, G. The activation energy at T_g and the fragility index of indomethacin, predicted from the influence of the heating rate on the temperature position and on the intensity of thermally stimulated depolarization current peak. *Pharm. Res.* **2002**, *19*(12), 1879-1884.
- ¹⁵ Tyllinski, M., Chua, Y. Z., Beasley, M. S., Schick, C., & Ediger, M. D. Vapor-deposited alcohol glasses reveal a wide range of kinetic stability. *J. Chem. Phys.* **2016**, *145*(17), 174506.
- ¹⁶ Hasebe, M., Musumeci, D., & Yu, L. Fast surface crystallization of molecular glasses: creation of depletion zones by surface diffusion and crystallization flux. *J. Phys. Chem. B*, **2017**, *119*(7), 3304-3311.
- ¹⁷ Zhu, L.; Wong, L.; Yu, L. Surface-Enhanced Crystallization of Amorphous Nifedipine. *Mol. Pharm.* **2008**, *5*, 921 – 926.
- ¹⁸ Hasebe, M.; Musumeci, D.; Powell, C. T.; Cai, T.; Gunn, E.; Zhu, L.; Yu, L. Fast Surface Crystal Growth on Molecular Glasses and Its Termination by the Onset of Fluidity. *J. Phys. Chem. B* **2014**, *118*, 7638 – 7646.
- ¹⁹ Zhu, L.; Jona, J.; Nagapudi, K.; Wu, T. Fast Surface Crystallization of Amorphous Griseofulvin Below T_g. *Pharm. Res.* **2010**, *27*, 1558 – 1567.
- ²⁰ Gunn, E. M.; Guzei, I. A.; Yu, L. Does Crystal Density Control Fast Surface Crystal Growth in Glasses? A Study with Polymorphs. *Cryst. Growth Des.* **2011**, *11*, 3979 – 3984.
- ²¹ Kestur, U. S.; Taylor, L. S. Evaluation of the Crystal Growth Rate of Felodipine Polymorphs in the Presence and Absence of Additives as a Function of Temperature. *Cryst. Growth Des.* **2013**, *13*, 4349 – 4354.
- ²² Barták, J., Málek, J., Bagchi, K., Ediger, M. D., Li, Y., & Yu, L. Surface mobility in amorphous selenium and comparison with organic molecular glasses. *J. Chem. Phys.* **2021**, *154*(7), 074703.
- ²³ Bartak, J., Martinkova, S., & Malek, J. Crystal growth kinetics in Se–Te bulk glasses. *Cryst. Growth Des.* **2015**, *15*(9), 4287-4295.
- ²⁴ Sallese, J. M., Ils, A., Bouvet, D., Fazan, P., & Merritt, C. Modeling of the depletion of the amorphous-silicon surface during hemispherical grained silicon formation. *J. Appl. Phys.* **2000**, *88*(10), 5751-5755.

-
- ²⁵ Chen, L., Cao, C. R., Shi, J. A., Lu, Z., Sun, Y. T., Luo, P., ... & Wang, W. H. Fast surface dynamics of metallic glass enable superlatticelike nanostructure growth. *Phys. Rev. Lett.* **2017**, *118*(1), 016101.
- ²⁶ Cao, C. R., Yu, L., Perepezko, J. H. Surface dynamics measurement on a gold based metallic glass. *Appl. Phys. Lett.* **2020**, *116*(23), 231601.
- ²⁷ Jukes, P. C., Das, A., Durell, M., Trolley, D., Higgins, A. M., Geoghegan, M., et al. Kinetics of surface crystallization in thin films of poly (ethylene terephthalate). *Macromolecules* **2015**, *38*(6), 2315-2320.
- ²⁸ Delcambre, S. P., Riggleman, R. A., de Pablo, J. J., & Nealey, P. F. Mechanical properties of antiplasticized polymer nanostructures. *Soft Matter* **2010**, *6*(11), 2475-2483.
- ²⁹ S. F. Swallen, K. L. Kearns, M. K. Mapes, Y. S. Kim, R. J. McMahon, M. D. Ediger, T. Wu, L. Yu and S. Satija, *Science* **2007**, *315*, 353.
- ³⁰ Ediger, M. D., de Pablo, J., & Yu, L. Anisotropic vapor-deposited glasses: Hybrid organic solids. *Acc. Chem. Res.* **2019**, *52*(2), 407-414.
- ³¹ Ediger, M. D. Perspective: Highly stable vapor-deposited glasses. *J. Chem. Phys.* **2017**, *147*(21), 210901.
- ³² Bishop, C., Thelen, J. L., Gann, E., Toney, M. F., Yu, L., DeLongchamp, D. M., & Ediger, M. D. Vapor deposition of a nonmesogen prepares highly structured organic glasses. *Proc. Natl. Acad. Sci.* **2019**, *116*(43), 21421-21426.
- ³³ Bishop, C., Chen, Z., Toney, M. F., Bock, H., Yu, L., & Ediger, M. D. Using Deposition Rate and Substrate Temperature to Manipulate Liquid Crystal-Like Order in a Vapor-Deposited Hexagonal Columnar Glass. *J. Phys. Chem. B* **2021**, *125*(10), 2761-2770.
- ³⁴ Chen, Y., Zhu, M., Laventure, A., Lebel, O., Ediger, M. D., & Yu, L. Influence of hydrogen bonding on the surface diffusion of molecular glasses: Comparison of three triazines. *J. Phys. Chem. B* **2017**, *121*(29), 7221-7227.
- ³⁵ Guo, Y., Morozov, A., Schneider, D., Chung, J. W., Zhang, C., Waldmann, M., ... & Priestley, R. D. Ultrastable nanostructured polymer glasses. *Nature Materials*, **2012**, *11*(4), 337-343.
- ³⁶ Zhang, K., Li, Y., Huang, Q., Wang, B., Zheng, X., Ren, Y., & Yang, W. (2017). Ultrastable amorphous Sb₂Se₃ film. *The Journal of Physical Chemistry B*, *121*(34), 8188-8194.
- ³⁷ Zhang, A., Jin, Y., Liu, T., Stephens, R. B., & Fakhraai, Z. (2020). Polyamorphism of vapor-deposited amorphous selenium in response to light. *Proceedings of the National Academy of Sciences*, *117*(39), 24076-24081.
- ³⁸ Yu, H. B., Luo, Y., & Samwer, K. Ultrastable metallic glass. *Advanced Materials*, **2013**, *25*(41), 5904-5908.
- ³⁹ J. Ma, C. Yang, X. Liu, B. Shang, Q. He, F. Li, T. Wang, D. Wei, X. Liang, X. Wu, Y. Wang, F. Gong, P. Guan, W. Wang, and Y. Yang, *Sci. Adv.* **2019**, *5*, eaax7256
- ⁴⁰ X. Li, C. Zhang, Y. Sha, L. Li, D. Zhou, Z. Zhang, G. Xue, and X. Wang, *Polymer* **2017**, *111*, 67
- ⁴¹ Paeng, K., Swallen, S. F., & Ediger, M. D. Direct measurement of molecular motion in freestanding polystyrene thin films. *J. Amer. Chem. Soc.* **2011**, *133*(22), 8444-8447.

-
- ⁴² Bishop, C., Gujral, A., Toney, M. F., Yu, L., & Ediger, M. D. Vapor-deposited glass structure determined by deposition rate–substrate temperature superposition principle. *J. Phys. Chem. Lett.* **2019**, *10*(13), 3536-3542.
- ⁴³ McKenzie, I., Fujimoto, D., Karner, V. L., Li, R., MacFarlane, W. A., McFadden, R. M., et al. A β -NMR study of the depth, temperature, and molecular-weight dependence of secondary dynamics in polystyrene: Entropy–enthalpy compensation and dynamic gradients near the free surface. *J. Chem. Phys.* **2022**, *156*(8), 084903.
- ⁴⁴ Hao, Z., Ghanekarade, A., Zhu, N., Randazzo, K., Kawaguchi, D., Tanaka, K., et al. Mobility gradients yield rubbery surfaces on top of polymer glasses. *Nature*, **2021**, *596*(7872), 372-376.
- ⁴⁵ Zhang, P., Maldonis, J. J., Liu, Z., Schroers, J., Voyles, P. M. Spatially heterogeneous dynamics in a metallic glass forming liquid imaged by electron correlation microscopy. *Nature Comm.* **2018**, *9*(1), 1-7.
- ⁴⁶ Diaz Vela, D., Ghanekarade, A., Simmons, D. S. Probing the metrology and chemistry dependences of the onset condition of strong “nanoconfinement” effects on dynamics. *Macromolecules*, **2020**, *53*(11), 4158-4171.
- ⁴⁷ Ellison, C. J., Torkelson, J. M. The distribution of glass-transition temperatures in nanoscopically confined glass formers. *Nature Mater.* **2003**, *2*(10), 695-700.
- ⁴⁸ Zhang, Y., Fakhraai, Z. Decoupling of surface diffusion and relaxation dynamics of molecular glasses. *Proc. Natl. Acad. Sci. U. S. A.* **2017**, *114*(19), 4915-4919.
- ⁴⁹ Mullins, W. W. Flattening of a Nearly Plane Solid Surface due to Capillarity. *J. Appl. Phys.* **1959**, *30*, 77-83.
- ⁵⁰ Cao, C. R., Lu, Y. M., Bai, H. Y., Wang, W. H. High surface mobility and fast surface enhanced crystallization of metallic glass. *Appl. Phys. Lett.* **2015**, *107*(14), 141606.
- ⁵¹ Cao, C. R., Yu, L., Perepezko, J. H. Surface dynamics measurement on a gold based metallic glass. *Appl. Phys. Lett.* **2020**, *116*(23), 231601.
- ⁵² Zhang, W., Yu, L. Surface diffusion of polymer glasses. *Macromolecules*, **2016**, *49*(2), 731-735.
- ⁵³ Martinková, S., Valdés, D., Slang, S., Pálka, K., Barták, J. Relationship between crystal growth and surface/volume mobilities in Se₉₅Te₅ bulk glasses and thin films. *Acta Materialia*, **2021**, *213*, 116953.
- ⁵⁴ Ruan, S. *Surface mobility of organic glasses probed by nano-particles and nano-holes*. The University of Wisconsin-Madison, **2017**
- ⁵⁵ Barták, J., Málek, J., Bagchi, K., Ediger, M. D., Li, Y., Yu, L. Surface mobility in amorphous selenium and comparison with organic molecular glasses. *J. Chem. Phys.* **2017**, *154*(7), 074703.
- ⁵⁶ Chai, Y., Salez, T., Forrest, J. A. Using Mw Dependence of Surface Dynamics of Glassy Polymers to Probe the Length Scale of Free-Surface Mobility. *Macromolecules*, **2020**, *53*(3), 1084-1089.
- ⁵⁷ Chai, Y., Salez, T., McGraw, J. D., Benzaquen, M., Dalnoki-Veress, K., Raphaël, E., Forrest, J. A. A direct quantitative measure of surface mobility in a glassy polymer. *Science*, **2014**, *343*(6174), 994-999.

-
- ⁵⁸ Salez, T., McGraw, J. D., Cormier, S. L., Bäumchen, O., Dalnoki-Veress, K., Raphaël, E. Numerical solutions of thin-film equations for polymer flows. *Eur. Phys. J. E* **2012**, *35*(11), 1-9.
- ⁵⁹ Sallèse, J. M., Ils, A., Bouvet, D., Fazan, P., Merritt, C. Modeling of the depletion of the amorphous-silicon surface during hemispherical grained silicon formation. *J. Appl. Phys.* **2000**, *88*(10), 5751-5755.
- ⁶⁰ Chen, H., Qu, B., Li, D., Zhou, R., Zhang, B. Atomic structure and dynamics properties of Cu₅₀Zr₅₀ films. *J. Appl. Phys.* **2018**, *123*(2), 025307.
- ⁶¹ Annamareddy, A., Li, Y., Yu, L., Voyles, P. M., Morgan, D. Factors correlating to enhanced surface diffusion in metallic glasses. *J. Chem. Phys.* **2021**, *154*(10), 104502.
- ⁶² Roder, A., Kob, W., Binder, K. Structure and dynamics of amorphous silica surfaces. *J. Chem. Phys.* **2001**, *114*(17), 7602-7614.
- ⁶³ Li, Y., Annamareddy, A., Morgan, D., Yu, Z., Wang, B., Cao, C. et al. Surface diffusion is controlled by bulk fragility across all glass types. *Phys. Rev. Lett.* **2022**, *128*(7), 075501.
- ⁶⁴ Annamareddy, A., Molina-Ruiz, M., Horton-Bailey, D., Hellman, F., Li, Y., Yu, L., Morgan, D. Compositional trends in surface enhanced diffusion in lead silicate glasses. *Comput. Mater. Sci.* **2022**, *206*, 111304.
- ⁶⁵ K. L. Ngai, Relaxation and Diffusion in Complex Systems. *Springer*, New York, **2011**.
- ⁶⁶ Capaccioli, S., Ngai, K. L., Paluch, M., Prevosto, D. Mechanism of fast surface self-diffusion of an organic glass. *Phys. Rev. E* **2012**, *86*(5), 051503.
- ⁶⁷ Lubchenko, V., Wolynes, P. G. Theory of structural glasses and supercooled liquids. *Annu. Rev. Phys. Chem.* **2007**, *58*, 235-266.
- ⁶⁸ Stevenson, J. D., Wolynes, P. G. On the surface of glasses. *J. Chem. Phys.* **2008**, *129*(23), 234514.
- ⁶⁹ Mirigian, S., Schweizer, K. S. Elastically cooperative activated barrier hopping theory of relaxation in viscous fluids. I. General formulation and application to hard sphere fluids. *J. Chem. Phys.* **2014**, *140*(19), 194506.
- ⁷⁰ Mirigian, S., Schweizer, K. S. Theory of activated glassy relaxation, mobility gradients, surface diffusion, and vitrification in free standing thin films. *J. Chem. Phys.* **2015**, *143*(24), 244705.
- ⁷¹ Phan, A. D., Schweizer, K. S. Influence of longer range transfer of vapor interface modified caging constraints on the spatially heterogeneous dynamics of glass-forming liquids. *Macromolecules*, **2019**, *52*(14), 5192-5206.
- ⁷² Scheidler, P., Kob, W., Binder, K. Cooperative motion and growing length scales in supercooled confined liquids. *EPL Europhysics Lett.* **2002**, *59*(5), 701.
- ⁷³ Li, Y., Bishop, C., Cui, K., Schmidt, J. R., Ediger, M. D., Yu, L. Surface diffusion of a glassy discotic organic semiconductor and the surface mobility gradient of molecular glasses. *J. Chem. Phys.* **2022**, *156*(9), 094710.
- ⁷⁴ Baschnagel, J., Varnik, F. Computer simulations of supercooled polymer melts in the bulk and in confined geometry. *J. Condens. Matter Phys.* **2005**, *17*(32), R851.

-
- ⁷⁵ Sussman, D. M., Schoenholz, S. S., Cubuk, E. D., Liu, A. J. Disconnecting structure and dynamics in glassy thin films. *Proc. Natl. Acad. Sci. U. S. A.* **2017**, *114*(40), 10601-10605.
- ⁷⁶ Zhu, L., Jona, J., Nagapudi, K., Wu, T. Fast surface crystallization of amorphous griseofulvin below T_g. *Pharm. Res.* **2010**, *27*(8), 1558-1567.
- ⁷⁷ Wu, T., Sun, Y., Li, N., de Villiers, M. M., Yu, L. Inhibiting surface crystallization of amorphous indomethacin by nanocoating. *Langmuir*, **2007**, *23*(9), 5148-5153.
- ⁷⁸ Li, Y., Yu, J., Hu, S., Chen, Z., Sacchetti, M., Sun, C. C., Yu, L. Polymer nanocoating of amorphous drugs for improving stability, dissolution, powder flow, and tableability: The case of chitosan-coated indomethacin. *Mol. Pharm.* **2019**, *16*(3), 1305-1311.
- ⁷⁹ Gui, Y., Chen, Y., Chen, Z., Jones, K. J., Yu, L. Improving stability and dissolution of amorphous clofazimine by polymer nano-coating. *Pharm. Res.* **2019**, *36*(5), 1-7.
- ⁸⁰ Zeng, A., Yao, X., Gui, Y., Li, Y., Jones, K. J., Yu, L. Inhibiting surface crystallization and improving dissolution of amorphous loratadine by dextran sulfate nanocoating. *J. Pharm. Sci.* **2019**, *108*(7), 2391-2396.
- ⁸¹ Genina, N., Rääkkönen, H., Ehlers, H., Heinämäki, J., Veski, P., Yliruusi, J. Thin-coating as an Alternative Approach to Improve Flow Properties of Ibuprofen Powder. *Int. J. Pharm.* **2010**, *387*, 65–70.
- ⁸² Sun, C. C. Decoding powder tableability: roles of particle adhesion and plasticity. *J. Adhes. Sci. Technol.* **2011**, *25*(4-5), 483-499.
- ⁸³ Shi, L., Sun, C. C. Overcoming poor tableability of pharmaceutical crystals by surface modification. *Pharm. Res.* **2011**, *28*(12), 3248-3255.
- ⁸⁴ Nagaoka, S., Akashi, R. Low-friction hydrophilic surface for medical devices. *Biomaterials*, **1990**, *11*(6), 419-424.
- ⁸⁵ Henry, L., Mezouar, M., Garbarino, G., Sifré, D., Weck, G., Datchi, F. Liquid–liquid transition and critical point in sulfur. *Nature*, **2020**, *584*(7821), 382-386.
- ⁸⁶ McMillan, P. F., Wilson, M., Daisenberger, D., Machon, D. A density-driven phase transition between semiconducting and metallic polyamorphs of silicon. *Nature Mater.* **2005**, *4*(9), 680-684.
- ⁸⁷ Katayama, Y., Mizutani, T., Utsumi, W., Shimomura, O., Yamakata, M., Funakoshi, K. I. A first-order liquid–liquid phase transition in phosphorus. *Nature*, **2000**, *403*(6766), 170-173.
- ⁸⁸ Van Thiel, M., Ree, F. H. High-pressure liquid-liquid phase change in carbon. *Phys. Rev. B*, **1993**, *48*(6), 3591.
- ⁸⁹ Brazhkin, V. V., Lyapin, A. G. High-pressure phase transformations in liquids and amorphous solids. *J. Phys. Condens. Matter* **2003**, *15*(36), 6059.
- ⁹⁰ Gallo, P., Amann-Winkel, K., Angell, C. A., Anisimov, M. A., Caupin, F., Chakravarty, C. et al. Water: A tale of two liquids. *Chem. Rev.* **2016**, *116*(13), 7463-7500.
- ⁹¹ Tanaka, H., Kurita, R., Mataka, H. Liquid-liquid transition in the molecular liquid triphenyl phosphite. *Phys. Rev. Lett.* **2004**, *92*(2), 025701.

-
- ⁹² Kurita, R., Tanaka, H. On the abundance and general nature of the liquid–liquid phase transition in molecular systems. *J. Phys. Condens. Matter* **2005**, *17*(27), L293.
- ⁹³ Zhu, M., Wang, J. Q., Perepezko, J. H., Yu, L. Possible existence of two amorphous phases of d-mannitol related by a first-order transition. *J. Chem. Phys* **2015**, *142*(24), 244504.
- ⁹⁴ Du, Q., Liu, X., Fan, H., Zeng, Q., Wu, Y., Wang, H. et al. Reentrant glass transition leading to ultrastable metallic glass. *Mater. today*, **2020**, *34*, 66-77.
- ⁹⁵ Tanaka, H. Liquid–liquid transition and polyamorphism. *J. Chem. Phys.* **2020**, *153*(13), 130901.
- ⁹⁶ Handa, Y. P., Mishima, O., Whalley, E. High-density amorphous ice. III. Thermal properties. *J. Chem. Phys.* **1986**, *84*(5), 2766-2770.
- ⁹⁷ Miltenburg, K. V., Blok, K. Calorimetric Investigation of a new solid phase in triphenylphosphite. *J. Chem. Phys.* **1996**, *100*(41), 16457-16459.
- ⁹⁸ Kobayashi, M., Tanaka, H. The reversibility and first-order nature of liquid–liquid transition in a molecular liquid. *Nature Comm.* **2016**, *7*(1), 1-8.
- ⁹⁹ Tanaka, H. Importance of many-body orientational correlations in the physical description of liquids. *Faraday Discuss.* **2013**, *167*, 9-76.
- ¹⁰⁰ Shimizu, R., Kobayashi, M., Tanaka, H. Evidence of liquid-liquid transition in triphenyl phosphite from time-resolved light scattering experiments. *Phys. Rev. Lett.* **2014**, *112*(12), 125702.
- ¹⁰¹ Mishima, O., Suzuki, Y. Propagation of the polyamorphic transition of ice and the liquid–liquid critical point. *Nature*, **2002**, *419*(6907), 599-603.
- ¹⁰² Murata, K. I., Tanaka, H. Liquid–liquid transition without macroscopic phase separation in a water–glycerol mixture. *Nature Mater.* **2012**, *11*(5), 436-443.
- ¹⁰³ Bizid, A., Bosio, L., Defrain, A., Oumezzine, M. Structure of high-density amorphous water. I. X-ray diffraction study. *J. Chem. Phys.* **1987**, *87*(4), 2225-2230.

Chapter 2 Surface diffusion in glasses of rod-like molecules posaconazole and itraconazole: Effect of interfacial molecular alignment and bulk penetration

Yuhui Li¹, Wei Zhang^{1,3}, Camille Bishop², Chengbin Huang¹, M. D. Ediger², Lian Yu^{1*}

¹ School of Pharmacy, University of Wisconsin-Madison, Madison, WI, 53705, USA

² Department of Chemistry, University of Wisconsin-Madison, Madison, WI, 53706, USA

³ Current Address: Genentech Inc., South San Francisco, CA, 94080, USA

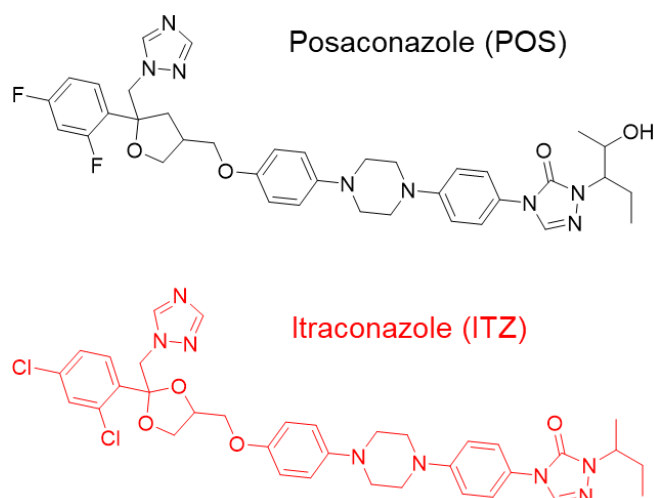
As published in *Soft Matter*, 2020, 16, 5062-5070

2.1 Abstract

The method of surface grating decay has been used to measure surface diffusion in the glasses of two rod-like molecules posaconazole (POS) and itraconazole (ITZ). While structurally similar antifungal medicines, ITZ forms liquid-crystalline phases while POS does not. Surface diffusion in these systems is significantly slower than in the glasses of quasi-spherical molecules of similar volume when compared at the glass transition temperature T_g . Between the two systems, ITZ has slower surface diffusion. These results are explained on the basis of the near-vertical orientation of the rod-like molecules at the surface and their deep penetration into the bulk where mobility is low. For molecular glasses without extensive hydrogen bonds, we find that the surface diffusion coefficient at T_g decreases smoothly with the penetration depth of surface molecules and the trend has the double-exponential form for the surface mobility gradient observed in simulations. This supports the view that these molecular glasses have a similar mobility vs depth profile and their different surface diffusion rates arise simply from the different depths at which molecules are anchored. Our results also provide support for a previously observed correlation between the rate of surface diffusion and the fragility of the bulk liquid.

2.2 Introduction

Surface mobility plays an important role in the physical stability of molecular glasses. Surface molecules can diffuse much faster than bulk molecules,^{1,2,3} and this has been attributed to reduced local caging effect and smaller elastic penalty for rearrangement.^{4,5} Surface mobility enables fast crystal growth in molecular glasses, reducing the shelf life of amorphous drugs^{6,7} and motivating coating technologies for stabilization.⁸ Surface mobility allows preparation of “ultra-stable glasses” by physical vapor deposition, taking advantage of the fast equilibration of just-deposited molecules before they are firmly embedded in the bulk.^{9,10}



Scheme 2.1. Molecular structures of posaconazole (POS) and itraconazole (ITZ).

Surface diffusion can be measured by observing the evolution of surface contours driven by surface tension.^{1,2,11,12,13,14} Previous work in this area has focused on molecular glasses containing quasi-spherical molecules or slightly elongated molecules.³ Motivated by recent attention to highly anisotropic glasses prepared with non-spherical molecules,¹⁵ we have studied surface diffusion in the glasses of two rod-like molecules, posaconazole (POS) and itraconazole (ITZ) (see Scheme 2.1), both antifungal drugs.^{16,17} While having similar structures, the two molecules differ in that ITZ forms liquid crystals (LC),¹⁸ while POS does not.¹⁹ This provides an opportunity to study the

effect of bulk LC structure on surface diffusion. We find that surface diffusion is significantly slower in the glasses of POS and ITZ than in the glasses of quasi-spherical molecules of similar volume. This is attributed to the near-vertical orientation of the rod-like molecules at the surface and their deeper penetration into the bulk where mobility is low. Between the two systems studied, ITZ has slower surface diffusion, likely a result of the deeper penetration of surface molecules in this system.

Apart from investigating new types of molecules, this work was motivated by developing capabilities to predict surface diffusion rates. Chen et al. have analyzed all published surface diffusion results on molecular glasses and noted that the surface diffusion coefficient decreases smoothly with molecular size for van der Waals systems (no extensive hydrogen bonds).³ They attributed this to a steep and generic mobility gradient beneath the surface of a molecular glass. Larger molecules insert themselves deeper into the bulk where mobility is lower, slowing down their center-of-mass diffusion. In this work we extend their investigation to even deeper bulk penetration using the rod-like molecules and observe a greater retardation of diffusion. Our results uphold the previous conclusion and our mobility vs depth profile displays the double-exponential form characteristic of surface mobility gradient seen in simulations.^{20,21} This finding is useful for predicting surface diffusion from molecular structures. We also examine a previously observed correlation between the rate of surface diffusion and the fragility of the bulk liquid.

2.3 Experimental Section

Posaconazole (POS, purity > 98%) was obtained from Biochempartner and itraconazole (ITZ, purity > 99%) from Alfa Aesar. The materials were used as received. To make a surface

grating, a master pattern was placed on a viscous liquid of POS or ITZ at 363 K and was peeled off after vitrifying the liquid at 298 K. This yielded a glass film with a sinusoidal surface contour. Master gratings of different wavelengths were obtained as follows: for $\lambda = 1000$ nm and 1984 nm, plastic gratings purchased from Rainbow Symphony were used; for $\lambda = 334$ nm, the masters were duplicated from a Blue-ray disc through a UV-curing polymer (Norland Optical Adhesive 61); for $\lambda = 553$ nm, the masters were duplicated from a glass grating (Spectrum Scientific) through the same polymer. All masters were coated with 10 nm gold before use (Sputter deposition system, Leica ACE600). The thickness of each embossed glass film was 50 – 100 μm , much larger than the wavelength of any surface grating used, ensuring that the evolution of the top surface was unaffected by the substrate.

The flattening of a surface grating over time was monitored by Atomic Force Microscopy (AFM, Bruker Veeco Multiple Mode IV) or laser diffraction. AFM was performed in the tapping mode at room temperature; the height profile was Fourier transformed to obtain the amplitude of the sinusoidal surface. Laser diffraction was measured in transmission and used to determine faster decay than feasible with AFM. A HeNe laser ($\lambda = 632.8$ nm, Uniphase Corp.) passed through a sample film perpendicularly and the first-order diffraction in transmission was recorded with a silicon amplified detector (Thorlabs) interfacing with a National Instruments LabVIEW program. The grating amplitude was verified to be proportional to the square root of diffraction intensity. The diffraction method was used only for POS since the cloudiness of LC phases made transmission experiments difficult for ITZ. The two methods yielded identical results within experimental error when applied to the same decay process. During grating decay, the sample was

purged with dry nitrogen and its temperature was controlled within 0.1 K with a Linkam microscope temperature stage or a custom-made mini-oven.

2.4 Mullins' Theory of Surface Evolution

According to Mullins,²² the amplitude h of a sinusoidal surface contour decreases exponentially over time, $h = h_0 \exp(-Kt)$, and the decay rate K is given by:

$$K = Fq + Aq^2 + (A' + C)q^3 + Bq^4 \quad (2.1)$$

where

$$q = 2\pi/\lambda$$

$$F = \frac{\gamma}{2\eta}$$

$$A = \frac{p_0\gamma\Omega^2}{(2\pi m)^{1/2}(kT)^{3/2}}$$

$$A' = \frac{\rho_0 D_G \gamma \Omega^2}{kT}$$

$$C = \frac{D_v \gamma \Omega}{kT}$$

$$B = \frac{D_s \gamma \Omega^2 \nu}{kT}$$

In eq. (2.1), λ is the grating wavelength, γ is the surface tension, η the viscosity, p_0 the vapor pressure at equilibrated state, Ω the molecular volume, m the molecular weight, ρ_0 the vapor density at equilibrated state, D_G the diffusion coefficient of the vapor molecules in an inert

atmosphere, D_v , the self-diffusion coefficient in the bulk, ν the areal density of molecules on the surface, and D_s the surface diffusion coefficient. The different terms in eq. (2.1) correspond to different mechanisms of surface evolution: viscous flow (the F term), evaporation-condensation (A and A'), bulk diffusion (C), and surface diffusion (B). For each decay mechanism, the decay rate has a characteristic dependence on the grating wavelength, useful for identifying the mechanism; for example, $K \propto \lambda^{-1}$ for viscous flow and $K \propto \lambda^{-4}$ for surface diffusion. Mullins' method has been applied to measure the surface diffusion of many materials, both crystalline²³ and amorphous.^{1,3} In the case of a glass-forming Lennard-Jones liquid, Malshe et al. showed by simulations that the surface diffusion constant determined by Mullins' method agrees with that calculated from the mean squared displacement of particles.²⁴

2.5 Results

Figure 2.1 shows the DSC traces of POS and ITZ. The two liquids have similar T_g s with the value for ITZ being slightly lower. The lower T_g of ITZ is consistent with the dielectric spectroscopy

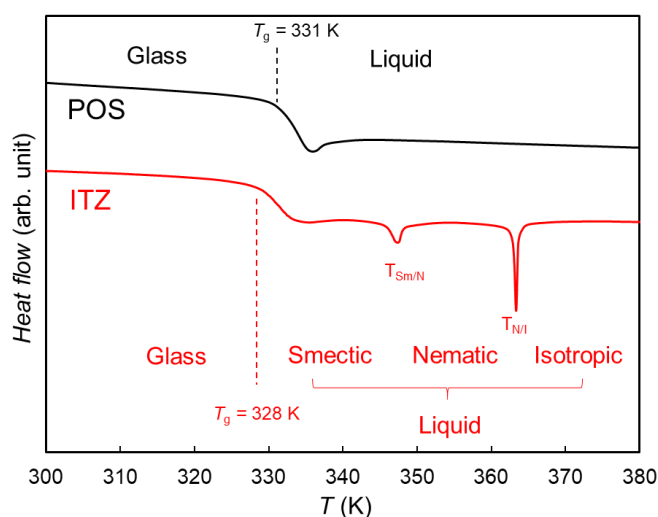


Figure 2.1. DSC traces of POS and ITZ during heating at 10 K/min. Both systems show a glass transition (T_g) and ITZ shows two LC transitions.

results,^{18,19} which show that ITZ has a shorter structural relaxation time at the same temperature. Different from POS, ITZ undergoes two phase transitions in the liquid state.¹⁸ Cooling from a high temperature, an isotropic liquid of ITZ transforms into a nematic phase ($T_{NI} = 363$ K) and then to a smectic phase ($T_{Sm/N} = 347$ K).

2.5.1 Posaconazole (POS)

Figure 2.2 shows the typical decay kinetics of a POS surface grating recorded by laser diffraction (Figure 2.2a) and by AFM (Figure 2.2b). In each case, the decay was exponential, consistent with

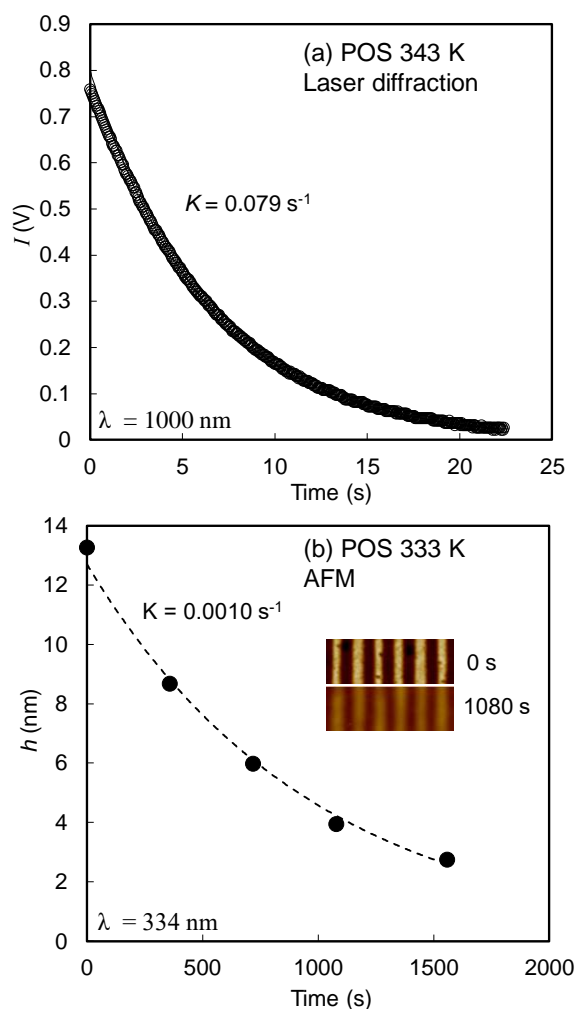


Figure 2.2. Typical decay kinetics of POS surface gratings. (a) At 343 K, recorded by laser diffraction ($\lambda = 1000$ nm). I is the diffraction intensity. (b) At 333 K recorded by AFM ($\lambda = 334$ nm). Inset: AFM images at two time points.

Mullins' theory.²² The data were fit to the function $\phi = \exp(-Kt)$, where ϕ is h/h_0 for AFM measurements and $(I/I_0)^{1/2}$ for diffraction measurements and K is the decay constant.

Figure 2.3a shows the decay constant K of POS at $\lambda = 334$ nm as a function of temperature. The structural relaxation time of the POS liquid¹⁸ is also shown for comparison; for this plot, we have extrapolated the experimental data below 331 K using the Vogel-Fulcher-Tammann (VFT) equation. At high temperatures, K closely tracks the structural relaxation time, $K \propto \tau_\alpha^{-1}$. Given that viscosity is generally proportional to τ_α , this indicates that viscous flow is the mechanism of surface flattening (the F term in eq. (2.1)). For this mechanism, the decay rate should be inversely proportional to the surface grating wavelength, $K \propto \lambda^{-1}$, and this was found to be the case (Figure 2.3b, see the 338 K result). This relation has been used to convert the K values measured at longer wavelengths to the values at $\lambda = 334$ nm so they can be included in Figure 2.3a to extend the measurement to higher temperatures.

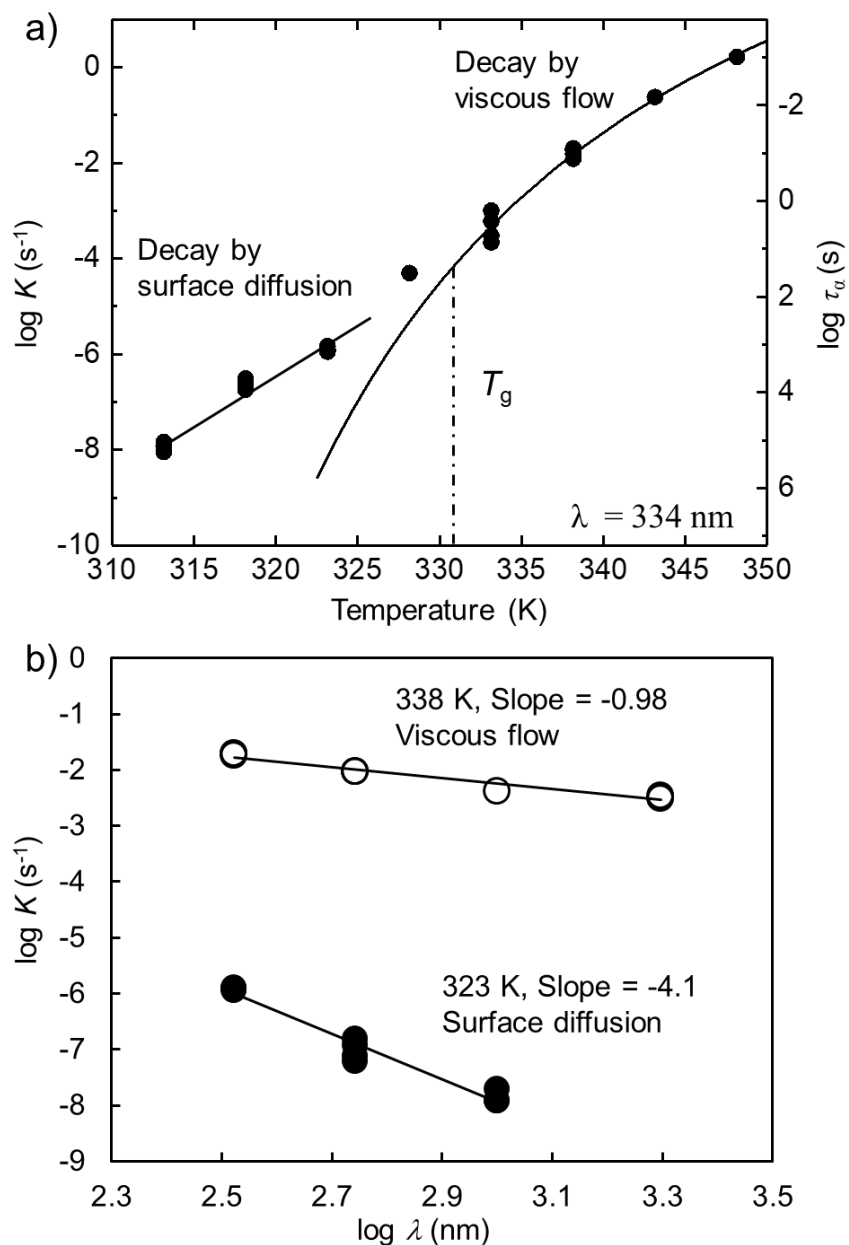


Figure 2.3. (a) Decay constant K of a POS surface grating at $\lambda = 334$ nm as a function of temperature. At high temperatures, K tracks the structural relaxation time τ_α (second y axis) indicating viscous flow controls surface evolution. Decay becomes faster below $T_g + 2$ K, indicating a change of surface flattening mechanism. (b) Wavelength dependence of K at two temperatures indicating decay by viscous flow at high temperatures and by surface diffusion at low temperatures.

Although viscous flow accounts for the decay rates observed at high temperatures, it does not at low temperatures (Figure 2.3a). The observed decay rate is “too fast” relative to viscous relaxation below 333 K ($T_g + 2$ K). This suggests a change of mechanism for surface evolution, as observed in other systems.¹ Figure 2.3b shows that in this lower temperature region, K has a stronger dependence on the surface grating wavelength, $K \propto \lambda^{-4}$, which is expected for the surface diffusion mechanism. Thus, we assign the mechanism of surface evolution to surface diffusion at low temperatures and use the observed decay rates to calculate the surface diffusion coefficients D_s (Figure 2.4). For this calculation, we assume $\gamma = 0.05$ N/m, a typical value for organic liquids, and obtain $\Omega = 0.92$ nm³ (molecular volume) from the density of a POS glass (1.27 g/cm³, assumed to be the same as that an ITZ glass²⁵) and its molecular weight (700.8 g/mol). For this rod-like molecule, we estimate its areal density at the liquid/vapor interface by taking into account its preferred orientation. Bishop et al. used NEXAFS to show that POS molecules are nearly vertical at the liquid/vapor interface.²⁶ Thus we estimate the areal density using: $\nu \approx L/\Omega = 2.8$ nm⁻², where L is the length of a POS molecule (2.6 nm, taken from its crystal structure).²⁷ If POS is treated as a spherical molecule at the surface as opposed to an oriented rod, we obtain $\nu \approx \Omega^{-2/3} = 1.0$ nm⁻² and the calculated D_s would be larger by a factor of 3; given the 5 order of magnitude spread of surface diffusion coefficients (Figure 2.4), this is a relatively small effect.

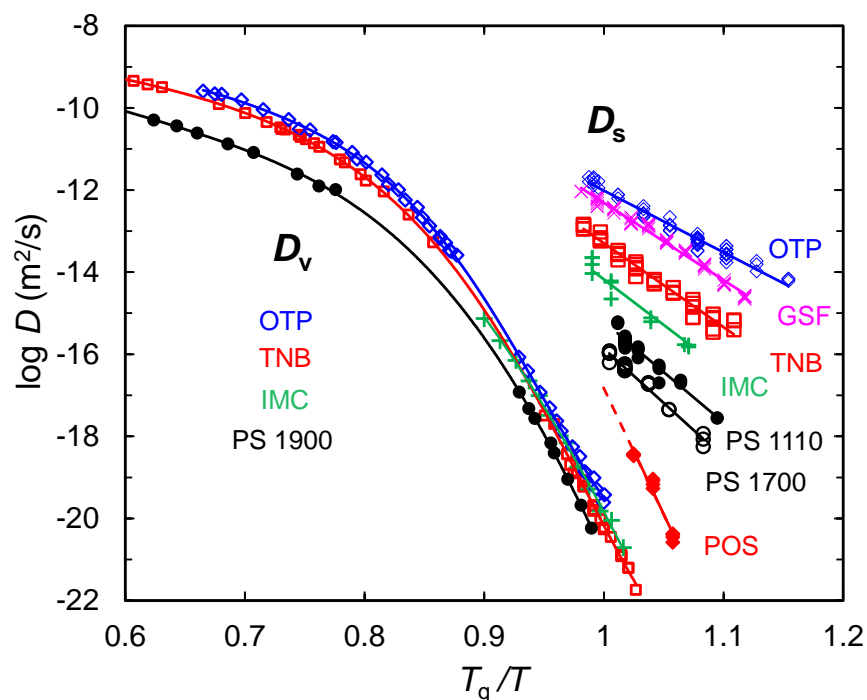


Figure 2.4. Surface diffusivity in POS and other molecular glasses. T_g is the onset temperature measured by DSC during heating at 10 K/min after cooling at the same rate.

Figure 2.4 compares the surface diffusion coefficient D_s of POS and other molecular glasses: *ortho*-terphenyl (OTP),²⁸ *tris*-naphthyl benzene (TNB),²⁹ griseofulvin (GSF),³⁰ indomethacin (IMC),¹ and polystyrene (PS) oligomers (1110 and 1700 g/mole).³¹ Figure 2.4 also shows the bulk diffusion coefficients D_v of the same systems when available.^{32, 33, 34, 35} After scaling the temperature by T_g , the D_v values cluster to a “master curve”. Relative to this, the D_s values are all larger and do not collapse into a single curve. Note that of all the systems studied to date, POS has the slowest surface diffusion in this comparison: its D_s at T_g , $\sim 10^{-17}$ m²/s (estimated by extrapolation), is 5 orders of magnitude smaller than the value for OTP. In addition, the D_s of POS has the strongest temperature dependence, with an activation energy (389 kJ/mol) close to that for bulk diffusion. The slow surface diffusion of POS will be discussed later and attributed to the near-vertical orientation of the surface molecules and their deep penetration into the bulk.

2.5.2 Itraconazole (ITZ)

Figure 2.5a shows the surface-grating decay constant K of ITZ at $\lambda = 334$ nm as a function of temperature. The bulk structural relaxation time¹⁸ is also shown for comparison. As in the case of POS, the relation $K \propto \tau_\alpha^{-1}$ is observed at high temperatures, indicating surface evolution by viscous flow. This is confirmed by wavelength tests (Figure 2.5b). At both 323 K and 333 K, we observe the relation $K \propto \lambda^{-1}$, as expected for the viscous-flow mechanism.

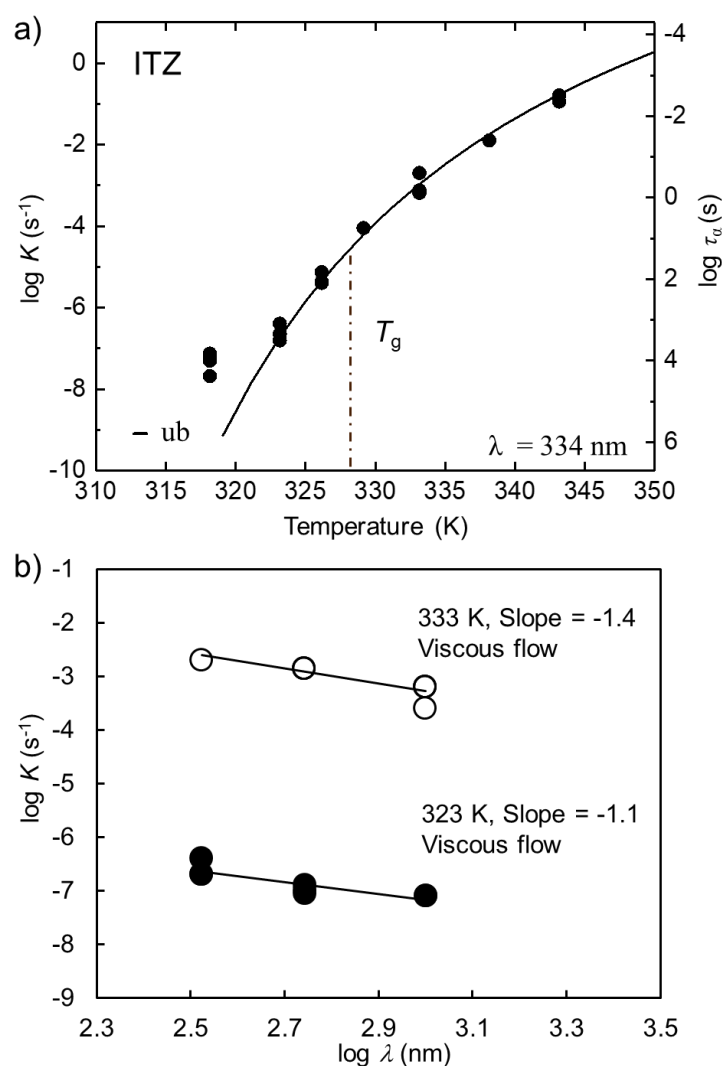


Figure 2.5. (a) Surface grating decay rate K of ITZ at $\lambda = 334$ nm as a function of temperature. "ub" indicates an upper bound from no significant decay in 250 days. (b) K as a function of grating wavelength λ at 323 K and 333 K.

The key difference between ITZ and POS is that in ITZ, viscous flow controls surface evolution down to a lower temperature relative to T_g . In ITZ, K tracks τ_α down to $T_g - 5$ K (Figure 2.5a), whereas in POS, this is the case only down to $T_g + 2$ K (Figure 2.3a), below which surface diffusion

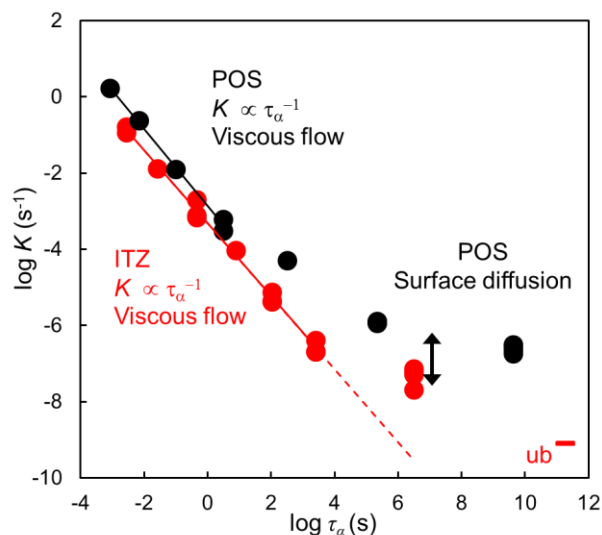


Figure 2.6. Surface-grating decay constant K at $\lambda = 334$ nm plotted against the bulk relaxation time τ_α for ITZ and POS. At high temperatures (short τ_α), $K \propto \tau_\alpha^{-1}$ holds, indicating surface evolution by viscous flow. At low temperatures (long τ_α), faster decay is observed signaling a new decay mechanism.

is fast enough to be the decay mechanism (Figure 2.3b). Thus, surface diffusion in ITZ must be slower than that in POS at the same temperature relative to T_g .

To see the point above more clearly, in Figure 2.6, we plot the decay constant K against the bulk relaxation time τ_α for both systems. This allows a comparison of the two surface processes at the same bulk mobility. At high temperatures (short τ_α), we find $K \propto \tau_\alpha^{-1}$, confirming surface evolution by viscous flow. In this region, the two systems have very similar decay rates at a common τ_α (bulk mobility), as expected for this mechanism. At low temperatures (long τ_α), the observed decay is faster relative to viscous flow, suggesting a change of decay mechanism. For POS, the new decay mechanism was shown to be surface diffusion by a wavelength test (Figure 2.3b). It is likely

that the ITZ undergoes the same transition to surface diffusion at the lowest temperature studied (we have not verified this by wavelength test due to the very slow decay rates). Under this assumption, we can assess the relative rates of surface diffusion in the two systems: in POS, the transition from viscous flow to surface diffusion occurs at a much higher bulk mobility ($\tau_\alpha \approx 3$ s) than in ITZ ($\tau_\alpha \approx 3000$ s). Thus, surface diffusion in POS is fast enough to be the decay mechanism when bulk mobility is relatively high, but this does not happen in ITZ even at a much lower bulk mobility. From Figure 2.6, we estimate surface diffusion in ITZ to be ~ 20 times slower than that of POS at $\tau_\alpha \approx 10^7$ s (double-sided arrow).

2.6 Discussion

The main result of this work is that surface diffusion is significantly slower in the glasses of the rod-like molecules POS and ITZ than in the previously studied systems (Figure 2.4). Between POS and ITZ, surface diffusion is slower in ITZ (Figure 2.6). We now discuss these results and suggest that the slow surface diffusion is a consequence of the deep penetration of the nearly vertically orientated surface molecules. We also use the new results to test a previously reported relation between surface mobility and bulk liquid fragility.

2.6.1 Correlation between Surface Diffusion and molecular surface penetration depth.

In Figure 2.7, we illustrate the essential difference between the surface structures of liquids composed of quasi-spherical molecules and rod-like molecules (POS and ITZ). For a liquid of quasi-spherical molecules, each surface molecule penetrates into the bulk by approximately its diameter $d \approx \Omega^{1/3}$, where Ω is the molecular volume. In the case of POS, Bishop et al. have shown

by NEXAFS that the rod-like molecules tend to be vertically aligned with $\theta_z \approx 33^\circ$, where θ_z is the average angle between the long axis of the molecule \mathbf{n}_L and the surface normal \mathbf{n}_z .²⁶ (For this discussion, we take each rod-like molecule as centrosymmetric and θ_z to be positive.) Preferred orientation at interfaces has been observed for many non-spherical molecules and is a result of free-energy minimization in an environment lacking translational symmetry.^{36, 37, 38} We estimate the depth of penetration for a surface molecule as $z = L \cos \theta_z$, where $L \approx 2.6$ nm is the length of a POS molecule in its crystals.²⁷ This yields a penetration depth of 2.2 nm, more than twice the value for a spherical molecule of the same volume ($d = 0.97$ nm), a direct result of preferred orientation.

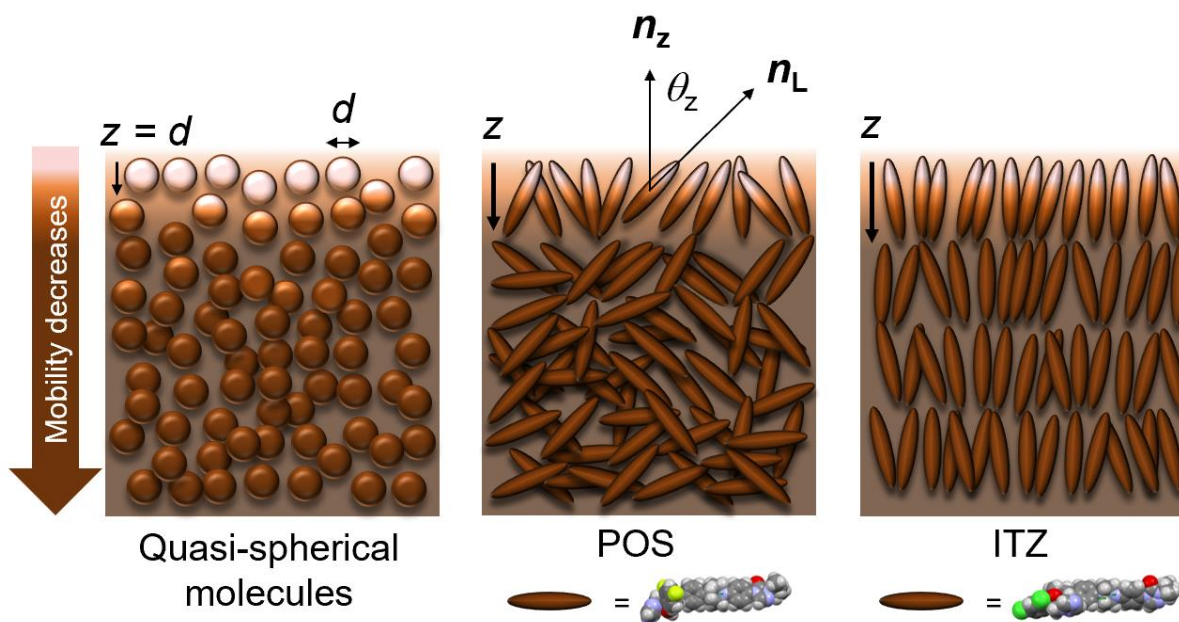


Figure 2.7. Different surface molecular structures of liquids of quasi-spherical molecules and rod-like molecules POS and ITZ. While both rod-shaped, ITZ molecules form a smectic LC phase whereas POS molecules produce an isotropic liquid. For quasi-spherical molecules, the depth of penetration of a surface molecule is approximately its diameter, $z = d$. The depth of penetration can be significantly larger for vertically oriented rod-like molecules. This anchors them deeper in the bulk where mobility is low, hindering their center-of-mass diffusion.

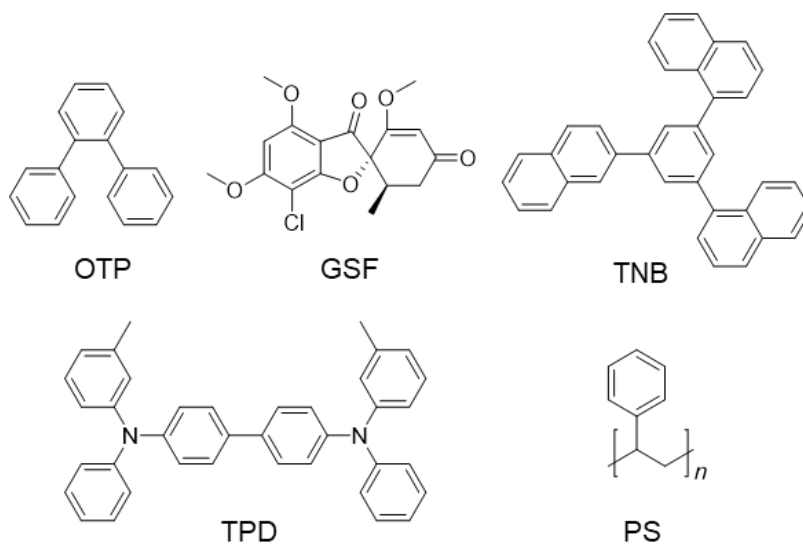
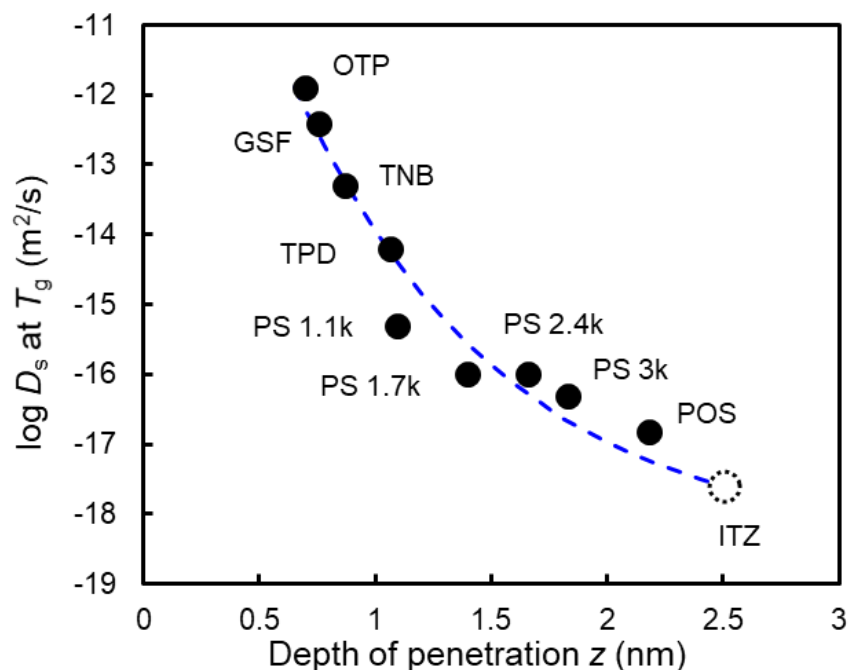


Figure 2.8. Surface diffusion coefficient D_s at T_g as a function of the penetration depth z . For quasi-spherical molecules OTP, GSF, and TNB, $z \approx d$ (mean molecular size). For rod-like molecules TPD, POS, and ITZ, $z = L \cos \theta_z$, where L is the length of the molecule and θ_z is the average angle between the molecular long axis and the surface normal. For chain-like PS oligomers, $z = R_{ee} \cos \theta_{zee}$, where R_{ee} is the end-to-end distance and θ_{zee} the average angle between the R_{ee} vector and the surface normal. The curve is a fit of the experimental data using a double-exponential form (eq. (2.2)) thought to represent the surface mobility gradient of a molecular glass. The arrow indicates the estimated D_s for ITZ based on extrapolation of the fitting curve.

In the case of ITZ, the bulk liquid is a smectic LC in the temperature range of our study, and this can influence the orientational order of surface molecules. In the bulk smectic phase, rod-like ITZ molecules tend to be parallel with the LC director forming an average angle of 27° .¹⁸ At the vapor interface, the LC director favors a vertical orientation (homeotropic alignment); this is seen from the annealing behavior of a vapor-deposited glass film.³⁹ The surface anchoring effect has been observed with other rod-like, LC-forming molecules.⁴⁰ Furthermore, simulations have shown that surface molecules of a LC can be slightly more vertically aligned than in the bulk.⁴¹ Together, these results indicate that ITZ molecules favor a vertical orientation at the free surface and that their orientational order should be higher than that of POS molecules. From its bulk orientational order and its length of 2.8 nm (in crystals),⁴² we estimate the depth of penetration for an ITZ surface molecule to be 2.5 nm.

Our central hypothesis is that the diffusion rate of surface molecules is determined by their depth of penetration into the bulk. Because mobility decreases rapidly across a vapor/glass interface, we expect the translational mobility of a surface molecule to be limited by its bottom part where mobility is the lowest, even if its top part is in a region of higher mobility. We test this idea in Figure 2.8 by plotting the surface diffusion coefficient at T_g as a function of the penetration depth of surface molecules, using data from this work and the literature. The molecular structures of the systems included are shown at the bottom of Figure 2.8 and in Scheme 2.1; Table 2.1 contains the numerical values. In this analysis, we regard OTP, GSF, and TNB as quasi-spherical molecules and use the mean molecular size $d = \Omega^{1/3}$ to represent the depth of penetration. For the mildly elongated TPD, penetration depth is estimated in the same way as POS and ITZ: $z = L \cos \theta_z$, where $L \approx 1.7$ nm and $\theta_z \approx 51^\circ$ is obtained by atomistic MD simulations.⁴⁸ This yields $z = 1.1$ nm,

slightly larger than the mean molecular size ($d = 0.9$ nm). For chain-like PS oligomers, penetration depth is calculated from $z = R_{ee} \cos \theta_z$, where R_{ee} is the end-to-end distance⁴³ and θ_z the average angle between the R_{ee} vector and the surface normal.⁵⁰ Given that hydrogen bonds have an independent effect on surface diffusion from molecular dimensions,³ Figure 2.8 only includes systems without extensive hydrogen bonds. Though hydrogen bonds might be present in a POS liquid, their contribution to the total vaporization energy is negligible ($\sim 5\%$, based on a group-additivity calculation^{3,44}) and we include this system in the analysis.

Table 2.1. Surface diffusion coefficients D_s of molecular glasses and other properties.

	T_g (K)	M (g/mol)	ρ (g/cm ³)	d (nm)	L or R_{ee} (nm)	S_z	θ_z (deg.)	z (nm)	$\log D_s$ at T_g (m ² /s)
OTP	246	230.3	1.12 ⁴⁵	0.70	—	—	—	0.70 ^a	-11.9 ²⁸
GSF	361	352.8	1.35 ⁴⁶	0.76	—	—	—	0.76 ^a	-12.4 ³⁰
TNB	347	456.6	1.15 ⁴⁷	0.87	—	—	—	0.87 ^a	-13.3 ²⁹
TPD	330	516.7	1.19 ²	0.90	1.7 ⁴⁸	0.1 ⁴⁸	51	1.1	-14.2 ²
PS1100	307	990	1.03 ⁴⁹	1.17	2.1 ⁴³	-0.1 ⁵⁰	58	1.1	-15.3 ³¹
PS1700	319	1600	1.03 ⁴⁹	1.37	2.6 ⁴³	-0.1 ⁵⁰	58	1.4	-16.0 ³¹
PS2400	337	2264	1.03 ⁴⁹	1.54	3.1 ⁴³	-0.1 ⁵⁰	58	1.7	-16.0 ¹³
PS3000	343	2752	1.03 ⁴⁹	1.64	3.5 ⁴³	-0.1 ⁵⁰	58	1.8	-16.3 ¹¹
POS	331	700.8	1.27 ^b	0.97	2.6 ²⁷	—	33 ²⁶	2.2	-16.8
ITZ	328	705.6	1.27 ²⁵	0.97	2.8 ⁴²	0.7 ^c	27 ¹⁸	2.5	(-17.8) ^d

^a The penetration depth of these quasi-spherical molecules are assumed to be the same as their mean molecular size, $z = d$.

^b Assumed to be the same as that of ITZ.

^c Calculated from the S_z value from Ref. 18 (bulk value).

^d Estimated based on trends in Figures 2.8 and 2.9.

Based on our hypothesis, we expect the rate of surface diffusion to decrease with the depth of penetration. This is indeed observed in Figure 2.8. We see a smooth falling trend starting from the three quasi-spherical molecules (OTP, GSF, and TNB), to the mildly elongated TPD, to the chain-like PS oligomers, and finally to the rod-like POS. These systems cover a 5 orders of magnitude

in D_s and a penetration depth from 0.7 nm (OTP) to 2.2 nm (POS). The open circle indicates the estimated D_s for ITZ by extrapolation (see below).

The smooth trend observed in Figure 2.8 suggests that the molecular glasses considered have a similar mobility vs depth profile when compared at T_g and that the different surface diffusion rates simply reflect the different depths at which surface molecules are anchored. In principle, each system in Figure 2.8 has its own mobility vs depth profile. But given the smooth trend observed, a reasonable first approximation is to treat it as a generic mobility profile for van der Waals molecular glasses at T_g . One support for this notion is that the profile in Figure 2.8 is consistent with the “double-exponential” form for surface mobility gradient observed in simulations:^{20,21}

$$\tau(z) = \tau_\alpha \exp[-A \exp(-z/\xi)] \quad (2.2)$$

where τ_α is the bulk relaxation time, A is a “surface-enhancement” factor, and ξ is the dynamical correlation length. This form is thought to arise from an activation barrier for local relaxation that increases exponentially with depth. Phan and Schweitzer have rationalized this as a consequence of geometric-like, layer-wise transfer of caging constraint from the surface to the bulk.^{51,52} The curve in Figure 2.8 is a fit of the data to eq. (2.2). In this fitting, we assume $\tau_\alpha = 10$ s at T_g and estimate $\tau(z)$ from the equation: $D_s(z) = d^2/[4\tau(z)]$. In essence, the last equation assumes the observed D_s is determined by the local mobility at the depth of penetration z . Figure 2.8 shows that eq. (2.2) can accurately describe the experimental data. This argues that despite their different chemistry, the molecular glasses considered have a similar mobility profile $\tau(z)$ at T_g . From this fitting, we obtain $\xi = 1$ nm, consistent with the values obtained from simulations.^{20,21}

We now turn to the slower surface diffusion of ITZ relative to POS. Based on the ideas developed above, the simplest explanation is that the deeper penetration of ITZ surface molecules (2.5 nm vs 2.2 nm) anchor them deeper in the bulk where mobility is lower. This leads to slower center-of-mass diffusion. In Figure 2.8, we extrapolate the double-exponential fit of the experimental data points to the penetration depth of ITZ to estimate its surface diffusion rate. This yields $\log D_s$ (m^2/s) = -17.6 at T_g , in agreement with our finding that surface diffusion is slower in ITZ than in POS (Figure 2.6).

Chen et al. have performed a similar analysis to that presented in Figure 2.8 using the mean molecular size d to represent the penetration depth.³ Their D_s vs d plot includes all the systems in Figure 2.8 except for POS and ITZ. Their plot shows a smooth decreasing trend, but when included in their plot, the rod-like molecules are outliers. For example, the D_s of POS is 30 times smaller than that of PS1110, but the two molecules have similar d values (Table 2.1). This is because d can represent the penetration depth of quasi-spherical molecules but not rod-shaped molecules like POS. Because of its near vertical orientation, POS penetrates deeper into the bulk than a spherical molecule of the same volume. It is interesting to note that for the chain-like PS oligomers, d is not greatly different from the estimated depth of penetration z (Table 2.1). This is because the R_{ee} vector of PS tends toward a parallel orientation at the surface,⁵⁰ reducing the depth of penetration.

2.6.2 Correlation between Surface Diffusion and Bulk Fragility.

Chen et al.⁵³ reported a correlation between the rate of surface diffusion and the fragility of the bulk liquid, with stronger liquids having slower surface diffusion when compared at T_g . This correlation is useful for predicting surface mobility from the dynamics of bulk liquids. In Figure

2.9, we test this correlation using the data from this work and the recently reported data on GSF.³⁰ We plot the D_s value at T_g against the viscosity of the bulk liquid at $1.25 T_g$ (Figure 2.9a), used as a measure of fragility.⁵³ While the m index (slope of each curve in Figure 2.9a taken at T_g) is often used to measure fragility, it is sensitive to errors of slope-taking in a temperature region where viscosity varies rapidly.⁵⁴ Our choice has the advantage of comparing experimental viscosity at a temperature at which displacement from the Arrhenius behavior is large. For GSF, the viscosity data are from Ref. 55, with a small extrapolation to high temperature through a VFT fit (Figure 2.S1). For POS and ITZ, the literature viscosity is extrapolated with the aid of τ_α assuming the two have the same temperature dependence (Figures 2.S2 and Figure 2.S3).¹⁹ Figure 2.9b shows that the new data points for GSF and POS both fall on the trend of the previous data, confirming the conclusion that stronger liquids have slower surface diffusion. In contrast to the strong dependence of D_s on fragility, the bulk diffusion coefficient D_v has a much weaker dependence (if at all). The surface diffusion coefficient of ITZ can be estimated by extrapolating the trend to the viscosity of ITZ at $1.25 T_g$. This yields $\log D_s \text{ (m}^2\text{/s)} = -17.9$, in good agreement with the estimate in Figure 2.8, $\log D_s \text{ (m}^2\text{/s)} = -17.6$, using the penetration depth of ITZ molecules. The average of these two values is entered in Table 2.1 as a preliminary result for ITZ.

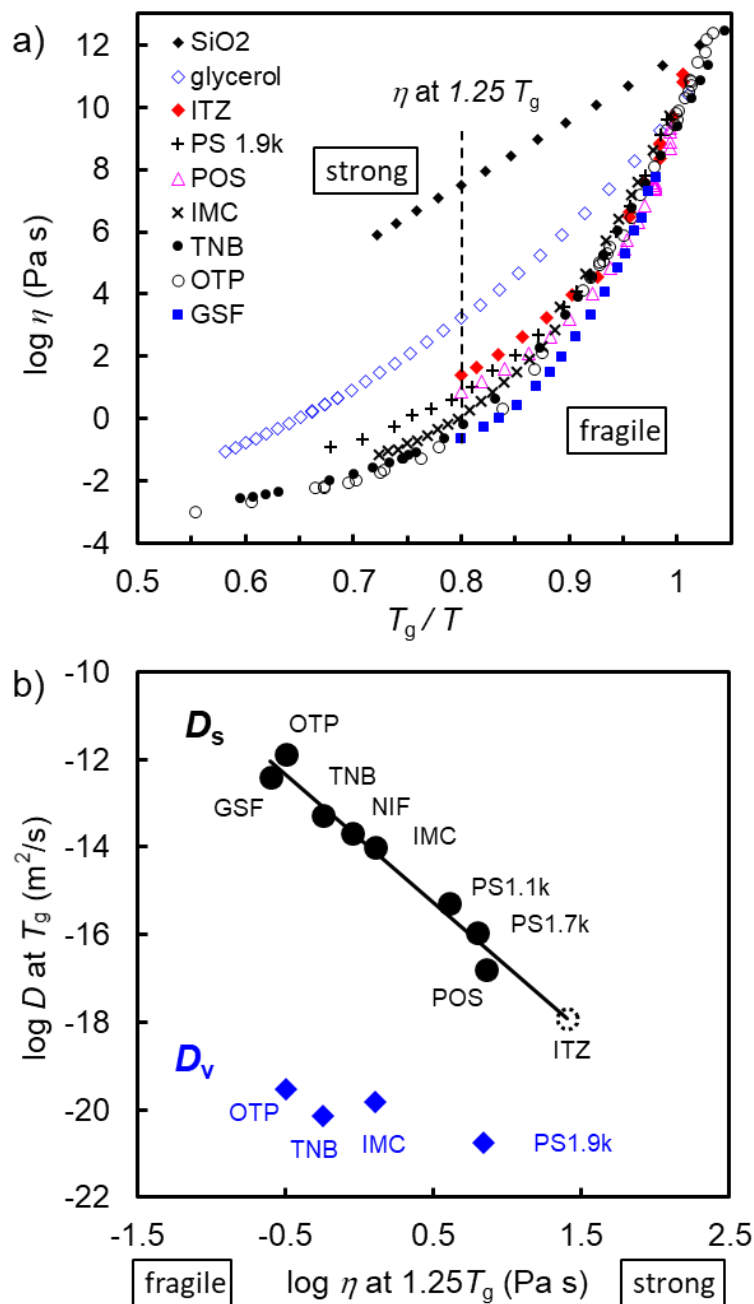


Figure 2.9. (a) Angell plot of viscosity of glass-forming liquids as a function of temperature scaled by DSC T_g . Viscosity at $1.25 T_g$ is used as a measure of fragility. (b) Correlation between diffusion coefficients and bulk liquid fragility. The ITZ point (open circle) is estimated by extrapolating the trend for the other data points to the viscosity of ITZ at $1.25 T_g$.

According to Chen et al.,⁵³ the correlation in Figure 2.9 is interpreted as follows. Fragility measures how easily a liquid's dynamics is excited when temperature is raised above T_g ; strong liquids resist this excitation, while fragile liquids is excited easily. The change of molecular environment from the bulk to the surface can also be regarded as a form of excitation (loss of nearest neighbors and decrease of density) and a stronger liquid might be expected to resist this excitation more than a fragile liquid. In its application to polymer melts, the elastically collective nonlinear Langevin equation (ECNLE) theory makes a connection between fragility and the relative importance of cage constraint and elastic penalty in segmental rearrangement and associates high fragility with dominance by elastic penalty.⁵⁶ Application of the theory to surface dynamics^{51,52} could provide a quantitative understanding of the observed correlation in Figure 2.9.

2.7 Conclusion

In summary, the method of surface grating decay has been used to measure surface diffusion in the glasses of two rod-like molecules POS and ITZ. Despite their similarity, the two systems differ in that ITZ forms liquid-crystalline phases while POS does not. We find that surface diffusion in these systems is significantly slower than in the glasses of quasi-spherical molecules of similar volume when compared at T_g . This is attributed to the near-vertical orientation of the rod-like molecules at the surface, allowing deep penetration into the bulk where mobility is low. At the same bulk mobility, ITZ has slower surface diffusion than POS. This is attributed to a deeper penetration of the ITZ surface molecules into the bulk.

We find that for van der Waals molecular glasses (without extensive hydrogen bonds), the surface diffusion rate slows down smoothly with the depth of penetration of surface molecules (Figure

2.8). The mobility vs depth profile is in good agreement with the double-exponential form observed by simulations and explained by the ECNLE theory. This argues for a generic surface mobility gradient for molecular glasses and the different surface diffusion rates simply reflect the different depths at which surface molecules are anchored. This picture, if valid, allows the use of surface diffusion rate as a probe for the surface mobility gradient, a topic of considerable current interest²⁰ and a challenging target for direct experimental investigations.

The smooth trend of surface diffusivity as a function of the penetration depth of surface molecules is potentially useful for predicting surface mobility (Figure 2.8). For quasi-spherical molecules, the penetration depth is simply the molecular size. For chain-like and rod-like molecules, the penetration depth depends on the orientation of surface molecules relative to the interface and this can be determined by experimental techniques such as NEXAFS²⁶ and SFG⁵⁷ and by MD simulations.⁴⁸ For the purpose of predicting surface mobility, another intriguing prospect is to use the correlation between the rate of surface diffusion and the fragility of the bulk liquid (Figure 2.9).

The surface mobility trend allows contact with recent studies of physical vapor deposition. During vapor deposition, surface mobility allows equilibration leading to formation of high stability, high density glasses.⁹ While the measure of surface mobility most relevant for vapor deposition may not be surface diffusion,³ Figure 2.8 allows the speculative conclusion that the best possible glass packing (the “ideal glass”) would be most easily approached with small molecules. Indeed, recent experiments have shown that ethylbenzene and toluene can closely approach ideal glass packing when prepared by vapor deposition.^{58,59,60}

To our knowledge, this work is the first to study the surface diffusion of an anisotropic organic solid (the vitrified liquid crystal of ITZ). We find that surface diffusion in ITZ is slower than that in the similar but non-LC system POS. At present it is unclear whether the effect is purely a result of the deeper penetration of ITZ molecules or reflects further constraints by the bulk crystalline phase. Further work in this area will provide insight on surface mobility in crystalline solids.

2.8 Acknowledgements

This research was primarily supported by NSF through the University of Wisconsin Materials Research Science and Engineering Center (Grant DMR-1720415). We thank Paul Voyles for helpful discussions.

2.9 Supporting Information

2.9.1 Viscosity and structural relaxation time for GSF

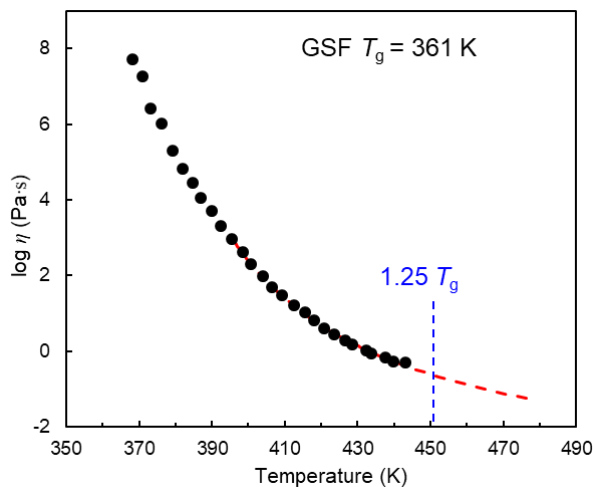


Figure 2.S1. Viscosity of GSF liquid.⁶¹ The red dashed line is a VFT fit of the viscosity data between 396 and 443 K and extended to higher temperature. The viscosity of GSF at $1.25 T_g$ (vertical line) is estimated to be 0.25 Pa·s.

2.9.2 Viscosity and structural relaxation time for POS and ITZ

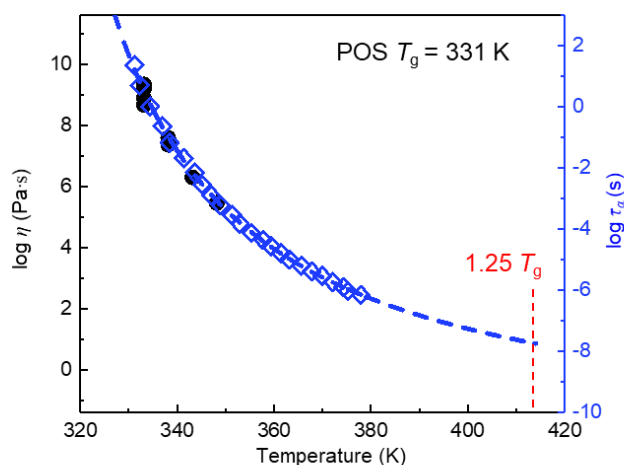


Figure 2.S2. Viscosity and structural relaxation time of POS. Solid circles are calculated viscosity from surface grating decay rates (this work) assuming $\gamma = 0.05 \text{ J/m}^2$. Open diamonds are the structural relaxation time τ_α from dielectric spectroscopy.⁶² The dashed curve is a VFT fit of τ_α . The two y axes are related by $\log \eta (\text{Pa}\cdot\text{s}) = \log \tau_\alpha (\text{s}) + 8.6$. The viscosity of POS at $1.25 T_g$ is estimated to be 7 Pa·s.

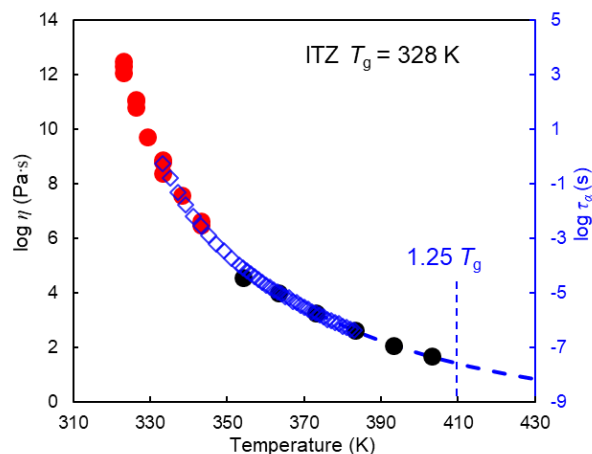


Figure 2.S3. Viscosity and structural relaxation time of ITZ. Black circles are viscosity data from Ref.⁶³. Red circles are calculated viscosity from surface grating decay rates (this work) assuming $\gamma = 0.05 \text{ J/m}^2$. The two methods of viscosity measurement are in good agreement. Open blue diamonds are the structural relaxation time τ_α from dielectric spectroscopy.⁶⁴ The dashed curve is a VFT fit of τ_α . The two y axes are related by $\log \eta (\text{Pa}\cdot\text{s}) = \log \tau_\alpha (\text{s}) + 9$. The viscosity of ITZ at $1.25 T_g$ is estimated to be $25 \text{ Pa}\cdot\text{s}$.

2.10 References

¹ L. Zhu, C. W. Brian, S. F. Swallen, P. T. Straus, M. D. Ediger and L. Yu, *Phys. Rev. Lett.*, 2011, **106**, 256103.

² Y. Zhang, R. Potter, W. Zhang and Z. Fakhraai, *Soft Matter*, 2016, **12**, 9115-9120.

³ Y. S. Chen, Z. X. Chen, M. Tylinski, M. D. Ediger and L. Yu, *J. Chem. Phys.*, 2019, **150**, 024502.

⁴ J. D. Stevenson and P. G. Wolynes, *J. Chem. Phys.*, 2008, **129**, 234514.

⁵ S. Mirigian and K. S. Schweizer, *J. Chem. Phys.*, 2015, **143**, 244705.

⁶ Y. Sun, L. Zhu, K. L. Kearns, M.D. Ediger and L. Yu, *Proc. Natl. Acad. Sci.*, 2011, **108**, 5990.

⁷ T. Wu and L. Yu, *Pharm. Res.*, 2006, **23**, 2350.

-
- ⁸ Y. Li, J. Yu, S. Hu, Z. Chen, M. Sacchetti, C.C. Sun and L. Yu, *Mol. Pharm.*, 2019, **16**, 1305.
- ⁹ S. F. Swallen, K. L. Kearns, M. K. Mapes, Y. S. Kim, R. J. McMahon, M. D. Ediger, T. Wu, L. Yu and S. Satija, *Science*, 2007, **315**, 353.
- ¹⁰ L. Berthier, P. Charbonneau, E. Flenner and F. Zamponi, *Phys. Rev. Lett.*, 2017, **119**, 188002.
- ¹¹ Y. Chai, T. Salez, J. D. McGraw, M. Benzaquen, K. Dalnoki-Veress, E. Raphaël and J. A. Forrest, *Science*, 2014, **343**, 994-999.
- ¹² Z. Fakhraai and J. A. Forrest, *Science*, 2008, **319**, 600-604.
- ¹³ Z. Yang, Y. Fujii, F. K. Lee, C. H. Lam and O. K. Tsui, *Science*, 2010, **328**, 1676-1679.
- ¹⁴ P. E. Acosta-Alba, O. Kononchuk, C. Gourdel and A. Claverie, *J. Appl. Phys.*, 2014, **115**, 134903.
- ¹⁵ M. D. Ediger, J. J. de Pablo and L. Yu, *Acc. Chem. Res.*, 2019, **52**, 407.
- ¹⁶ E. J. Rachwalski, J. T. Wierzchowicz and M. H. Scheetz, *Ann. Pharm.*, 2008, **42**, 1429.
- ¹⁷ M. Boogaerts, D. J. Winston, E. J. Bow, G. Garber, A. C. Reboli, A. P. Schwarzer, N. Novitzky, A. Boehme, E. Chwetzoff and K. De Beule, *Annals of internal medicine*, 2001, **135**, 412.
- ¹⁸ M. Tarnacka, K. Adrjanowicz, E. Kaminska, K. Kaminski, K. Grzbowska, K. Kolodziejczyk, P. Włodarczyk, L. Hawelek, G. Garbacz, A. Kocot and M. Paluch, *Phys. Chem. Chem. Phys.*, 2013, **15**, 20742.
- ¹⁹ K. Adrjanowicz, K. Kaminski, P. Włodarczyk, K. Grzybowska, M. Tarnacka, D. Zakowiecki, G. Garbacz, M. Paluch and S. Jurga, *Mole. Pharm.*, 2013, **10**, 3934.
- ²⁰ P. Scheidler, W. Kob and K. Binder, *Europhys. Lett.*, 2002, **59**, 701
- ²¹ K. S. Schweizer and D. S. Simmons, *J. Chem. Phys.*, 2019, **151**, 240901.
- ²² W.W. Mullins, *J. Appl. Phys.*, 1959, **30**, 77.
- ²³ P. S. Maiya and J. M. Blakely, *J. Appl. Phys.*, 1967, **38**, 698-704.
- ²⁴ R. Malshe, M. D. Ediger, L. Yu and J. J. de Pablo, *J. Chem. Phys.*, 2011, **134**, 194704.
- ²⁵ K. Six, G. Verreck, J. Peeters, M. Brewster and G. V. D. Mooter, *J. Pharm.Sci.*, 2004, **93**, 124
- ²⁶ C. Bishop, J. L. Thelen, E. Gann, M. F. Toney, L. Yu, D. M. DeLongchamp and M. D. Ediger, *Proc. Natl. Acad. Sci.*, 2019, **116**, 21421.
- ²⁷ D. K. McQuiston, M. R. Mucalo and G. C. Saunders, *J. Mol. Struct.*, 2019, **1179**, 477.
- ²⁸ W. Zhang, C. W. Brian and L. Yu, *J. Phys. Chem. B.*, 2015, **119**, 5071.
- ²⁹ S. Ruan, W. Zhang, Y. Sun, M. D. Ediger and L. Yu, *J. Chem. Phys.* 2016, **145**, 064503.
- ³⁰ C. Huang, S. Ruan, T. Cai and L. Yu, *J. Phys. Chem. B.*, 2017, **121**, 9463.

-
- ³¹ W. Zhang and L. Yu, *Macromolecules*, 2016, **49**, 731.
- ³² M. K. Mapes, S. F. Swallen and M. D. Ediger, *J. Phys. Chem. B*, 2006, **110**, 507.
- ³³ S. F. Swallen, K. Traynor, R. J. McMahon, M. D. Ediger and T. E. Mates, *J. Phys. Chem. B*, 2009, **113**, 4600.
- ³⁴ S. F. Swallen, and M. D. Ediger, *Soft Matter*, 2011, **7**, 10339.
- ³⁵ O. Urakawa, S. F. Swallen, M. D. Ediger and E. D. von Meerwall, *Macromolecules*, 2004, **37**, 1558.
- ³⁶ H. Kimura and H. Nakano, *J. Phys. Soc. Japan*, 1985, **54**, 1730.
- ³⁷ A. Haji-Akbari and P. G. Debenedetti, *J. Chem. Phys.*, 2015, **143**, 214501
- ³⁸ M. Sadati, H. Ramezani-Dakhel, W. Bu, E. Sevgen, Z. Liang, C. Erol, M. Rahimi, N. Taheri Qazvini, B. Lin, N. Abbott, B. Roux, M. Schlossman and J. de Pablo, *J. Amer. Chem. Soc.*, 2017, **139**, 3841.
- ³⁹ C. Bishop, A. Gujral, M. F. Toney, L. Yu and M. D. Ediger, *J. Phys. Chem. Lett.*, 2019, **10**, 3536.
- ⁴⁰ B. Jerome, *Rep. Pro. Phys.*, 1991, **54**, 391.
- ⁴¹ M. F. Palermo, L. Muccioli and C. Zannoni, *Phys. Chem. Chem. Phys.*, 2015, **17**, 26149.
- ⁴² M. Lahtinen, E. Kolehmainen, J. Haarala and A. Shevchenko, *Crys. Growth Des.*, 2013, **13**, 346. See the CSD (C. R. Groom, I. J. Bruno, M. P. Lightfoot and S. C. Ward, *Acta Cryst.*, 2016, **B72**, 171.) for a complete list of known ITZ crystal structures, including polymorphs (code TEHZIP and code TEHZIP03) and solvates (code REWTUK). In all known ITZ crystal structures, the rod-like molecule is approximately 2.8 nm long, indicating the robustness of this value.
- ⁴³ L. J. Fetters, D. J. Lohse, D. Richter, T. A. Witten and A. Zirkel, *Macromolecules*, 1994, **27**, 4639.
- ⁴⁴ J. S. Chickos and W. E. Acree, *J. Phys. Chem. Ref. Data*, 2003, **32**, 519
- ⁴⁵ M. Naoki and S. Koeda, *J. Phys. Chem.*, 1989, **93**, 948.
- ⁴⁶ L. Zhu, J. Jona, K. Nagapudi and T. Wu, *Pharm. Res.*, 2010, **27**, 1558.
- ⁴⁷ D. J. Plazek and J. H. Magill, *J. Chem. Phys.*, 1966, **45**, 3038.
- ⁴⁸ I. Lyubimov, L. Antony, D. M. Walters, D. Rodney, M. D. Ediger and J. J. de Pablo, *J. Chem. Phys.*, 2015, **143**, 094502.
- ⁴⁹ S. L. Simon, J. W. Sobieski and D. J. Plazek, *Polymer*, 2001, **42**, 2555.
- ⁵⁰ A. N. Rissanou and V. Harmandaris, *Macromolecules*, 2015, **48**, 2761.
- ⁵¹ A.D. Phan, K.S. Schweizer, *J. Chem. Phys.*, 2019, **150**, 044508.
- ⁵² A.D. Phan, K.S. Schweizer, *Macromolecules*, 2019, **52**, 5192.
- ⁵³ Y. Chen, W. Zhang and L. Yu, *J. Phys. Chem. B*, 2016, **120**, 8007.
- ⁵⁴ R. Richert and C. A. Angell, *J. Chem. Phys.* 1998, **108**, 9016.

-
- ⁵⁵ Q. Shi, J. Tao, J. Zhang, Y. Su, T. Cai, *Crys. Growth Des.*, 2019, **20**, 24.
- ⁵⁶ S.J. Xie, K.S. Schweizer, *Macromolecules*, 2016, **49**, 9655.
- ⁵⁷ H. K. Nienhuys and M. Bonn, *J. Phys. Chem. B.*, **2009**, **113**, 7564.
- ⁵⁸ M. S. Beasley, C. Bishop, B. J. Kasting and M. D. Ediger, *J. Phys. Chem. Lett.* 2019, **10**, 4069.
- ⁵⁹ E. Leon-Gutierrez, A. Sepúlveda, G. Garcia, M. T. Clavaguera-Mora and J. Rodríguez-Viejo, *Phys. Chem. Chem. Phys.* 2016, **18**, 8244.
- ⁶⁰ M. D. Ediger, *J. Chem. Phys.* 2017, **147**, 210901.
- ⁶¹ Q. Shi, J. Tao, J. Zhang, Y. Su and T. Cai, *Crys. Growth Des.*, 2019, **20**, 24-28.
- ⁶² K. Adrjanowicz, K. Kaminski, P. Włodarczyk, K. Grzybowska, M. Tarnacka, D. Zakowiecki, G. Garbacz, M. Paluch and S. Jurga, *Mole. Pharm.*, 2013, **10**, 3934-3945.
- ⁶³ S. Zhang, T. W. Lee and A. H. Chow, *Crys. Growth Des.*, 2016, **16**, 3791-3801.
- ⁶⁴ M. Tarnacka, K. Adrjanowicz, E. Kaminska, K. Kaminski, K. Grzbowska, K. Kolodziejczyk, P. Włodarczyk, L. Hawelek, G. Garbacz, A. Kocot and M. Paluch, *Phys. Chem. Chem. Phys.*, 2013, **15**, 20742-20752.

Chapter 3 Surface diffusion of a glassy discotic organic semiconductor and the surface mobility gradient of molecular glasses

Yuhui Li¹, Camille Bishop², Kai Cui², J. R. Schmidt², M. D. Ediger², Lian Yu^{1*}

¹ School of Pharmacy, University of Wisconsin-Madison, Madison, WI, 53705, USA

² Department of Chemistry, University of Wisconsin-Madison, Madison, WI, 53706, USA

As published in *J. Chem. Phys.* 2022, 156, 094710

3.1 Abstract

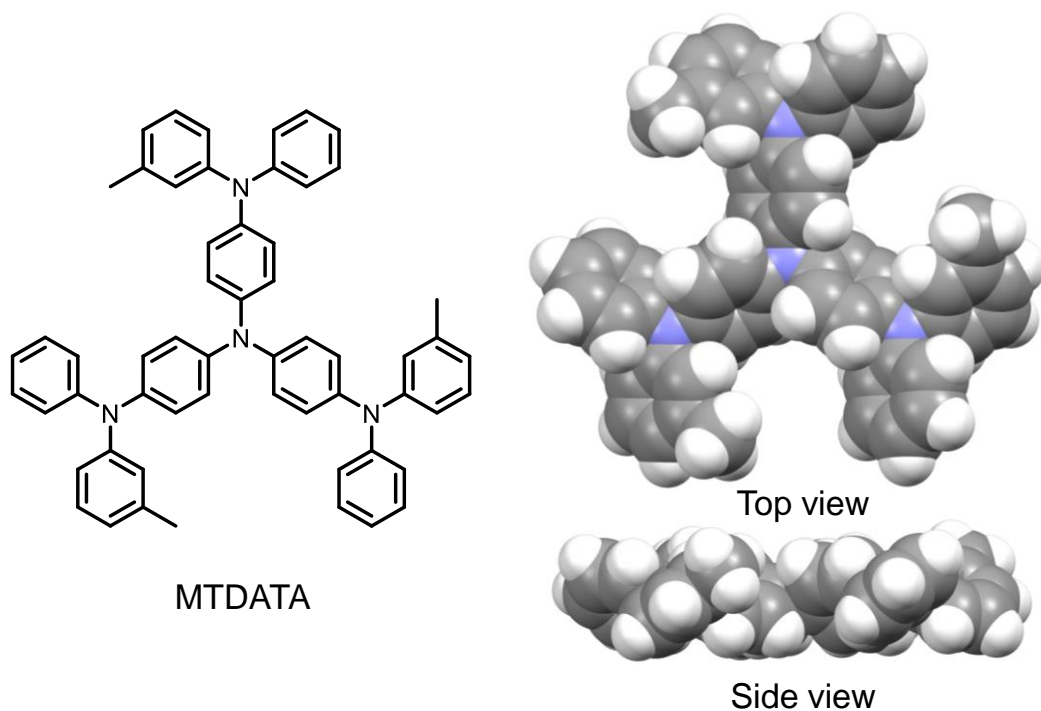
Surface diffusion has been measured in the glass of an organic semiconductor, MTDATA, using the method of surface grating decay. The decay rate was measured as a function of temperature and grating wavelength, and the results indicate that the decay mechanism is viscous flow at high temperatures and surface diffusion at low temperatures. Surface diffusion in MTDATA is enhanced by 4 orders of magnitude relative to bulk diffusion when compared at the glass transition temperature T_g . The result on MTDATA has been analyzed along with the results on other molecular glasses without extensive hydrogen bonds. In total, these systems cover a wide range of molecular geometries from rod-like to quasi-spherical to discotic and their surface diffusion coefficients vary by 9 orders of magnitude. We find that the variation is well explained by the existence of a steep surface mobility gradient and the anchoring of surface molecules at different depths. Quantitative analysis of these results supports a recently proposed double-exponential form for the mobility gradient: $\log D(T, z) = \log D_v(T) + [\log D_0 - \log D_v(T)] \exp(-z/\xi)$, where $D(T, z)$ is the depth-dependent diffusion coefficient, $D_v(T)$ is the bulk diffusion coefficient, $D_0 \approx 10^{-8}$ m²/s, and $\xi \approx 1.5$ nm. Assuming a representative bulk diffusion coefficient for these fragile glass formers, the model reproduces the presently known surface diffusion rates within 0.6 decade. Our result provides a general way to predict predicting the surface diffusion rates in molecular glasses.

3.2 Introduction

Molecules at the surface of a liquid or glass experience a different environment from those in the bulk and as a result, can have different packing arrangements and dynamics.^{1,2,3} The surface dynamics of glasses plays a key role in their stability and fabrication; for example, surface mobility

enables fast local crystal growth,^{4,5} preparation of ultra-stable glasses by physical vapor deposition (PVD),^{6,7} transformation of nanostructures,^{8,9} and cold welding.¹⁰

The substance of this study, 4,4',4''-Tris[(3-methylphenyl)phenylamino]triphenylamine (MTDATA, Scheme 3.1), exemplifies a discotic “starburst” molecule synthesized as a hole-transport material in organic light-emitting diodes (OLEDs).^{11,12,13,14} Given that active layers in OLEDs are often amorphous films prepared by physical vapor deposition, understanding the surface dynamics during deposition helps control film structure and device performance.^{15,16} Efficient surface equilibration enables the preparation of high-density, high-stability glass films¹⁷ with controlled anisotropic packing.¹⁸ In this work, we investigate the surface diffusion of MTDATA, an important measure of its surface mobility.



Scheme 3.1. Molecular structure of MTDATA and the DFT optimized geometry in top and side views.

Apart from its importance in organic electronics, the discotic geometry MTDATA is relevant for understanding surface diffusion in molecular glasses. Previous work has observed a large variation of the surface diffusion coefficient D_s between glassy materials.¹⁹ For molecular glasses without extensive hydrogen bonds (e.g., MTDATA), Li et al. observed that the variation of D_s correlates with the depth of penetration of surface molecules.²⁰ That is, the deeper a molecule penetrates into the bulk, the slower its surface diffusion. This is attributed to the existence of a steep mobility gradient beneath the surface and to the fact that the lateral diffusion of a molecule is essentially limited by its deepest part where mobility is the lowest. The collection of molecules on which their conclusion is based have quasi-spherical, chain-like, and rod-like geometries, but not discotic geometry. Here we test the conclusion for a discotic molecule. In addition, we examine the depth profile of surface mobility using all available data at all measurement temperatures.

We report that surface diffusion in an MTDATA glass significantly outpaces bulk diffusion, by approximately 4 orders of magnitude when compared at T_g . Despite its new discotic geometry, the MTDATA result is fully consistent with the previous conclusion that the depth of penetration controls the lateral diffusion of surface molecules. We show that all the molecular glasses studied to date without extensive hydrogen bonds are characterized by a similar surface mobility gradient. The depth profile of this mobility gradient has the double-exponential form observed by simulations^{21,22} and we use the available surface-diffusion data to determine the parameters that characterize the mobility gradient.

3.3 Experimental Section

4,4',4''-Tris[(3-methylphenyl)phenylamino]triphenylamine (MTDATA, sublimed, purity > 98%) was obtained from Ossila and used as received. The T_g of MTDATA was determined as the onset of glass transition during 10 K/min heating using Differential Scanning Calorimetry (DSC, TA Q2000). To make a surface grating, a master pattern was placed on a viscous liquid of MTDATA at 388 K. The master was removed after vitrifying the liquid at 323 K, producing a corrugated surface. Master gratings of different wavelengths were purchased or fabricated. For $\lambda = 1000$ nm and 1984 nm, plastic gratings were purchased from Rainbow Symphony; for $\lambda = 334$ nm and 729 nm, the masters were duplicated from a Blu-ray or DVD disc through a UV-curing polymer (Norland Optical Adhesive 61); for $\lambda = 424$ and 3322 nm, the masters were duplicated from a glass grating (Spectrum Scientific) through the same transfer process. All masters were coated with 10 nm of gold before use (Sputter Deposition System, Leica ACE600) to minimize contamination during subsequent use. The thickness of each embossed MTDATA glass film was 50 – 100 μm , much larger than the wavelength of any surface grating used, ensuring that the evolution of the top surface was unaffected by the substrate.

The evolution of a surface grating was measured by either Atomic Force Microscopy (AFM, Bruker Veeco Multiple Mode IV) or laser diffraction. AFM was performed in the tapping mode; the amplitude h of the sinusoidal surface was obtained by Fourier transforming the height profile. Laser diffraction was used to determine faster decays than feasible with AFM. A HeNe laser ($\lambda = 632.8$ nm, Uniphase Corp.) passed through a surface grating sample and the first-order diffraction was captured by a silicon amplified detector (Thorlabs) interfacing with a National Instruments LabVIEW program. The two methods yielded identical results within experimental error when applied to the same decay process. During grating decay, the sample was purged with dry nitrogen

and its temperature was controlled within 0.1 K with a Linkam microscope temperature stage or a custom-made mini-oven.

Density functional theory (DFT) calculations were performed in Molpro 2015 software²³ through the atomic simulation environment (ASE) interface²⁴, using the Perdew-Burke-Ernzerhof exchange-correlation functional²⁵ combined with DFT-D3 dispersion correction.²⁶ Dunning style aug-cc-pVDZ basis sets²⁷ were used. Geometry of the molecule was relaxed until maximum force on atoms was less than 0.01 eV/Å.

3.4 Results

The method of surface grating decay was used to investigate the surface diffusion in amorphous MTDATA. Figure 3.1 shows the typical decay kinetics recorded by laser diffraction (Figure 3.1a) and by AFM (Figure 3.1b). Laser diffraction was used to measure fast decays at high temperatures and AFM to measure slow decays at low temperatures. We observed exponential decays. The decay constant K was obtained by fitting the grating amplitude h from AFM to the function $h = h_0$

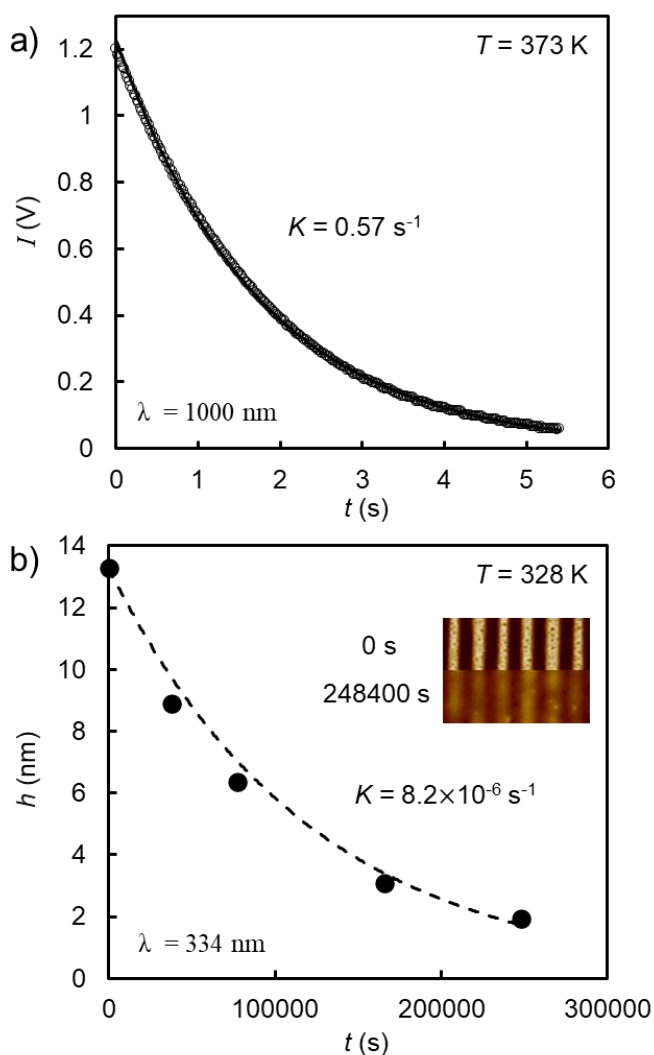


Figure 3.1. Decay kinetics of MTDATA surface gratings. (a) At 373 K, recorded by laser diffraction ($\lambda = 1000 \text{ nm}$). (b) At 328 K, recorded by AFM ($\lambda = 334 \text{ nm}$). Inset: AFM images at two time points.

$\exp(-Kt)$ and the diffraction intensity I to $(I/I_0)^{1/2} = \exp(-Kt)$, accounting for the fact that $I \propto h^2$.

The decay constant is plotted in Figure 3.2 as a function of temperature for $\lambda = 334$ nm.

According to Mullins,²⁸ the amplitude h of a sinusoidal surface contour decreases exponentially over time and the decay constant K is given by:

$$K = Fq + Aq^2 + (A' + C)q^3 + Bq^4 \quad (3.1)$$

In eq. 3.1, $q = 2\pi/\lambda$, where λ is the wavelength of the grating, and the different terms correspond to the different mechanisms of surface evolution: viscous flow (the F term), evaporation-condensation (A and A'), bulk diffusion (C), and surface diffusion (B). Among these, viscous flow and surface diffusion are the dominant mechanisms for surface evolution of molecular glasses near T_g .^{1,20} These two terms are given by: $F = \gamma/2\eta$ and $B = D_s\gamma\Omega^2v/(kT)$, where γ is the surface tension,

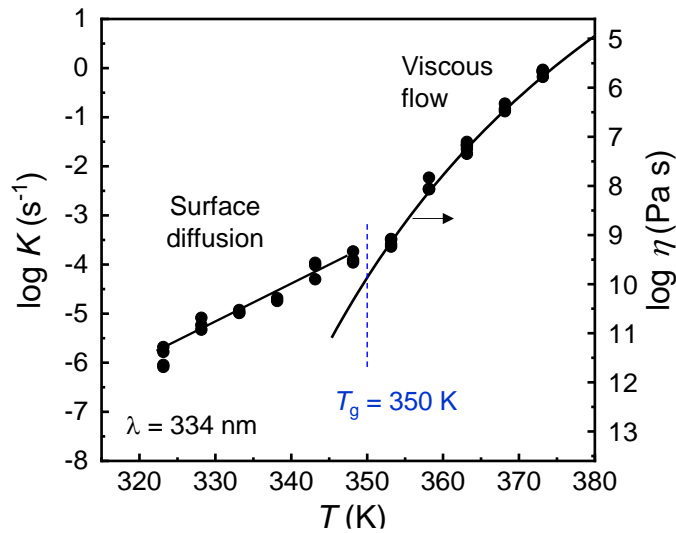


Figure 3.2. Grating decay constant K plotted against temperature. Viscosity is calculated from the decay constant and shown using the second y axis.

h the viscosity, D_s the surface diffusion coefficient, Ω the molecular volume, ν the areal density of surface molecules, and k the Boltzmann constant.

Figure 3.2 shows that the decay constant K has stronger temperature dependence at high temperature than at low temperatures and the transition occurs near the DSC T_g (vertical line). To determine the mechanism of surface evolution, we measured the wavelength dependence of K . According to Mullins (eq. 3.1), viscous relaxation of a surface is characterized by $K \propto \lambda^{-1}$, whereas flattening by surface diffusion by $K \propto \lambda^{-4}$. Figure 3.3 shows the wavelength dependence of K at 363 K and 343 K, with 363 K falling in the high-temperature region of Figure 3.2 and 343 K in

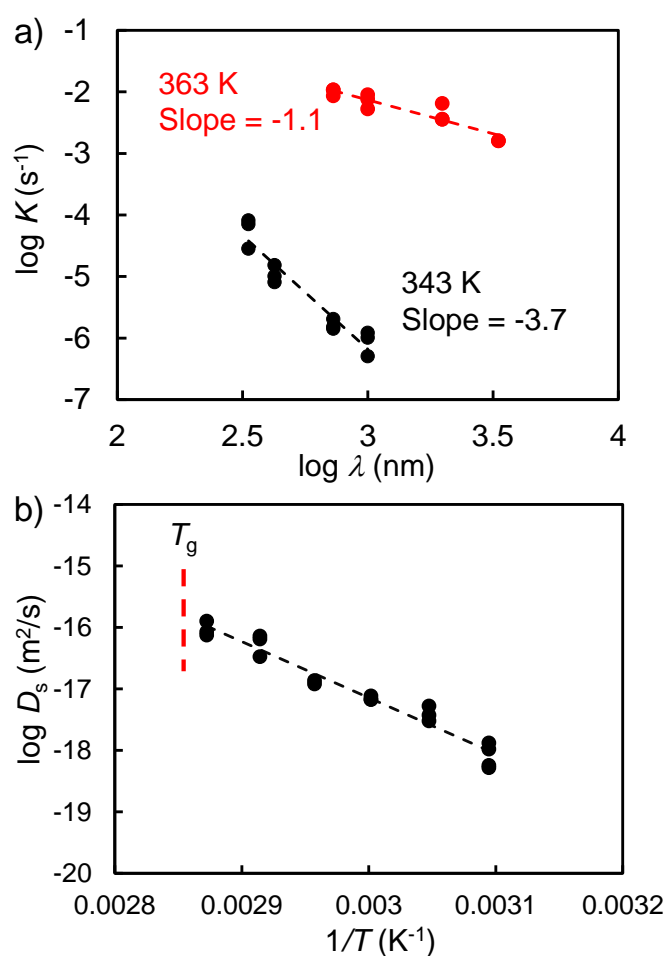


Figure 3.3. (a) Grating decay constants plotted against wavelength of the surface gratings. (b) Surface diffusion rate as a function of temperature.

the low-temperature region. At 363 K, we observe $K \propto \lambda^{-1.1}$, and at 343 K, $K \propto \lambda^{-3.7}$. Thus the wavelength test verifies a change of decay mechanism from viscous flow at high temperatures to surface diffusion at low temperatures.

As a further test of viscous flow as the high-temperature decay mechanism, we calculate the viscosity of MTDATA from the decay constant above 353 K. For this decay mechanism, $K = Fq = \pi\gamma/(\lambda\eta)$, yielding $\eta = \pi\gamma/\lambda K$. The calculated viscosity is shown in Figure 3.2 using the second y axis. In this calculation, we assume $\gamma = 0.05$ N/m, a typical value for the surface tension of organic liquids. The upper curve in Figure 3.2 is a fit of the calculated viscosity to the Vogel-Fulcher-Tammann (VFT) equation, $\log \eta = A + B / (T - T_0)$. This function is known to accurately describe the temperature dependence of viscosity. Thus the quality of the VFT fit supports the assignment of viscous flow as the decay mechanism. When extrapolated to low temperatures, the VFT curve is below the observed decay constants, signaling the activation of a faster decay mechanism (surface diffusion). From the extrapolation, we obtain $\eta_g = 10^{10}$ Pa s at the DSC T_g (350 K), in agreement with the typical values for organic liquids;²⁹ for example, $\eta_g = 10^{9.9}$ Pa s for *ortho*-terphenyl (OTP)³⁰ and $10^{9.5}$ Pa s for *tris*-naphthyl benzene (TNB).³¹ In addition, we obtain the fragility of MTDATA, $m = 85$, a typical value for organic liquids.

From the decay constant at low temperatures, we calculate the surface diffusion coefficient D_s of MTDATA (eq. 3.1) and the results are shown in Figure 3.3b. For this calculation, we assume $\gamma = 0.05$ N/m. $\Omega = 1.09$ nm³ is obtained from the bulk density (assumed to be 1.20 g/cm³) and the molecular weight (789.2 g/mol), and v is obtained from $v = \Omega^{-2/3} = 0.94/\text{nm}^2$. In the temperature

range of study, surface diffusion has an Arrhenius kinetics with an activation energy of $E_a = 175$ kJ/mol.

Figure 3.4 compares the D_s values of MTDATA and other molecular glasses: OTP,³² TNB,³³ indomethacin (IMC),¹ polystyrene (PS) oligomers (1110 and 1700 g/mole),³⁴ and posaconazole (POS).²⁰ The bulk diffusion coefficients D_v are also plotted when available.^{35,36,37,38} The temperature has been scaled by T_g and in this format, the D_v values cluster together, while the D_s values are widely different. The D_s of MTDATA is at the low end of the measured D_s values, but

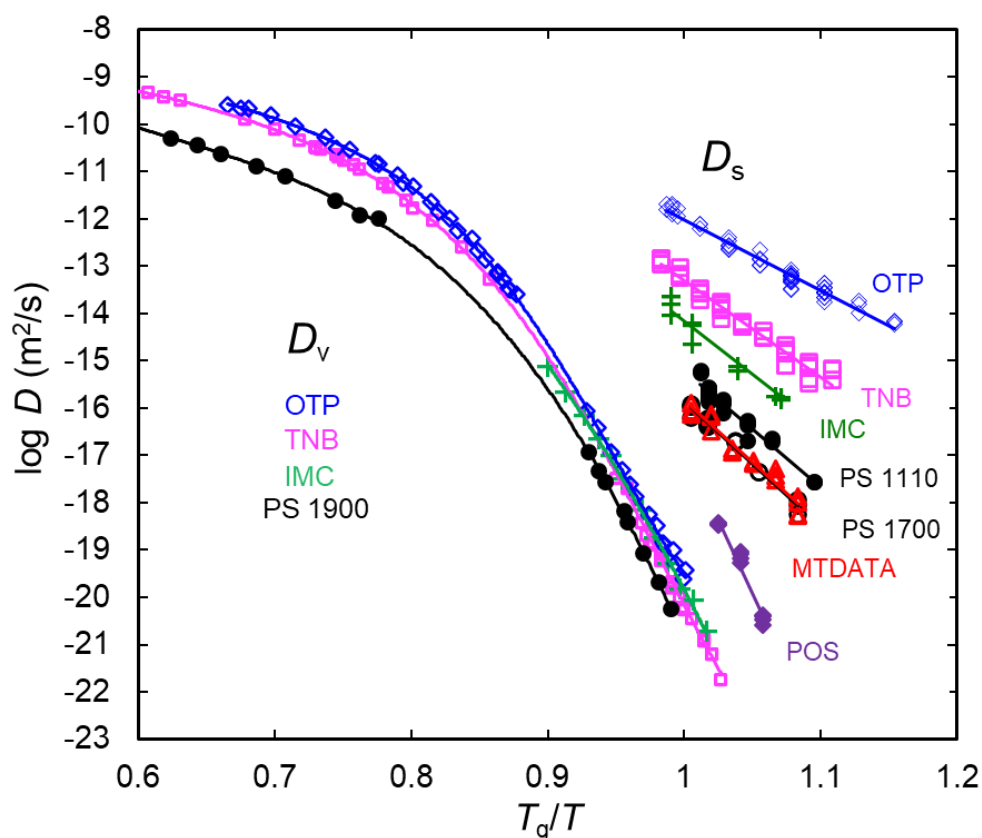


Figure 3.4. Surface and bulk diffusion coefficients of MTDATA and other organic glasses. T_g is the onset temperature of glass transition measured by DSC during heating at 10 K/min.

still significantly larger than the clustered D_v values, by approximately 4 orders of magnitude when compared at T_g . On this plot, MTDATA and PS 1700 are nearly coincident despite their rather different molecular weights (789 g/mole and 1700 g/mole). As we discuss later, this could arise from their similar penetration depths into the bulk glass.

3.5 Discussion

We have measured the surface diffusion in the glass of the discotic molecule MTDATA using the method of surface grating decay. Similar to other molecular glasses, surface evolution occurs by viscous flow at high temperatures and by surface diffusion at low temperatures. The low-temperature data allowed calculation of the surface diffusion coefficient of MTDATA (Figure 3.3b) for comparison with the values of other systems (Figure 3.4). The surface diffusion of MTDATA is enhanced relative to the typical bulk rate by 4 orders of magnitude when evaluated at T_g . This finding is consistent with the enhanced stability of MTDATA glasses prepared by PVD relative to the ordinary liquid-cooled counterpart.³⁹ We now discuss the MTDATA result in relation to the other systems investigated and show that the depth of penetration of surface molecules plays a central role in defining the rate of surface diffusion. This allows a quantitative depth profiling of the surface mobility gradient and our result supports double-exponential form recently observed by simulations.

Li et al. investigated the effect of the penetration depth of surface molecules on the rate of surface diffusion.²⁰ They plotted the surface diffusion coefficient D_s at T_g as a function of the penetration depth z and observed a downward trend. We reproduce their plot in Figure 3.5 and add the new MTDATA point. The central idea in this analysis is that a surface molecule can penetrate into the bulk by one to a few nanometers and according to simulations, local mobility can decrease

substantially in this depth range.²² As a result, the bottom of the molecule experiences a different, lower-mobility environment from the top and it is the bottom of the molecule that determines the rate of its lateral diffusion. By this reasoning, the deeper the penetration, the slower the surface diffusion. Li et al. have treated the calculation of the penetration depths of quasi-spherical and rod-like molecules as illustrated at the bottom of Figure 3.5. For a discotic molecule like MTDATA, $z = D \sin \alpha$, where D is the disc diameter and α is the average angle between the disc normal and the surface normal. For MTDATA, $D = 1.9$ nm from DFT calculations. As for the angle α , we recall that the glass film of MTDATA prepared by PVD onto a substrate held near T_g shows no strong molecular orientation.⁴⁰ In contrast, significant molecular orientation exists in the glass film of rod-like molecules deposited near T_g , by inheriting the preferred orientation at the interface.⁴¹ We interpret this to mean that MTDATA molecules do not have strongly preferred orientations at the liquid/vapor interface. This interpretation is consistent with the nearly isotropic near-surface orientation of a similar discotic molecule, *tris*(4-carbazoyl-9-ylphenyl)amine (TCTA) recently determined by Polarization Resonant Soft X-ray Reflectivity.⁴² Thus, we take the average value of α to be 55° , corresponding to random orientation, and obtain $z = 1.6$ nm. Figure 3.5 shows that the MTDATA point joins the previously observed trend for other molecular shapes. This result indicates that regardless of the detailed molecular shape, surface diffusion rate is mainly determined by how deeply the molecule penetrates into the bulk.

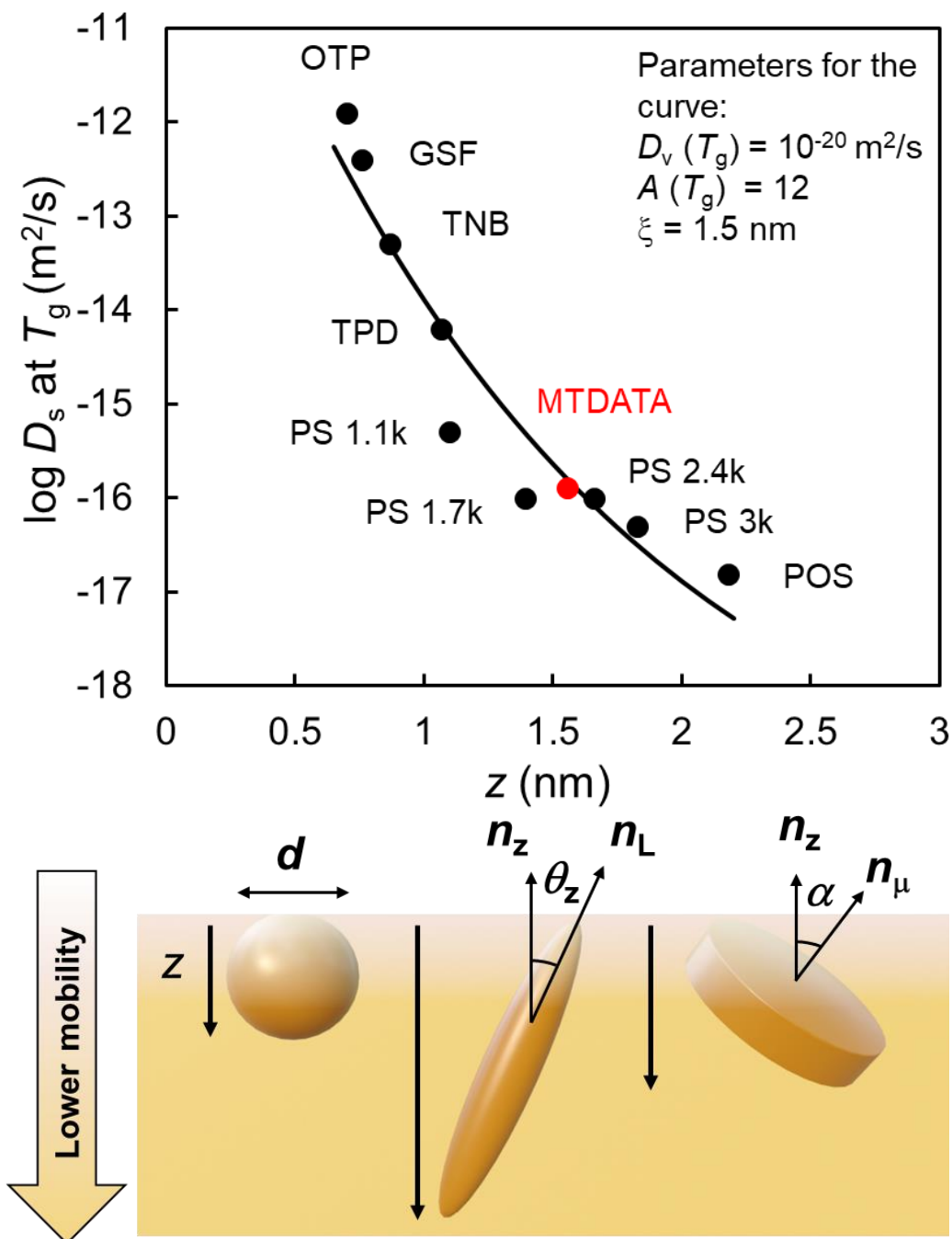


Figure 3.5. Surface diffusion coefficient D_s at T_g vs. the penetration depth z . The curve is a fit of the data to eq. 3.2. The calculation of the penetration depth z is illustrated at the bottom for quasi-spherical, rod-like and discotic molecules. $z = d$ for a quasi-spherical molecule, where d is molecular diameter. $z = L \cos \theta_z$ for a rod-like molecule where L is rod length and θ_z the average angle between the long axis and the surface normal. $z = D \sin \alpha$ for a discotic molecule, where D is the disc diameter and α is the average angle between the disc normal and the surface normal.

In Figure 3.5, the D_s vs penetration depth data have been fitted using a double-exponential function:

$$\log D_s(T) = \log D_v(T) + A(T) \exp(-z/x) \quad (3.2)$$

This function is inspired by the finding by simulations that near-surface structural relaxation time, t , has a double-exponential dependence on depth.^{21,22} This form has been rationalized as a consequence of geometric-like, layer-wise transfer of caging constraint.^{43,44} In using this form,²⁰ we follow Ref. 5 and assume that diffusivity is inversely proportional to t in the mobile surface layer. The physical meaning of eq. 3.2 is (1) the activation barrier for diffusion increases exponentially with depth, and (2) the surface diffusion rate for a given molecule is determined by its deepest part where mobility is the lowest. In eq. 3.2, $A(T)$ describes the temperature-dependent difference between surface and bulk mobility, and x describes the rate at which mobility decreases with depth. In this fitting, we fix $D_v(T_g)$ at 10^{-20} m²/s, a typical value for molecular glasses at T_g (see Figure 3.4) and obtain: $A(T_g) = 12$ and $x = 1.5$ nm. In principle, each system in Figure 3.5 has its own A and x values, but the successful fitting of all the data to eq. 3.2 indicates that these systems are well described by a *common* set of parameters. That is, a similar surface mobility gradient characterizes all these systems. In this mobility gradient (valid for T_g), the diffusion rate decreases by 12 orders of magnitude from the surface ($z = 0$) to the bulk ($z = \infty$), and the activation energy for diffusion increases exponentially with depth with a characteristic length of $x = 1.5$ nm. This is a remarkable result given the large differences between these systems in molecular weight (a factor of 10) and shape (quasi-spherical, rod-like, chain-like and discotic). One common feature of these systems is the absence of extensive hydrogen bonding, which has an independent slowing effect on surface diffusion.¹⁹

Given the success of eq. 3.2 to describe the surface diffusion rates at T_g , we now explore the possibility to generalize it to *all* temperatures. For this purpose, we recall that the D_s and D_v values for the same system measured at different temperatures follow a power law.¹⁹ In Figure 3.6, we plot D_s against D_v for the three systems for which both properties have been measured: OTP,^{28,35} TNB,^{29,36} and IMC.^{1,37} For each system, the data are well described by a power law:

$$D_s = D_v^x D_0^{1-x} \quad (3.3)$$

where x is a coupling constant ($0 - 1$) and D_0 corresponds to the high-temperature condition at which $D_s = D_v$. For all three systems, $D_0 = 10^{-8} \text{ m}^2/\text{s}$ is consistent with the high-temperature extrapolation of the data, converging at the + sign in Figure 3.6. For OTP, the validity of eq. 3.3 and the D_0 value is further supported by simulations performed near $D_v = 10^{-11} \text{ m}^2/\text{s}$.⁴⁵ Eq. 3.3 is also consistent with simulation results on other systems (not yet studied experimentally) as summarized in Ref. 19 and with the theories of surface mobility.^{2,5,21,46} The value $D_0 = 10^{-8} \text{ m}^2/\text{s}$ corresponds to the dynamic state at which the structural relaxation time is approximately 10 ps (calculated from $\tau = d^2/(6 D)$, where $d \approx 0.8 \text{ nm}$ is the approximate size of OTP, TNB, and IMC). This value is comparable to the theoretically predicted condition under which surface and bulk mobility are equal: $\tau_\alpha = 1 \text{ ps}$ (Ref. 2), $1 - 10 \text{ ps}$ (Ref. 22), 2 ps (Ref. 46). Empirically, the D_0 value of $10^{-8} \text{ m}^2/\text{s}$ is lower than the typical gas-phase diffusivity ($10^{-5} \text{ m}^2/\text{s}$)⁴⁷ and without invoking deep interpretation, comparable to the diffusivity at the critical point at which the distinction vanishes between liquid and vapor.^{48,49}

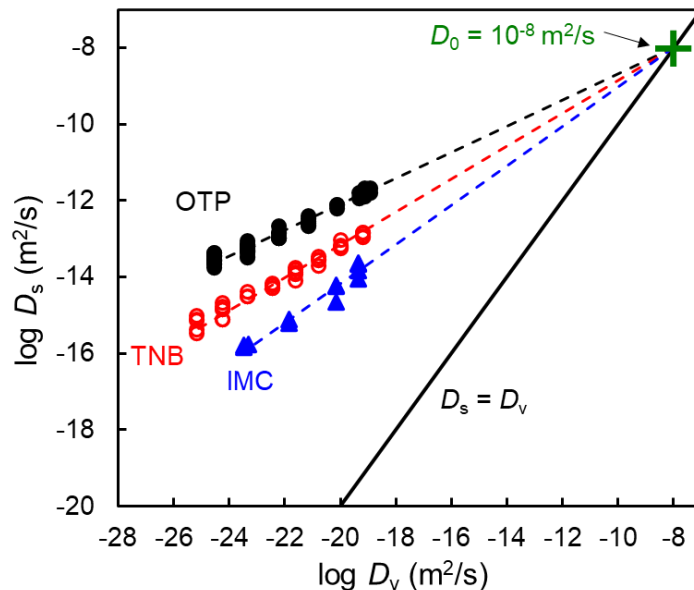


Figure 3.6. D_s plotted against D_v for 3 systems for which both properties have been measured. The power law $D_s = D_v \times D_0^{1-x}$ holds for each system, where $D_0 \approx 10^{-8} \text{ m}^2/\text{s}$ corresponds to the high-temperature condition at which $D_s = D_v$. The exponent x is 0.34 for OTP, 0.43 for TNB, and 0.51 for IMC.

Eq. 3.3 can be rearranged to read: $\log D_s (T) = \log D_v (T) + [\log D_0 - \log D_v (T)] (1 - x)$, and comparison with eq. 3.2 yields:

$$A(T) = \log D_0 - \log D_v(T) \quad (3.4)$$

$$\exp(-z/x) = 1 - x \quad (3.5)$$

Combining eqs. 2, 4, and 5, we obtain:

$$\log D_s (T) = \log D_v (T) + [\log D_0 - \log D_v (T)] \exp(-z/x) \quad (3.6)$$

Eq. 3.6 allows the calculation of D_s at any temperature T from the D_v value at that temperature, the molecule-dependent penetration depth z , and the characteristic length for the mobility gradient x .

The validity of eq. 3.6 depends on the validity of eqs. 2 and 3. We now test the ability of eq. 3.6 to describe the temperature dependence of the measured D_s values. For the systems whose D_v values are known (OTP, TNB, and IMC), the only adjustable parameter in eq. 3.6 is x . We optimize x for each system to best fit the measured D_s . Figure 3.7a compares the measured and fitted D_s values. We find an excellent agreement between the two. From the fits, we obtain $x = 1.7$ nm for OTP, 1.5 nm for TNB, and 1.3 nm for IMC. These values are reasonably close, consistent with the notion that the three systems share a similar mobility gradient. For PS1100 and PS1700, D_v has not been measured but is known at a similar molecular weight (1900 g/mole).³⁸ We estimate the D_v of PS1100 and PS1700 from that of PS1900 by T_g scaling, and then perform the same test of eq. 3.6 as described above. The results are included in Figure 3.7a. Again, the measured D_s values agree well with the fitted values, yielding $x = 1.4$ nm for PS1100 and 1.5 nm for PS1700. Finally, for the systems whose D_v has not been measured, we use an approximation inspired by the clustering of the D_v values when plotted against T_g/T (Figure 3.4):

$$\log D_v(T) = \log D_v(T_g) + m_D(1 - T_g/T) \quad (3.7)$$

Eq. 3.7 is intended to describe the D_v value near T_g where m_D is a fragility index for diffusivity, in analogy to the m index for viscosity. From a joint fit of the data on OTP, TNB, IMC, and PS1900 for $T < 1.05 T_g$, we obtain $D_v(T_g) = 10^{-20}$ m²/s and $m_D = 53$. Eq. 3.7 reproduces the measured D_v values for the 4 systems with a standard deviation of 0.3 decade. Using eq. 3.7, we perform the same test above for griseofulvin (GSF),⁵⁰ POS and MTDATA and the results are shown in Figure 3.7b. We observe a good agreement between measured and calculated D_s values and obtain $x = 1.7$ nm for GSF, 1.4 nm for POS, and 1.6 nm for MTDATA. These values are all consistent with those obtained for the other systems.

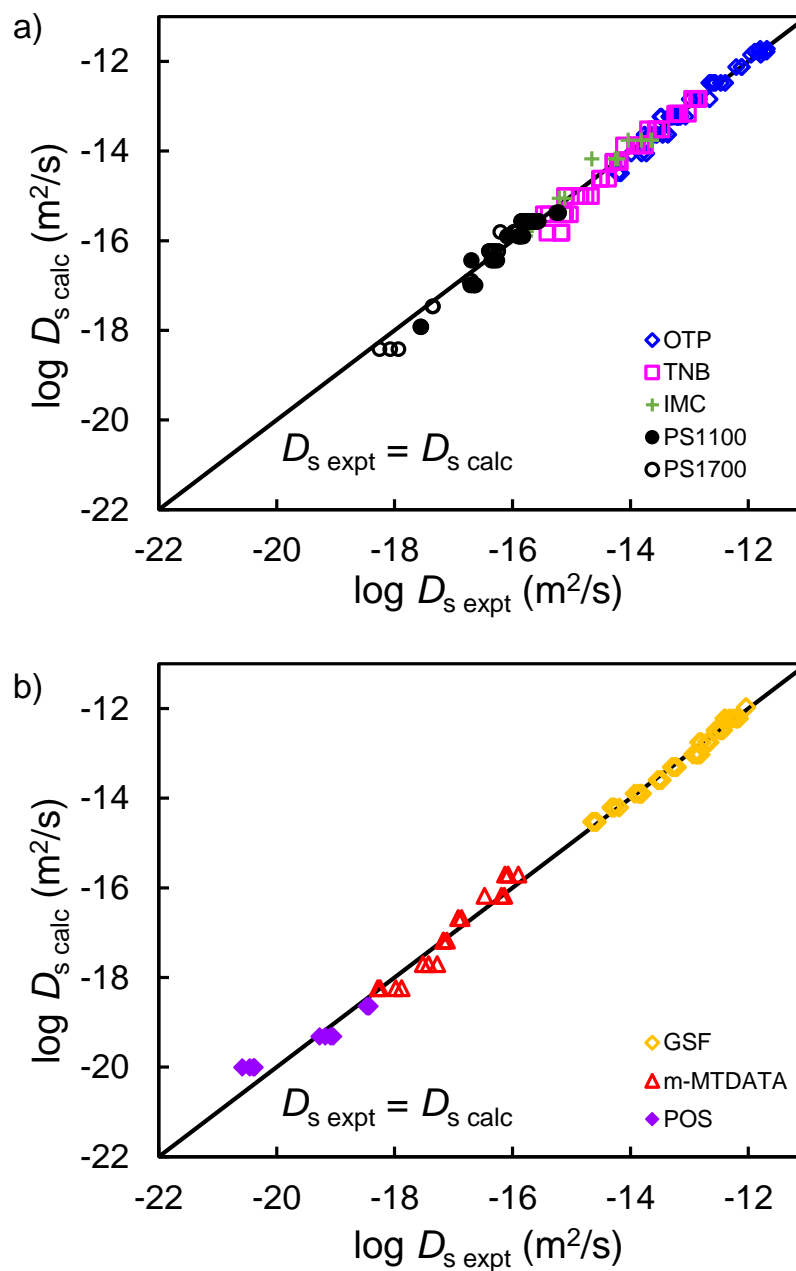


Figure 3.7. Comparison of measured surface diffusivity, $D_{s, \text{expt}}$ and the value $D_{s, \text{calc}}$ calculated from eq. 3.6 for the systems whose D_v is known (a) and unknown (b). For (b), a generic D_v is assumed (eq. 3.7). In both cases, ξ has been adjusted to best fit the data.

Table 3.1. Parameters for surface and bulk diffusion in molecular glasses.

	M (g/mol)	T_g (K)	d (nm)	z (nm)	x	λ (nm)	m_D	$\log D_{v,g}$ (m ² /s)
			a					
OTP	230.3	246	0.70	0.70	0.34	1.7	48.7	-19.5
TNB	456.6	347	0.87	0.87	0.43	1.5	55.4	-20.2
IMC	357.8	315	0.76	0.89 ^b	0.51	1.3	52.0	-19.9
PS1110	990	307	1.17	1.10	0.55 ^c	1.4	55.7	-20.8
PS1700	1600	319	1.37	1.39	0.60 ^c	1.5	55.7	-20.8
GSF	352.8	361	0.76	0.76	-	1.7	53 ^d	-20 ^e
MTDATA	789.2	350	1.03	1.56	-	1.6	53 ^d	-20 ^e
POS	700.8	331	0.97	2.18	-	1.4	53 ^d	-20 ^e

^a d is the molecular size calculated from $d = \Omega^{1/3}$, where Ω is the molecular volume (molar volume/Avogadro's number). All values are from Ref. 20 except for that for MTDATA, which is $\Omega = 1.09 \text{ nm}^3$.

^b Enlarged slightly from d to reflect hydrogen bonding.¹⁹

^c D_v used for fitting (eq. 3.3) is calculated from the data on PS1900 (Ref. 38) by T_g scaling.

^{d,e} Fixed at typical value for molecular glasses.

The success of eq. 3.6 to describe the known D_s results using a similar set of parameters suggests a possibility to predict the surface diffusion rate for any molecular glass. For this purpose, we use eq. 3.6 to predict the D_s for all van der Waals molecular glasses whose D_s has been measured, with $D_0 = 10^{-8} \text{ m}^2/\text{s}$ and $x = 1.5 \text{ nm}$. We use eq. 3.7 to calculate the D_v values (setting aside the experimentally measured D_v values), with $D_v(T_g) \approx 10^{-20} \text{ m}^2/\text{s}$ and $m_D = 53$. The results are shown in Figure 3.8, without distinguishing the individual systems. We see a reasonably good agreement between predicted and experimental values with a standard deviation of 0.6 decade. Given the overall span of the D_s data over 9 orders of magnitude, the preliminary success is encouraging. One source of error for this model is the accuracy of eq. 3.7 to describe bulk diffusion rates (the

standard deviation already amounts to 0.3 decade). The additional error comes from the slight system-to-system variation of the x value (Table 3.1). Nevertheless, this model and its refinement have the potential to predict the surface diffusion rate in any non-hydrogen-bonded molecular glass from nothing more than its molecular structure.

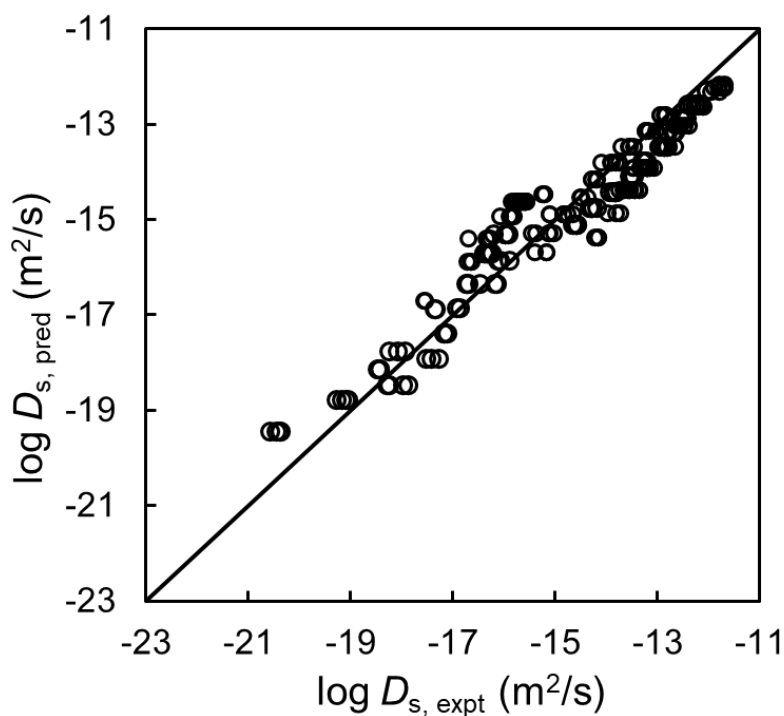


Figure 3.8. Comparison of measured and predicted surface diffusivity, $D_{s,\text{expt}}$ and $D_{s,\text{pred}}$. Eqs. 6 and 7 are used for this prediction with $\xi = 1.5$ nm, $D_0 = 10^{-8}$ m²/s, $D_v(T_g) = 10^{-20}$ m²/s, and $m_D = 53$.

Although this work was conducted to understand surface diffusion in glasses, the results provide information on the near-surface mobility gradient, a topic of current interest.^{21,51} Below we discuss our two key conclusions and relate them to the literature: (1) the power-law relation between surface and bulk mobility (eq. 3.3) and (3.2) a generic surface mobility gradient with a double exponential dependence on depth z .

Eq. 3.3 is an empirical formula that describes the experimental data on three systems (OTP, TNB, and IMC; Figure 3.6). For each system, eq. 3.3 describes the relationship between the surface and bulk diffusivity, D_s and D_v , measured over a range of temperature. The three systems show different degrees of decoupling between D_s and D_v (different x) but have a similar high-mobility state ($D_0 \approx 10^{-8}$ m²/s) at which $D_s = D_v$. We now show that eq. 3.3 is consistent with an equation based on the simulation results of Diaz-Vela et al.⁵² and augmented later:²¹

$$\tau(T, z) = \tau_a(T)^{1-\varepsilon(z)} \tau^* \varepsilon(z) \quad (3.8)$$

where $\tau(T, z)$ is the depth (z)-dependent structural relaxation time, $\tau_a(T)$ is the bulk structural relaxation time, $\varepsilon(z)$ is a decoupling index between 0 and 1, and $\tau^* = 1 - 10$ ps.²¹ ε characterizes the degree to which $\tau(T, z)$ decouples from $\tau_a(T)$ with $\varepsilon \approx 1$ signifying large decoupling that occurs near the top of the surface and 0 for no decoupling deep in the bulk. Diaz-Vela et al. showed that at low enough bulk mobility ($\tau_a \gg \tau^*$), ε is weakly dependent on temperature and a function of z only.

If we assume a surface molecule's penetration depth into the bulk is weakly dependent on temperature, its bottom position z in the surface mobility gradient is nearly constant. Assuming the molecule's lateral mobility (surface diffusion) is limited by the mobility of its deepest part, we obtain

$$\tau_s(T) = \tau_a(T)^{1-\varepsilon} \tau^* \varepsilon \quad (3.9)$$

where t_s is the surface relaxation time. (z is dropped in eq. 3.9 as it is nearly constant for a given molecule.) Eq. 3.9 leads to eq. 3.3 if we assume $D \propto \tau^{-1}$. The constant x in eq. 3.3 is related to ϵ in eq. 3.9 by: $x = 1 - \epsilon$. For consistency, D_0 in eq. 3.3 should correspond to t^* in eq. 3.9, both describing the dynamic state at which surface and bulk mobility are equal. To test this, we recall the earlier result that $D_0 = 10^{-8} \text{ m}^2/\text{s}$ corresponds to $\tau \approx 10 \text{ ps}$ for $d \approx 0.8 \text{ nm}$, which is close to $\tau^* = 1 - 10 \text{ ps}$.²¹ We view this coherent picture as an experimental support for Eq. 3.8, a simulation-based result.

We now turn to the features of the surface mobility gradient inferred from our study of surface diffusion rates. For non-hydrogen-bonding molecular liquids, our results suggest a generic surface mobility gradient of the form:

$$\log D(T, z) = \log D_v(T) + A(T) \exp(-z/x) \quad (3.10)$$

where $D(T, z)$ is the depth-dependent local diffusivity, and all other parameters have been defined above. Note that eq. 3.10 is different from eq. 3.2 in that it describes the *variation of mobility with depth* z , while eq. 3.2 describes how the *overall* surface diffusion rate D_s depends on the depth of penetration (for a given system the penetration depth is fixed; see Table 3.1). We justify eq. 3.10 on the basis that (1) eq. 3.2 accurately describes our D_s results (Figures 3.7 and 3.8) and (2) each observed D_s probes the mobility at the bottom of a surface molecule. Based on this work, the parameters in eq. 3.10 are: $x \approx 1.5 \text{ nm}$, $A(T) = \log D_0 - \log D_v(T)$, where $D_0 \approx 10^{-8} \text{ m}^2/\text{s}$. At the DSC T_g , $A(T_g) \approx 12$.

Given that a double-exponential profile of the surface mobility gradient has been proposed based on simulation results and theoretical analysis, we view its ability to describe our results as an experimental support for this profile. Our finding of $x \approx 1.5$ nm for non-hydrogen-bonding molecular liquids is in reasonable agreement the simulation and theoretical results ($\xi = 2-3 d$, where d is the bead diameter).^{21,43} It is noteworthy, however, that the values from simulations and theories are often reported to scale with the molecular size d . While our values (Table 3.1) do not appear to show such scaling behavior. As for the amplitude A in eq. 3.10, the simulations summarized in Ref. 21 indicate $A = 2-4$, obtained for simulated systems of higher mobility ($t_a \sim 1$ ns) than the experimental systems. Using 1 ns for t_a and our expression for $A(T)$ in eq. 3.10, we estimate $A(T) \approx 2$, in fair agreement with the simulation results. Based on their theory, Phan and Schweizer obtain $A(T_g) = 12$ for hard spheres and 11–17 for real polymers mapped onto their model, where T_g is the temperature at which $t_a = 100$ s (close to the value at the DSC T_g , ~ 10 s).⁴³ Overall, there is encouraging agreement between simulations, theories, and experiment on the double-exponential profile for the surface mobility gradient, while the details of the gradient and its system dependence awaits future clarification.

3.6 Conclusions

In this work, we have applied the method of surface grating decay to measure the surface diffusion in the glass of a discotic organic semiconductor, MTDATA. The high-temperature decay occurs by viscous flow and the low-temperature decay by surface diffusion (Figures 3.2 and 3.3). The surface diffusion of MTDATA is enhanced relative to the bulk diffusion by 4 orders of magnitude at T_g (Figure 3.4). The MTDATA result joins the previously observed trend between surface diffusivity and penetration depth (Figure 3.5). This argues for a generic surface mobility gradient

for non-hydrogen-bonded molecular glasses with a double-exponential decrease of mobility with depth (eq. 3.2). The power-law relation between surface and bulk diffusivity (eq. 3.3) provides access to the parameters characterizing the double-exponential mobility gradient, leading to an equation (eq. 3.6) useful for fitting (Figure 3.7) and predicting (Figure 3.8) the surface diffusion coefficient. This model has the potential to predict surface diffusion rates in molecular glasses from the molecular structure alone. Such capability is relevant for predicting surface crystallization rates and the likelihood of forming ultra-stable glasses by PVD in the manufacture of organic electronic devices.

Under the assumption that surface diffusion is limited by the mobility at the deepest anchoring point of surface molecules, our results can be used to provide the depth profile of the near-surface mobility. Our results support the recently proposed double-exponential form for the surface mobility gradient and give a quantitative description of this gradient in terms of diffusivity (eq. 3.10) with $D_0 \approx 10^{-8} \text{ m}^2/\text{s}$ and $x \approx 1.5 \text{ nm}$. It is intriguing that despite the different molecular weights and shapes of the systems investigated, they all appear to have a similar surface mobility gradient. This finding can be further examined by simulations where molecular size and geometry are systematically varied to test the robustness of a generic mobility gradient. While this work has focused on non-hydrogen-bonding molecular glasses, how the introduction of hydrogen bonds affects the mobility gradient deserves future investigation.

3.7 Acknowledgements

This research was primarily supported by NSF through the University of Wisconsin Materials Research Science and Engineering Center (Grant DMR-1720415). We thank Kushal Bagchi for helpful conversations.

3.8 References

-
- ¹ L. Zhu, C. W. Brian, S. F. Swallen, P. T. Straus, M. D. Ediger, and L. Yu, *Phys. Rev. Lett.* **106**, 256103 (2011).
 - ² J. D. Stevenson, and P. G. Wolynes, *J. Chem. Phys.* **129**, 234514 (2008).
 - ³ S. Mirigian, and K. S. Schweizer, *J. Chem. Phys.* **143**, 244705 (2015).
 - ⁴ Y. Sun, L. Zhu, K. L. Kearns, M.D. Ediger and L. Yu, *Proc. Natl. Acad. Sci.* **108**, 5990 (2011).
 - ⁵ T. Wu, and L. Yu, *Pharm. Res.* **23**, 2350 (2006).
 - ⁶ M. D. Ediger, *J. Chem. Phys.* **147**(21), 210901 (2017).
 - ⁷ A. N. Raegen, J. Yin, Q. Zhou, and J. A. Forrest, *Nat. Mat.* **19**(10), 1110-1113 (2020).
 - ⁸ K. Yoshimoto, T. S. Jain, P. F. Nealey, and J. J. De Pablo, *J. Chem. Phys.* **122**(14), 144712 (2005).
 - ⁹ S. P. Delcambre, R. A. Riggelman, J. J. de Pablo, and P. F. Nealey, *Soft Matter* **6**(11), 2475-2483 (2010).
 - ¹⁰ X. Li, X. Liang, Z. Zhang, J. Ma, and J. Shen, *Scripta Materialia* **185**, 100-104 (2020).
 - ¹¹ Y. Shirota, T. Kobata, and N. Noma, *Chem. Lett.* **18**(7), 1145-1148 (1989).
 - ¹² Y. Kuwabara, H. Ogawa, H. Inada, N. Noma, and Shirota, Y. *Adv. Mater.* **6**(9), 677-679 (1994).
 - ¹³ Y. Shirota, *J. Mater. Chem.* **15**(1), 75-93 (2005).
 - ¹⁴ C. W. Tang, and S. A. VanSlyke, *Appl. Phys. Lett.* **51**(12), 913-915 (1987).
 - ¹⁵ K. Bagchi, M. E. Fiori, C. Bishop, M. F. Toney, and M. D. Ediger, *J. Phys. Chem. B* **125**(1), 461-466 (2020).
 - ¹⁶ K. Bagchi, and M. D. Ediger, *J. Phys. Chem. Lett.* **11**(17), 6935-6945 (2020).
 - ¹⁷ S. F. Swallen, K. L. Kearns, M. K. Mapes, Y. S. Kim, R. J. McMahon, M. D. Ediger, T. Wu, L. Yu, and S. Satija, *Science* **315**(5810), 353-356 (2007).
 - ¹⁸ M. D. Ediger, J. de Pablo, and L. Yu, *Acc. Chem. Res.* **52**(2), 407-41 (2019).
 - ¹⁹ Y. Chen, W. Zhang, and L. Yu, *J. Phys. Chem. B* **120**, 8007-8015 (2016).

-
- ²⁰ Y. Li, W. Zhang, C. Bishop, C. Huang, M.D. Ediger, and L. Yu, *Soft. Matt.* **16**, 5062-5070 (2020).
- ²¹ K. S. Schweizer, and D. S. Simmons, *J. Chem. Phys.* **151**, 240901 (2019).
- ²² P. Scheidler, W. Kob and K. Binder, *Europhysics Letters (EPL)* **59**(5), 701-707 (2002).
- ²³ H. J. Werner, P. J. Knowles, G. Knizia, F. R. Manby, and M. Schütz, *Mol. Sci.* **2**, 242–253 (2012).
- ²⁴ A. H. Larsen, J. J. Mortensen, J. Blomqvist, I. E. Castelli, R. Christensen, M. Duřak, J. Friis, M. N. Groves, B. Hammer, C. Hargus, et al. *J. Phys.: Condens. Matter* **29**, 273002 (2017).
- ²⁵ J. P. Perdew, K. Burke, and M. Ernzerhof, *Phys. Rev. Lett.* **77**, 3865–3868 (1996).
- ²⁶ S. Grimme, J. Antony, S. Ehrlich, and H. Krieg, *J. Chem. Phys.* **132**, 154104 (2010).
- ²⁷ T. H. Dunning, *J. Chem. Phys.* **90**, 1007–1023 (1989).
- ²⁸ W.W. Mullins, *J. Appl. Phys.* **30**, 77 (1959).
- ²⁹ L. M. Martinez, and C. A. Angell, *Nature* **410**, 663-667 (2001).
- ³⁰ D. J. Plazek, C. A. Bero, and I. C. Chay, *J. Non-Cryst. Solids* **172**, 181–190 (1994).
- ³¹ D. J. Plazek, and J. H. Magill, *J. Chem. Phys.* **45**, 3038–3050 (1966).
- ³² W. Zhang, C. W. Brian, and L. Yu, *J. Phys. Chem. B* **119**, 5071 (2015).
- ³³ S. Ruan, W. Zhang, Y. Sun, M. D. Ediger, and L. Yu, *J. Chem. Phys.* **145**, 064503 (2016).
- ³⁴ W. Zhang, and L. Yu, *Macromolecules*. **49**, 731 (2016).
- ³⁵ M. K. Mapes, and S. F. Swallen, and M. D. Ediger, *J. Phys. Chem. B* **110**, 507 (2006).
- ³⁶ S. F. Swallen, K. Traynor, R. J. McMahon, M. D. Ediger, and T. E. Mates, *J. Phys. Chem. B* **113**, 4600 (2009).
- ³⁷ S. F. Swallen, and M. D. Ediger, *Soft Matter* **7**, 10339 (2011).
- ³⁸ O. Urakawa, S. F. Swallen, M. D. Ediger, and E. D. von Meerwall, *Macromolecules* **37**, 1558 (2004).
- ³⁹ D. M. Walters, L. Antony, J. J. de Pablo, and M. D. Ediger, *J. Phys. Chem. Lett.* **8**(14), 3380-3386 (2017).
- ⁴⁰ A. Gujral, J. Gomez, S. Ruan, M. F. Toney, H. Bock, L. Yu, and M. D. Ediger, *Chem. Mater.* **29**(21), 9110-9119 (2017).
- ⁴¹ C. Bishop, J. L. Thelen, E. Gann, M. F. Toney, L. Yu, D. M. DeLongchamp and M. D. Ediger, *Proc. Natl. Acad. Sci. U. S. A.*, **116**, 21421 (2019)
- ⁴² T. J. Ferron, J. L. Thelen, K. Bagchi, C. Deng, E. Gann, J. J. de Pablo, M. D. Ediger, D. F. Sunday, and D. M. DeLongchamp, *ACS Appl. Mater. Interfaces* **14**, 3455 (2022).
- ⁴³ A. D. Phan, K.S. Schweizer, *J. Chem. Phys.* **150**, 044508 (2019).

-
- ⁴⁴ A. D. Phan, and K. S. Schweizer, *Macromolecules*, **52**, 5192 (2019).
- ⁴⁵ Y. Li, A. Annamareddy, D. Morgan, Z. Yu, B. Wang, C. R. Cao, J. H. Perepezko, M. D. Ediger, P. M. Voyles and L. Yu, *Phys. Rev. Lett.* **128**, 075501 (2022).
- ⁴⁶ S. Capaccioli, K. L. Ngai, M. Paluch, and D. Prevosto, *Phys. Rev. E* **86**, 051503 (2012).
- ⁴⁷ D. Jakubczyk et al., *J. Phys. Chem. A* **114**, 3483 (2010).
- ⁴⁸ H. Hamann, C. Hoheisel, and H. Richtering, *Berichte der Bunsengesellschaft für physikalische Chemie*, **76**(3-4), 249-253 (1972).
- ⁴⁹ T. Saitoh, N. Yoshio, and S. Shigezo, *Bull. Chem. Soc. Jpn.* **65**, 3480-3481 (1992).
- ⁵⁰ C. Huang, S. Ruan, T. Cai, and L. Yu, *J. Phys. Chem. B* **121**, 9463 (2017).
- ⁵¹ A. Ghanekarade, A. D. Phan, K. S. Schweizer, and K. S. Simmons, *Proc. Natl. Acad. Sci.* **118**(31), (2021).
- ⁵² D. Diaz-Vela, J.-H. Hung, and D. S. Simmons, *ACS Macro Lett.* **7**, 1295 (2018).

Chapter 4 Surface diffusion is controlled by bulk fragility across all glass types

Yuhui Li¹, Ajay Annamareddy², Dane Morgan², Zheng Yu³, Bu Wang³, Chengrong Cao², John H. Perepezko², M. D. Ediger⁴, Paul M. Voyles² and Lian Yu^{1,4*}

¹ School of Pharmacy, University of Wisconsin-Madison, Madison, WI, 53705, USA

² Department of Materials Science and Engineering, University of Wisconsin-Madison, Madison, WI, 53706, USA

³ Department of Civil and Environmental Engineering, University of Wisconsin-Madison, Madison, WI, 53706, USA

⁴ Department of Chemistry, University of Wisconsin-Madison, Madison, WI, 53706, USA

As published in *Phys. Rev. Lett.* 2022, 128, 075501

4.1 Abstract

Surface diffusion is vastly faster than bulk diffusion in some glasses, but only moderately enhanced in others. We show that this variation is closely linked to bulk fragility, a common measure of how quickly dynamics is excited when a glass is heated to become a liquid. In fragile molecular glasses, surface diffusion can be a factor of 10^8 faster than bulk diffusion at the glass transition temperature, while in the strong system SiO_2 , the enhancement is a factor of 10. Between these two extremes lie systems of intermediate fragility, including metallic glasses and amorphous selenium and silicon. This indicates that stronger liquids have greater resistance to dynamics excitation from bulk to surface and enables prediction of surface diffusion, surface crystallization, and formation of stable glasses by vapor deposition.

4.2 Results and Discussion

Glasses have liquid-like spatial uniformity and crystal-like mechanical strength, having countless applications from optics to electronics to drug delivery.^{1,2,3} Recent work has highlighted the importance of surface mobility in the fabrication and stability of glasses. Utilizing high surface mobility,^{4,5} crystal growth can be much faster on the free surface than in the bulk⁶ and ultra-stable glasses can be prepared by vapor deposition.^{7,8} In other areas, surface mobility impacts the stability of nanostructures, the resolution of nanolithography,^{9,10} catalysis,¹¹ and particle sintering.¹² Because of this central role, understanding and predicting surface mobility is of strong interest.

Recent work has shown that surface diffusion rates can vary greatly across different glasses. For molecular glasses at the glass transition temperature T_g , the ratio of surface to bulk diffusivity, D_s/D_v , can be as large as 10^8 and as small as 10^4 , while the bulk diffusivity is approximately

constant ($\sim 10^{-20}$ m²/s).^{4,13,14,15} Simulations have observed similar effect for systems at higher mobility. For example, at $D_v = 10^{-12}$ m²/s, $D_s/D_v = 1,000$ for the Kob-Andersen Lennard-Jones (KA LJ) mixture,¹⁶ 20 for the metallic glass-former CuZr,^{17,18} and 2 for the network system SiO₂.¹⁹ There has been progress in the theory of surface mobility,^{20,21,22} but the large variation across systems remains poorly understood.

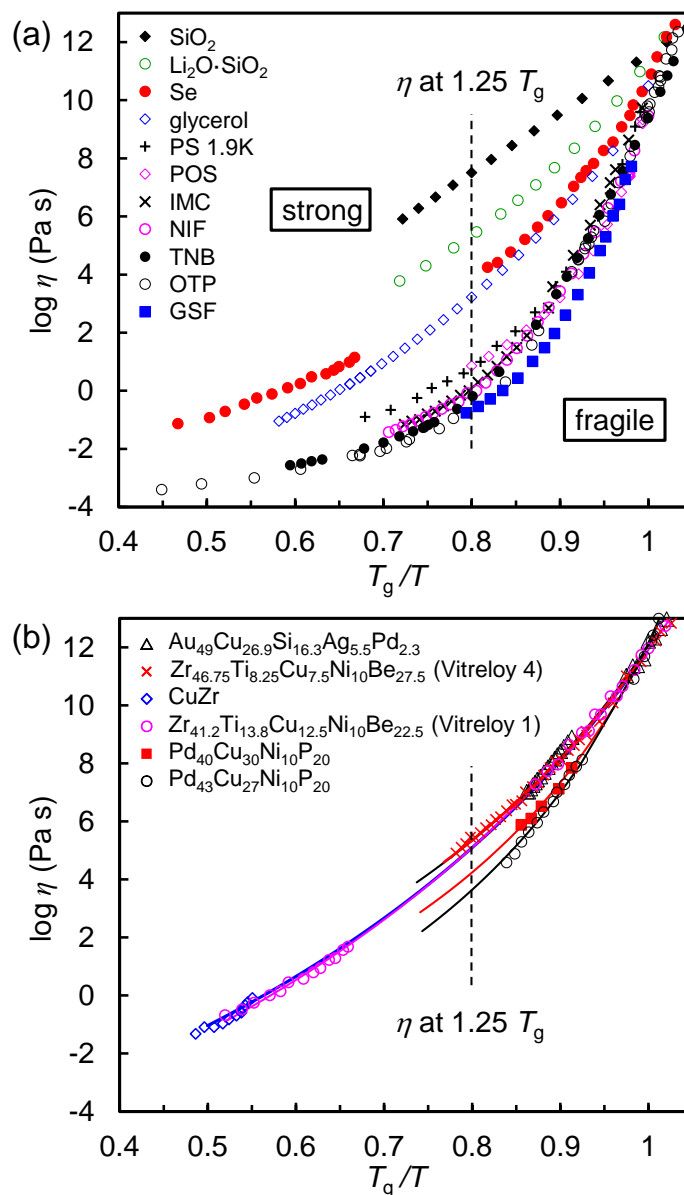


Figure 4.1 Angell plots of the viscosities of different materials. (a) Molecular liquids, selenium, and oxides. (b) Glass-forming metallic liquids. See Table 4.1 for references.

We report that the large difference in surface diffusion rate between glasses is closely related to the fragility of bulk dynamics. Fragility is a widely used measure of the ease with which dynamics is excited when a glass is heated to become a liquid.²³ As Figure 4.1 shows, a strong system like SiO₂ resists such excitation, while a fragile system like *o*-terphenyl (OTP) quickly gains mobility above T_g . The strong character of SiO₂ results from the robustness of its 3D network of covalent bonds, while the fragility of OTP from the rapid unraveling of its local structure maintained by weak van der Waals interactions. Recently, Chen et al. reported a correlation between surface diffusivity and bulk fragility for a group of molecular glass-formers, with high surface mobility associated with high fragility.²⁴ Their work only covered the fragile organic systems, and here we show that the conclusion holds for glasses across the entire fragile-strong spectrum, including chalcogenide, silicon, metallic, and oxide glasses. Overall, these results now form the critical mass of evidence, leading to an important universal conclusion for all glass types featuring widely different interparticle forces.

Figure 4.1 shows the viscosities of the systems investigated as functions of T_g scaled temperature (Angell plot). Metallic systems are plotted separately, in Figure 4.1(b), for clarity and for less complete data due to crystallization. In the Angell plot, the strong liquid SiO₂ shows Arrhenius behavior, whereas a fragile liquid such as OTP shows super-Arrhenius behavior. In this work, we use the viscosity at $1.25 T_g$ as the fragility measure (the vertical lines in Figure 4.1). While the concept of fragility is firmly rooted in glass science, its quantitative measure, using a single parameter, has not been standardized, with the current choices being m , D , $F_{1/2}$, and viscosity (or τ_α) at $1.25 T_g$. While m is often used, as Richert and Angell point out, “it is disconcertingly unreliable due to author subjectivity in slope-taking at T_g as well as experimental subtleties in this

slowly equilibrating regime”²⁵ For this reason we compare the viscosities at $1.25 T_g$ where displacement from the Arrhenius behavior is large for better distinction of the systems. For the systems studied, the viscosities at $1.25 T_g$ span 8 orders of magnitude (Table 4.1). Molecular liquids lie at the fragile end with $\eta(1.25 T_g) \approx 1 \text{ Pa s}$, while SiO_2 resides at the strong end with $\eta(1.25 T_g) \approx 10^7 \text{ Pa s}$. In the middle, we find silicates, selenium, and metallic glasses, with $\eta(1.25 T_g) \approx 10^5 \text{ Pa s}$.

Table 4.1 summarizes all the surface diffusion coefficients D_s of the glasses known at present. The D_s values are compared at the laboratory T_g , that is, at approximately the same bulk mobility. Over the past decade, D_s has been measured experimentally for various systems by following the evolution of surface contours driven by surface tension by our team and others.^{4,13,14,15,26,27,28,29,30,31,32,33} In addition, Table 4.1 includes D_s values from MD simulations for systems that have not been studied experimentally or are oversimplified for real systems. Because simulations were conducted at higher mobility than experiments, we extrapolate the results to the laboratory T_g for comparison with experimental values. For this, a power-law relation is applied between surface and bulk dynamics: $D_s \propto D_v^x$, where x is a constant between 0 and 1. This relation has been predicted by theories of surface mobility^{20,21,46} and as shown in Figure 4.2, verified for systems for which both experimental and simulation results are available. For OTP (Figure 4.2(a)), experimental (solid circles)¹³ and simulation (open symbols)³⁴ results connect smoothly by a straight line corresponding to the power law with $x = 0.32$. The same is true for polystyrene (PS) 10-mer (Figure 4.2(b)) for which experimental¹⁵ and simulation³⁵ results follow the power law with $x = 0.57$. The larger x value for PS reflects a smaller mobility enhancement from bulk to surface relative to OTP.¹⁵ For PS, we use the relaxation time τ from simulations³⁵ to calculate the diffusion coefficient: $D = d^2/(6\tau)$, where $d = 1.1 \text{ nm}$ is the size of the 10-mer.^{21,36} For these systems,

the power law provides an excellent description of the relation between D_s and D_v , over a wide range of mobility (15 decades in D_v). This result, along with its theoretical basis,^{20,21,46} justifies our use of the power law to extrapolate simulation results to estimate D_s at the laboratory T_g (Figure 4.S3). To our knowledge, this is the first test of the relation $D_s \propto D_v^x$ over a large mobility range accessed by both experiments and simulations. The validation of the relation opens a new avenue to estimate dynamic properties at laboratory timescales from simulations.

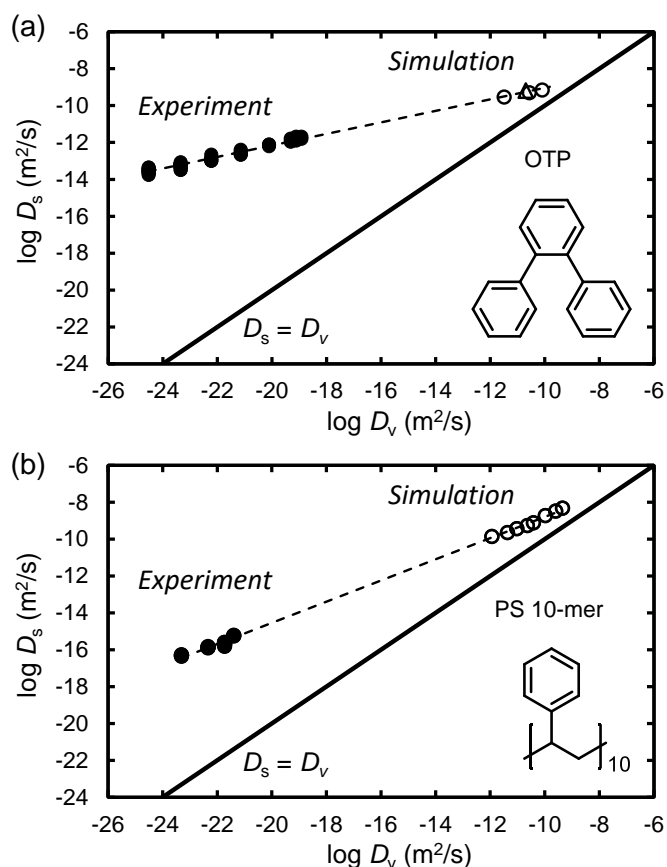


Figure 4.2 Power-law relation between surface and bulk diffusivity. (a) OTP. (b) PS 10-mer.

For OTP, the simulation results are from this work (\circ , see the SI for details³⁹) and Ref. 34 (\triangle). For each system, the dashed line is the power-law fitting of the experimental and simulation results. The power law describes the relation between surface and bulk dynamics over a wide mobility range (15 decades in D_v).

Table 4.1 Surface and bulk diffusion coefficients of glasses.

Systems	T_g , K	$\log D_s$ (m ² /s) at T_g	$\log D_v$ (m ² /s) at T_g	$\log \eta$ (Pa s) at 1.25 T_g	Method (ref.)
Kob-Anderson LJ	-	-11.5	-	-0.8	D_s (MD,16, ³⁷), η (MD, ³⁸)
Ortho-terphenyl (OTP)	246	-11.9	-19.5	-0.5	D_s (surface grating, 13; MD, 34, this work (see SI) ³⁹), D_v & η ⁽⁴⁰⁾
Griseofulvin (GSF)	361	-12.4	-	-0.6	D_s (surface grating, 26)
Tris-naphthyl benzene (TNB)	347	-13.3	-20.2	-0.3	D_s (surface grating, 27), D_v & η (⁴¹)
Nifedipine (NIF)	315	-13.7	-	-0.1	D_s (surface grating, 28)
Indomethacin (IMC)	315	-14.0	-19.8	0.1	D_s (surface grating, 4), D_v (⁴²)
PS 1.1k	307	-15.3	-	0.6	D_s (surface grating, 15)
PS 1.7k	319	-16.0	-	0.8	D_s (surface grating, 15)
PS 1.9k	332	-	-20.8	0.8	D_v & η (⁴³)
PS 2.4k	337	-16.0	-	0.9	D_s (surface roughening, 33)
PS 3k	343	-16.3	-	1.0	D_s (surface step, 32)
Posaconazole (POS)	331	-16.8	-	0.9	D_s (surface grating, 14)
Se	308	-16.1	-	3.6	D_s (nano-hole filling, 31), η (⁴⁴)
Si	843 ^a	-16.7	-21.5	4	D_s (surface groove near crystal, ⁴⁵ D_v (⁴⁷))
Pd ₄₀ Cu ₃₀ Ni ₁₀ P ₂₀	566	-15.9 (519 K)	-	4.2	D_s (surface grating, 29, ⁴⁸), η (⁴⁹)
Pd ₄₃ Cu ₂₇ Ni ₁₀ P ₂₀	580	-	-21.5	3.8	D_v (⁵⁰), η (⁵¹)
Au ₆₀ Cu _{15.5} Ag _{7.5} Si ₁₇	358	-17.1	-	5.3 ^b	D_s (surface grating, 30), η (⁵²)
CuZr	673	-16.9, -17.2	-	5.1	D_s (MD, 17, 18), η (⁵³)
Zr _{46.75} Ti _{8.25} Cu _{7.5} Ni ₁₀ Be ₂ 7.5 (Vitreyloy 4)	622	-	-21.9	5.3	D_v (⁵⁴), η (⁵⁵)
SiO ₂	1480	-20.7 (Si)	-21.9 (Si)	7.4	D_s (MD, 19, this work (see SI) 39), D_v (⁵⁶), η (⁵⁷)

^a T_g obtained by Monte Carlo simulations (Ref. ⁵⁸)

^b Taken to be the same as the value for Au₄₉Cu_{26.9}Ag_{5.5}Si_{16.3}Pd_{2.3} (Ref. 52)

In Figure 4.3, we plot the D_s and D_v values at T_g against the fragility of the bulk liquid. The D_s values exhibit a large variation, spanning 10 orders of magnitude for the systems investigated. We observe a strong correlation between D_s and fragility. The most fragile systems show a large enhancement of diffusion from the bulk to the free surface, by a factor of 10^8 for OTP. Within the molecular glasses, D_s decreases as the system becomes less fragile (stronger). SiO_2 , the strongest liquid, shows a much smaller surface diffusion enhancement, by a factor of 10. Between these two extremes lie the systems of intermediate fragility: selenium, silicon, and metallic glasses. These systems show enhanced surface diffusion, but the enhancement factors are smaller than those for typical molecular glasses. The overall trend is that higher surface diffusivity is associated with higher fragility. In contrast to the large variation of D_s , the D_v values show a relatively small difference across the systems, averaging around 10^{-21} m^2/s for all glass types. The weak dependence of D_v on fragility arises from the facts that (1) viscosity at the calorimetric T_g , used here to normalize temperature, increases slightly with decreasing fragility (see Ref. ⁵⁹ and Figure 4.S5), leading to lower D_v assuming validity of the Stokes-Einstein (SE) relation, and (2) the SE relation breaks down to a greater extent near T_g in the more fragile systems, causing an apparent enhancement of diffusion.⁶⁰

Figure 4.3 includes two systems that deserve special comments. KA LJ is a computer model for glass-forming liquids,⁶¹ and according to Royall et al.,³⁸ has a similar fragility as OTP with $\eta(1.25 T_g) = 0.2$ Pa s. This system has the highest D_s value in Figure 4.3 at the laboratory T_g (based on extrapolation discussed earlier, see Figure 4.S3). For amorphous silicon, a strong to fragile transition is proposed⁶² and its viscosity at $1.25 T_g$ is estimated by interpolating the best available data (Figure 4.S4). The estimated value (10^4 Pa s) is comparable to that of amorphous selenium.

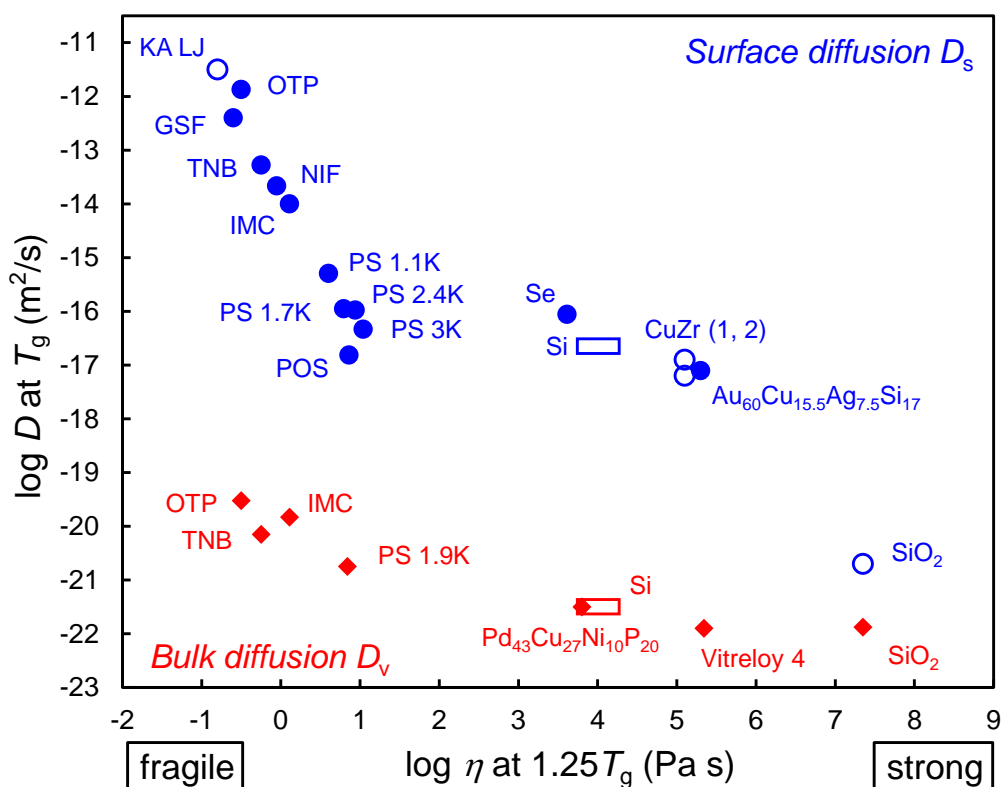


Figure 4.3 Correlation between diffusivity in glasses (D_s and D_v) and bulk fragility. For D_s , solid circles are experimental results and open circles are simulation results. All D_v values are experimental results. See Table 4.1 for data sources. For a-Si (open rectangles), the viscosity value is less certain due to a strong to fragile transition (see Ref. 62 and Figure 4.S4).

Why is surface diffusion related to bulk fragility? By definition, strong systems have high resistance to thermal excitation around T_g . For SiO_2 , this high resistance results from the robustness of the strong network bonds between atoms. These bonds are largely intact as a glass is heated to become a liquid, leading to an Arrhenius dependence of viscosity on temperature. In contrast, fragile systems are composed of molecules that interact through non-directional van der Waals forces to form closely packed structures. Upon heating above T_g , the viscosity of a fragile system decreases sharply in a super Arrhenius manner, indicating a dramatic unraveling of the local bonding environment. The change of local environment from bulk to surface can also be regarded as a type of excitation (density reduction), analogous to thermal excitation. The local structure of a strong system is expected to be more resistant against this excitation, leading to a smaller increase of mobility. For SiO_2 , simulations have found that the local environment of Si is largely unchanged from the bulk to the surface: in both environments, each Si is bonded to approximately 4 O atoms.¹⁹ Surface atoms reorganize themselves to preserve the low-energy tetrahedral bonding. Thus, in SiO_2 , the diffusion of a Si atom faces essentially the same kinetic barrier, no matter whether it is in the bulk or on the surface. The picture is very different for a fragile van der Waals system. Simulations have shown a significant loss of nearest neighbors, by approximately 40 %, ⁶³ when a bulk particle is transferred to the surface. For metallic systems, simulations have observed similar loss of nearest neighbors from bulk to surface.^{17,18} This translates to a weakening of the caging effect that restricts motion and to a large surface enhancement of diffusion.^{20,21} For a polymer in a surface layer, the different segments have different, depth-dependent environment and mobility.⁶⁴ The lateral diffusion rate of the whole chain is controlled by the deepest, slowest-moving segments. With increase of MW, D_s decreases, as seen in Figure 4.3 for the MW range 1 – 3 kg/mole and shown by Chai et al. up to 22 kg/mole.⁶⁵ Meanwhile, fragility decreases with increase of molecular

weight (MW) according to $\log \eta$ at $1.25 T_g$.⁶⁶ For amorphous silicon, simulations have shown a significant change of structure from bulk to surface; for example, most atoms are four-coordinated in the bulk but many are three-coordinated on the surface,⁶⁷ leading to enhanced surface diffusion.^{45,46}

The systematic trend in Figure 4.3 provides a foundation to predict the surface diffusion of amorphous materials and the transformations enabled by surface dynamics. Given that fast surface crystal growth is supported by fast surface diffusion,^{26,31} we expect the phenomenon to be more significant in fragile glass-formers. Indeed, fast surface crystal growth is prevalent among molecular glasses,²⁶ but less striking in stronger systems (e.g., a Pd-based metallic glass,²⁹ Se,³¹ Si,⁶⁸ and silicates^{69,70}). Similarly, given the importance of surface mobility in preparing ultra-stable glasses by vapor deposition,^{7,8} we expect stable-glass formation to be a phenomenon that is more pronounced in fragile systems and less so in strong systems. This expectation is consistent with the correlation observed within molecular systems between the stability of vapor-deposited glasses and fragility.⁷¹ For this group of molecules, the decrease of fragility is associated with the introduction of directional hydrogen bonds. Stable-glass formation has been reported for Se,⁷² Si,⁷³ and metallic systems,⁷⁴ while the degree of stability enhancement appeared to be less than that observed for fragile organic systems.^{72,74} In the case of SiO₂, vapor deposition typically produces high-energy, low-density structures relative to the glasses prepared by liquid cooling.^{75,76} Though further work is needed, the available literature is consistent with the notion that fragility influences the stability of vapor-deposited glasses.

4.3 Conclusion

In summary, our survey of all the available literature finds that the surface diffusion rate in glasses strongly depends on the fragility of bulk dynamics. This trend extends through all glass types: molecular, polymeric, chalcogenide, silicon, metallic, and oxide. The correlation is attributed to the robustness of covalent network bonds present in strong liquids, making them more resistant to environmental excitation from bulk to surface. At present, the surface diffusion data are more extensive on molecular glasses than on other glass types. Further work is warranted to learn whether a similar trend exists within each glass type, with the metallic glasses being a potentially fruitful target.¹⁸ This finding helps understand and predict surface mobility to develop amorphous materials with high stability for their diverse applications.

4.4 Acknowledgement

We acknowledge support from NSF through the University of Wisconsin Materials Research Science and Engineering Center (Grant DMR-1720415). A.A., D.M., Z.Y., and B.W. are grateful to the Extreme Science and Engineering Discovery Environment (XSEDE) supported by NSF (Grant ACI-1548562), and the Center for High Throughput Computing at UW-Madison.

4.5 Supporting Information.

4.5.1 Surface and bulk diffusion of OTP by simulations

Molecular dynamics (MD) simulations of OTP were performed by applying an all-atom model from Yungbluth et al⁷⁷ using LAMMPS⁷⁸. Each simulation contained 6400 atoms (200 OTP molecules). The cubic simulation box was initially equilibrated for 1 ns at 500 K and cooled in 20

K decrements at a rate of $\sim 10^{10}$ K/s. NPT conditions (at zero nominal pressure) were employed during cooling and periodic boundary conditions (PBCs) were applied in all three directions.

Bulk and surface diffusion were studied at 320 K, 340 K, and 360 K. To study bulk diffusion, the final configuration at the temperature of interest during cooling was used as the starting point for production runs in NVT with PBCs in all directions. For surface dynamics, with the same configuration obtained from the cooling process as above, free surfaces were created by inserting a vacuum of 10 nm above and below the film.⁷⁹ NVT conditions and PBCs were applied and the system was initially equilibrated for 1 ns to ensure that the newly created surfaces were relaxed before the production run. Atoms in the top 0.5 nm layer were used to study surface diffusion. Translational diffusivity D was calculated from the mean-squared-displacement (MSD) of atoms in the Fickian regime (Figure 4.S1) using the Einstein relation:

$$D = \lim_{t \rightarrow \infty} \frac{1}{(2d)Nt} \langle \sum_{i=1}^N |r_i(t) - r_i(0)|^2 \rangle \quad (1)$$

where d is the dimensionality (3 for bulk diffusion, 2 for surface diffusion), N is the number of atoms, $r_i(t)$ is the position of atom i at time t , and the angular brackets indicate ensemble average. For surface diffusion, only the lateral displacement of atoms present in the surface layer at both the initial and the final time was considered.

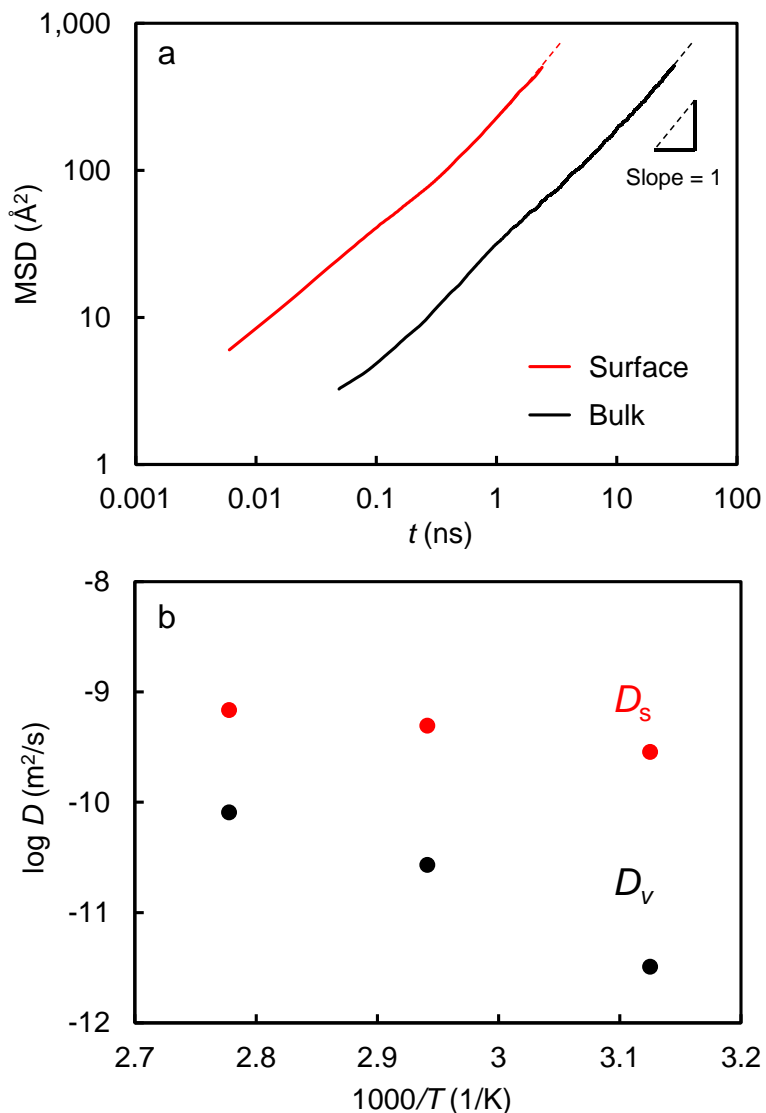


Figure 4.S1. MD simulations of OTP. (a) Surface and bulk MSD vs. time at 340 K. Dashed lines indicate Fickian diffusion (slope = 1). (b) Surface and bulk diffusion coefficients, D_s and D_v , vs. temperature.

4.5.2 Surface and bulk diffusion of silica by simulations

MD simulations of silica were performed by applying the BKS potential with a cutoff of 6 \AA ⁸⁰ using GROMACS.⁸¹ The bulk system contained 4536 atoms (1512 SiO_2 units) in a cubic

simulation box. The surface system was a 8-nm-thick film containing 9072 atoms; the film had two free surfaces, each contacting a 3 nm-thick vacuum layer. NPT ensemble with 1 bar pressure was used for bulk simulations and NVT ensemble for surface simulations. The PBCs were applied. To shorten equilibration time, the initial structure for a diffusion simulation was obtained from a cooling simulation from 5000 K to the temperature of interest at a cooling rate of 10^{10} K/s. The diffusion constant D was obtained from the MSD in the Fickian regime as described above. The bulk and surface diffusion of Si atoms was studied at 10 temperatures between 2500 K and 4000 K. For surface diffusion, only the lateral displacement of Si atoms present the top 2 nm layer during the entire trajectory was considered. Changing the layer thickness from 2 to 1 nm had no significant effect on the D_s value obtained (Figure 4.S2a). The D_v and D_s values from this work agree with those of Roder et al.⁸² and the D_v values from both works are consistent with the experimental values measured at lower temperatures (Figure 4.S2b).^{83,84}

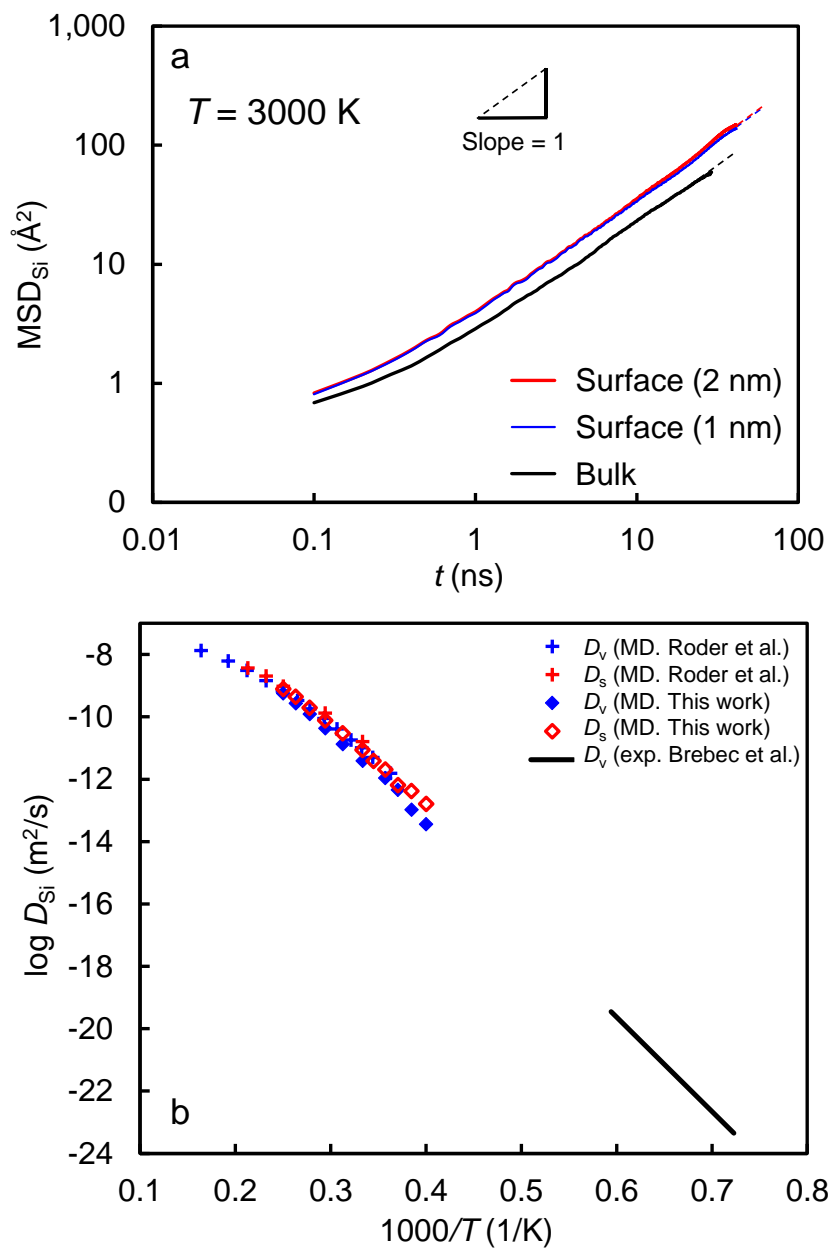


Figure 4.S2. MD simulations of SiO₂. (a) Surface and bulk MSD of Si vs. time at 3000 K. Dashed lines indicate Fickian diffusion (slope = 1). For the surface MSD, results are shown for two surface layer thicknesses: 2 nm (red) and 1 nm (blue); the results are in agreement. (b) Comparison of surface and bulk diffusion coefficients of Si from simulations. The simulation results agree with experimental D_v values measured at lower temperatures (solid line).

4.5.3 Extrapolation of Surface Diffusivity from Simulations to Laboratory T_g

As described in the main text, surface and bulk diffusivity are related by the power law $D_s \propto D_v^\xi$ over a wide range of mobility (Figure 4.2), consistent with theoretical predictions.^{85,86,87} This allows estimation of D_s at laboratory T_g from simulations performed at higher mobility. Figure 4.S3 shows this procedure applied to three systems: Kob-Andersen Lennard Jones (KA LJ) mixture,^{88,89} metallic glass CuZr,^{90,91} and SiO₂ (results described above). For this extrapolation, the laboratory T_g is assigned as the temperature at which $D_v = 10^{-21}$ m²/s, the average experimental value (Figure 4.3 in main text). The extrapolated values are given in Table 4.1 and Figure 4.3.

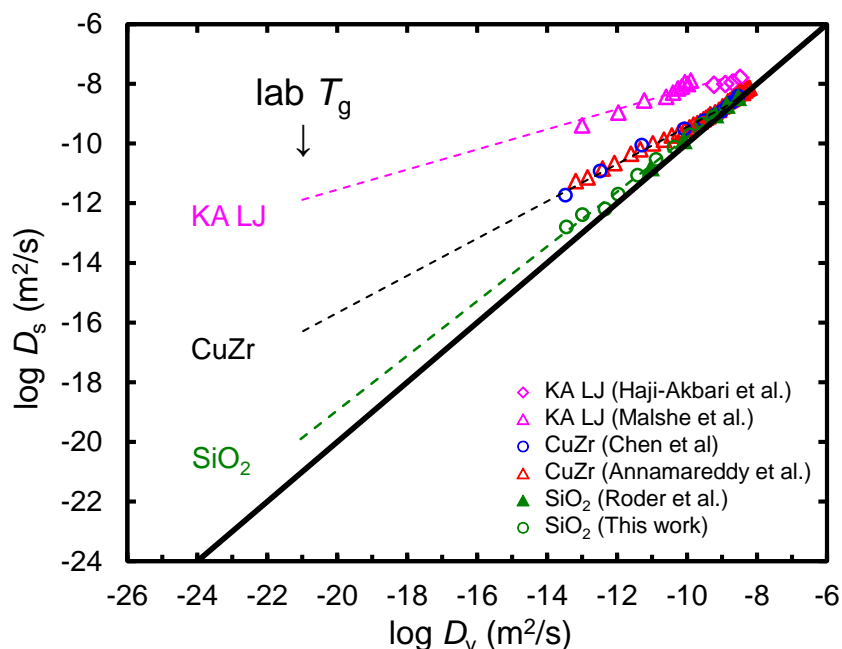


Figure 4.S3. Extrapolation of simulation results to obtain D_s at laboratory T_g . For each system, two simulations have been performed and the results are distinguished by symbols. The two simulation results are in good agreement and only one extrapolation line is shown for clarity.

4.5.4 Viscosity of silicon

Figure 4.S4 shows the viscosity of amorphous Si as a function of temperature. Viscosity of liquid Si was measured near the crystal melting point^{92,93,94,95} and compiled in Ref. ⁹⁶. Here, we use the data from Sasaki et al.⁹³ which is representative of all results. Viscosity at low temperatures was calculated from diffusivity^{97,98,99,100,101} using the relation $\eta \propto 1/D$ and overlaying the two properties at high temperatures. The simulation $T_g = 843$ K (ref.¹⁰²) corresponds to the temperature at which D_v is $10^{-21.5}$ m²/s, consistent with the values for known systems (Figure 4.3). Amorphous silicon undergoes a strong-to-fragile transition,¹⁰¹ and $1.25 T_g$ falls close to the transition temperature. The symbol in the middle of Figure 4.S4 is an estimate of the viscosity at $1.25 T_g$, 10^4 Pa s. This value is highly speculative.

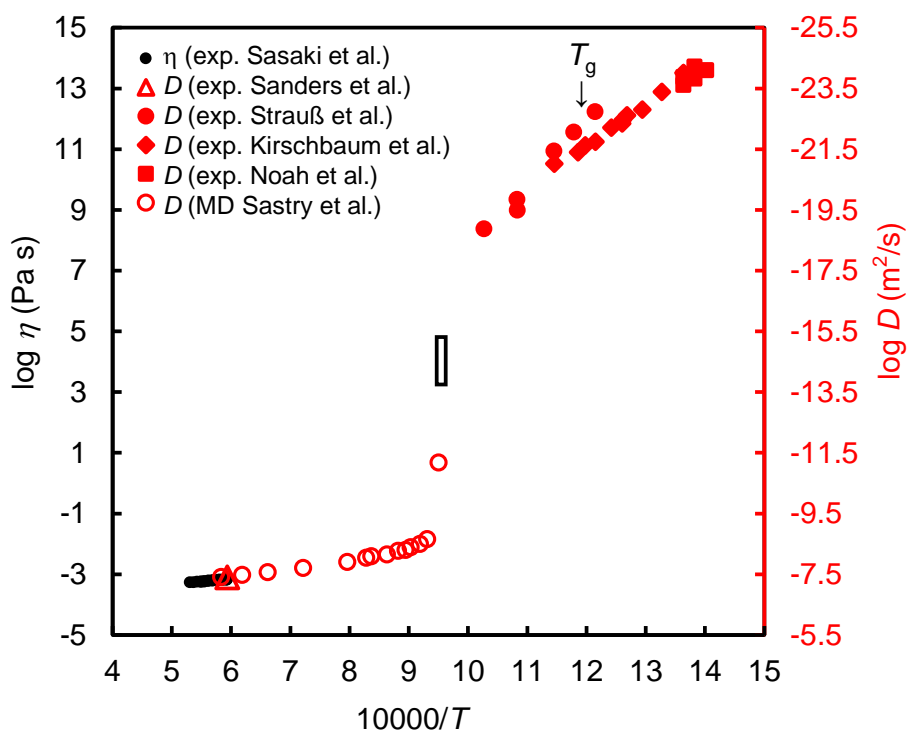


Figure 4.S4. Viscosity of a-Si from direct measurement and calculated from diffusivity. The symbol in the middle is an estimate of the viscosity at $1.25 T_g$.

Viscosity at T_g plotted against fragility

In Figure 4.S5, viscosity at the calorimetric T_g is plotted against viscosity at $1.25 T_g$, a measure of fragility, for various systems. Data sources are given in Table 4.1 in the main text and given below for additional systems: $\text{Li}_2\text{O}\cdot 2\text{SiO}_2$,^{103,104} glycerol,¹⁰⁵ maltitol,¹⁰⁶ sorbitol,¹⁰⁶ CKN,^{107,108} and Salol.¹⁰⁹ The results indicate that at the calorimetric T_g , viscosity is not constant but increases slightly with decreasing fragility (increasing strength).¹¹⁰ This effect contributes to the decrease of bulk diffusivity when plotted against fragility (Figure 4.3).

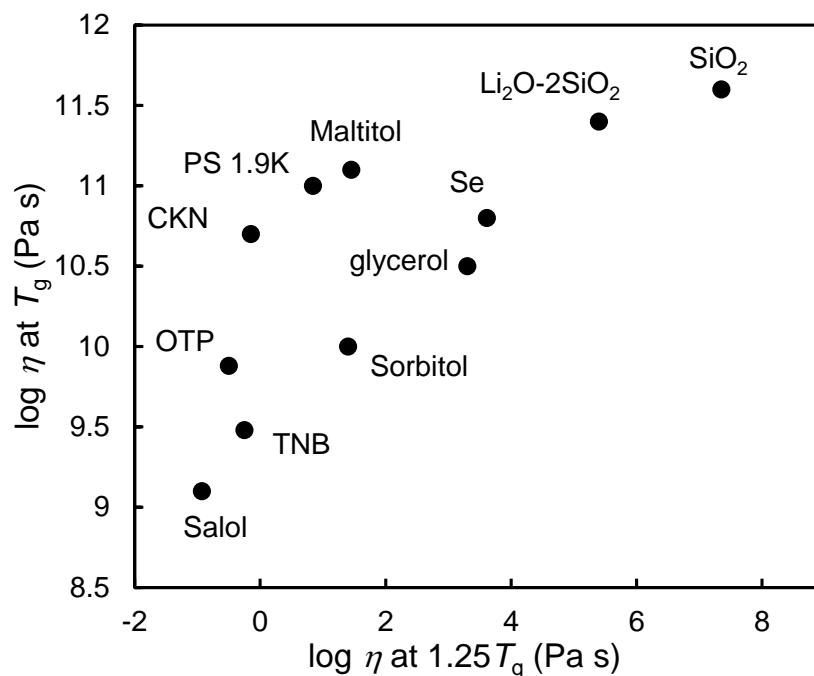


Figure 4.S5. Viscosity at T_g plotted against fragility.

4.6 References

¹ N. Granzow et al. Opt. Express **21**, 10969-10977 (2013).

-
- ² M. F. Ashby and A. L. Greer, *Scr. Mater.* **54**, 321-326 (2006).
- ³ L. Yu, *Adv. Drug Delivery Rev.* **48**, 27-42 (2001).
- ⁴ L. Zhu, C. W. Brian, S. F. Swallen, P. T. Straus, M. D. Ediger and L. Yu, *Phys. Rev. Lett.* **106**, 256103 (2011).
- ⁵ G. Sun, S. Saw, I. Douglass and P. Harrowell, *Phys. Rev. Lett.* **119**, 245501 (2017).
- ⁶ L. Yu, *Drug Delivery Rev.* **100**, 3–9 (2016).
- ⁷ S. F. Swallen, K. L. Kearns, M. K. Mapes, Y. S. Kim, R. J. McMahon, M. D. Ediger, T. Wu, L. Yu and S. Satija, *Science* **315**, 353-356 (2007).
- ⁸ M. D. Ediger, *J. Chem. Phys.* **147**, 210901 (2017).
- ⁹ K. Yoshimoto, T. S. Jain, P. F. Nealey and J. J. De Pablo, *J. Chem. Phys.* **122**, 144712 (2005).
- ¹⁰ S. P. Delcambre, R. A. Riggleman, J. J. de Pablo and P. F. Nealey, *Soft Matter* **6**, 2475-2483 (2010).
- ¹¹ R. Gomer, *Rep. Prog. Phys.* **53**, 917 (1990).
- ¹² X. Li, X. Liang, Z. Zhang, J. Ma and J. Shen, *Scr. Mater.* **185**, 100-104 (2020).
- ¹³ W. Zhang, C. W. Brian and L. Yu, *J. Phys. Chem. B* **119**, 5071-5078 (2015).
- ¹⁴ Y. Li, W. Zhang, C. Bishop, C. Huang, M. D. Ediger and L. Yu, *Soft Matter* **16**, 5062-5070 (2020).
- ¹⁵ W. Zhang and L. Yu, *Macromolecules* **49**, 731-735 (2016).
- ¹⁶ R. Malshe, M. D. Ediger, L. Yu and J. J. De Pablo, *J. Chem. Phys.* **134**, 194704 (2011).
- ¹⁷ H. Chen, B. Qu, D. Li, R. Zhou and B. Zhang, *J. Appl. Phys.* **123**, 025307 (2018).
- ¹⁸ A. Annamareddy, Y. Li, L. Yu, P.M. Voyles and D. Morgan, *J. Chem. Phys.* **154**, 104502 (2021).
- ¹⁹ A. Roder, W. Kob and K. Binder, *J. Chem. Phys.* **114**, 7602, (2001).
- ²⁰ J. D. Stevenson and P. G. Wolynes, *J. Chem. Phys.* **129**, 234514 (2008).
- ²¹ S. Mirigian and K. S. Schweizer, *J. Chem. Phys.* **143**, 244705 (2015).
- ²² S. Capaccioli, K. L. Ngai, M. Paluch and D. Prevosto, *Phys. Rev. E* **86**, 051503 (2012).
- ²³ C. A. Angell, *Science*, **267**, 1924-1935 (1995).
- ²⁴ Y. Chen, W. Zhang and L. Yu, *J. Phys. Chem. B* **120**, 8007-8015 (2016).
- ²⁵ R. Richert and C. A. Angell, *J. Chem. Phys.* **108**, 9016 (1998).
- ²⁶ C. Huang, S. Ruan, T. Cai and L. Yu, *J. Phys. Chem. B* **121**, 9463 (2017).

-
- ²⁷ S. Ruan, W. Zhang, Y. Sun, M. D. Ediger and L. Yu, *J. Chem. Phys.* **145**, 064503 (2016).
- ²⁸ C. W. Brian and L. Yu, *J. Phys. Chem. A* **117**, 13303-13309 (2013).
- ²⁹ C. R. Cao, Y. M. Lu, H. Y. Bai and W. H. Wang, *Appl. Phys. Lett.* **107**, 141606 (2015).
- ³⁰ C. R. Cao, L. Yu and J. H. Perepezko, *Appl. Phys. Lett.* **116**, 231601 (2020).
- ³¹ J. Bartak, J. Malek, K. Bagchi, M. D. Ediger, Y. Li and L. Yu, *J. Chem. Phys.* **154**, 074703 (2021)
- ³² Y. Chai, T. Salez, J. D. McGraw, M. Benzaquen, K. Dalnoki-Veress, E. Raphaël and J. A. Forrest, *Science*, **343**, 994-999, (2014).
- ³³ Z. Yang, Y. Fujii, F. K. Lee, C. H. Lam and O. K. Tsui, *Science* **328**, 1676-1679 (2010).
- ³⁴ J. Ghosh and R. Faller, *J. Chem. Phys.* **125**, 044506 (2006).
- ³⁵ Y. Zhou and S. T. Milner, *Macromolecules* **50**, 5599-5610 (2017).
- ³⁶ Y. S. Chen, Z. X. Chen, M. Tyllinski, M. D. Ediger and L. Yu, *J. Chem. Phys.* **150**, 024502 (2019).
- ³⁷ A. Haji-Akbari and P. G. Debenedetti, *J. Chem. Phys.* **141**, 024506 (2014).
- ³⁸ C. P. Royall, A. Malins, A. J. Dunleavy and R. Pinney, *J. Non-Cryst. Solids* **407**, 34–43 (2015).
- ³⁹ See Supplemental Materials at [url] for surface and bulk diffusion by simulations (OTP and silica), extrapolation of surface diffusivity from simulations to laboratory T_g , viscosity of silicon, and viscosity at calorimetric T_g plotted against fragility, which includes Ref. 77-97.
- ⁴⁰ M. K. Mapes, S. F. Swallen and M. D. Ediger, *J. Phys. Chem. B* **110**, 507-511 (2006).
- ⁴¹ S. F. Swallen et al. *J. Phys. Chem. B* **113**, 4600-4608 (2009).
- ⁴² S. F. Swallen and M. D. Ediger, *Soft Matter* **7**, 10339-10344 (2011).
- ⁴³ O. Urakawa, S. F. Swallen, M. D. Ediger and E. D. von Meerwall, *Macromolecules* **37**, 1558-1564 (2004).
- ⁴⁴ P. Košťál and J. Málek, *J. Non-Cryst. Solids* **356**, 2803-2806 (2010).
- ⁴⁵ J. M. Sallese, A. Ils, D. Bouvet, P. Fazan and C. Merritt, *J. Appl. Phys.* **88**, 5751-5755 (2000).
- ⁴⁶ D. Llera-Hurlburt, A. S. Dalton and E. G. Seebauer, *Surf. Sci.* **504**, 244–252 (2002).
- ⁴⁷ J. Kirschbaum et al. *Phys. Rev. Lett.* **120**, 225902 (2018).
- ⁴⁸ K. L. Ngai et al. *J. Non-Cryst. Solids* **463**, 85–89 (2017).
- ⁴⁹ N. Nishiyama and A. Inoue, *Mater. Trans. JIM* **40**, 64-71 (1999).
- ⁵⁰ A. Bartsch, K. Rätzke, A. Meyer and F. Faupel, *Phys. Rev. Lett.* **104**, 195901 (2010).

-
- ⁵¹ G. J. Fan, H. J. Fecht and E. J. Lavernia, *Appl. Phys. Lett.* **84**, 487-489 (2004).
- ⁵² I. Gallino, *Entropy* **19**, 483 (2017).
- ⁵³ Q. Wang et al. *Phys. Rev. B* **83**, 014202 (2011).
- ⁵⁴ F. Faupel, *Rev. Mod. Phys.* **75**, 237 (2003).
- ⁵⁵ R. Busch, E. Bakke and W. L. Johnson, *Acta Mater.* **46**, 4725-4732 (1998).
- ⁵⁶ G. Brebec, R. Seguin, C. Sella, J. Bevenot and J. C. Martin, *Acta Metall.* **28**, 327-333 (1980).
- ⁵⁷ K. U. Hess, D. B. Dingwell and E. Rössler, *Chem. Geol.* **128**, 155-163 (1996).
- ⁵⁸ C. R. Miranda and A. Antonelli, *J. Chem. Phys.* **120**, 11672-11677 (2004).
- ⁵⁹ L. M. Martinez and C. A. Angell, *Nature* **410**, 663-667 (2001).
- ⁶⁰ M. D. Ediger, *Annu. Rev. Phys. Chem.* **51**, 99-128 (2000).
- ⁶¹ W. Kob, *J. Phys. Condens. Matter* **11**, R85 (1999).
- ⁶² S. Sastry and C. A. Angell, *Nat. Mater.* **2**, 739-743 (2003).
- ⁶³ V. V. Hoang and T. Q. Dong, *Phys. Rev. B* **84**, 174204 (2011).
- ⁶⁴ D. Diaz-Vela, J. H. Hung and D. S. Simmons, *ACS Macro Letters* **7**, 1295-1301 (2018).
- ⁶⁵ Y. Chai, T. Salez and J. A. Forrest, *Macromolecules* **53**, 1084-1089 (2020).
- ⁶⁶ A. L. Agapov, V. N. Novikov, T. Hong, F. Fan and A. P. Sokolov, *Macromolecules* **51**, 4874-4881 (2018).
- ⁶⁷ S. Hara, S. Izumi, T. Kumagai and S. Sakai, *Surf. Sci.* **585**, 17-24 (2005).
- ⁶⁸ A. Sakai, T. Tatsumi and K. Ishida, *J. Vac. Sci. Tech. A* **11**, 2950-2953 (1993).
- ⁶⁹ N. Diaz-Mora, E. D. Zanotto, R. Hergt and R. Müller, *J. Non-Cryst. Solids* **273**, 81-93 (2000).
- ⁷⁰ M. L. F. Nascimento and E. Dutra Zanotto, *J. Chem. Phys.* **133**, 174701 (2010).
- ⁷¹ M. Tyllinski et al. *J. Chem. Phys.* **145**, 174506 (2016).
- ⁷² A. Zhang, Y. Jin, T. Liu, R. B. Stephens and Z. Fakhraai, *Proc. Nat. Aca. Sci.* **117**, 24076-24081 (2020).
- ⁷³ X. Liu, D. R. Queen, T. H. Metcalf, J. E. Karel, F. Hellman, *Phys. Rev. Lett.* **113**, 025503 (2014).
- ⁷⁴ H. B. Yu, Y. Luo and K. Samwer, *Adv. Mater.* **25**, 5904-5908 (2013).
- ⁷⁵ Z. Wang, T. Du, N. M. A. Krishnan, M. M. Smedskjaer and M. Bauchy, *J. Chem. Phys.* **152**, 164504 (2020).

-
- ⁷⁶ J. Konnert, P. D'antonio, M. Huffman and A. Navrotsky, *J. Am. Ceram. Soc.* **70**, 192-196 (1987).
- ⁷⁷ J. C. Yungbluth, G. A. Medvedev, B. M. Savoie and J. M. Caruthers, *J. Chem. Phys.* **152**, 094504 (2020).
- ⁷⁸ S. Plimpton, *J. Comput. Phys.* **117**, 1–19 (1995).
- ⁷⁹ B. W. H. van Beest, G. J. Kramer and R. A. van Santen, *Phys. Rev. Lett.* **64**, 1955–1958 (1990).
- ⁸⁰ M. J. Abraham, T. Murtola, R. Schulz, S. Páll, J. C. Smith, B. Hess, E. Lindahl, *SoftwareX* **1**, 19–25 (2015).
- ⁸¹ J. Horbach and W. Kob, *Phys. Rev. B* **60**, 3169 (1999).
- ⁸² S. Nishimura, S. Matsumoto and K. Terashima, *J. Cryst. Growth* **237**, 1667-1670 (2002).
- ⁸³ H. Sasaki, E. Tokizaki, X. M. Huang, K. Terashima and S. Kimura, *Jpn. J. Appl. Phys.* **34**(7R), 3432 (1995).
- ⁸⁴ Y. Sato, Y. Kameda, T. Nagasawa, T. Sakamoto, S. Moriguchi, T. Yamamura and Y. Waseda, *J. Cryst. Growth* **249**, 404-415 (2003).
- ⁸⁵ Z. Zhou, S. Mukherjee and W. K. Rhim, *J. Cryst. Growth* **257**, 350-358 (2003).
- ⁸⁶ M. J. Assael et al. *J. Phys. Chem. Ref. Data* **41**, 033101 (2012).
- ⁸⁷ F. Strauß, L. Dörrer, T. Geue, J. Stahn, A. Koutsoubas, S. Mattauch, and H. Schmidt, *Phys. Rev. Lett.* **116**, 025901 (2016).
- ⁸⁸ M. A. Noah, D. Flötotto, Z. Wang and E. J. Mittemeijer, *J. Appl. Phys.* **117**, 165306 (2015).
- ⁸⁹ P. G. Sanders and M. J. Aziz, *J. Appl. Phys.* **86**, 4258-4261 (1999).
- ⁹⁰ M. L. F. Nascimento, V. M. Fokin, E. D. Zanotto and A. S. Abyzov, *J. Chem. Phys.* **135**, 194703 (2011).
- ⁹¹ R. Al-Mukadam, D. Di Genova, H. Bornhöft and J. Deubener, *J. Non-Cryst. Sol.* **536**, 119992 (2020).
- ⁹² K. Schröter and E. Donth, *J. Chem. Phys.* **113**, 9101-9108 (2000).
- ⁹³ A. Nakheli et al. *J. Phys.: Condens. Matter* **11**, 7977 (1999).
- ⁹⁴ H. Senapati, K. K. Kadiyala and C. A. Angell, *J. Phys. Chem.* **95**, 7050-7054 (1991).
- ⁹⁵ H. Tweer, N. Laberge and P. B. Macedo, *J. Am. Ceram. Soc.* **54**, 121-123 (1971).
- ⁹⁶ W. T. Laughlin and D. R. Uhlmann, *J. Phys. Chem.* **76**, 2317-2325 (1972).
- ⁹⁷ L. M. Martinez and C. A. Angell, *Nature* **410**, 663-667 (2001).
- ⁷⁷ J. C. Yungbluth, G. A. Medvedev, B. M. Savoie and J. M. Caruthers, *J. Chem. Phys.* **152**, 094504 (2020).
- ⁷⁸ S. Plimpton, *J. Comput. Phys.* **117**, 1–19 (1995).

-
- ⁷⁹ J. Ghosh and R. Faller, *J. Chem. Phys.* **125**, 044506 (2006).
- ⁸⁰ B. W. H. van Beest, G. J. Kramer and R. A. van Santen, *Phys. Rev. Lett.* **64**, 1955–1958 (1990).
- ⁸¹ M. J. Abraham, T. Murtola, R. Schulz, S. Páll, J. C. Smith, B. Hess, E. Lindahl, *SoftwareX* **1**, 19–25 (2015).
- ⁸² A. Roder and W. Kob, *K. Binder, J. Chem. Phys.* **114**, 7602 (2001).
- ⁸³ J. Horbach and W. Kob, *Phys. Rev. B* **60**, 3169 (1999).
- ⁸⁴ G. Brebec, R. Seguin, C. Sella, J. Bevenot and J. C. Martin, *Acta Metall.* **28**, 327 (1980).
- ⁸⁵ J. D. Stevenson and P. G. Wolynes, *J. Chem. Phys.* **129**, 234514 (2008).
- ⁸⁶ S. Mirigian and K. S. Schweizer, *J. Chem. Phys.* **143**, 244705 (2015).
- ⁸⁷ S. Capaccioli, K. L. Ngai, M. Paluch and D. Prevosto, *Phys. Rev. E* **86**, 051503 (2012).
- ⁸⁸ R. Malshe, M. D. Ediger, L. Yu and J. J. De Pablo, *J. Chem. Phys.* **134**, 194704 (2011).
- ⁸⁹ A. Haji-Akbari and P. G. Debenedetti, *J. Chem. Phys.* **141**, 024506 (2014).
- ⁹⁰ H. Chen, B. Qu, D. Li, R. Zhou, B. Zhang, *J. Appl. Phys.* **123**, 025307 (2018).
- ⁹¹ A. Annamareddy, Y. Li, L. Yu, P.M. Voyles and D. Morgan, *J. Chem. Phys.* **154**, 104502 (2021).
- ⁹² S. Nishimura, S. Matsumoto and K. Terashima, *J. Cryst. Growth* **237**, 1667-1670 (2002).
- ⁹³ H. Sasaki, E. Tokizaki, X. M. Huang, K. Terashima and S. Kimura, *Jpn. J. Appl. Phys.* **34**(7R), 3432 (1995).
- ⁹⁴ Y. Sato, Y. Kameda, T. Nagasawa, T. Sakamoto, S. Moriguchi, T. Yamamura and Y. Waseda, *J. Cryst. Growth* **249**, 404-415 (2003).
- ⁹⁵ Z. Zhou, S. Mukherjee and W. K. Rhim, *J. Cryst. Growth* **257**, 350-358 (2003).
- ⁹⁶ M. J. Assael et al. *J. Phys. Chem. Ref. Data* **41**, 033101 (2012).
- ⁹⁷ F. Strauß, L. Dörrer, T. Geue, J. Stahn, A. Koutsioubas, S. Mattauch, and H. Schmidt, *Phys. Rev. Lett.* **116**, 025901 (2016).
- ⁹⁸ J. Kirschbaum T. Teuber, A. Donner, M. Radek, D. Bougeard, R. Böttger, J. Lundsgaard Hansen, A. Nylandsted Larsen, M. Posselt, and H. Bracht, *Phys. Rev. Lett.* **120**, 225902 (2018).
- ⁹⁹ M. A. Noah, D. Flötotto, Z. Wang and E. J. Mittemeijer, *J. Appl. Phys.* **117**, 165306 (2015).
- ¹⁰⁰ P. G. Sanders and M. J. Aziz, *J. Appl. Phys.* **86**, 4258-4261 (1999).
- ¹⁰¹ S. Sastry and C. A. Angell, *Nat. Mater.* **2**, 739-743 (2003).

-
- ¹⁰² C. R. Miranda and A. Antonelli, *J. Chem. Phys.* **120**, 11672-11677 (2004).
- ¹⁰³ M. L. F. Nascimento, V. M. Fokin, E. D. Zanotto and A. S. Abyzov, *J. Chem. Phys.* **135**, 194703 (2011).
- ¹⁰⁴ R. Al-Mukadam, D. Di Genova, H. Bornhöft and J. Deubener, *J. Non-Cryst. Sol.* **536**, 119992 (2020).
- ¹⁰⁵ K. Schröter and E. Donth, *J. Chem. Phys.* **113**, 9101-9108 (2000).
- ¹⁰⁶ A. Nakheli et al. *J. Phys.: Condens. Matter* **11**, 7977 (1999).
- ¹⁰⁷ H. Senapati, K. K. Kadiyala and C. A. Angell, *J. Phys. Chem.* **95**, 7050-7054 (1991).
- ¹⁰⁸ H. Tweer, N. Laberge and P. B. Macedo, *J. Am. Ceram. Soc.* **54**, 121-123 (1971).
- ¹⁰⁹ W. T. Laughlin and D. R. Uhlmann, *J. Phys. Chem.* **76**, 2317-2325 (1972).
- ¹¹⁰ L. M. Martinez and C. A. Angell, *Nature* **410**, 663-667 (2001).

Chapter 5 Surface mobility of amorphous indomethacin containing moisture and surfactant: A concentration-temperature superposition principle

Yuhui Li,¹ Janguang Yu,¹ Xiao Tan,¹ Lian Yu^{1*}

¹ School of Pharmacy, University of Wisconsin-Madison, Madison, WI, 53705, USA

Mol. Pharm. In review.

5.1 Abstract

An amorphous material can have vastly higher mobility on the surface than in the bulk and shows fast surface crystallization as a result. Most amorphous materials contain multiple components, but the effect of composition on surface dynamics remains poorly understood. In this study, the surface mobility of amorphous indomethacin was measured using the method of surface grating decay in the presence of moisture and the surfactant Tween 20. It is found that both components significantly enhance the surface mobility, and their effects are well described by the principle of *concentration-temperature superposition* (CTS); that is, the same surface dynamics is observed at the same T_g -normalized temperature T/T_g , where T_g the composition-dependent glass transition temperature. For systems showing CTS, the mechanism of surface evolution transitions from viscous flow at high temperatures to surface diffusion at low temperatures at $1.04 T_g$. For the surfactant-doped system, the T_g used is the value for the surface layer to account for the surface enrichment of the surfactant (measured by X-ray Photoelectron Spectroscopy). At high surfactant concentration ($> 10\%$ by weight), the surface-grating decay rate in the surface diffusion regime is limited by the large, slow diffusing surfactant molecules; in this case, CTS holds only for the viscous flow regime. The CTS principle allows the prediction of the surface dynamics of multi-component amorphous materials.

5.2 Introduction

There has been significant progress in developing amorphous pharmaceutical formulations to enhance solubility and bioavailability over the traditional crystalline formulations.¹ It is recognized that the free surface of an amorphous drug can have vastly higher mobility than the

molecular mobility and crystallization of amorphous drugs.^{20,21} Given their similar mobility-enhancing effects, we investigate moisture and the surfactant Tween 20 together in this work.

We find that moisture and Tween 20 significantly increase the surface mobility of amorphous IMC. For both dopants, the effects are well described by the principle of *concentration-temperature superposition* (CTS); that is, the same surface dynamics is observed at the same temperature relative to the composition-dependent glass transition temperature T_g . The mechanism of surface evolution changes from viscous flow at high fluidity (high dopant concentration and high temperature) to surface diffusion at low fluidity, and the transition occurs around $T = 1.04 T_g$ for both pure and doped IMC. For Tween 20, the T_g used refers to that of the surface layer where the surfactant accumulates. At a high Tween 20 concentration (> 10 %), the slow diffusing dopant molecules limit the surface evolution in the surface-diffusion regime and CTS holds only for the viscous flow regime. According to the CTS, the effect of a dopant on surface mobility can be understood as a first approximation from the shift of T_g . This result is relevant for predicting the surface mobility of multi-component amorphous formulations.

5.3 Experimental Section

Indomethacin (IMC, purity > 99%) was purchased from Sigma-Aldrich and Tween 20 from EMD Millipore Corporation. Both were used as received. IMC/Tween 20 mixtures were prepared by cryomilling (SPEX CertiPrep 6750) with liquid nitrogen as coolant. Each mixture (1 g) was milled at 10 Hz for 5 cycles, each lasting 2 minutes with a 2-minute cooldown between cycles.

Differential scanning calorimetry (DSC) was performed with a TA Instrument Q2000 unit equipped with a refrigerated cooler. About 5 mg of material was weighed into an aluminum pan and analyzed under 50 mL/min N₂ purge. T_g was determined as the onset of the glass transition during 10 K/min heating.

To make a surface grating, a master pattern was placed on a viscous liquid of IMC (pure or doped) at $T_g + 40$ K and peeled off after vitrification at $T_g - 20$ K. This yielded a glass film with a sinusoidal surface contour. Master gratings of different wavelengths were obtained as follows: for $\lambda = 1000$ nm and 1984 nm, plastic gratings purchased from Rainbow Symphony were used; for $\lambda = 729$ nm and 1478 nm, the masters were duplicated from a DVD or CD, respectively, through a UV-curing polymer (Norland Optical Adhesive 61); for $\lambda = 553$ nm, 3322 nm or 8248 nm, the masters were duplicated from a glass grating (Spectrum Scientific) through the same transfer polymer. All masters were coated with 10 nm gold before use (Sputter deposition system, Leica ACE600). The thickness of each embossed glass film was 50 – 100 μ m, much larger than the wavelength of any surface grating used, ensuring that the evolution of the top surface was unaffected by the substrate.

The flattening of a surface grating over time was monitored by Atomic Force Microscopy (AFM, Bruker Veeco Multiple Mode IV), laser diffraction, or optical microscopy (Nikon Optiphot 2). AFM was performed in the tapping mode at room temperature; the height profile was Fourier transformed to obtain the amplitude of the sinusoidal surface. Laser diffraction was used to determine faster decay than feasible with AFM. A HeNe laser ($\lambda = 632.8$ nm, Uniphase Corp.) passed through a sample film perpendicularly and the first-order diffraction in transmission was recorded with a silicon amplified detector (Thorlabs) interfacing with a National Instruments

LabVIEW program. The grating amplitude was verified to be proportional to the square root of diffraction intensity. For long measurements at temperatures below the room temperature, an optical microscope was placed in a walk-in cold room and used to record the diffraction pattern of the surface grating through a Bertrand lens. The incident light was 530 nm obtained by filtering white light with a 20 nm band-pass filter. The sample temperature was controlled with a Linkam microscopic temperature stage or a custom-made mini-oven. The three methods yielded identical results within experimental error when applied to the same decay process.

For control of environmental humidity, nitrogen purge was used to obtain the dry condition (0 % RH) and saturated salt solutions to obtain elevated humidity: Potassium Acetate (21% RH), Potassium Carbonate (43%), Magnesium Nitrate (51%), Potassium Iodide (67%), Sodium Chloride (75%), Potassium Chloride (84%), Potassium Nitrate (92%).²² For AFM measurements, each surface grating sample was stored in a sealed container of constant RH and removed periodically for analysis. For laser diffraction measurements, a saturated salt solution was placed in the custom-built temperature stage and sealed with the sample (see the inset of Figure 5.2a).

X-ray Photoelectron Spectroscopy (XPS) was performed with a Thermo Scientific K-alpha equipped with an Al K α X-ray source (1486.6 eV). XPS was used to determine the surface compositions of amorphous IMC/Tween 20 films. Each film was prepared by melting a mixture of interest, annealing at 343 K for 1 min, and quenching to room temperature by contact with an aluminum block. The films were kept in a desiccator before measurements. The X-ray spot size was 400 μm . The pass energy was 200 eV (1 eV step resolution) for survey scans and 50 eV (0.1 eV step resolution) for high-resolution scans. The XPS data were analyzed using the Avantage

software (Thermo Scientific) and the Cl 2p peak at 200.2 eV of benzyl chloride was used to calibrate the binding energy. The peak area of each element was converted to its surface atomic composition using the Relative Sensitivity Factor.²³ The mass fraction of Tween 20 at the free surface was calculated as follows:

$$w_{T20} = \frac{(4 x_{Cl/O} - 1) \cdot M_{T20}}{(4 x_{Cl/O} - 1) \cdot M_{T20} - 26 x_{Cl/O} \cdot M_{IMC}} \quad (5.1)$$

where $x_{Cl/O}$ is the ratio of the Cl and O peaks, M_{IMC} and M_{T20} are the molecular weights of IMC and Tween 20, and the factors 4 and 26 are the numbers of oxygen atoms in each IMC and Tween 20 molecule, respectively.

5.4 Results

Both dopants investigated in this work, water and Tween 20, enhance the *bulk* mobility of amorphous IMC. Figure 5.1a shows the DSC traces of IMC doped with Tween 20. Each mixture exhibits a single glass transition temperature (T_g) whose value decreases with increasing Tween 20 concentration. These results indicate that IMC and Tween 20 are miscible in the range of concentration tested.²⁴ Figure 5.1b plots the T_g of the mixture against the concentration of Tween 20 as well as the literature data on water.²⁵ For both dopants, the effect on IMC T_g is well fitted by the Gordon-Taylor equation:²⁶

$$T_{g\,mix} = \frac{w_1 T_{g1} + k w_2 T_{g2}}{w_1 + k w_2} \quad (5.2)$$

Where w_1 is the weight fraction of water or Tween 20, w_2 is the weight fraction of IMC, T_{g1} is the T_g of water (135 K) or Tween 20 (208 K), T_{g2} is the T_g of IMC (315 K), and k is a model parameter treated here as a fitting constant. For water as the second component, $k = 0.11$,²⁵ and for Tween 20, $k = 0.46$.

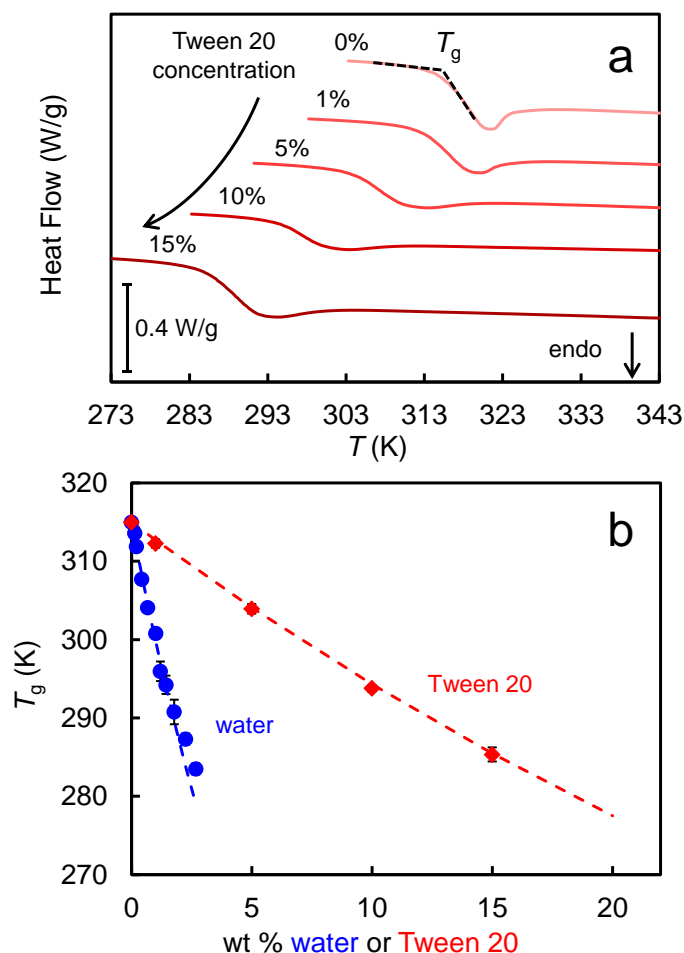


Figure 5.1. (a) DSC traces of Tween 20/IMC mixture for T_g . (b) T_g vs. the concentration of water²⁵ or Tween 20 in IMC. The dashed lines are fits to the Gordon-Taylor equation.

5.4.1 Effect of Moisture on IMC Surface Mobility.

Figure 5.2 shows the typical surface grating decay curves. For a laser-diffraction measurement (Figure 5.2a), a homemade sample cell was used to maintain the temperature and humidity of the sample (see the drawing in the inset). The small gap between the sample and the saturated-salt solution ensured rapid equilibration of humidity. The intensity of the first-order diffraction peak I was found to decrease exponentially over time. For an AFM measurement (Figure 5.2b), the amplitude of the sinusoidal surface grating, h , was measured as a function of time and is seen to decrease exponentially. Considering the fact that $I \propto h^2$, the decay curves were fitted to the function,

$I = I_0 \exp(-2Kt)$ for the diffraction data and $h = h_0 \exp(-Kt)$ for the AFM data, where K is the decay constant.

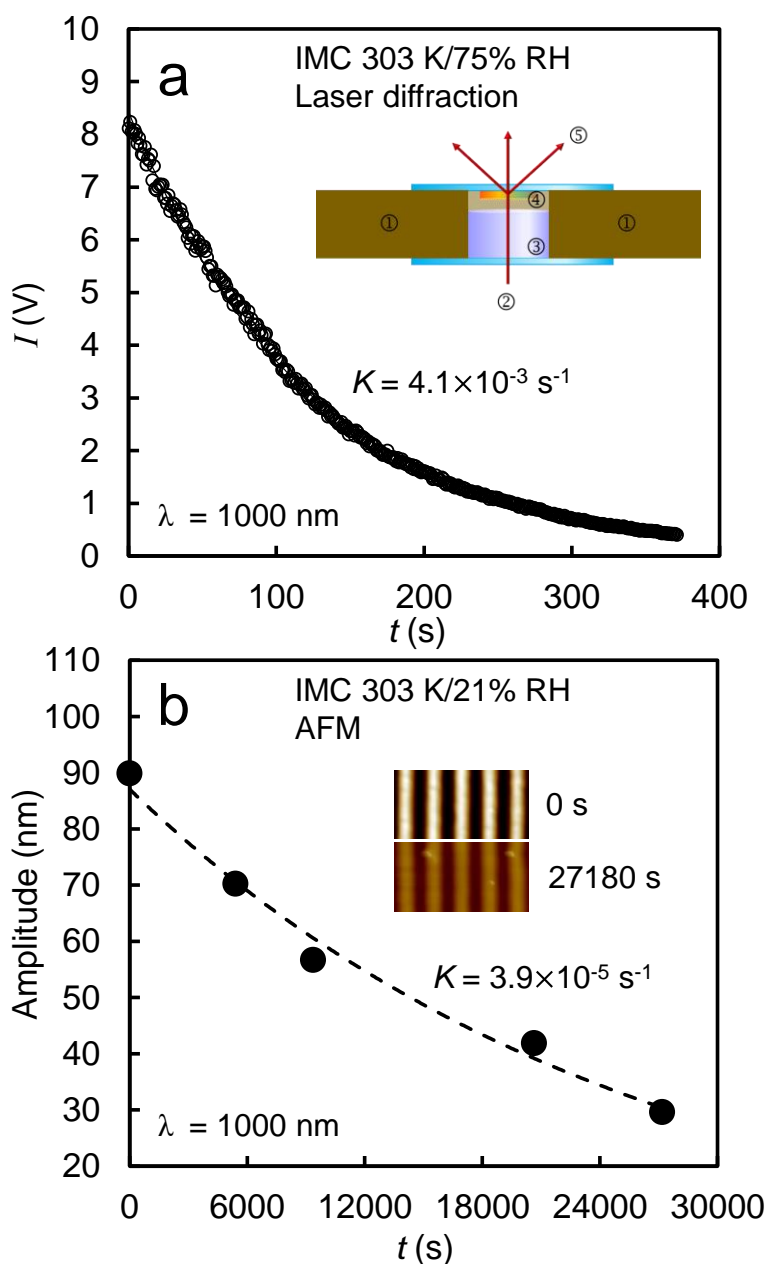


Figure 5.2. (a) IMC surface grating decay at 303 K and 75 % RH measured by laser diffraction. Inset: experimental setup. ①Copper block for temperature control. ②Laser. ③Saturated salt solution for humidity control. ④Surface grating. ⑤First-order diffraction. (b) IMC surface grating decay at 303 K and 21 % RH measured by AFM. Inset: AFM images at two time points.

Figure 5.3 shows the decay curves of a 1000 nm wavelength IMC surface grating at different RH at 298 K and 303 K. With increasing RH, the decay rate significantly increases. At 298 K, it took two days for the grating amplitude to decrease 50 % under the dry condition, while it only took several minutes at 92 % RH. The curves running through the data points are the exponential fits, from which we obtain the surface-grating decay constant K . In Figure 5.3c, K is plotted against RH at 298 K and 303 K. From 0 to 92 % RH, K increases by roughly 4 orders of magnitude at each temperature. The decay constant shows a stronger dependence on RH at higher RH values and this reflects a change of surface-evolution mechanism (see below).

According to Mullins, a sinusoidal surface grating decays exponentially with a decay constant K given by:²⁷

$$K = Fq + Aq^2 + (A' + C)q^3 + Bq^4 \quad (5.3)$$

where $q = 2\pi/\lambda$ is the spatial frequency of the grating with λ being the grating wavelength and the different terms correspond to the different mechanisms of surface evolution: viscous flow (F), evaporation-condensation (A and A'), bulk diffusion (C), and surface diffusion (B). For amorphous materials, viscous flow and surface diffusion are often found to be the two leading mechanisms,³ with viscous flow being the collective movement of a liquid and surface diffusion the migration of individual atoms or molecules in the surface layer. For each decay mechanism, the decay rate has a characteristic dependence on the grating wavelength; for example, $K \propto \lambda^{-1}$ for viscous flow and $K \propto \lambda^{-4}$ for surface diffusion. This is the basis for a wavelength test of the decay mechanism. By this test, Zhu et al. showed that for pure IMC, viscous flow and surface diffusion are the

dominant mechanisms for surface evolution⁹ and we apply the same test to the binary systems of this study.

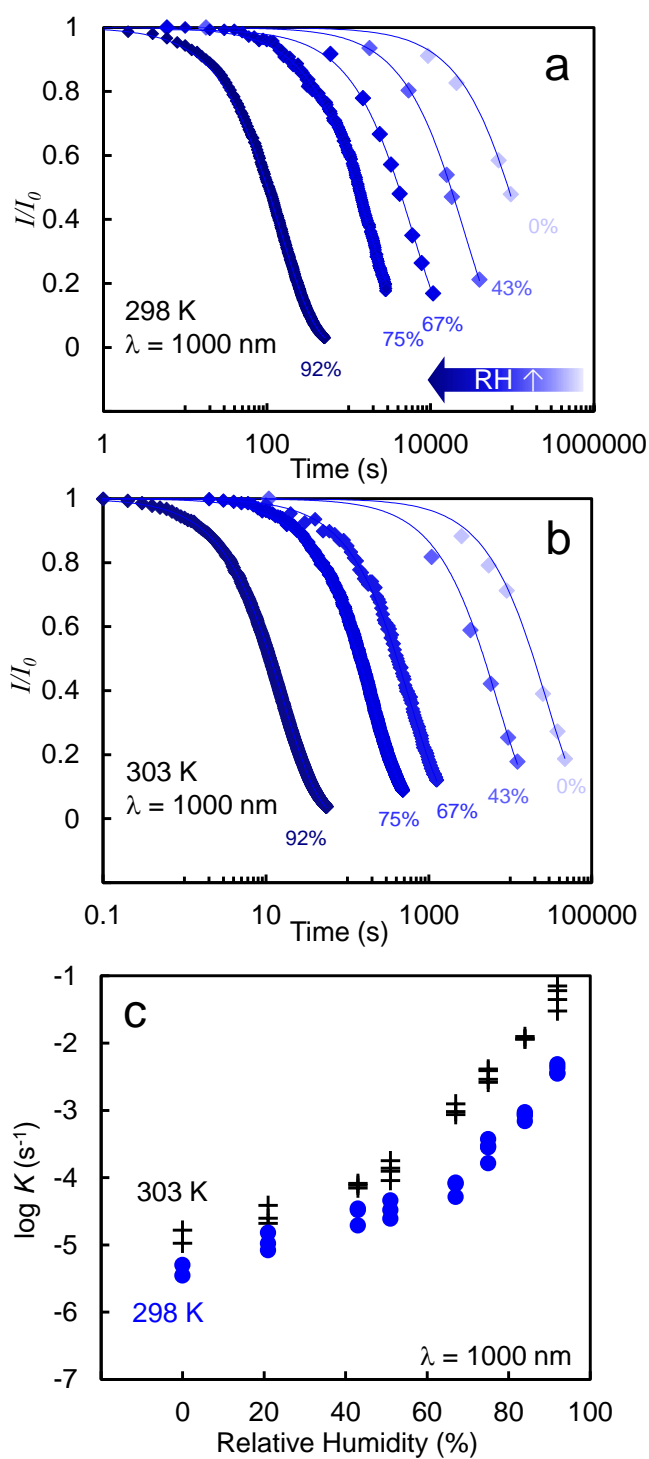


Figure 5.3. (a) Decay curves at 298 K and different RH. (b) Decay curves at 303 K and different RH. The solid lines are exponential fits. (c) Humidity dependence of the decay constant, K , for IMC surface gratings at 303 K and 298 K.

Figure 5.4a shows the wavelength dependence of the decay constant K for IMC at 303 K and different RH. At 75 % RH, K is proportional to λ^{-1} , consistent with the viscous flow mechanism, whereas at 0 % RH and 21% RH, a stronger wavelength dependence is observed, $K \propto \lambda^{-4}$, indicating the surface diffusion mechanism. This transition of the surface-evolution mechanism is confirmed by the exposure of nanoparticles during grating decay. Ruan et al. showed that despite its high chemical purity, indomethacin contains a small amount ($\sim 0.3\%$ in volume fraction) of nanoparticles approximately 100 nm in size, and these nanoparticles can be exposed or remain embedded depending on the mechanism of surface evolution.²⁸ If the mechanism is viscous relaxation, the particles flow with the liquid and remain embedded; however, if the mechanism is surface diffusion, they become exposed as the fast-diffusing IMC molecules vacate the peaks of the surface grating for the valleys. Figure 5.4b shows the AFM images of the surface gratings after partial decay from the initial amplitude of 100 nm to 30 nm at four RH levels at 303 K. Nanoparticles are exposed during decay at 0 % RH and 21 % RH, but not observed at high 67 % RH; at 51% RH, we observe an intermediate behavior with hints of particle exposure. These results are in agreement with the change of the surface-evolution mechanism concluded above.

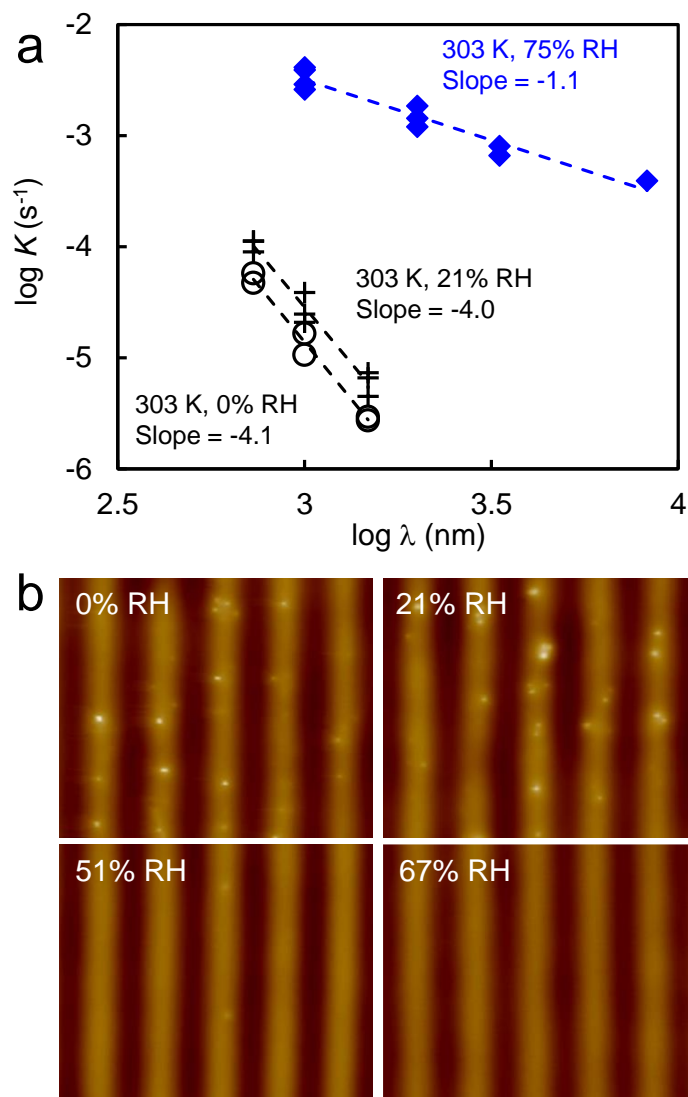


Figure 5.4. (a) Wavelength dependence of IMC at different humidity levels at 303 K. (b) AFM images of IMC surface gratings at 303 K at different RH. The initial grating amplitude was 100 nm and the samples were observed after the amplitudes decayed to 30 nm.

In Figure 5.5, the surface grating decay constant is plotted against the T_g -normalized temperature. The black open circles correspond to dry IMC at different temperatures;⁹ the other symbols correspond to moist IMC at different RH at 298 and 303 K. In this format, the data points approximately collapse to a common trend regardless of whether they were measured as a function of RH at a fixed temperature or as a function of temperature under a dry condition. Also plotted in

Figure 5.5 is the viscosity of pure IMC²⁹ using the second y axis. At high fluidity (high T/T_g), the decay constants K track the viscosity, $K \propto \eta^{-1}$, confirming the assignment of the surface-evolution mechanism as viscous flow. At low fluidity (low T/T_g), the decay is faster than the viscosity trend, indicating a change of the surface-evolution mechanism with the new decay mechanism being surface diffusion by the wavelength test (Figure 5.4a).

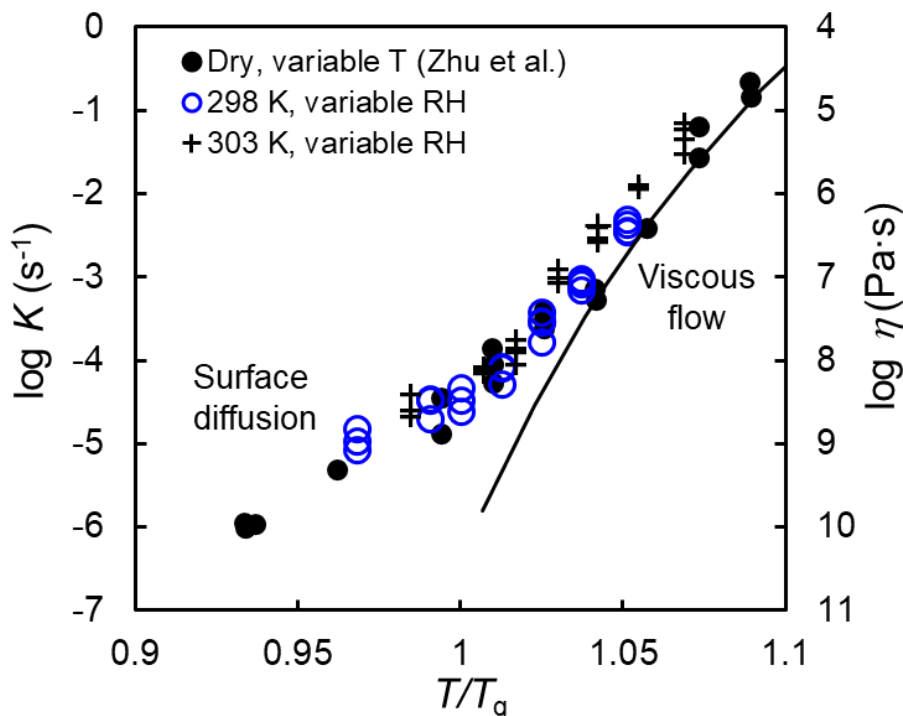


Figure 5.5. Surface grating decay constants of dry and moist IMC as a function of T/T_g , where T_g is the composition-dependent glass transition temperature. The solid curve is the viscosity of IMC under dry condition.

This data collapse seen in Figure 5.5 means that the surface grating of water-containing IMC decays at approximately the same rate as that of dry IMC if the comparison is made at the same temperature normalized by T_g . We call this result Concentration-Temperature Superposition (CTS), in analogy to Time-Temperature Superposition (TTS) in polymer dynamics³⁰ and Rate-Temperature Superposition (RTS) in vapor deposition.³¹ According to CTS, the effect of moisture on surface dynamics can be understood on the basis of the temperature effect on surface dynamics

in the dry material and a decrease of T_g by water absorption. For both dry and moist IMC, surface evolution occurs by viscous flow at high fluidity and by surface diffusion at low fluidity, with the transition occurring near $T = 1.04 T_g$ for the 1000 nm wavelength surface grating. This principle is potentially useful for predicting the effect of a second component on surface mobility and we show below that it is also valid for a surfactant as a second component.

5.4.2 Effect of Surfactant Tween 20 on IMC Surface Mobility.

Figure 5.6a shows the typical data on the effect of Tween 20 on IMC surface mobility. Here we compare IMC containing Tween 20 at different concentrations at 303 K. As the Tween 20 concentration increases, the surface grating flattens at a faster rate. For these samples, the time required to flatten the grating decreases from one day for pure IMC to 10 seconds if 15 % Tween 20 is present. The curves through the data points are the exponential fits, from which we obtain the decay constants K .

In Figure 5.6b, the decay constants of IMC containing Tween 20 are plotted against temperature. For comparison, we also plot the decay rate of pure IMC⁹ and its bulk viscosity.²⁹ The doping of Tween 20 greatly accelerates the surface grating decay. Note that at 1 % or 5 % Tween 20, the K vs. temperature plot shows a kink, as seen with pure IMC. This suggests a change of the mechanism of surface evolution. To investigate this, a wavelength test similar to that in Figure 5.4a was performed for the 5 % sample and the result is shown in Figure 5.7. This test established that the decay mechanism is viscous flow at a high temperature (318 K) and surface diffusion at a low temperature (298 K).

At 15 % Tween 20, there is no obvious kink in the K vs T curve and the decay mechanism is presumably viscous flow at all the temperatures investigated. At 10 % Tween 20, there is a weak hint of a kink, possibly indicating a transition to surface diffusion at low temperatures.

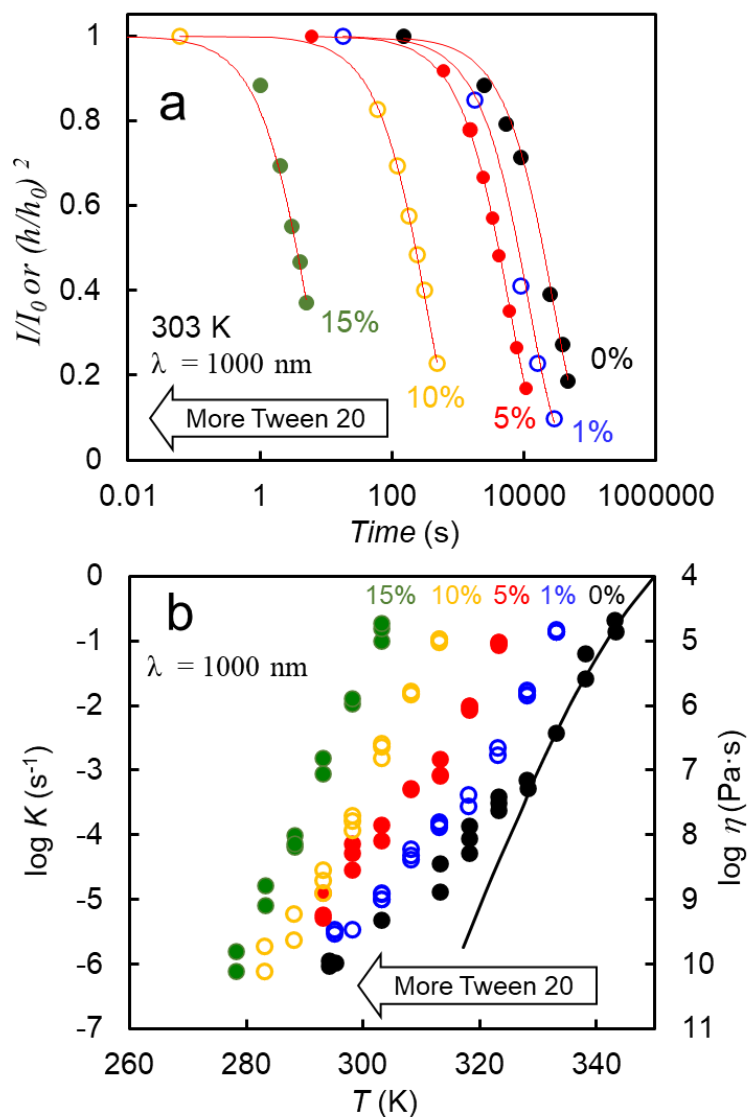


Figure 5.6. (a) Surface-grating decay kinetics of IMC containing Tween 20 at 303 K. The solid lines are the exponential fits. (b) Decay constant K vs. temperature for IMC containing Tween 20.

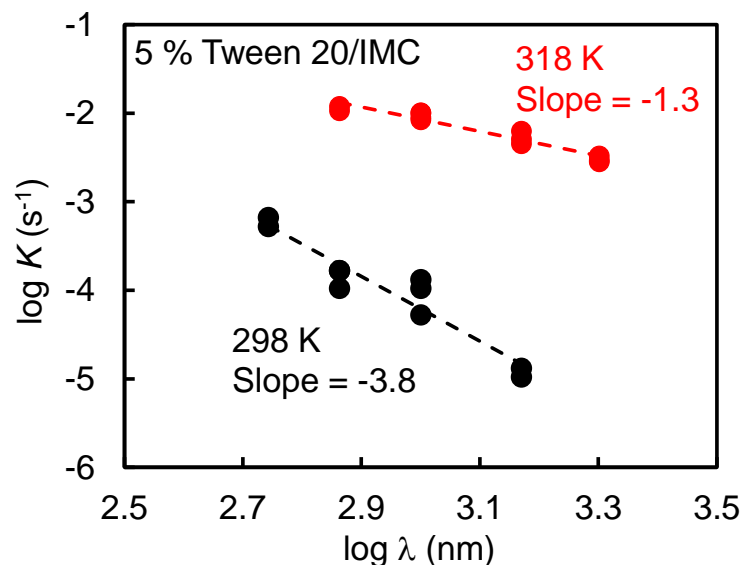


Figure 5.7. Wavelength dependence of the surface-grating decay constant K for IMC containing 5 % Tween 20 at 298 K and 318 K.

To test the validity of CTS in describing the IMC/surfactant system, in Figure 5.8a, we plot the surface-grating decay constants K against T/T_g as in Figure 5.5. We observe a significant collapse of data points, while the quality of the collapse is slightly worse than that of Figure 5.5. At high T/T_g , the data points for the surfactant-containing samples show a good master curve, but they lie above the points for pure IMC by approximately one order of magnitude. This suggests that Tween 20 has a larger effect on the mobility at the free surface than it does in the bulk. Furthermore, the surfactant-containing samples do not form a master curve at low T/T_g : the lighter-doped samples (1 and 5 %) roughly join the points for pure IMC, but the heavier-doped samples (10 and 15 %) have significantly lower values. This is attributed to the slow surface diffusion rate of surfactant and will be addressed later.

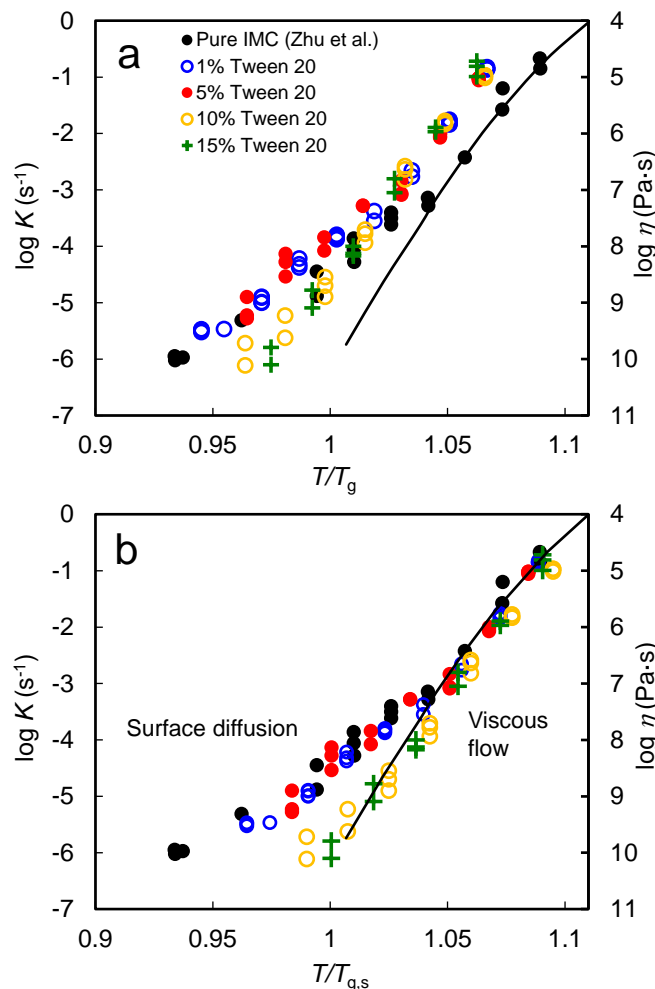


Figure 5.8. Surface-grating decay constant of IMC containing Tween 20 as a function of T/T_g , where T_g is the composition-dependent bulk glass transition temperature (a) or the surface glass transition temperature $T_{g,s}$ after correction for the surface enrichment of Tween 20.

Given that a surfactant can preferentially enrich at the surface of an amorphous drug,³² we investigated whether this effect occurs in Tween 20 doped IMC and thus leads to the imperfect data collapse in Figure 5.8a. Surfactants are known to enrich at the air/water interface and Yu et al. reported recently that the same can occur at the free surface of the amorphous drugs. We measured the surface concentration of Tween 20 using XPS.^{33,34} Figure 5.9 shows the spectra of Cl 2p and O 1s in our samples. With increasing Tween 20 concentration, the Cl peak decreases and the O peak increases. From these results, the surface concentrations of Tween 20 were calculated (eq. 5.1) and the results are given in Table 5.1 and plotted in Figure 5.9c.

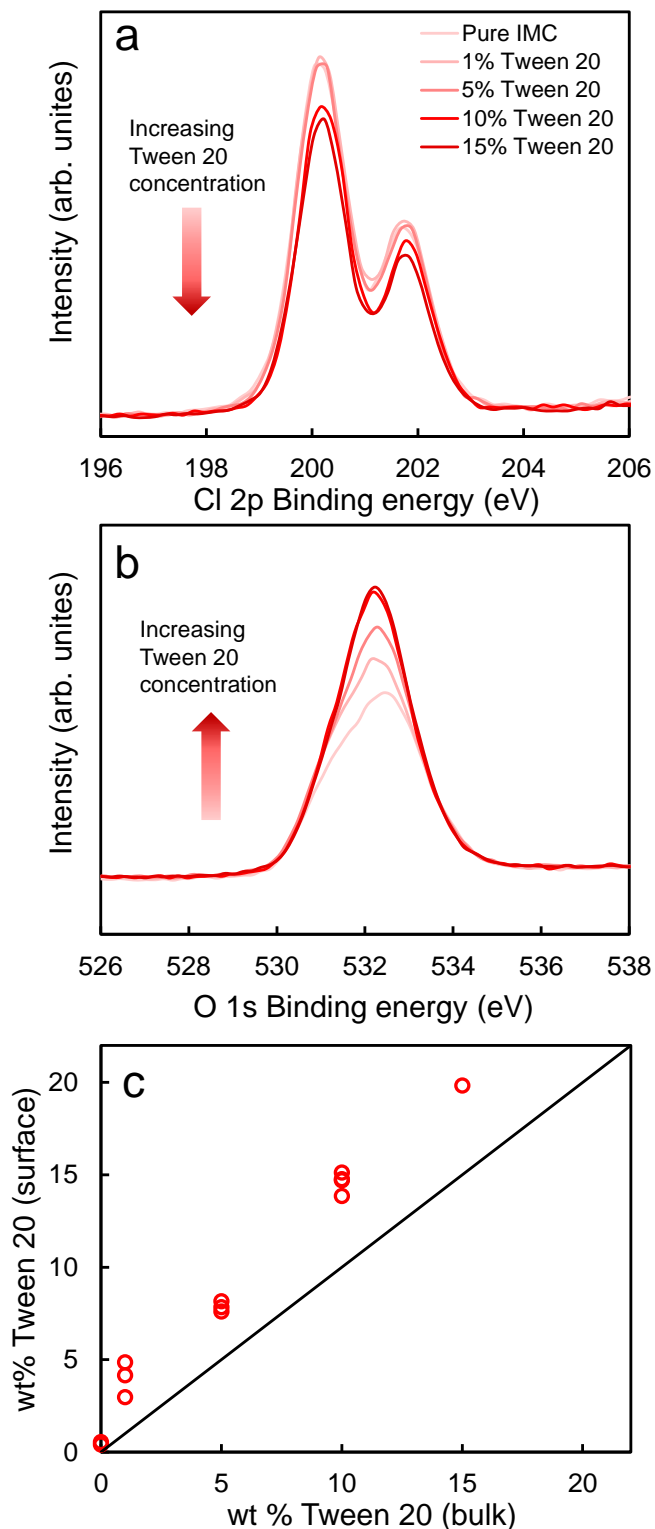


Figure 5.9. XPS spectra of Cl 2p (a) and O 1s (b) of IMC containing Tween 20 at concentrations indicated. (c) Surface concentration of Tween 20 vs. bulk concentration. The surface concentration is higher than the bulk concentration; the diagonal line indicates the condition that the two concentrations are equal.

Figure 5.9c shows that the surface concentration of Tween 20 is systematically higher than its bulk concentration. This finding is consistent with the recent report on other drug-surfactant systems.³² Given that Tween 20 plasticizes IMC (Figure 5.1), its enrichment on the surface means that the surface T_g is lower than the bulk T_g . To calculate the surface T_g of IMC containing Tween 20, we assume that the same plasticizing effect in the bulk (Figure 5.1b) occurs in the surface region. The calculation was performed using eq. 5.2, whose parameters were obtained by fitting the bulk data. The results of this calculation are shown in Table 5.1. According to this calculation, the surface T_g is 6 – 8 K below the bulk T_g . This effect qualitatively explains why in Figure 5.8a the surfactant-doped samples as a group show faster surface dynamics relative to pure IMC.

For a quantitative test of our conclusion, in Figure 5.8b, we replot the data in Figure 5.8a using the surface glass transition temperature $T_{g,s}$ as the normalizing temperature. We observe significantly improved data collapse. The overall pattern is similar to that for water-containing IMC (Figure 5.5). At high fluidity (high T/T_g), the decay constants K track the viscosity, $K \propto \eta^{-1}$, confirming viscous flow as the surface-evolution mechanism. At low fluidity (low T/T_g), the two lighter-doped mixtures (1 and 5 %) join the trend of pure IMC; their decay rates are faster than the viscosity trend, indicating a new mechanism for surface evolution. The transition occurs near $T = 1.04 T_g$ and the new mechanism was determined to be surface diffusion by the wavelength test (Figure 5.7). For these lighter-doped mixtures, we observe a collapse of data points with pure IMC; that is, the systems follow CTS.

For the two heavier-doped mixtures (10 and 15 %), the deviation from the viscosity trend at low fluidity is less pronounced. This indicates that surface diffusion is slower in these systems,

allowing viscous flow to dominate surface evolution down to lower temperatures. These two systems do not follow the CTS behavior of IMC containing water and IMC containing Tween 20 at low concentrations.

The inhibitory effect of Tween 20 on the surface diffusion in amorphous IMC is analogous to the observation of Zhang et al. They reported that 1 % of polystyrene (PS) by weight in amorphous *o*-terphenyl (OTP) has little effect on the rate of surface-grating decay in the viscous-flow regime, but a significant inhibitory effect in the surface-diffusion regime.⁶ They explained the effect as follows: in the viscous-flow regime, PS and OTP flow together, whereas in the surface-diffusion regime, the faster-diffusing OTP vacates the peaks of a surface grating while the slower diffusing PS is stranded behind, resulting in a slower apparent decay rate. The same explanation appears to apply to Tween 20 doped IMC. Tween 20 is a larger molecule than IMC with a molecular weight of 1227.5 g/mol to IMC's 357.8 g/mol, and it could be strongly oriented in the surface layer as a surfactant.^{35,36} These let surface Tween 20 molecules have a deeper penetration into the bulk and slower surface diffusion than IMC molecules.^{2,37,38} At low concentrations (1 and 5 %), our results indicate that the Tween 20 molecules can flow and surface-diffuse with the IMC molecules, resulting in the master-curve behavior in Figure 5.8b. At high concentrations (10 and 15 %), the inhibitory effect of Tween 20 becomes noticeable in the surface-diffusion regime, where the slow-diffusing molecules are stranded in the surface regions vacated by IMC, causing a slow surface-grating decay. With water as the dopant, the complexity described above for PS⁶ and Tween 20 does not arise. Water is a faster diffuser than the IMC host molecules; in the viscous-flow regime, water flows with the host molecules; in the surface-diffusion regime, water never gets stranded in

the regions vacated by the host molecules. As a result, the IMC-water mixtures show CTS in the entire concentration range.

Table 5.1 Bulk and surface concentrations of Tween 20 and T_g

bulk %	Bulk Cl/O	surface Cl/O	surface %	T_g , K	$T_{g,s}$, K
0	0.250	-	-	315	-
1	0.245	0.231 (0.0042)	3.99 (0.95)	312	306
5	0.227	0.215 (0.0012)	7.87 (0.28)	304	298
10	0.207	0.188 (0.0020)	14.6 (0.53)	294	286
15	0.187	0.171 (0.0004)	19.8 (0.11)	285	278

In each parenthesis is the standard deviation calculated from three measurements of the same sample.

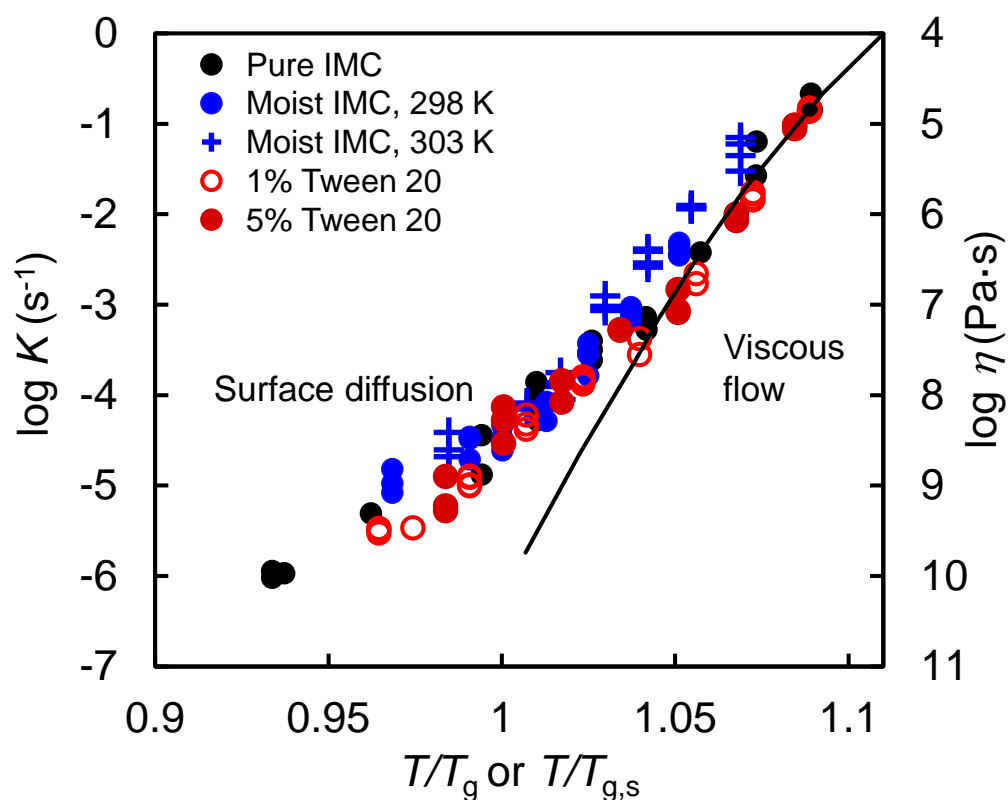


Figure 5.10. Grating decay constants of pure or doped IMC as a function of temperature.

In Figure 5.10, we plot the data on the two dopants (moisture and Tween 20) together. For the Tween 20 systems, only the two lighter-doped mixtures (1 and 5 %) are plotted. We observe a reasonably good data collapse for all the systems. They all show a similar transition from the viscous flow regime to the surface-diffusion regime with the transition temperature near $1.04 T_g$ and the transition viscosity approximately 10^7 Pa s.

5.5 Conclusion

This study has found that moisture and the surfactant Tween 20 can significantly accelerate the surface mobility of amorphous indomethacin. The magnitude of the acceleration is well described by the principle of Concentration-Temperature Superposition (CTS). According to CTS, the same surface dynamics is observed at the same temperature relative to the composition-dependent glass transition temperature T_g . The evolution mechanism changes from viscous flow at high fluidity to surface diffusion at low fluidity with the transition occurring near $1.04 T_g$ for both pure and doped IMC. For Tween 20, CTS is observed after taking into account its surface enrichment effect characterized by XPS. In the high-temperature region where viscous flow dominates surface evolution, CTS holds for all the systems, whereas in the low-temperature region where surface diffusion dominates surface evolution, CTS is observed for IMC containing moisture at any concentration and for Tween 20 at lower concentrations (1 and 5 %). At higher Tween 20 concentrations, we observe deviation from CTS and attribute the effect to the large difference between the surface diffusion rates of the guest and host molecules. We anticipate that CTS can be used for predicting surface mobility in multi-component amorphous materials. Given that fast surface dynamics enables fast crystal growth at the free surface of amorphous drugs,³⁹ the two dopants investigated here, water and surfactant, are expected to accelerate the surface

crystallization process. It is of interest to learn whether the previously observed correlation between the surface diffusion coefficient and the surface crystal growth rate for pure systems still holds for binary systems.³⁹ If so, CTS could be extended to predict crystal growth rates in multi-component amorphous formulations. Given the high degree of surface enrichment observed in some drug-surfactant systems,³² it is of interest to learn whether CTS holds under such extreme conditions.

5.6 References

¹ Yu, L. Amorphous Pharmaceutical Solids: Preparation, Characterization and Stabilization. *Adv. Drug Deliv. Rev.* **2001**, *48*, 27

² Yu, L. Surface mobility of molecular glasses and its importance in physical stability. *Adv. Drug Deliv. Rev.* **2016**, *100*, 3-9.

³ Li, Y.; Zhang, W.; Bishop, C.; Huang, C.; Ediger, M.D.; Yu, L. Surface diffusion in glasses of rod-like molecules posaconazole and itraconazole: Effect of interfacial molecular alignment and bulk penetration. *Soft. Matt.* **2020**, *16*, 5062-5070.

⁴ Sun, Y.; Zhu, L.; Kearns, K. L.; Ediger, M.D.; Yu, L. Glasses crystallize rapidly at free surfaces by growing crystals upward. *Proc. Natl. Acad. Sci.* **2011**, *108*, 5990

⁵ Wu, T.; Yu, L. Surface crystallization of indomethacin below T_g. *Pharm. Res.* **2006**, *23*, 2350

⁶ Zhang, W.; Teerakapibal, R.; Yu, L. Surface mobility of amorphous o-terphenyl: a strong inhibitory effect of low-concentration polystyrene. *J. Phys. Chem. B* **2016**, *120*(27), 6842-6847.

⁷ Bannow, J.; Karl, M.; Larsen, P. E.; Hwu, E. T.; Rades, T. Direct Measurement of Lateral Molecular Diffusivity on the Surface of Supersaturated Amorphous Solid Dispersions by Atomic Force Microscopy. *Mol. Pharm.* **2020**, *17*(5), 1715-1722.

⁸ Liu, J.; Hwu, E.T.; Bannow, J.; Grohgan, H.; Rades, T. Impact of Molecular Surface Diffusion on the Physical Stability of Co-Amorphous Systems. *Mol. Pharm.* **2022**, *19*, 1183-1190

⁹ Zhu, L.; Brian, C. W.; Swallen, S. F.; Straus, P. T.; Ediger, M. D.; Yu, L. Surface self-diffusion of an organic glass. *Phys. Rev. Lett.* **2011**, *106*(25), 256103.

¹⁰ Miyazaki, T.; Yoshioka, S.; Aso, Y.; Kawanishi, T. Crystallization rate of amorphous nifedipine analogues unrelated to the glass transition temperature. *Int. J. Pharm.* **2007**, *336*(1), 191-195.

-
- ¹¹ Greco, S.; Authelin, J. R.; Leveder, C.; Segalini, A. A practical method to predict physical stability of amorphous solid dispersions. *Pharm. Res.* **2012**, *29*(10), 2792-2805.
- ¹² Mehta, M.; Kothari, K.; Ragoonanan, V.; Suryanarayanan, R. Effect of water on molecular mobility and physical stability of amorphous pharmaceuticals. *Mol. Pharm.* **2016**, *13*(4), 1339-1346.
- ¹³ Mehta, M.; Suryanarayanan, R. Accelerated physical stability testing of amorphous dispersions. *Mol. Pharm.* **2016**, *13*(8), 2661-2666.
- ¹⁴ Purohit, H. S.; Ormes, J. D.; Saboo, S.; Su, Y.; Lamm, M. S.; Mann, A. K.; Taylor, L. S. Insights into nano- and micron-scale phase separation in amorphous solid dispersions using fluorescence-based techniques in combination with solid state nuclear magnetic resonance spectroscopy. *Pharm. Res.*, **2017**, *34*(7), 1364-1377.
- ¹⁵ Waterman, K. C.; Carella, A. J.; Gumkowski, M. J.; Lukulay, P.; MacDonald, B. C.; Roy, M. C.; Shamblin, S. L. Improved protocol and data analysis for accelerated shelf-life estimation of solid dosage forms. *Pharm. Res.* **2007**, *24*(4), 780-790.
- ¹⁶ Shalaev, E. Y.; Zografi, G. How does residual water affect the solid-state degradation of drugs in the amorphous state? *J. Pharm. Res.* **1996**, *85*(11), 1137-1141.
- ¹⁷ Saboo, S.; Bapat, P.; Moseson, D. E.; Kestur, U. S.; Taylor, L. S. Exploring the Role of Surfactants in Enhancing Drug Release from Amorphous Solid Dispersions at Higher Drug Loadings. *Pharmaceutics*, **2021**, *13*(5), 735.
- ¹⁸ Sekhon, B. S. Surfactants: pharmaceutical and medicinal aspects. *J. Pharm. Technol. Res. Manag.* **2014**, *1*(1), 43-68.
- ¹⁹ Solanki, N. G.; Lam, K.; Tahsin, M.; Gumaste, S. G.; Shah, A. V.; Serajuddin, A. T. Effects of surfactants on itraconazole-HPMCAS solid dispersion prepared by hot-melt extrusion I: miscibility and drug release. *J. Pharm. Sci.* **2019**, *108*(4), 1453-1465.
- ²⁰ Zhang, J.; Shi, Q.; Tao, J.; Peng, Y.; Cai, T. Impact of Polymer Enrichment at the Crystal-Liquid Interface on Crystallization Kinetics of Amorphous Solid Dispersions. *Mol. Pharm.* **2019**, *16*(3), 1385-1396.
- ²¹ Mosquera-Giraldo, L. I.; Trasi, N. S.; Taylor, L. S. Impact of surfactants on the crystal growth of amorphous celecoxib. *Int. J. Pharm.* **2014**, *461*(1-2), 251-257.
- ²² Greenspan, L. Humidity fixed points of binary saturated aqueous solutions. *J. Res. Nat. Bur. Stand.* **1977**, *81*(1), 89-96.
- ²³ Wagner, C. D.; Davis, L. E.; Zeller, M. V.; Taylor, J. A.; Raymond, R. H.; Gale, L. H. Empirical atomic sensitivity factors for quantitative analysis by electron spectroscopy for chemical analysis. *Surf. Interface Anal.* **1981**, *3*(5), 211-225.
- ²⁴ Sun, Y.; Tao, J.; Zhang, G. G. Z.; Yu, L. Solubilities of crystalline drugs in polymers: an improved analytical method and comparison of solubilities of indomethacin and nifedipine in PVP, PVP/VA, and PVAc. *J. Pharm. Sci.* **2010**, *99*, 4023-4031.
- ²⁵ Andronis, V.; Yoshioka, M.; Zografi, G. Effects of sorbed water on the crystallization of indomethacin from the amorphous state. *J. Pharm. Sci.* **1997**, *86*(3), 346-351.
- ²⁶ Gordon, M.; Taylor, J. S. Ideal copolymers and the second-order transitions of synthetic rubbers. I. Non-crystalline copolymers. *J. Appl. Chem.* **1952**, *2*(9), 493-500.

-
- ²⁷ Mullins, W.W. Flattening of a nearly plane solid surface due to capillarity. *J. Appl. Phys.* **30**, 77 (1959).
- ²⁸ Ruan, S.; Musumeci, D.; Zhang, W.; Gujral, A.; Ediger, M. D.; Yu, L. Surface transport mechanisms in molecular glasses probed by the exposure of nano-particles. *J. Chem. Phys.* **2017**, *146*(20), 203324.
- ²⁹ Andronis, V.; Zografis, G. Molecular mobility of supercooled amorphous indomethacin, determined by dynamic mechanical analysis. *Pharm. Res.* **1997**, *14*(4), 410-414.
- ³⁰ Hiemenz, P. C.; Lodge, T. P. *Polymer chemistry*. CRC press. **2007**
- ³¹ Bishop, C.; Gujral, A.; Toney, M. F.; Yu, L.; Ediger, M. D. Vapor-deposited glass structure determined by deposition rate–substrate temperature superposition principle. *J. Chem. Phys. Lett.* **2019**, *10*(13), 3536-3542.
- ³² Yu, J.; Li, Y.; Yao, X.; Que, C.; Huang, L.; Hui, H.W.; Gong, Y.C.; Yu, L. Surface Enrichment of Surfactants in Amorphous Drugs: An X-Ray Photoelectron Spectroscopy Study. *Mol. Pharm.*, **2022**, *19*, 654-660
- ³³ Wan F.; Bohr, A.; Maltesen M.J.; Bjerregaard S.; Foged C.; Rantanen J. et al. Critical solvent properties affecting the particle formation process and characteristics of celecoxib-loaded PLGA microparticles via spray-drying. *Pharm Res.* **2013**, *30*(4), 1065–76.
- ³⁴ Davies M.C.; Wilding I.R.; Short R.D.; Khan M.A.; Watts J.F.; Melia C.D. An analysis of the surface chemical structure of polymethacrylate (Eudragit) film coating polymers by XPS. *Int. J. Pharm.* **1989**, *57*(3), 183–187.
- ³⁵ Ward, R.; Davies, P.; Bain, C., Orientation of surfactants adsorbed on a hydrophobic surface. *J. Phys. Chem.* **1993**, *97*(28), 7141-7143.
- ³⁶ Rasing, T.; Shen, Y.; Kim, M. W.; Valint Jr, P.; Bock, J. Orientation of surfactant molecules at a liquid-air interface measured by optical second-harmonic generation. *Phys. Rev. A* **1985**, *31*(1), 537.
- ³⁷ Li, Y.; Bishop, C.; Cui, K.; Schmidt, J. R.; Ediger, M. D.; Yu, L. Surface diffusion of a glassy discotic organic semiconductor and the surface mobility gradient of molecular glasses. *J. Chem. Phys.* **2022**, *156*, 094710
- ³⁸ Schweizer, K. S.; Simmons, D. S. Progress towards a phenomenological picture and theoretical understanding of glassy dynamics and vitrification near interfaces and under nanoconfinement. *J. Chem. Phys.* **2019**, *151*, 240901.
- ³⁹ Huang, C., Ruan, S., Cai, T., Yu, L. Fast surface diffusion and crystallization of amorphous griseofulvin. *J. Phys. Chem. B* **2017**, *121*(40), 9463-9468.

Chapter 6 Polymer nanocoating of amorphous drugs for improving stability, dissolution, powder flow, and tableability: The case of chitosan-coated indomethacin

Yuhui Li¹, Junguang Yu¹, Shenye Hu², Zhenxuan Chen¹, Mark Sacchetti,³ Changquan Calvin Sun², Lian Yu^{1*}

¹ School of Pharmacy, University of Wisconsin-Madison, Madison, WI, 53705, USA

² School of Pharmacy, University of Minnesota, Minneapolis, MN, 55455, USA

³ Zeeh Pharmaceutical Experiment Station, School of Pharmacy, University of Wisconsin-Madison, Madison, WI, 53705, USA

As published in *Mol. Pharm.* 2019, 16, 1305-1311

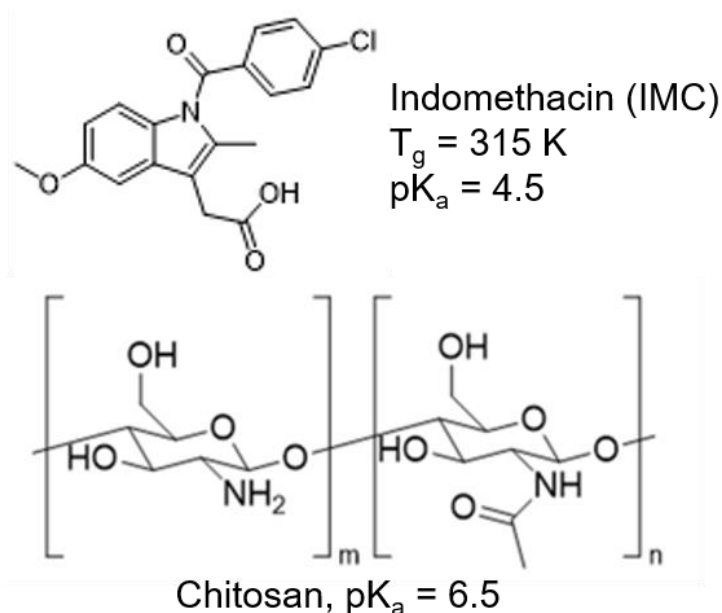
6.1 Abstract

Due to its higher molecular mobility, the surface of amorphous drugs can grow crystals much more rapidly than the bulk, causing poor stability and slow dissolution of drug products. We show that a nano-coating of chitosan (a pharmaceutically acceptable polymer) can be deposited on the surface of amorphous indomethacin by electrostatic deposition, leading to significant improvement of physical stability, wetting by aqueous media, dissolution rate, powder flow, and tableability. The coating condition was chosen so that the positively charged polymer deposits on the negatively charged drug. Chitosan coating is superior to gelatin coating with respect to stability against crystallization and agglomeration of coated particles.

6.2 Introduction

An active pharmaceutical ingredient can exist in many solid forms, both crystalline and amorphous. Amorphous formulations have attracted recent attention as a general method to improve the solubility and dissolution rate of poorly soluble drugs.¹ A key issue in this effort is the stability against crystallization since amorphous drugs tend to crystallize over time and crystallization would eliminate their advantages. Recent work has shown that molecular mobility can be extremely high on the free surface of amorphous drugs and this leads to rapid crystal growth on the surface while bulk crystal growth is relatively slow.^{2,3,4} These results suggest that preventing surface crystallization is an efficient way to improve the stability of amorphous drugs.

Wu et al. showed that a nano-coating of polymers can effectively inhibit the surface crystallization of an amorphous drug, as well as improving the power flow.⁵ Their coating process relied on electrostatic deposition in which a polyelectrolyte deposits on an amorphous drug of the opposite charge. For indomethacin (IMC, Scheme 5.1, a weak acid with $pK_a = 4.5$), coating was performed at $pH = 5$ at which the drug is negatively charged so that the polycation polydiallyldimethylammonium chloride (PDDA) can deposit on it. The polymer coating protects the drug against surface crystallization because under the coating, surface molecules are immobilized. An attractive feature of this approach is that the coating can be extremely thin, on the order of several nanometers, since the neutralization of charges stops further deposition of charged polymer molecules. As a result, only a small amount of polymer is needed to significantly improve stability. This ability is useful for producing high-drug-loading formulations and for saving room in the formulation for other excipients needed to enhance disintegration and dissolution.



Scheme 6.1. Molecular structure of indomethacin and chitosan.

Because PDDA is not a pharmaceutical polymer, Teerakapibal et al. tested gelatin as a coating polymer.⁶ Unlike PDDA, gelatin is a weak polyelectrolyte and not a homopolymer, having both acidic and basic amino acid segments. They found that a gelatin coating can offer a similar protective effect against crystallization, and that a gelatin coating is “forgiving” in that it does not require strict pairing of opposite charges. At a given pH, the amino acid segments in gelatin can be both positive and negative. As a result, gelatin-drug interactions are less well defined as in the case of a homopolymer, with local variations according to the amino acid segments.

The present study investigated the use of chitosan as a pharmaceutically acceptable coating material to replace PDDA and to improve upon gelatin as a coating polymer. Chitosan (Scheme 1) is a linear polysaccharide derived from chitin, whose chain segments are randomly distributed D-glucosamine and N-acetyl-D-glucosamine. The glucosamine group is weakly basic and protonated below pH ~ 6.5 (the pK_a of chitosan),⁷ making chitosan a polycation at low pH. Chitosan has been used as a polymer for electrostatic deposition to create ultra-thin coatings (several nanometers for each chitosan layer).⁸ From the pK_a values of chitosan (6.5) and IMC (4.5), we expect that in the pH range 4.5 – 6.5, IMC is negatively charged and chitosan is positively charged, enabling coating by electrostatic deposition. This hypothesis will be tested here. Since chitosan has lower charge density when ionized than PDDA (owing to partial amide formation), it is of interest to compare their performance in inhibiting surface crystallization. We report that the principle of electrostatic deposition can be extended to the chitosan-IMC system to prepare protective coatings to inhibit surface crystallization. The polycation chitosan can be deposited on the negatively charged IMC to suppress surface crystallization, and the resulting material shows significant improvement in dissolution rate, powder flow, and tableability relative to uncoated ones. We find that chitosan is

superior to gelatin for coating amorphous IMC with respect to stability against crystallization and agglomeration of coated particles.

6.3 Materials and methods

Indomethacin [1-(p-chlorobenzoyl)-5-methoxy-2-methylindole-3-acetic acid, $\geq 99\%$, IMC], chitosan (medium molecular weight grade, MW ~ 190 -310 kg/mole), gelatin from porcine skin (Type A, ~ 300 bloom, MW 50-100 kg/mole), and gelatin from bovine skin (Type B, ~ 225 bloom, MW 50-100 kg/mole) were purchased from Sigma Aldrich (St. Louis, MO) and used as received. were purchased from Sigma Aldrich and used as received. Chitosan was dissolved in 0.3 wt % acetic acid (prepared by dissolving $\geq 99.7\%$ pure acetic acid purchased from Sigma Aldrich in Milli-Q water) at a concentration of 2 mg/mL. The solution pH was adjusted to 5 by adding 1 M NaOH, which increased the solution volume by $\sim 4\%$.

An amorphous IMC film with an open surface was prepared by melting 5 mg of the as-received crystalline material at 190 °C for 1 minute between two microscope coverslips, cooling to room temperature, and gently removing one coverslip. To form a protective coating, the sample with a free surface was dipped in a chitosan solution for 10 second, dried with an absorbent tissue, and further dried at 295 K under vacuum for 3 hours. To prepare chitosan or gelatin coated amorphous particles, 1 g of crystalline IMC was melted and cooled to room temperature to make a bulk glass. The bulk glass was broken into particles in the presence of 2 mL coating solution using 4 methods: Retsch Mill, Vortex, magnetic stirrer, and homogenizer. In the Retsch Mill method (MM 301, Retsch Inc., Newtown, PA), amorphous chunks were poured into a 20 mL metal tube together with eleven 5 mm steel balls. Particles were collected after milling for 75 s at a frequency of 25 Hz. In

the Vortex method, amorphous chunks were poured into a 20 mL glass vial containing two half inch steel balls. Particles were collected after milling for 60 s at the intensity scale of 7 using a Vortex (S8223, Scientific Industries Inc, Bohemia, NY). In the magnetic stirrer method, amorphous chunks were poured into a 20 mL glass vial together with one 2.5 cm stir bar and the vial was placed on its side on a stir plate. Particles were collected after stirring for 4 min at a speed of 100 rpm. In the homogenizer method (Polytron PT 1200 E, Kinematica AG, Switzerland), amorphous chunks were placed in a 10 mL glass beaker. Particles were collected after milling for 60 s with the homogenizer probe operating at 180 rpm. During the coating process, the pH of the coating solution did not change significantly (< 0.01). With each method, after particle size reduction, the slurry was filtered and dried at room temperature under vacuum for 3 hours. As control, uncoated particles were also prepared by the homogenizer method but in the absence of a coating solution. Particle size distributions were determined by dispersing the particles in an immersion medium for microscopy and measuring their sizes through a light microscope (Nikon Optiphot Pol 2 equipped with a digital camera).

For crystallization studies, the temperature was maintained by ovens to ± 1 °C. Two levels of relative humidity (RH) were used: (1) 75% RH maintained by a saturated NaCl solution and (2) a “dry” condition (0-5 % RH) maintained by storage in a desiccator loaded with Drierite. The stability test was performed under 3 conditions: 40 °C/dry, 40 °C/75% RH, and 30 °C/75% RH. The degree of crystallinity was calculated from the XRD patterns using:

$$\text{Crystallinity (\%)} = A_{\text{cryst}} / A_{\text{total}} \times 100$$

where A_{cryst} is the area of the crystalline peaks in an XRD pattern and A_{total} is the total area of the crystalline peaks and the amorphous halo. The XRD patterns were integrated using the program EVA from Bruker-XAS.

X-ray powder diffraction (XRD) was performed with a Bruker D8 Advance X-ray diffractometer, which was equipped with a Cu $K\alpha$ source ($\lambda = 1.54056 \text{ \AA}$) operating at a tube load of 40 kV and 40 mA. Each sample was scanned between 2° and 40° (2θ) with a step size of 0.02° and a maximum scan rate of 3 s/step. Samples of small quantity were analyzed on a Si (510) zero-background holder.

The dissolution rate of IMC particles was measured at 37°C . Uncoated and chitosan coated amorphous particles were prepared using the homogenizer method and tested immediately. IMC crystalline particles (γ polymorph as confirmed by XRD) were obtained by crystallizing uncoated amorphous particles under the 40°C /dry condition. All the samples were sieved and the 45 - 100 μm sieve cut was used. After equilibrating 25 mg of particles in a dry dissolution vessel at 37°C , 100 mL of Milli-Q water pre-warmed to 37°C was poured into the vessel. The mixture was stirred at a paddle speed of 150 rpm. At each time point, 2 mL of solution was withdrawn from the vessel and replaced with 2 mL of Milli-Q water at 37°C . The withdrawn solution was filtered through 0.2 μm membrane filter and its concentration was determined by UV-visible spectrometry (8453, Agilent Technologies, Inc.) at 318 nm against a standard curve obtained by measuring IMC solutions of known concentrations. Each dissolution profile (concentration versus time) was the average of at least 3 samples.

To measure the angle of repose, 200 mg of IMC powder in the sieve cut 45 – 100 μm was poured through a funnel whose outlet (3 mm inside diameter) was placed 0.5” above a horizontal receiving surface. A picture was taken of the rested powder from its side and the angle of repose was measured from the image. Powder flowability was measured using a ring shear tester (RST-XS; Dietmar Schulze, Wolfenbüttel, Germany) at a pre-shear normal stress of 1 kPa under ambient conditions (23 °C and 50-55% RH). A 10 mL shear cell was used and the measurement was made in triplicates. The normal stresses for shear testing were 230, 400, 550, 700, 850, and 230 Pa. Data were analyzed using standard methods.⁹ Un-confined yield strength (f_c) and major principal stress (σ_n) were obtained from each yield locus by drawing Mohr’s circles. The flowability index, ff_c , was calculated using Eq. (6.1):

$$ff_c = \frac{\sigma_n}{f_c} \quad (6.1)$$

For tableability assessment, approximately 100 mg of powder was manually filled into a 6 mm diameter die and compressed using flat-faced punches on a Universal Material Testing Machine (model 1485; Zwick/Roell, Ulm, Germany) at a speed of 5 mm/min. Tablets were allowed to relax under ambient conditions for 24 h before measuring their diameters, thicknesses, and weights. Care was taken to remove the flashing before measuring tablet thickness.¹⁰ The diametrical breaking force was then measured using a texture analyzer (TA-XT2i; Texture Technologies Corporation, Scarsdale, New York) at a speed of 0.01 mm/s. Tablet tensile strength was calculated from the maximum breaking force and tablet dimensions using Eq. (6.2):¹¹

$$\sigma = \frac{2F}{10^6 \pi DT} \quad (6.2)$$

where σ is tensile strength (MPa), F is the breaking force (N), D is the tablet diameter (m), and T is the tablet thickness (m). Each tabletability profile is a plot of tensile strength vs. compaction pressure.

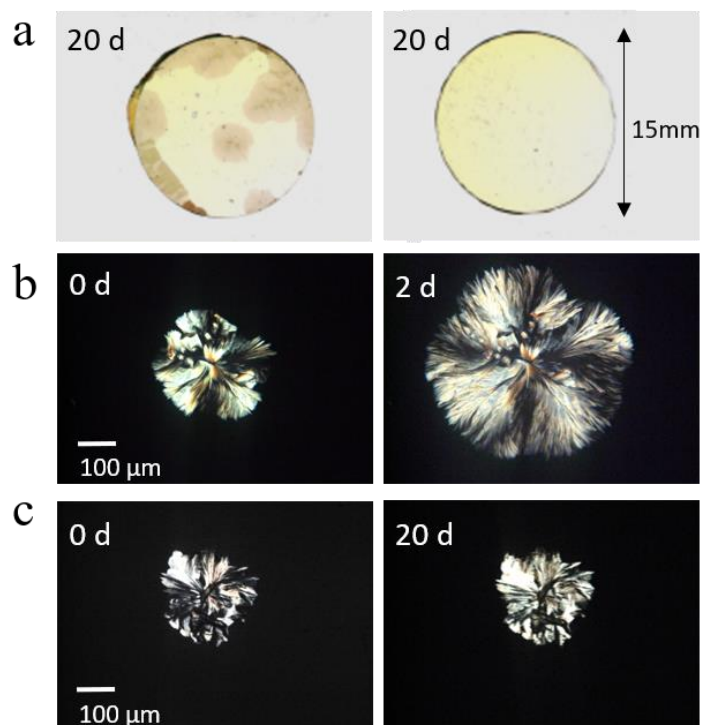


Figure 6.1. Effect of chitosan coating on surface crystal growth in an amorphous IMC film at 40 °C. Without coating (panel a, left), crystallization is evident in 20 days; with a chitosan coating (panel a, right), no crystallization is observed after 20 days. The as-prepared film was free of crystals (like the one on the right). Each film was prepared on a round glass coverslip (15 mm in diameter). (b) Progress of crystal growth in an uncoated film viewed through a microscope. Obvious growth is seen in 2 days. (c) Same as (b), except that the film is coated with chitosan. No significant growth is seen in 20 days.

6.4 Results and discussions

6.4.1 Stability Test in Film Geometry.

The stability of chitosan coated amorphous IMC was first tested in the film geometry. As shown in Figure 6.1a, without coating, significant crystallization occurred in 20 days. The crystals were opaque regions in an otherwise transparent amorphous film of light-yellow color. In contrast, a chitosan-coated film remained amorphous under the same condition, indicating the ability of a chitosan coating to inhibit surface crystallization. Furthermore, the growth of preexisting crystals with and without coating was followed. The preexisting crystals were formed by annealing an open-surface sample for three to four days. These partially crystallized samples were then split into two groups: the first group was uncoated control; the second group was coated to evaluate the effect of coating. Without coating, crystal growth was evident in 2 days at 40 °C (Figure 6.1b); the growth rate was 0.7 ± 0.1 nm/s ($n = 5$) in the γ polymorph, consistent with the previous report.¹² In contrast, under a chitosan coating, no growth was detected even after 20 days (Figure 6.1c).

6.4.2 Stability of Coated Amorphous Particles.

In addition to coated films, the effect of chitosan coating on the surface crystallization and other physical properties of amorphous particles was also studied. All coated particles were prepared with the homogenizer method (see Materials and Methods), which as we discuss below, is superior to the other methods under the conditions tested. The coated particles were tens of micrometers in size (Figure 6.S1) and their size distribution was similar to that of the uncoated particles, consistent with the small thickness of the coating and the absence of coating-induced granulation. Figure 6.2 shows the typical XRD data for testing physical stability. XRD patterns are compared for uncoated and coated particles at 30 °C and 75 % RH. The uncoated particles show significant crystallization, while coated particles remain amorphous, indicating improved stability.

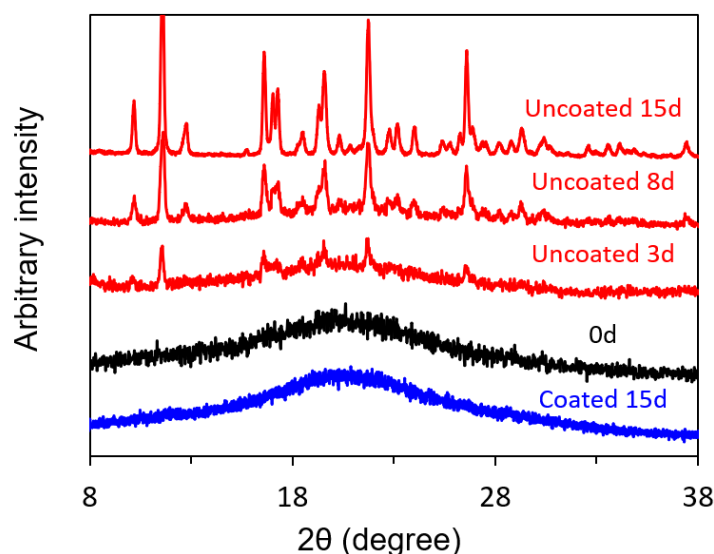


Figure 6.2. X-ray diffraction patterns of uncoated and chitosan-coated amorphous IMC particles at time zero and after specified times at 30°C and 75% RH. Uncoated particles showed significant crystallization, while coated particles remained amorphous.

Figure 6.3 compares the change of crystallinity of amorphous particles coated with chitosan and gelatin (A and B) under three different conditions: 40 °C/dry, 40 °C/75% RH, and 30 °C/75% RH. Under all the conditions tested, coated particles were more resistant to crystallization than uncoated particles. At 40°C (Figure 6.3a), the chitosan coating performed significantly better than the gelatin coating (A or B). The same is true at 40 °C and 75% RH (Figure 6.3b). At 30°C and 75% RH, chitosan and gelatin coatings had similar performance in suppressing crystallization (Figure 6.3c). Overall, these results indicated that chitosan is better than gelatin as a coating material for inhibiting crystallization. This could be a result of the higher charge density of chitosan relative to gelatin, enabling stronger ionic interactions between chitosan and IMC.

The data in Figure 6.3 show that moisture can greatly accelerate the crystallization process even under a polymer coating. Uncoated particles remain mostly amorphous after 30 days at 40 °C under a dry condition, but at 40°C and 75% RH, crystallization is complete in one day. This effect has been reported previously and attributed to increased molecular mobility in the presence of absorbed moisture.^{13,14} Our polymer coating is extremely thin (several nanometers) and chitosan is hydrophilic in nature. Such a coating is not expected to prevent the entry of moisture into the amorphous drug. Future work could investigate other polymer systems to learn whether the performance under humid conditions can be improved.

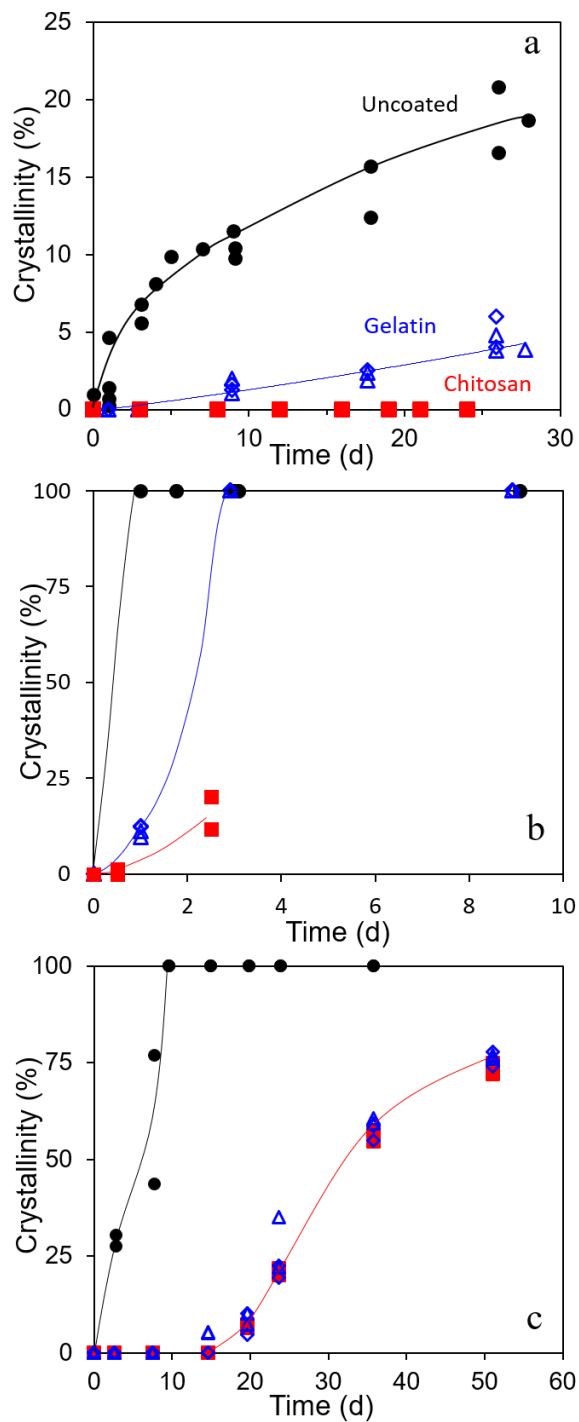


Figure 6.3. Effect of chitosan coating on the physical stability of amorphous IMC particles under different conditions: (a) 40°C and dry (0-5 % RH), (b) 40 °C and 75% RH, (c) 30°C and 75 % RH. Black circles: uncoated particles. Blue open triangles: gelatin A coated particles. Blue open diamonds: gelatin B coated particles. Red squares: chitosan coated particles".

6.4.3 Comparison of Particle Formation Methods.

As described in the Materials and Methods Section, several methods were used to prepare coated amorphous particles. These methods differ in terms of energy input and particle formation; they are expected to cause different degrees of in-process crystal nucleation and produce particles with different stability on storage. In Figure 6.4, we compare the rates of crystallization of coated amorphous particles prepared by different methods. With all the methods used, the as-prepared particles were amorphous according to XRD. At 40 °C, particles prepared by the homogenizer method remained amorphous for at least 20 days, while particles prepared by the other methods all crystallized faster. This result suggests that among the four methods under the conditions we

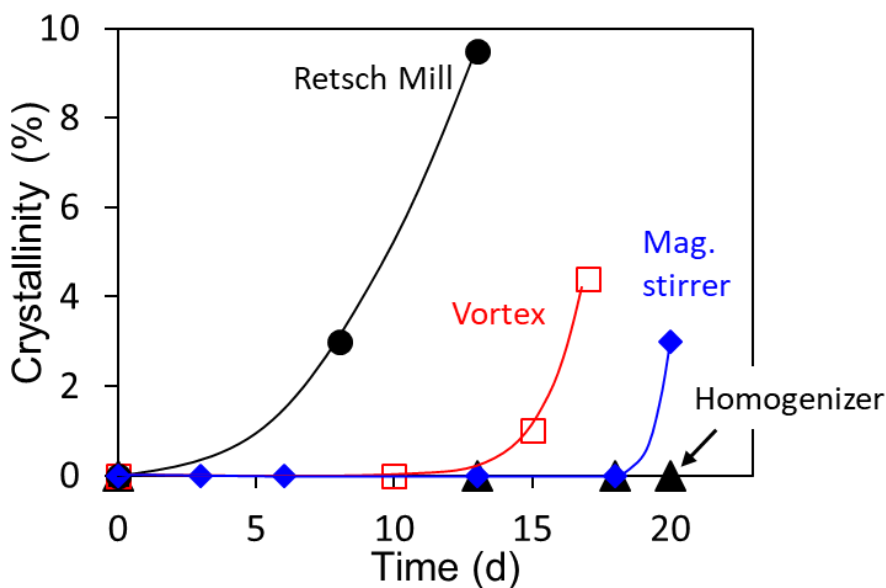


Figure 6.4. Stability of particles prepared by different methods at 40 °C. The particles prepared by the homogenizer method show the best stability against crystallization.

tested them, the homogenizer method performed the best. This is possibly because of its efficient mixing and low energy input during particle formation.

6.4.4 Dissolution Rate.

Figure 6.5 shows the effect of chitosan coating on the dissolution rate of amorphous IMC particles. To be able to compare our results with the previous results on uncoated particles,^{15,16} we performed dissolution measurements in unbuffered Milli-Q water. As a point of reference, we also measured the dissolution kinetics of uncoated crystalline IMC particles (γ polymorph) under the same condition. The plateau concentration of 8.5 $\mu\text{g/mL}$ reached by the crystalline particles corresponds to the solubility of γ IMC, which agrees with the result of Hancock and Park (5 $\mu\text{g/mL}$ at 25 °C and 12 $\mu\text{g/mL}$ at 45 °C).¹⁵ For the uncoated amorphous particles, we observed faster dissolution rate relative to the uncoated crystalline particles, in agreement with the previous reports.^{15,16} Note, however, the dissolution profile of our uncoated amorphous particles (Figure 6.5) is missing a transient concentration peak seen in previous studies.^{15,16} This is attributed to a lower particle loading into the dissolution vessel, as discussed below. Over time, the solution concentration reached by uncoated amorphous particles approaches the crystal solubility, indicating that the amorphous particles crystallized during testing. This was confirmed by post-dissolution XRD analysis and by the color change of the IMC powder from yellow to white; it is also consistent with the previous interpretation of the amorphous IMC dissolution kinetics.^{15,16} It is noteworthy that the solution concentration reached by uncoated amorphous particles approaches the crystal solubility but within the time of observation, does not quite attain it. This may be due to incomplete crystallization and/or crystallization to a different polymorph.^{15,16} In contrast to uncoated amorphous particles, chitosan-coated amorphous particles show significantly enhanced dissolution rate, producing a peak concentration that lasts for several hours, which gradually decreases in the course of one day.

The enhanced dissolution of chitosan coated particles is attributed to improved wetting and prevention of crystallization. During the dissolution test, chitosan coated particles were observed to circulate freely in the dissolution medium with stirring, whereas uncoated or crystalline particles tended to float on the surface. A derivative of cellulose, chitosan is more hydrophilic than indomethacin. Thus, coated particles are more easily wetted by water, which increases the

dissolution rate. It is also noteworthy that the dissolution of *uncoated* amorphous particles did not create a peak concentration (the “spring effect”). This is because the uncoated particles crystallized quickly on contact with water, resulting in a solution concentration that is close to the crystal solubility (Figure 6.5). In contrast, coated amorphous particles show a peak concentration around 100 min, which “parachutes” down gradually in the course of one day. This indicates that a

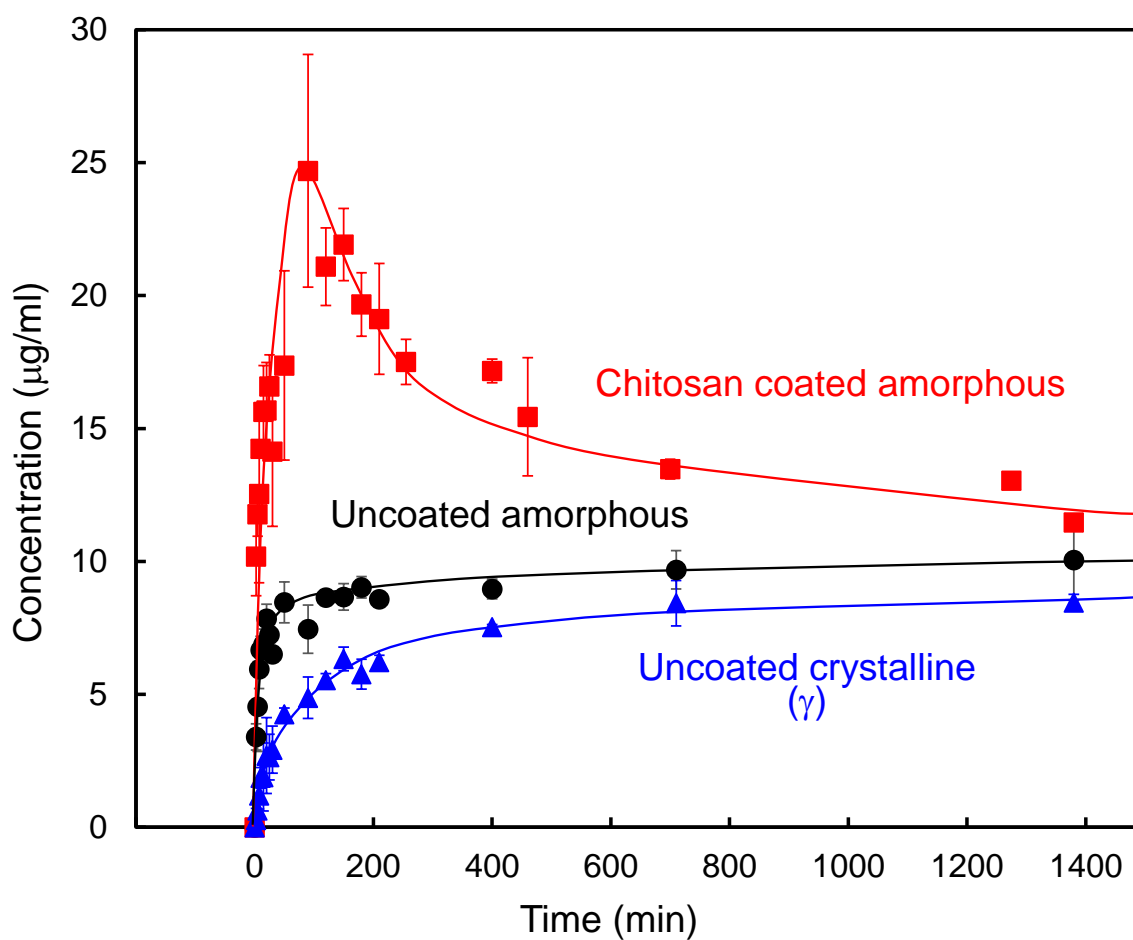


Figure 6.5. Effect of chitosan coating on the dissolution rate of amorphous IMC particles at 37 °C. Each data point shown is the average of 3 independent measurements.

chitosan coating delayed the crystallization process, allowing the solution to reach and sustain high supersaturation.

In the case of uncoated amorphous particles, previous workers observed a peak concentration during dissolution.^{15,16} This is in contrast to the absence of such a peak in our result (Figure 6.5). We attribute this difference to the *amount* of the particles loaded into the dissolution vessel. The previous workers used a loading level of 2 mg/mL, while our loading level was much lower (0.25 mg/mL), chosen to represent the pharmaceutical condition for an oral dosage form. Presumably, at a higher particle loading, the total surface area of amorphous particles is larger, leading to a higher flux of dissolved molecules into the solution and creating a more pronounced peak in the concentration vs. time profile.

6.4.5 Powder Flow.

Table 5.1 compares the flowability of uncoated and coated IMC particles in two different ways. First, the angle of repose is significantly smaller for chitosan-coated particles, indicating better flowability. Second, the flowability indices (ff_c) indicate that the uncoated powder is cohesive ($ff_c = 4.1$), while the coated powder is free flowing ($ff_c = 10.1$).¹⁷ This improved flowability is adequate for high speed tableting, since the ff_c value is higher than that of microcrystalline cellulose, Avicel PH102, which flows adequately during such a process.¹⁸

Table 5.1. Comparison of the flowability of particles using the angle of repose and flow function coefficient ff_c .

	Uncoated	Coated
Flowability Test		
Angle of Repose, deg.	41.4 ± 3.6 (n=3)	34.5 ± 4.1 (n=3)
ff_c	4.1 ± 0.2 (n=3)	10.1 ± 1.9 (n=3)

The improved powder flow by polymer coating can be understood in terms of modified physical and chemical environment on the surface. A polymer coating may make a surface smoother and cover its defects and pores, as shown by the significantly reduced roughness of HPMC coated ibuprofen particles.¹⁹ It is also possible that a polymer coating reduces the cohesion between drug particles. This latter effect is supported by the similar f_{fc} values between chitosan (10.4) and coated IMC particles (10.1).

We observed a significant difference between gelatin and chitosan coated particles in terms of flowability upon storage (Figure 6.6). After two months at 30°C/75% RH, chitosan coated particles



Figure 6.6. Comparison of gelatin- and chitosan-coated particles. Storage at 30 °C and 75%RH causes gelatin-coated particles to stick together and to the container, whereas chitosan-coated particles remain free-flowing.

remained free flowing; in contrast, gelatin coated particles stuck to each other and to the container wall within several days. Gelatin is known to swell and become sticky after absorbing moisture, and this may lead to poor flowability of gelatin-coated particles. With respect to both stability and flowability, chitosan is a better coating material than gelatin.

6.4.6 Tableability.

Figure 6.7 compares the tensile strength of tablets prepared with uncoated and coated amorphous IMC particles as a function of compaction pressure. Below 200 MPa pressure, tablets prepared with chitosan coated IMC consistently exhibit higher tensile strength than those prepared with uncoated IMC. This indicates that even an ultra-thin chitosan coating can improve the tableability of amorphous particles. It is remarkable that, without any additional excipients, the coated amorphous particles already show acceptable tableability, reaching 2 MPa (horizontal line) at 125 MPa of pressure. When the compaction pressure exceeded 125 MPa, over-compression phenomenon was observed. In this high-pressure region, the tablets delaminated upon ejection or during the diametrical breaking test, which led to a strength decrease and higher variations in measured tensile strength. No crystallization was detected by XRD as a result of compaction (see Figure 6.S2).

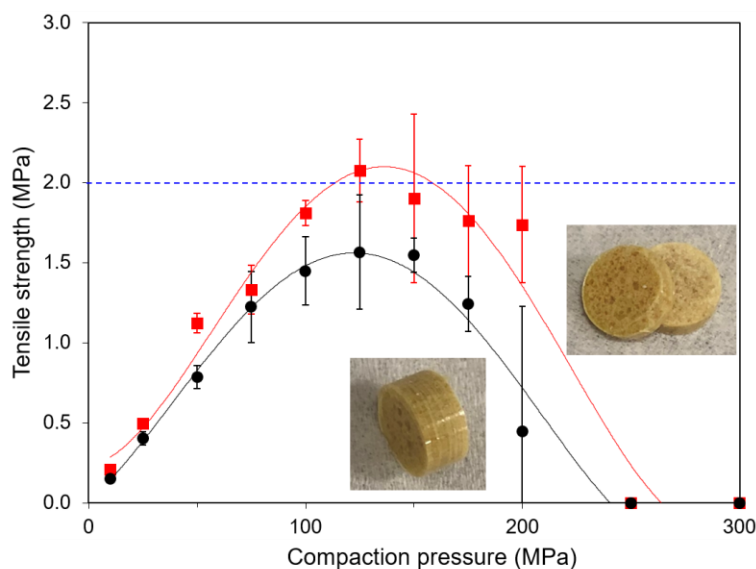


Figure 6.7. Effect of chitosan coating on the tensile strength of tablets prepared with amorphous IMC particles. Tensile strength of the tablet is plotted against compaction pressure. Black circles: uncoated particles. Red squares: chitosan-coated particles. Up to 200 MPa, the tablet of chitosan-coated particles is consistently stronger. Above this compaction pressure, the tablets are “over-compressed” and delaminated (see photo). Each data point shown is the average of 3 independent measurements.

A polymer coating is known to improve tableability of poorly compressible materials, such as silica, acetaminophen, and polymer beads.^{20,21,22} This effect has been attributed to a simultaneous increase of bonding strength and bonding area of polymer-coated particles. This effect may also account for the improvement of tableability observed in this work. A key feature of this work is that the polymer coating is extremely thin (several nanometers), suggesting the potential for improving tableability even with ultra-thin polymer coatings.

6.5 Conclusion.

This work has shown that the surface crystallization of amorphous indomethacin can be inhibited by a nano-coating of a pharmaceutically acceptable polyelectrolyte, chitosan. The coating improves the physical stability against crystallization not only in the solid state but also in a dissolution medium. Chitosan coated particles show faster dissolution, a result of better wetting and retarded crystallization. Furthermore, a chitosan coating improves powder flow and tableability. It is worth emphasizing that a chitosan coating prepared by electrostatic deposition is extremely thin (several nanometers) and this could facilitate the preparation of stable amorphous formulations at a high drug loading.

Since coatings prepared by electrostatic deposition are extremely thin, it is useful to examine the advantages and limitations of this technology. A potential issue for any thin coating is that it could be fragile and easily damaged. This concern can be assessed from the standpoint of performance. As this and previous work^{5,6} show, a polymer nano-coating can inhibit the growth of surface crystals on an amorphous drug. The process of crystal growth causes volume change and local stress and the nano-coating is effective in this highly stressful environment. In addition, the coated particles were sieved prior to stability and dissolution testing and this mechanical stress had no detrimental effect on the coating. Finally, even in contact with a dissolution medium, the coating remains effective in slowing down drug crystallization. All these observations indicate that despite its small thickness, a polymer nano-coating can be quite strong. This is consistent with the strong ionic interactions between chitosan and IMC. In future work, nano-coating by electrostatic deposition can be explored with other pharmaceutical polymers and extended to other amorphous

drugs. In addition to acidic drugs like indomethacin, basic drugs can be protonated at low pH and coated by polyanions.

6.6 Supporting Information

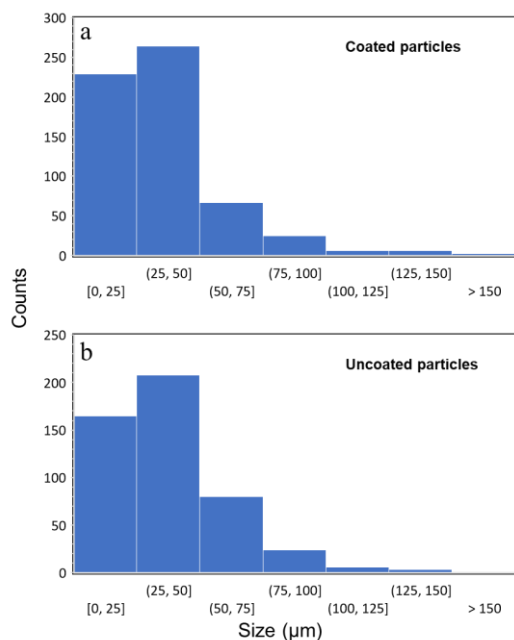


Figure 6.S1. Particle distributions of coated and uncoated particles.

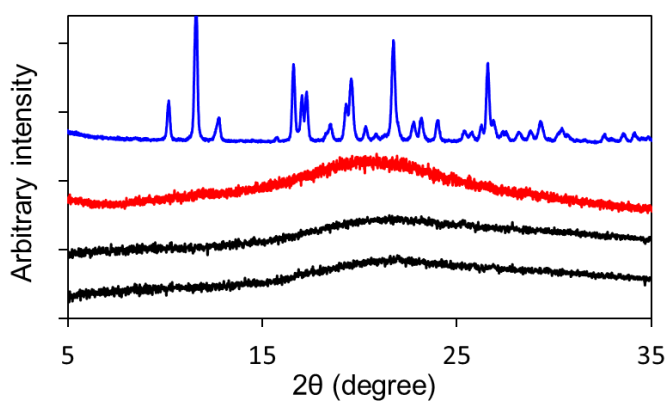


Figure 6.S2. X-ray diffraction patterns of crystalline IMC (γ polymorph, blue trace), as-coated amorphous particles (red), and coated amorphous particles after compaction (black, duplicate measurements). These data indicate that no crystallization occurred as a result of compaction.

6.7 References

-
- ¹ Yu, L., Amorphous Pharmaceutical Solids: Preparation, Characterization and Stabilization. *Adv. Drug Delivery Rev.* **2001**, *48* (1), 27.
- ² Zhu, L.; Brian, C.; Swallen, S. F.; Straus, P. T.; Ediger, M. D.; Yu, L. Surface Self Diffusion of an Organic Glass. *Phys. Rev. Lett.* **2011**, *106*, 256103-1 to 256103-4.
- ³ Yu, L. Surface Mobility of Molecular Glasses and Its Importance in Physical Stability. *Adv. Drug Delivery Rev.* **2016**, *100*, 3–9.
- ⁴ Huang, C.; Ruan, S.; Cai, T.; Yu, L. Fast Surface Diffusion and Crystallization of Amorphous Griseofulvin. *J. Phys. Chem. B* **2017**, *121*, 9463–9468.
- ⁵ Wu, T.; Sun, Y.; Li, N.; de Villiers, M.; Yu, L. Inhibiting Surface Crystallization of Amorphous Indomethacin by Nanocoating. *Langmuir* **2007**, *23*, 5148-5153.
- ⁶ Teerakapibal, R.; Gui, Y.; Yu, L., Gelatin Nano-coating for Inhibiting Surface Crystallization of Amorphous Drugs, *Phar. Res.*, **2018**, *35*, 23
- ⁷ Qi, Z.; Xi, G.; Nan, L.; Shi, X.; Cheng, S.; Xiang, H.; Chen, G., Protonation constants of chitosan with different molecular weight and degree of deacetylation. *Carbohydrate Polymers*, **2006**, *65* (2), 194-201.
- ⁸ Alves, N.M.; Picart, C.; Mano, J.F., Self-Assembling and Crosslinking of Polyelectrolyte Multilayer films of Chitosan and alginate studied by QCM and IR Spectroscopy. *Macromol. Biosci.*, **2009**, *9*, 776-785
- ⁹ Shi, L.; Chatteraj, S.; Sun, C.C., Reproducibility of flow properties of microcrystalline cellulose—Avicel PH102. *Powder Technol.*, **2011**, *212*, 253-257
- ¹⁰ Paul, S., Chang, S.-Y.; Sun, C.C., The phenomenon of tablet flashing — Its impact on tableting data analysis and a method to eliminate it. *Powder Technol.*, **2017**. *305*, 117-124.
- ¹¹ Fell, J.T.; Newton, J.M., Determination of tablet strength by the diametral-compression test. *J. Pharm. Sci.*, **1970**. *59*, 688-91
- ¹² Musumeci, D.; Hasebe, M.; Yu, L., Crystallization of Organic Glasses: How Does Liquid Flow Damage Surface Crystal Growth? *Crystal Growth & Design*, **2016**, *16* (5)
- ¹³ Andronis, V.; Zografi, G., The Molecular Mobility of Supercooled Amorphous Indomethacin as a Function of Temperature and Relative Humidity. *Pharm. Res.*, **1998**, *15*, 835-842
- ¹⁴ Andronis, V.; Yoshioka, M.; Zografi, G., Effects of Sorbed Water on the Crystallization of Indomethacin from the Amorphous State. *J. Pharm. Sci.* **1997**, *86*
- ¹⁵ Hancock, B. C.; Parks, M., What is the True Solubility Advantage for Amorphous Pharmaceuticals? *Phar. Res.*, **2000**, *17*, 397-404
- ¹⁶ Murdande, S. B.; Pikal, M. J.; Shanker, R. M.; Bogner, R. H., Solubility Advantage of Amorphous Pharmaceuticals: I. A Thermodynamic Analysis. *J. Pharm. Sci.* **2010**, *99*, 1254-1264

-
- ¹⁷ Carr, R. L., Evaluation Flow Properties of Solids. *Chem. Eng.*, **1965**, 18, 163-169
- ¹⁸ Sun, C.C., Setting the bar for powder flow properties in successful high speed tableting. *Powder Technol.*, **2010**, 201, 106-108
- ¹⁹ Genina, N.; Yliruusi, J., Thin-coating as an Alternative Approach to Improve Flow Properties of Ibuprofen Powder. *Int. J. Pharm.*, **2010**, 387, 65-70
- ²⁰ Shi, L.; Sun, C.C., Transforming Powder Mechanical Properties by Core/Shell Structure: Compressible Sand. *J. Pharm. Sci.*, **2010**, 99, 4458-4462
- ²¹ Shi, L.; Sun, C.C., Overcoming poor tableability of pharmaceutical crystals by surface modification. *Pharm. Res.*, **2011**, 12, 3248-3255
- ²² Osei-Yeboah, F.; Sun, C.C., Tableability modulation through surface engineering. *J. Pharm. Sci.*, **2015**, 104, 2645–2648

Chapter 7 A low-density second amorphous phase of D-mannitol with novel 3 nm mesoscopic order

Yuhui Li,¹ Zhenxuan Chen¹, Chengbin Huang¹, Men Zhu², Chris Benmore⁴, Yongchao Su⁵,
Chengrong Cao,³ J. H. Perepezko³, and Lian Yu^{1,2}

¹School of Pharmacy, University of Wisconsin-Madison, Madison, WI 53705, USA

²Department of Chemistry, University of Wisconsin-Madison, Madison, WI 53705, USA

³Department of Materials Science and Engineering, University of Wisconsin-Madison,
Madison, Wisconsin 53706, USA

⁴X-ray Science Division, Advanced Photon Source, Argonne National Laboratory, IL 60439,
USA

⁵MRL, Merck & Co., Inc., Kenilworth, NJ 07033, USA

To be submitted.

7.1 Abstract.

Polyamorphism, the existence of two amorphous phases of the same substance separated by a first-order transition, is an important and often controversial phenomenon. The polyamorphism of D-mannitol has been described as “the most recent (and perhaps the cleanest) example”. We show that the normal liquid of D-mannitol transforms near its glass transition temperature to a low-density amorphous phase (LDA) with new mesoscopic order, notably a 3 nm density modulation. In the LDA, the non-polar hydrocarbon groups are farther apart from each other, while the hydrogen-bonded (HB) structure is more ordered. The reorganization of the HB network occurs by rearranging the second coordination shells and beyond, leading to the prepeaks in the scattering pattern. The LDA has enhanced smectic-like order as seen in the crystalline structures, but the new 3 nm density modulation is completely devoid of any crystalline counterpart. This new length scale is attributed to the densely nucleated LDA domains in the normal liquid.

7.2 Introduction

Polyamorphism is the existence of two amorphous phases of the same substance related by a first-order transition. It is analogous to the polymorphism of crystals, but is far more rare and often controversial.¹ For a single-component molecular substance, the best studied systems are water^{2,3} and triphenyl phosphite (TPP).^{4,5} D-mannitol^{6,7,8} is a more recent entry and has been called by Austin Angell “the most recent (and perhaps the cleanest) example” of polyamorphism.⁹ The normal liquid of D-mannitol undergoes an exothermic transition near its glass transition temperature ($T_g = 284$ K), producing a second, lower-density amorphous phase.^{6,7,8} This second amorphous phase is designated LDA (low-density amorphous phase), in contrast to the normal liquid (HDA, high-density amorphous phase).

X-ray and neutron scattering is a powerful tool for studying the structure of liquids and glasses.^{10,11,12,13} The scattering measurements yield the atomic pair distribution functions (PDF) which play an important role in describing liquid structures and testing theories of liquids. With a high-energy and high-brilliance synchrotron source, scattering measurements can be performed up to a high momentum transfer, providing the data needed for constructing accurate PDFs.¹⁴ For polyalcohols, of which D-mannitol is an example, X-ray scattering can probe the structure formed by the close packing of the non-polar hydrocarbon groups, as well as the structure formed by the hydrogen bonding of the polar hydroxyl groups.¹⁵ In recent years, a great progress has been seen in the field of solid-state NMR (ssNMR). By probing the chemical shift of specific atom, ssNMR provides atomic information in high resolution for determining molecular structure, dynamics and domain morphology of solid materials.¹⁶ In this work, the two techniques were used to investigate the structures of D-mannitol's two amorphous phases and the mechanism of their conversion.

We find that the transformation of the normal liquid of D-mannitol to the second amorphous phase introduces new mesoscopic order, notably a 3 nm density modulation absent in any of the known crystal structures. In the LDA, the non-polar hydrocarbon groups are farther apart from each other, while the hydrogen-bonded (HB) structure is significantly reorganized. The reorganization occurs by rearranging the second coordination shells and beyond, resulting in supramolecular aggregates that give rise to low-angle scattering peaks. The LDA has enhanced smectic-like order as seen in the crystals but the new 3 nm density modulation has no crystalline counterpart. We discuss the origin of this new length scale and attribute it to the density modulation created by the high nucleation rate of the LDA domains in the normal liquid.

7.3 Experimental Section

D-mannitol (ACS reagent, >99%) was purchased from Sigma-Aldrich and used as received. 1,6-¹³C labeled D-mannitol was purchased from Cambridge Isotope Laboratories, Inc. For X-ray scattering experiments, a crystalline powder was filled in a silica capillary tube (Charles Supper Company, 1.5 mm O.D., 10 μm wall thickness) and the tube was flame-sealed. The sample was melted, quenched in an ice/water bath to form a glass, and mounted on a sample holder waiting at 275 K. The sample temperature was controlled by an Oxford Cryosystem 700 to ± 0.1 K. After measurement at 275 K, temperature was raised to 298 K to allow transformation to the second amorphous phase (LDA) and its measurement at 298 K. In other runs, the sample temperature was increased in 2 K steps to study the process of transformation. Acquisition time was 3 or 5 min.

Synchrotron X-ray diffraction was performed in the transmission geometry on the 6-ID-D beamline at the Advanced Photon Source (APS), Argonne National Laboratory (Illinois, USA). The X-ray wavelength was $\lambda = 0.12543 \text{ \AA}$. A Perkin-Elmer amorphous silicon 2D detector was utilized to collect the scattered X-ray intensity with an active area of $409.6 \times 409.6 \text{ mm}^2$ (2048×2048 pixels with a pixel size of $200 \times 200 \text{ }\mu\text{m}^2$). The detector was placed at a distance 32 to 45 cm from the sample (the precise distance was determined by measuring the diffraction of a CeO₂ powder). The instrument resolution was determined from the diffraction peak width of CeO₂.¹⁷ The normalized diffraction peak of CeO₂ can be represented by a normalized Gaussian function $s(q) = \frac{1}{w\sqrt{2/\pi}} \exp\left(-2\frac{(q-q_0)^2}{w^2}\right)$, where q_0 is peak position and $w = 0.069 \text{ \AA}^{-1}$ is peak width. The contribution from instrumental resolution to the structure factor was removed using the method of Jones and Misell.¹⁸

The two-dimensional scattering patterns showed no preferred orientation and were integrated azimuthally in the FIT2D software to produce a one-dimensional plot of intensity vs. momentum transfer q , where $q = \frac{4\pi}{\lambda} \sin\theta$ (2θ is the scattering angle), over the range of 0.44 to 25 \AA^{-1} .^{19,20} Corrections were made for container, flat plate, sample self-absorption, multiple scattering, oblique incidence, and Compton scattering using the program PDFgetX2.²¹ The corrected coherent scattering intensity $I(q)$ was normalized to obtain the atom-averaged X-ray structure factor:¹⁴

$$S(q) = 1 + \frac{I(q) - \langle f^2(q) \rangle}{\langle f(q) \rangle^2} \quad (1)$$

where $\langle f^2(q) \rangle$ is the atom-averaged self-scattering and $\langle f(q) \rangle^2$ is the atom-averaged scattering of the molecule ($f(q)$ refers to the atomic form factor).

Small-Angle X-ray Scattering (SAXS) was measured in the q range of 0.1 to 1.7 \AA^{-1} a customized Xenocs Ganesha unit with a Cu $K\alpha$ source, which was conditioned using a graphite monochromator under a power of 30 W. The beam was collimated using two sets of Si knife edge apertures set to gaps of $0.4 \times 0.4 \text{ mm}^2$ and $0.9 \times 0.9 \text{ mm}^2$. Data were recorded using a position sensitive 1M pixel Dectris 2D Eiger detector, which was placed at a distance 15.6 cm from the sample. The sample temperature was controlled by circulating a coolant through the sample holder and was read from a thermal couple that occupied a slot in the sample holder. The whole chamber was evacuated to 10^{-5} Torr to minimize air scattering during measurement. The recorded 2D scattering pattern was integrated azimuthally to obtain the 1D intensity vs. q plot. The q value was calibrated using silver behenate and the D-mannitol crystals formed in situ. The intensity was corrected for container and scaled to match the corrected scattering pattern obtained with the

synchrotron source as described above. This yielded a combined set of $I(q)$ and $S(q)$ from WAXS and SAXS.

The differential PDF, $D(r)$, was obtained by a Fourier sine transform of the function $F(q) = q(S(q) - 1)$:¹⁴

$$D(r) = \frac{2}{\pi} \int_0^{q_{\max}} F(q) \sin(qr) dq, \quad (2)$$

where q_{\max} is the upper bound of usable $S(q)$. To minimize the termination ripples in $D(r)$, q_{\max} is chosen at 21.5 \AA^{-1} (a zero for $[S(q) - 1]$).²² The $S(q)$ below 0.1 \AA^{-1} was obtained by interpolating the function $F(q)$ to $q = 0$. Other than truncation at q_{\max} (equivalent to multiplying $F(q)$ by a box function of unit height in eq. 2), no other modification function was applied.

The total PDF $T(r)$ is calculated by:¹⁴

$$T(r) = 4\pi n_a r + D(r), \quad (3)$$

where n_a is the atomic density (atoms/ \AA^3). n_a is calculated from the bulk density ρ (g/cm^3)⁷ using $n_a = n_0 \rho N_A / M$, where n_0 is the number of atoms per molecule, N_A is Avogadro's number, and M is the molecular weight. A peak in $T(r)$ corresponds to a particular atomic pair correlation and can be fitted using standard procedures to yield the corresponding bond length, coordination number, and the Debye-Waller factor.^{23,24}

Magic Angle Spinning (MAS) NMR experiments were performed on a 9.4 T Bruker HD AVANCE III spectrometer with Larmor frequency of 100.63 MHz for ^{13}C nuclei in the

Biopharmaceutical NMR Laboratory (BNL) in in Pharmaceutical Sciences at Merck & Co, Inc. (West Point, PA 18914, United States). A Bruker triple-resonance 4 mm H/F/X MAS probe tuned to ^1H and ^{13}C double-resonance mode was used for all experiments. A BCU unit was used to control the sample temperature. The typical 90° pulse length was $2.5\ \mu\text{s}$ on ^1H channel and $3.0\ \mu\text{s}$ on ^{13}C channels. All experiments were conducted at a MAS frequency of 12 kHz. In the 1D ^1H - ^{13}C cross-polarization (CP) MAS experiments, the contact time for ramped CP transfer was 2 ms and the recycle delay time was 100 s. The T_1 relaxation times of carbon atoms used for all experiments were measured using saturation recovery and were analyzed using Bruker TopSpin software. All ^{13}C spectra were referenced to tetramethylsilane (TMS) as external reference.

The spectra of crystalline D-mannitol were collected using both natural-abundance and ^{13}C labeled materials. The crystalline powder was filled in a customized fluoride polymer tube and inserted in NMR rotor (4 mm O.D.). After data collection, the crystalline powder (β polymorph) was melted and annealed at room temperature to crystallize into the α polymorph. The spectrum of the α polymorph was then collected under the same condition. The HDA of D-mannitol was prepared by melting a crystalline powder in the fluoride polymer tube and quenching it in an ethanol/dry ice bath. The quenched sample was quickly inserted into the NMR rotor and maintained at 270 K in the MAS probe. The ^{13}C CP MAS spectrum was collected at 270 K. Afterwards, the temperature was raised to 298 K for 10 min to allow transformation to the second amorphous phase (LDA) and the temperature was returned to 270 K for data collection. Signals of crystalline D-mannitol (α polymorph) were observed during measurement and removed by subtracting a scaled spectrum of pure α D-mannitol produced after complete crystallization of the sample in the rotor.

High-rate Flash Differential Scanning Calorimetry (FDSC) was performed with a Mettler Toledo Flash DSC(Flash DSC2, Columbus, OH, USA)) with chip sensor (UFS1). A tiny piece of D-mannitol crystal (1 μg) was placed on the chip center. Before isotherm, the sample was heated to 458 K, held for 2 s for complete melting and cooled to the experimental temperature with 1000 K/s cooling rate. During the isotherm, the acquisition frequency ranged from 1 Hz to 100 Hz, depending on the transformation time. The calibration of each chip was performed by the manufacturer and further validated against the melting point of D-mannitol.

7.4 Results

7.4.1 X-Ray Scattering.

Figure 7.1a shows the coherent X-ray scattering intensity $I(q)$ of D-mannitol's two amorphous phases. The HDA was obtained by cooling molten D-mannitol at approximately 20 K/s to 273 K, forming a glass ($T_g = 285$ K), and the LDA was obtained by heating the glass above the T_g .^{6,7} $I(q)$ has been measured over a wide q range ($0.1 - 25 \text{ \AA}^{-1}$) for accurate determination of the PDF¹⁴ and normalized on the atom-averaged self-scattering power $\langle f^2 \rangle$. Fig. 7.1b provides an enlarged view of the low q region to highlight the differences between HDA and LDA and the transformation process. The HDA shows a prominent peak (“main peak”) at 1.4 \AA^{-1} , as well as a broad feature near 0.95 \AA^{-1} . Upon transformation to the LDA, the main peak shifts to lower q , consistent with a decrease of density⁷ and an increase of the average molecular spacing. Meanwhile new features emerge at $q = 0.24, 0.66, 1.09 \text{ \AA}^{-1}$ and the broad peak of HDA at 0.95 \AA^{-1} decreases. This indicates that the LDA has more “structure” than the HDA. Despite the increased structural order, the LDA's scattering peaks are significantly broader than those of the crystalline phase (produced by heating the LDA *in situ*), confirming its amorphous nature. The *in situ* crystallized material is the α polymorph (see the reference patterns at the bottom of Figure 7.1b). It is significant that none of the D-mannitol crystalline phases exhibits the low q peak at 0.24 \AA^{-1} . This indicates that the LDA is not the nanocrystalline form of the known polymorphs. The low q scattering peak corresponds to a structural order in the real space with a periodicity of $2\pi/q = 3 \text{ nm}$. This length scale greatly exceeds the molecular size ($\sim 1 \text{ nm}$), indicating enhanced supramolecular organization in the LDA.

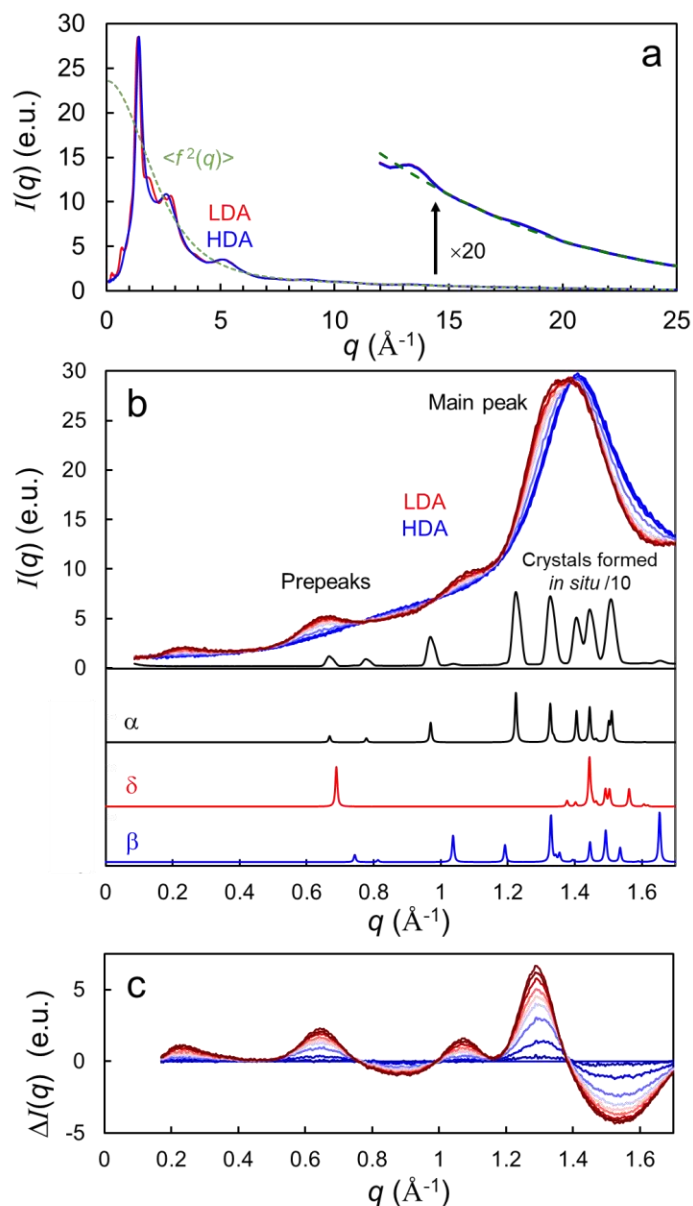


Fig. 7.1 (a) Coherent X-ray scattering intensities $I(q)$ of D-mannitol's two amorphous phases, LDA (275 K) and HDA (298 K). $\langle f^2 \rangle$ is the self-scattering power of an average atom (dashed curve). (b) The low q region of $I(q)$ showing the main peak and the prepeaks. The HDA \rightarrow LDA transition was measured by heating from 275 K to 296 K in 2 K steps. The *in situ* crystallization upon heating the LDA yielded the α polymorph (measured at 313 K) which shows sharp Bragg peaks. The diffraction patterns of D-mannitol's crystal polymorphs are shown at bottom: δ (CSD refcode DMANTL12), β (DMANTL07), α (DMANTL01). (c) Differential $I(q)$ to highlight the temperature effect on $I(q)$.

As q approaches zero, $I(q)$ should approach the compressibility limit: $I(0) = k_B T n \kappa \langle Z \rangle^2$, where n is the atomic number density, κ the compressibility, and $\langle Z \rangle$ the average number of electrons per atom (appropriate for our atom-based normalization of $I(q)$). Taking $n = 0.122 \text{ \AA}^{-3}$ for HDA and 0.120 \AA^{-3} for LDA,⁷ $\kappa = 7.5 \times 10^{-11} \text{ Pa}^{-1}$ (the value for D-sorbitol, an isomer of D-mannitol),²⁵ and $\langle Z \rangle = 3.8$, we obtain $I(0) \approx 0.5 \text{ e.u.}$ for the temperature range investigated. This is consistent with our experimental results.

Previous work has observed that the HDA-to-LDA transition has a two-state kinetics⁷ and this behavior is also seen for the new SAXS peaks reported here. Figure 7.1b shows that the low q peaks grow simultaneously and in proportion to each other. This is shown more clearly in Figure 7.1c where the difference is calculated between the $I(q)$ of an arbitrary temperature and that at 283 K, the last temperature before the transition to LDA commences. Note the simultaneous and proportional rise and fall of the scattering intensity in the different regions. These different regions are separated by a series of stationary (isosbestic) points located at $q = 0.45, 0.77, 0.99, 1.39$, and 1.75 \AA^{-1} , another indicator of the two-state kinetics. The two-state kinetics supports the notion that the transition to the LDA occurs by a nucleation and growth process.

Fig. 7.2a shows the X-ray weighted structure factors $S(q)$ of D-mannitol's HDA and LDA. This function is used to accentuate the structural differences between the two amorphous phases. Note the nearly identical patterns for the HDA and the LDA for $q > 6 \text{ \AA}^{-1}$. In this region, scattering is dominated by intramolecular correlations between atoms whose positions are well defined by covalent bonds. This is expected since the two amorphous phases are composed of identical molecules. At lower q , we note significant differences between the two phases already described above. Fig. 7.2b shows the differential PDF $D(r)$ obtained by the Fourier transform of the structure factor (eq. 2). As we discuss below, the sharp peaks at short distances ($r < 2.5 \text{ \AA}$) correspond to intramolecular distances, while the broad ripples at long distances to intermolecular correlations. The digital records of $S(q)$ and $D(r)$ are found in the Supporting Information.

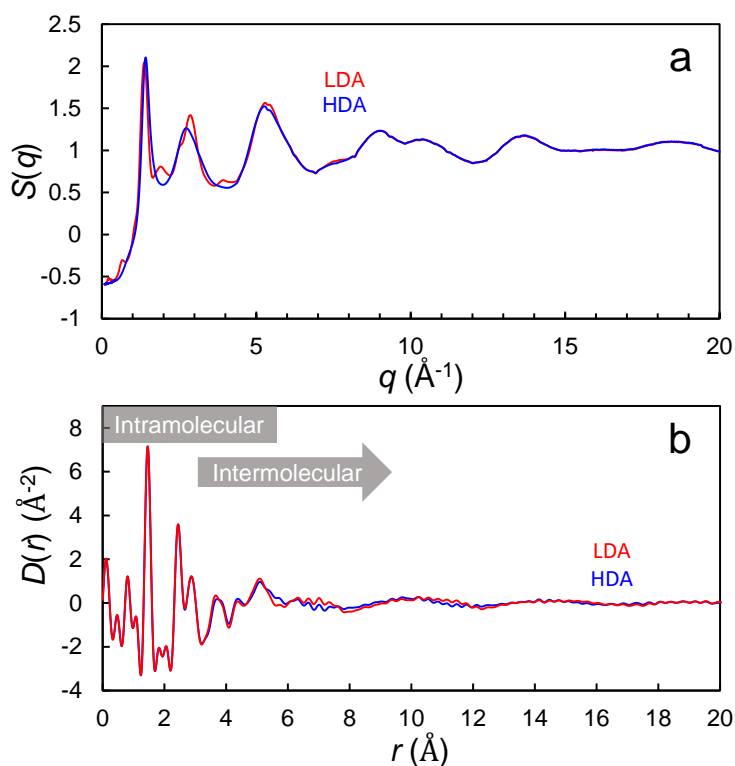


Fig. 7.2 (a) Structure factors $S(q)$ of D-mannitol's LDA (275 K) and HDA (298 K). (b) Differential PDF $D(r)$ s of the two phases.

7.4.2 Kinetics of Transformation.

Given the new observation of the SAXS of the LDA, we report the kinetics of D-mannitol's polyamorphic transition using the evolution of low-angle peaks and relate them to the kinetics observed using FDSC for constructing the TTT curve.

Figure 7.3 shows the transformation kinetics monitored by X-ray scattering, either as a function of temperature (a) or as a function of time at 285 K (b). The value of the fraction was obtained as the scaling factor to match the differential $I(q)$ at a specific temperature or time point with that of 100 % LDA (Figure 7.1c). From Figure 7.3a, we see the onset temperature is approximately 285 K, the T_g of the normal liquid of D-mannitol. From Figure 7.3b, we see the isothermal

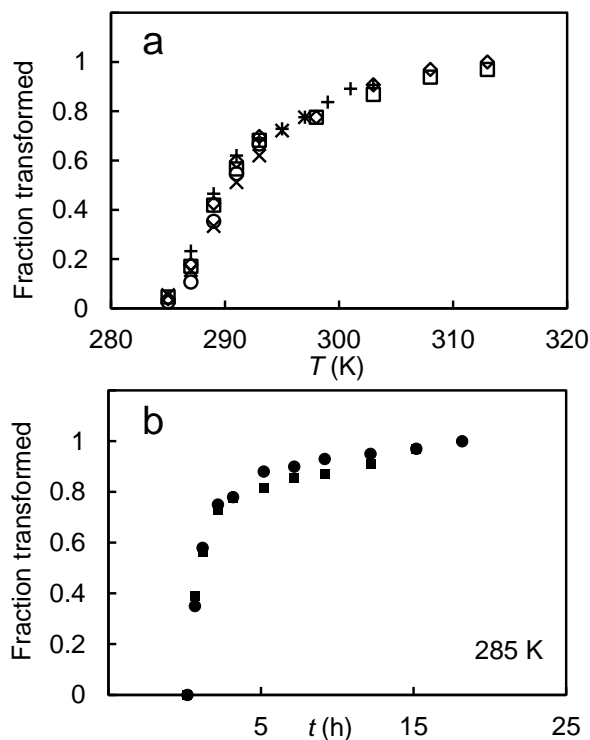


Fig. 7.3. Transformation kinetics monitored by X-ray scattering as a function of temperature (a) and as a function of time at 285 K (b).

transformation is initially fast and slows down over time, consistent with a nucleation and growth mechanism.

Figure 7.4 illustrates the measurement of the isothermal transformation kinetics by FDSC for $T = 316$ K. FDSC was able to follow fast transformations for which our X-ray experiment was unable to. A melt was cooled at a fast rate of 1000 K/s to 316 K and held at that temperature while recording the heat flow. The heat flow shows a well-defined symmetrical peak. The time for the peak (6 s in this case) is taken to be $t_{0.5}$. Integration of the peak yields the enthalpy change as a function of time. This enthalpy profile is well described by the Avrami model assuming a nucleation and growth process in a 3D sample. The data are inconsistent with a spinodal

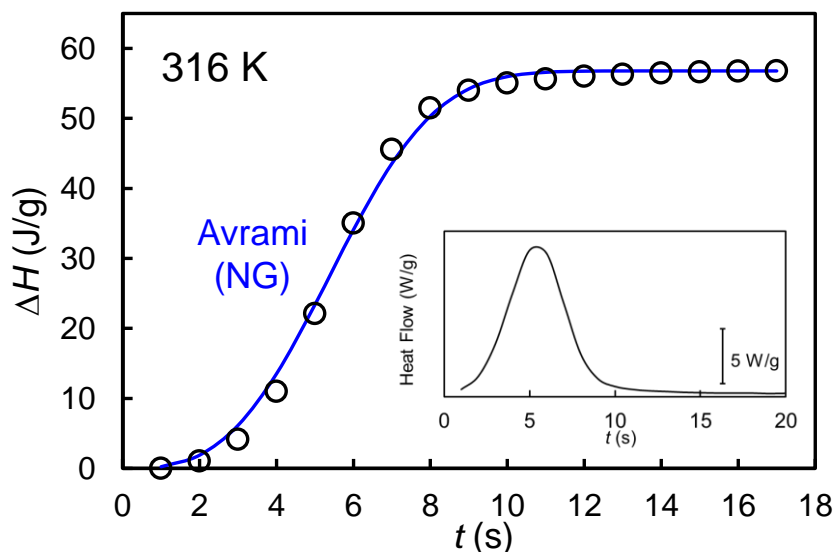


Fig. 7.4. Isothermal transformation kinetics at 316 K monitored by FDSC. The enthalpy change is obtained by integrating the heat flow data in the inset. The HDL was formed by quenching at 1000 K/s. The curve is the Avrami fit of the data assuming a nucleation and growth process in a 3D sample.

decomposition process, which predicts an exponential increase of enthalpy without the rapidly established plateau.

Figure 7.5 shows the TTT curve for the HDA-LDA transition, where the halftime of transition $t_{0.5}$ is plotted against temperature. The TTT curve has a U shape and terminates at the LDA-to-HDA transition temperature (333 K, vertical line). The curve is constructed using data from many kinds of measurements, including X-ray scattering (Figure 7.3 and Ref. 7), SDSC,⁶ NIR,⁷ and FDSC (Figure 7.4). Each point in the TTT curve was obtained by cooling a melt to a temperature of interest and measuring the $t_{0.5}$ of the transformation. The results from the different measurements are in good agreement. It is noteworthy that in these measurements, the sample amounts were very different from tens of milligrams (X-ray scattering) to milligrams (SDSC), and to tens of nanograms (FDSC). Within the FDSC measurements, the sample amounts ranged from 50 to 1000 nanograms. Furthermore, some samples had no exposed free surfaces (X-ray scattering, most SDSC runs), while others did (FDSC). The fact that all these experiments yielded a consistent TTT curve indicates that the transition measured is an intrinsic, volumetric process. The fact that a change of sample mass by orders of magnitude argues that the process had extremely high nucleation rate; otherwise, the nanoscopic samples would show a highly stochastic behavior.

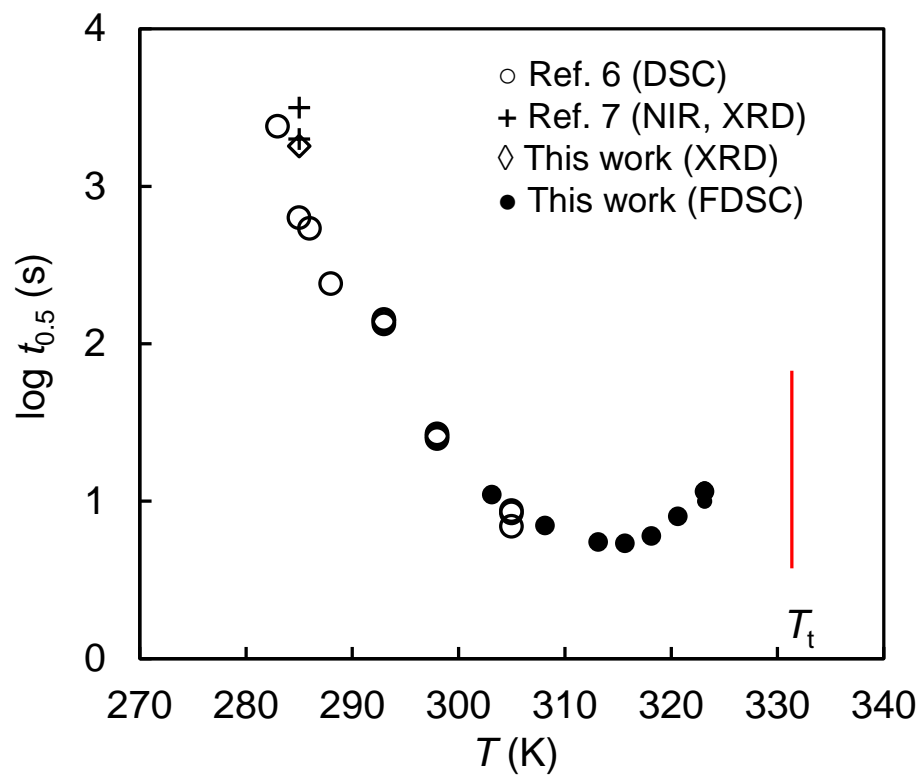


Fig. 7.5. TTT curves for the LDA transition and crystallization. The vertical line indicates the LDA-to-HDA transition temperature at which the TTT curve terminates.

7.4.3 ssNMR.

Fig. 7.6a shows the spectra of 1,6 ^{13}C labelled and 2,5 ^{13}C labelled D-mannitol in its HDA and LDA phases, as well as the natural abundance ^{13}C spectra of three polymorphs (α , β , and δ) of D-mannitol. The spectrum of the δ polymorph is from Ref. ²⁶ and the others from this work; the chemical shifts are summarized in Table 1.^{26,27} While the 3 polymorphs all have different spectra, their difference is best revealed by the spectra of the terminal carbons (1 and 6). For this reason, we used the 1,6- ^{13}C labelled D-mannitol to investigate the chemical environment in the HDA and the LDA and whether the environment has any resemblance to that in the crystal polymorphs. As shown in Fig. 7.6a, the two terminal carbons in δ D-mannitol show a single, unresolved peak, indicating nearly identical chemical environments, but in the other polymorphs, the terminal carbons show two resolved peaks, indicating different chemical environments. Furthermore, the chemical shifts of the terminal carbons correlate with the strength of HBs formed by the terminal OH groups,^{26, 27} as measured by the HO...O distances available from single-crystal diffraction.^{43,28,29} As Fig. 7.6b shows, the terminal OH groups in the δ polymorph form the strongest HBs, with the shortest R_{OO} , and the corresponding terminal carbons have the largest chemical shifts. From the δ polymorph to β and α , HBs weaken (R_{OO} lengthen) and the chemical shifts of the terminal carbons decrease.⁴⁴

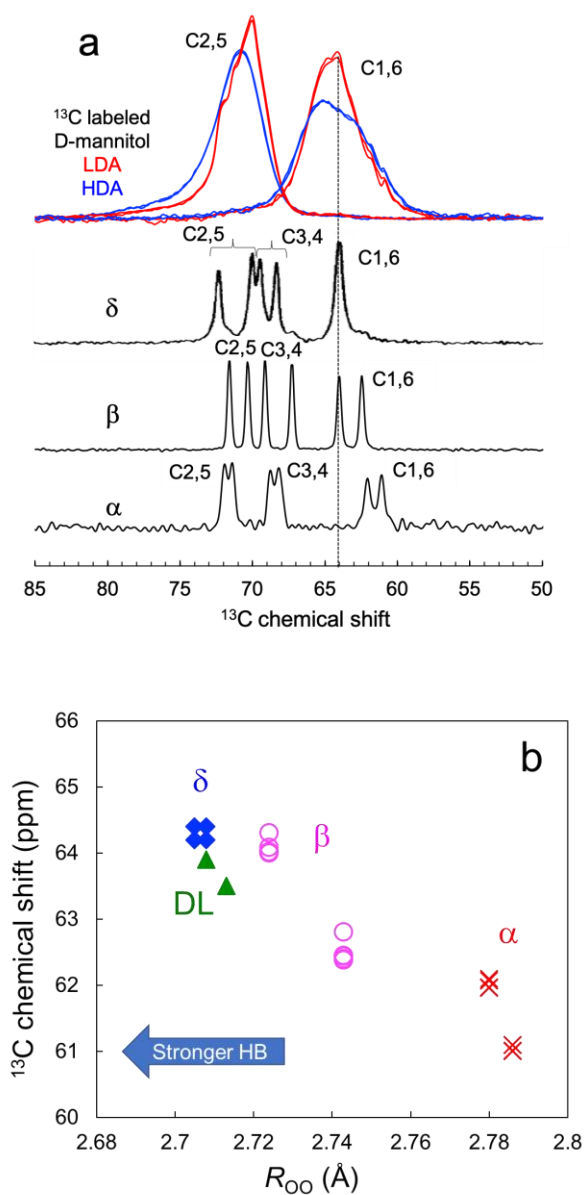


Fig. 7.6. (a) ^{13}C ssNMR spectra of HDA, LDA and three polymorphs of D-mannitol. δ form is taken from Ref. 26. The polymorph designations follow Ref. 26. (b) Correlation between the chemical shift of C1,6 and the strength of HBs formed by the terminal OH. DL refers to DL-mannitol.²⁷ Each point represents an individual measurement. The crystal spectra are from Ref. 26, Copyright (2002), with permission from Elsevier.

Fig. 7.6a indicates that the spectra of both amorphous phases are much broader than those of the crystalline phases, as expected, since an amorphous phase contains a wide distribution of chemical environments for the probe nuclei. Note that the peak of the LDA is narrower than that of HDA, consistent with a more ordered structure.³⁰ The average chemical shifts of C1 and C6 in LDA (64.42 ppm) and the HDA (64.43 ppm) are similar and have the closest match with that of δ D-mannitol (vertical line), though the left peak of the β polymorph is also a good match and the right peak a modest match. The C1 and C6 peaks of the α polymorph are a poor match with the spectra of the amorphous phases. In comparison to the terminal carbons, the internal carbons C2 and C5 are less discriminating with respect to the different polymorphs. As a result of the HDA \rightarrow LDA transition, the LDA C1/C6 spectrum becomes sharper and the increase of intensity, at 64 ppm, matches the best with the peak of the δ polymorph. Given HBs are stronger in the δ polymorph, the increase of the δ -like structure is consistent with the observation that HBs are stronger in the LDA.⁷ The area added to the top of the HDA peak (and subtracted from its wings) is approximately 15 % of the total area and this is consistent with the conclusion based on NIR that the HDA \rightarrow LDA transition rearranges \sim 10 % HBs and with the enthalpy of transition.⁷

Table 7.1. ^{13}C chemical shift of D-mannitol polymorphs.

polymorph	C-1	C-2	C-3	C-4	C-5	C-6	Ref.
α	62.1	71.9	68.7	68.1	71.4	61.1	27
β	64.3	71.7	69.3	67.4	70.5	62.8	
δ	64.4	72.5	69.7	68.5	70.2	64.4	
α	62.0	71.9	68.8	68.2	71.3	61.0	This work
β	64.0	71.6	69.1	67.3	70.3	62.4	

Note: Data in reference 27 and this work were collected on 200 MHz and 400 MHz ssNMR spectrometers, respectively.

7.5 Discussion

Previous work on liquid alcohols has shown that the main scattering peak arises from the correlation between the non-polar hydrocarbon groups (CH₂ and CH₃) and tracks the change of the bulk density, whereas the prepeak from the O...O correlation maintained by hydrogen bonds and the resulting supramolecular structure.^{31,32,33} For the polyalcohol glycerol, molecular simulations have shown that the main peak arises mainly from the intermolecular C...C correlations,^{34,35,36,37} and we give the same origin to D-mannitol's main peak. While the polyalcohols do not exhibit strong prepeaks, Chen et al. have shown that their X-ray scattering can be still analyzed in real space and in reciprocal space to access these two aspects of structure.¹³ Here we follow the same approach and present the structural change associated with the main peak and the prepeaks.

7.5.1 Structure Associated with the Main Peak: C...C Correlation.

Fig. 7.4 shows how the position of the main peak q_1 evolves during the HDA→LDA transition. To obtain q_1 , the peak was fitted using a standard function. For the HDA, the function was:³⁸

$$S(q) = \frac{a_0[2q_{corr}q_0 \cos \theta + (q_{corr}^2 - q_0^2 + q^2) \sin \theta]}{[q_{corr}^2 + (q - q_0)^2][q_{corr}^2 + (q + q_0)^2]} \quad (1)$$

This function is the Fourier sine transform of an exponentially damped sinusoidal density wave, often used to describe the structure of simple liquids,³⁹ where a_0 characterizes the amplitude of oscillation, q_0 is the spatial frequency ($L_0 = 2\pi/q_0$ is the wavelength of density modulation), q_{corr} is the inverse correlation length, and θ is the phase. For the LDA, the function was

$$S(q) = a_0 \frac{\sqrt{\pi}}{4q_{corrG}} \left(e^{-\frac{(q-q_0)^2}{4q_{corrG}^2}} - e^{-\frac{(q+q_0)^2}{4q_{corrG}^2}} \right) / q \quad (2)$$

This function is the Fourier sine transform of a Gaussian-damped sinusoidal density wave where the parameters have the same physical meaning.

Fig. 7.7a shows the main peaks are well fitted by these functions and it is noteworthy that the conventional function (eq. 1) does not provide a satisfactory fit of the LDA main peak. Figure 7.7b shows that the position of the main peak q_1 evolves as a function of temperature during the HDA→LDA transition. For reference, the data are shown for D-sorbitol, an isomer of D-mannitol, which does not undergo a polyamorphic transition. For D-sorbitol, a normal evolution of q_1 is observed: with heating, q_1 gradually decreases, corresponding to an increase of the average C...C spacing; the rate of decrease is faster above the glass transition temperature (275 K) than below, reflecting the greater thermal expansion coefficient (TEC) of the liquid phase. The normal glass of D-mannitol shows a similar thermal expansion behavior as the D-sorbitol glass, but upon transitioning to the LDA phase, q_1 drops very rapidly and the temperature slope is significantly steeper than that for the D-sorbitol liquid. This anomalous behavior is a consequence of the volume expansion associated with the phase transition. Even the transition is from a liquid phase to a solid phase,⁷ the volume expansion makes the apparent TEC larger than the typical liquid-state TEC.

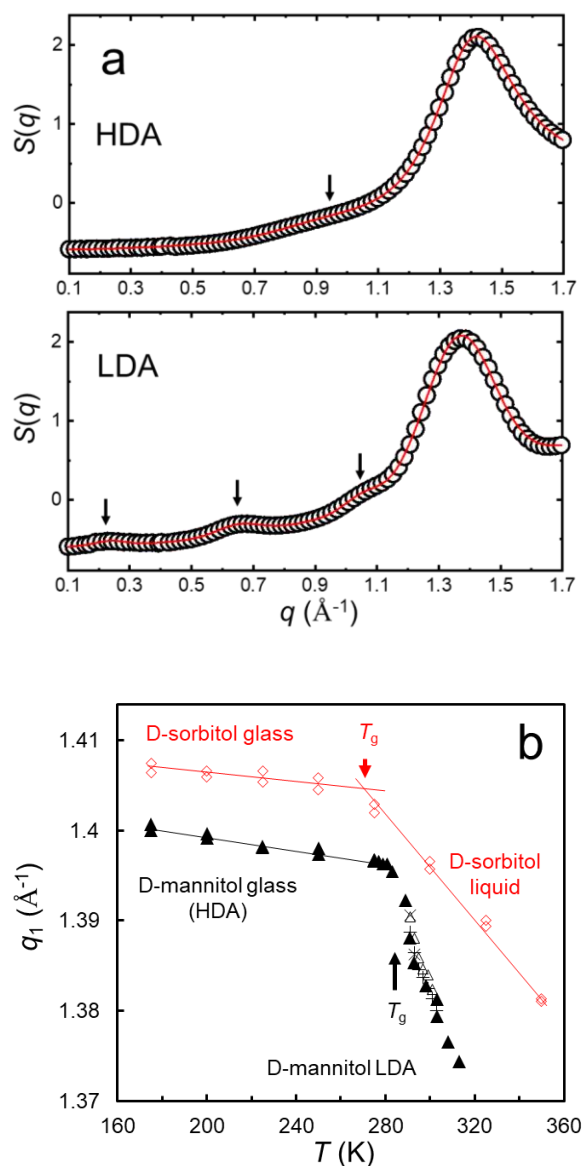


Fig. 7.7. (a) Fitting of the main peak of the HDA and the LDA. (b) Evolution of the main peak position during the HDA \rightarrow LDA transition in D-mannitol. Data are also shown for D-sorbitol,

A common feature for many liquids and glasses is a main scattering peak, which in real space corresponds to an extended density modulation beyond the molecular size (ripples in the PDF). These ripples often have the form of exponentially damped sine wave in the function $D(r)$,^{39, 38, 40}

or equivalently, the main scattering peak has the Lorentzian form (eq. 1).^{38,41} These regularities are observed with the HDA of D-mannitol and with the liquids and glasses of its isomers dulcitol and D-sorbitol, for which no polymorphism has been observed. Density modulation in all these systems has a similar wavelength (~ 4.5 Å) and has the form of exponentially damped sine in $D(r)$ with similar persistence length (~ 7 Å). In this sense, the HDA is a “normal” liquid. On the other hand, the LDA of D-mannitol exhibits local density modulation of a different character: the waveform is a Gaussian damped sine wave and the persistence length is longer. In this sense, the LDA is not a “normal” liquid. Ryu et al. reported different peak shapes for the FSDPs of metallic liquids (Lorentzian and Gaussian) and regarded the Lorentzian profile as representative of “normal” liquid structures.⁴² Despite its exotic features, the LDA of D-mannitol is an amorphous structure that is better understood as a liquid with enhanced order. Its density modulation with a single dominant wavelength L_0 is a hallmark of liquids as opposed to crystals with packing regularity in multiple length scales.

7.5.2 Hydrogen Bond Network.

Having investigated the structure associated with the main scattering peak, we now turn to the structure associated with the HBs. We will first consider the nearest-neighbor structure with the aid of the PDFs and then investigate the longer-range structure using the prepeaks. Fig. 7.8a shows the total PDF $T(r)$. The atomic densities needed for calculating $T(r)$ are obtained from Ref. ⁴³ for the α polymorph and Ref. 7 for HDA and LDA. Note the close match of these functions below 2.6 Å, indicating that the three phases have identical covalent bond lengths and angles. The 1.45 Å peak corresponds to the covalent bonds C-C and C-O (unresolved in the PDF); in the crystals of D-mannitol, these bonds have the average lengths of 1.53 Å and 1.43 Å, respectively,⁴⁴ which are

too close to be resolved by our measurements. The peak at 2.4 Å corresponds to the intramolecular “1-3 distances”; that is, the distances between the atoms across two consecutive covalent bonds. The 1-3 distance is also expected to be nearly invariant due to the constancy of covalent bond lengths and angles. The first significant difference between the $T(r)$ curves occurs near 2.8 Å. In this region are found the O...O distances in intermolecular HBs seen in the crystal structure, with $R_{OO} = 2.74$ Å on average in the α polymorph.^{43,44} The higher intensity of the crystal $T(r)$ indicates a higher number of HBs in the crystal per OH group, whereas the similar intensities of the HDA and LDA peaks indicate a similar number of HBs in these two amorphous phases.

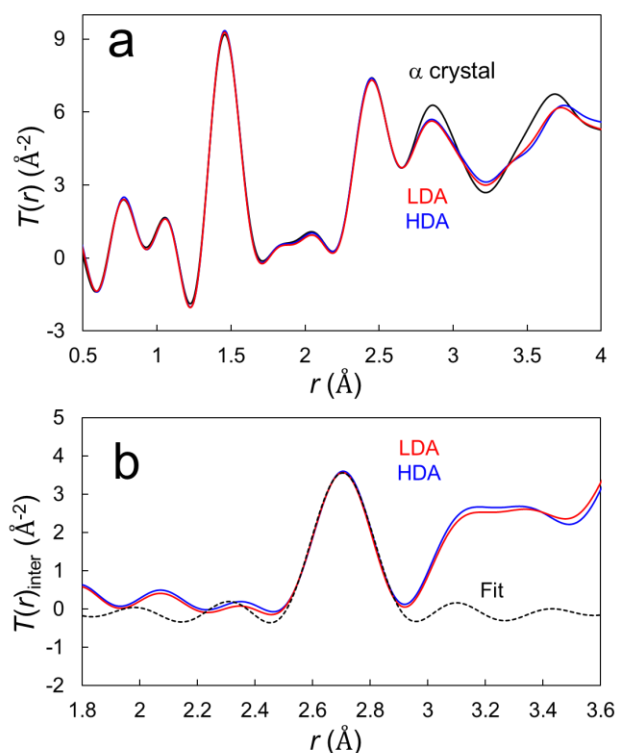


Fig. 7.8. (a) Total PDF $T(r)$ of D-mannitol’s α polymorph (black), HDA (blue) and LDA (red).

(b) Intermolecular PDF $T(r)_{\text{inter}}$ of the three phases showing isolated O...O correlation in HBs.

The dotted curve is the fit of the O...O correlation peak, yielding with $n_{\text{HB}} = 1.8$ per OH for the two amorphous phases.

To quantify the number of HBs in each phase, we remove the intramolecular contribution to $T(r)$ to isolate the intermolecular HB peak: $T(r)_{\text{inter}} = T(r) - T(r)_{\text{intra}}$, where $T(r)_{\text{intra}}$ is calculated from the known molecular structure in the crystal⁴³ using the program DiffPy-CMI.⁴⁵ Fig. 7.8b shows the results for HDA and LDA. In this calculation, the displacement factor $U_{\text{iso}} = 0.003 \text{ \AA}^{-2}$ is used so that the subtraction removes cleanly the intramolecular correlation at 2.4 \AA , isolating the intermolecular O...O correlation. This peak is then fitted using the program NXFit (dotted curve).²³ For the α polymorph, we recover the known number of HBs per OH, $n_{\text{HB}} = 2$, in the crystal structure.⁴³ In the crystal, each OH forms 2 HBs, serving as donor once and acceptor once. For the amorphous phases, we obtain $n_{\text{HB}} = 1.8$ HBs; that is, each OH group forms $\sim 10\%$ fewer HBs in the amorphous phases than in the α crystal. This difference can be ascribed to the existence of hydrogen-bonded clusters in the amorphous phases, in contrast to the infinite hydrogen-bonded network in the crystal.

The similar number of HBs per OH in D-mannitol's amorphous phases indicates that they have a similar structure in terms of the nearest O...O neighbors (the *first* coordination shell). Given that vibrational spectroscopy shows a strengthening of HBs after the HDA \rightarrow LDA transition,^{6,7} we expect changes in the HB network. We observe these changes in the *second* coordination shell. To highlight the difference between LDA and HDA, we show in Fig. 7.9 the difference between their $D(r)$. The $\Delta D(r)$ is featureless until about 2.8 \AA : we observe small positive peaks at 2.6 and 2.9 \AA and a negative peak at 3.1 \AA . These features are small but reproducible, as indicated by the two independent measurements overlain in Fig. 7.9. We attribute these features to very subtle rearrangement of the nearest O...O neighbors, visible only after magnification. The first prominent feature in the $\Delta D(r)$ trace is a positive peak at 3.6 \AA followed by a negative peak at 4.0 \AA . These

features are attributed to the rearrangement of O...O correlations in the second coordination shell (R_2 in the schematic in Fig. 7.9). In the schematic, drawn based on the crystal structures of D-mannitol⁴⁴ and the liquid structures of water and methanol,^{46,47} R_1 is the nearest-neighbor O...O distance in a HB (~ 2.8 Å), R_{1p} the nearest-neighbor O...O distance in a poor HB or non-HB (~ 3.1 Å), and R_2 the second-nearest-neighbor O...O distance in a HB (3.5-4.5 Å) based on D-mannitol crystals⁴⁴. Thus, we attribute the positive peak at 3.6 Å and the negative peak at 4.0 Å to a rearrangement in the second coordination shell where O atoms move closer, from 4.0 Å apart to 3.6 Å apart. To test this, we simulated the effect of this reorganization in the second coordination shell on the $\Delta D(r)$ function using the program NXFit.²³ The red curve in Fig. 7.9 shows the expected change when for every tagged O atom, 0.23 of its second nearest neighbors makes the specified change. This change is consistent with the previous report that approximately 10% of the HBs are rearranged by the HDA to LDA transition.⁷ The calculated effect matches very well the observed features, supporting our hypothesis.

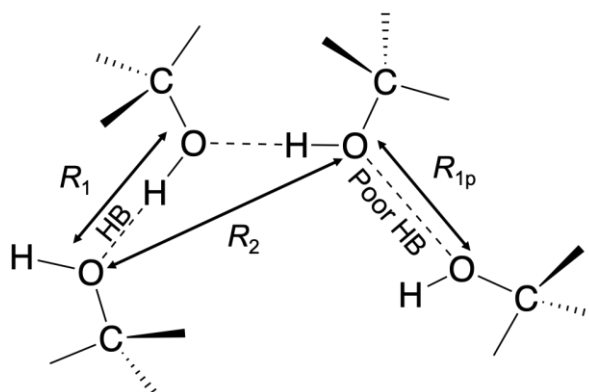
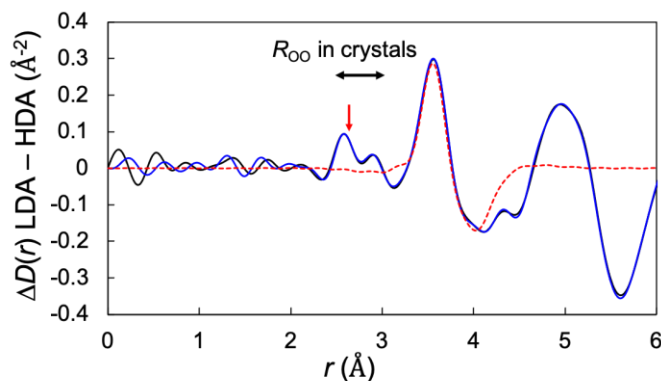


Fig. 7.9. $\Delta D(r)$ between LDA and HDA. Two data sets are shown to indicate noise level and reproducible features. The double-sided arrow indicates the range of R_{OO} (O...O distance in HBs). The down arrow indicates a short R_{OO} (2.65 Å) in the δ polymorph.⁴⁴ The drawing at bottom indicates characteristic distances in the HB network.⁴⁴ R_1 is the nearest-neighbor O...O distance; R_2 is the second nearest-neighbor O...O distance.

We have just characterized the short-range structure of the HB network up to approximately 5 Å with the aid of the PDFs. We now investigate the longer-range structure in reference to the prepeaks (Figure 7.1b) that emerge during the HDA \rightarrow LDA transition. The prepeaks at 0.24 and 0.66, and 1.09 Å⁻¹ correspond to real-space periodicities of 26, 9.5, and 5.9 Å, respectively. These peaks are significantly sharper than the main peak by approximately a factor of 2. This indicates

that the corresponding structure extends farther in space and supports the notion that these prepeaks characterize a different aspect of structure from the main peak. Based on previous work, we assign these prepeaks to the O...O correlations associated with the HBs. Based on X-ray scattering and ssNMR, we further attribute the 0.66 \AA^{-1} peak to the enhanced smectic-like order in the LDA. As shown in Figure 7.10, in the δ polymorph of D-mannitol, the molecules form smectic layers. In each layer, the molecules are parallel to each other and perpendicular to the layer. In the δ polymorph, the layer spacing is 9.1 \AA at 100 K, producing a low q diffraction peak at 0.69 \AA^{-1} (Figure 7.1b bottom). D-mannitol is a rod-like molecule with an extended carbon chain. The extended-chain conformation of D-mannitol is robust since all known polymorphs have this conformation and the same conformation is observed in solutions by NMR.⁴⁸ We speculate that the HDA \rightarrow LDA transition leads to the formation of the smectic-like structure, such as the one in Figure 7.10. In an amorphous phase, the 9.1 \AA spacing in the δ polymorph at 100 K is expected to increase because of reduced density and increased disorder. Although the word “smectic” suggests a highly ordered liquid crystal, the proposed smectic order in the LDA is extremely weak: its correlation length estimated from the width of the scattering peak at 0.66 \AA^{-1} is 28 \AA , approximately 3 molecular layers, in contrast to the much longer correlation in true liquid crystals (10^2 to 10^3 layers).⁴⁹ That is, the LDA is predominantly amorphous with modestly enhanced mesoscopic order. We regard the prepeak at 1.09 \AA^{-1} (Figure 7.1b), with a real-space periodicity

of 5.9 Å, as part of the enhanced mesoscopic order, perhaps related to distances within the layers, because this order grows simultaneously with the smectic order discussed above.

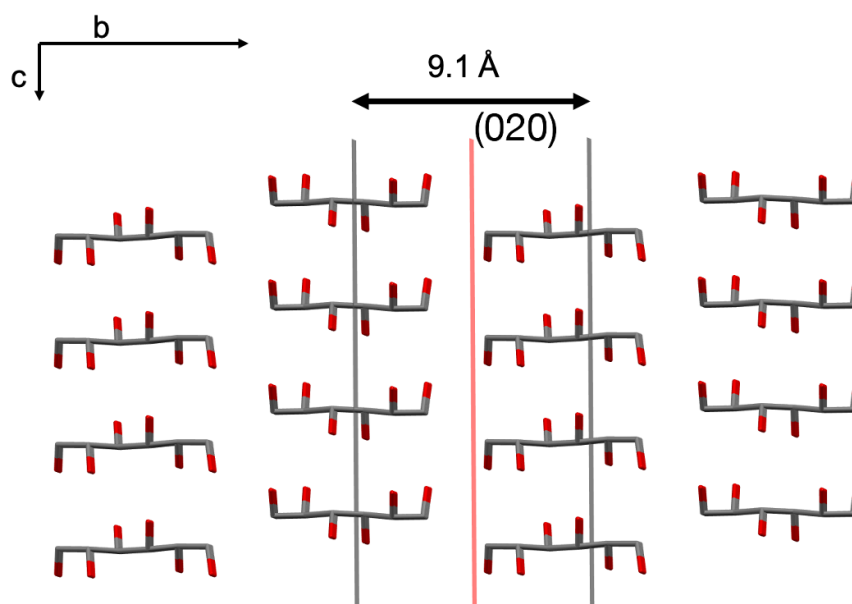


Fig. 7.10. Smectic like layers in the δ polymorph D-mannitol (CSD code: DMANTL10).⁴⁴ The layer thickness of (020) plane is 9.1 Å at 100 K.

Finally, we discuss the prepeak at $q = 0.24 \text{ \AA}^{-1}$. Whereas the other prepeaks can be assigned counterparts, this prepeak cannot (Figure 7.1b). This argues against the LDA being a nanocrystalline version of the known polymorphs. The real-space periodicity that corresponds to this peak, 26 Å, far exceeds the molecular dimension. We attribute this peak to supramolecular clusters created by the polyamorphic transition. Given the nucleation and growth mechanism for the transition, the 26 Å periodicity could be a consequence of a high nucleation rate of the LDA in the HDA. Because the transition occurs in a highly viscous medium, the creation of low-density domains in a previously high density liquid could result in a nanoscale spatial variation of density.

It is interesting to note that in the case of triphenyl phosphite (TPP), the transformation to the second amorphous phase is also accompanied by the creation of mesoscopic order with a 3 nm periodicity, although TPP is unable to form HBs.⁵⁰

7.6 Conclusions

The structural difference of two amorphous phases of D-mannitol has been studied by synchrotron X-ray scattering and ssNMR. The two amorphous phases have the same intramolecular structure, but different intermolecular correlations. The HDA \rightarrow LDA transition causes the non-polar hydrocarbon groups to be farther apart from each other and reorganizes the HB network. The reorganization of the HB network happens in the second coordination shell and beyond and creates long-propagating mesoscopic order that manifests itself as low q peaks in the scattering pattern. Some of the prepeaks can be associated with the smectic-like layers seen in the crystalline phase, but the lowest-angle scattering at 0.24 \AA^{-1} has no crystalline counterpart and reveals a novel mesoscopic order associated with hydrogen-bonded clusters. This mesoscopic order could be a result of the high nucleation rate of the LDA in the HDA, creating nanoscale spatial modulation of density. The structure factors and the ssNMR spectra reported here provide constraints for Reverse Monte Carlo (RMC) simulations to extract the PDFs for various atom-atom pairs. It is of interest to learn how the properties of an amorphous phase, such as crystal nucleation rate, is influenced by a polyamorphic transition.

7.7 Acknowledgements

We thank the National Science Foundation for supporting this work through the University of Wisconsin – Madison MRSEC (DMR-1720415). We thank Dr. Geoff Rojas and Dr. Ilia Guzei for their help on X-ray scattering experiments.

7.8 References

-
- ¹ Tanaka, Hajime. Liquid–liquid transition and polyamorphism. *J. Chem. Phys.* **2020**, *153*(13), 130901.
 - ² Mishima, O.; Calvert, L.; Whalley, E. ‘Melting Ice’ I at 77 K and 10 Kbar: A New Method of Making Amorphous Solids. *Nature* **1984**, *310* (5976), 393-395.
 - ³ Mishima, O.; Suzuki, Y. Propagation of The Polyamorphic Transition of Ice and The Liquid–Liquid Critical Point. *Nature* **2002**, *419* (6907), 599-603.
 - ⁴ Cohen, I.; Ha, A.; Zhao, X.; Lee, M.; Fischer, T.; Strouse, M.; Kivelson, D. A Low-Temperature Amorphous Phase in A Fragile Glass-Forming Substance. *J. Phys. Chem.* **1996**, *100* (20), 8518-8526.
 - ⁵ Kobayashi, M.; Tanaka, H. The Reversibility and First-Order Nature of Liquid–Liquid Transition in A Molecular Liquid. *Nat. Commun.* **2016**, *7* (1), 1-8.
 - ⁶ Zhu, M.; Wang, J.; Perepezko, J.; Yu, L. Possible Existence of Two Amorphous Phases of D-Mannitol Related by A First-Order Transition. *J. Chem. Phys.* **2015**, *142* (24), 244504.
 - ⁷ Zhu, M.; Yu, L. Polyamorphism of D-Mannitol. *J. Chem. Phys.* **2017**, *146* (24), 244503.
 - ⁸ Tang, W.; Perepezko, J. Polyamorphism and Liquid-Liquid Transformations in D-Mannitol. *J. Chem. Phys.* **2018**, *149* (7), 074505.
 - ⁹ Angell, C. A., Postface–A Personal Retrospective. *Encyclopedia of Glass Science, Technology, History, and Culture* **2021**, *2*, 1457-1462
 - ¹⁰ Skinner, L.; Benmore, C.; Neufeind, J.; Parise, J. The Structure of Water Around the Compressibility Minimum. *J. Chem. Phys.* **2014**, *141* (21), 214507.

-
- ¹¹ Narten, A.; Habenschuss, A. Hydrogen Bonding in Liquid Methanol and Ethanol Determined by X-Ray Diffraction. *J. Chem. Phys.* **1984**, *80* (7), 3387-3391.
- ¹² Takamuku, T.; Maruyama, H.; Kittaka, S.; Takahara, S.; Yamaguchi, T. Structure of Methanol Confined In MCM-41 Investigated by Large-Angle X-Ray Scattering Technique. *J. Phys. Chem. B* **2005**, *109* (2), 892-899.
- ¹³ Zhenxuan Chen, Chengbin Huang, Xin Yao, Chris J. Benmore, Lian Yu. Structure of supercooled glycerol, xylitol, and D-sorbitol by synchrotron X-ray scattering and relation to dynamic fragility. *J. Chem. Phys.* **2021**, *155*, 244508.
- ¹⁴ Benmore, C. J. X-Ray Diffraction from Glass. In *Modern Glass Characterization*, Affatigato, M., Ed.; 2015; pp 1-30.
- ¹⁵ Zhenxuan Chen, Chengbin Huang, Xin Yao, Chris J. Benmore, Lian Yu. Structure of supercooled glycerol, xylitol, and D-sorbitol by synchrotron X-ray scattering and relation to dynamic fragility. *J. Chem. Phys.* **2021**, *155*, 244508.
- ¹⁶ Phyto, P.; Zhao, X.; Templeton, A. C.; Xu, W.; Cheung, J. K.; Su, Y. Understanding molecular mechanisms of biologics drug delivery and stability from NMR spectroscopy. *Adv. Drug Deliv. Rev.* **2021**, *174*, 1-29.
- ¹⁷ de Lima Batista, A.; Miranda, M.; Martins, F.; Morilla Santos, C.; Sasaki, J. Synthesis of Cerium Oxide (CeO₂) By Co-Precipitation for Application as A Reference Material for X-Ray Powder Diffraction Peak Widths. *Powder Diffr.* **2018**, *33* (1), 21-25.
- ¹⁸ Jones, A.; Misell, D. A Practical Method for The Deconvolution of Experimental Curves. *Br. J. Appl. Phys.* **1967**, *18* (10), 1479-1483.
- ¹⁹ Leonard, G.; McCarthy, J.; Nurizzo, D.; Thibault, X. Technical Report: Automatic Experiments at The European Synchrotron Radiation Facility MX Beam-Lines. *Synchrotron Radiat. News* **2007**, *20* (3), 18-24.
- ²⁰ Hammersley, A.; Svensson, S.; Hanfland, M.; Fitch, A.; Hausermann, D. Two-Dimensional Detector Software: From Real Detector to Idealised Image or Two-Theta Scan. *High Pressure Res.* **1996**, *14* (4-6), 235-248.
- ²¹ Qiu, X.; Thompson, J.; Billinge, S. Pdfgetx2: A GUI-Driven Program to Obtain the Pair Distribution Function from X-Ray Powder Diffraction Data. *J. Appl. Crystallogr.* **2004**, *37* (4), 678-678.
- ²² Gaskell, P. Medium-Range Structure in Glasses and Low-Q Structure in Neutron and X-Ray Scattering Data. *J. Non-Cryst. Solids* **2005**, *351* (12-13), 1003-1013.
- ²³ Pickup, D.; Moss, R.; Newport, R. Nxfit: A Program for Simultaneously Fitting X-Ray and Neutron Diffraction Pair-Distribution Functions to Provide Optimized Structural Parameters. *J. Appl. Crystallogr.* **2014**, *47* (5), 1790-1796.

-
- ²⁴ Etherington, G.; Wright, A.; Wenzel, J.; Dore, J.; Clarke, J.; Sinclair, R. A Neutron Diffraction Study of The Structure of Evaporated Amorphous Germanium. *J. Non-Cryst. Solids* **1982**, *48* (2-3), 265-289.
- ²⁵ Naoki, M.; Ujita, K.; Kashima, S. Pressure-volume-temperature relations and configurational energy of liquid, crystal, and glasses of D-sorbitol. *J. Chem. Phys.* **1993**, *97*(47), 12356-12362.
- ²⁶ Yoshinari, T.; Forbes, R.; York, P.; Kawashima, Y. Moisture Induced Polymorphic Transition of Mannitol and Its Morphological Transformation. *Int. J. Pharm.* **2002**, *247* (1-2), 69-77.
- ²⁷ Grindley, T.; McKinnon, M.; Wasylshen, R. Towards Understanding ¹³C-N.M.R. Chemical Shifts of Carbohydrates in The Solid State. The Spectra Of D-Mannitol Polymorphs and Of DL-Mannitol. *Carbohydr. Res.* **1990**, *197*, 41-52.
- ²⁸ Botez, C.; Stephens, P.; Nunes, C.; Suryanarayanan, R. Crystal Structure of Anhydrous δ -D-Mannitol. *Powder Diffr.* **2003**, *18* (3), 214-218.
- ²⁹ Berman, H.; Jeffrey, G.; Rosenstein, R. The Crystal Structures of the α' and β Forms Of D-Mannitol. *Acta Crystallogr., Sect. B: Struct. Crystallogr. Cryst. Chem.* **1968**, *24* (3), 442-449.
- ³⁰ Su, Y.; Hong, M. Conformational Disorder of Membrane Peptides Investigated from Solid-State NMR Line Widths and Line Shapes. *J. Phys. Chem. B* **2011**, *115* (36), 10758-10767.
- ³¹ Stewart, G. W.; Morrow, R. M. X-ray diffraction in liquids: primary normal alcohols. *Phys. Rev.* **1927**, *30*(3), 232.
- ³² Pozar, M.; Bolle, J.; Sternemann, C.; Perera, A. On the X-ray scattering pre-peak of linear mono-ols and the related microstructure from computer simulations. *J. Chem. Phys. B* **2020**, *124*(38), 8358-8371.
- ³³ Cerar, J.; Jamnik, A.; Tomšič, M. Supra-molecular structure and rheological aspects of liquid terminal 1, n-diols from ethylene glycol, 1, 3-propandiol, 1, 4-butanediol to 1, 5-pentanediol. *J. Mol. Liq.* **2019**, *276*, 307-317.
- ³⁴ Root, L.; Stillinger, F. Short-Range Order in Glycerol. A Molecular Dynamics Study. *J. Chem. Phys.* **1989**, *90* (2), 1200-1208.
- ³⁵ Chelli, R.; Procacci, P.; Cardini, G.; Della Valle, R.; Califano, S. Glycerol Condensed Phases Part I. A Molecular Dynamics Study. *Phys. Chem. Chem. Phys.* **1999**, *1* (5), 871-877.
- ³⁶ Towey, J.; Soper, A.; Dougan, L. The Structure of Glycerol in The Liquid State: A Neutron Diffraction Study. *Phys. Chem. Chem. Phys.* **2011**, *13* (20), 9397.
- ³⁷ Root, L.; Berne, B. Effect of Pressure on Hydrogen Bonding in Glycerol: A Molecular Dynamics Investigation. *J. Chem. Phys.* **1997**, *107* (11), 4350-4357.

-
- ³⁸ Korsunsky, V.; Naberukhin, Y. An Analytical Method of Computation of Radial Distribution Functions At Large Distances for Liquids and Amorphous Substances. *Acta Crystallogr. Sect. A Cryst. Phys., Diffr., Theor. Gen. Crystallogr.* **1980**, *36* (1), 33-39.
- ³⁹ Evans, R.; Leote de Carvalho, R.; Henderson, J.; Hoyle, D. Asymptotic Decay of Correlations in Liquids and Their Mixtures. *J. Chem. Phys.* **1994**, *100* (1), 591-603.
- ⁴⁰ Yarnell, J.; Katz, M.; Wenzel, R.; Koenig, S. Structure Factor and Radial Distribution Function for Liquid Argon At 85 °K. *Phys. Rev. A* **1973**, *7* (6), 2130-2144.
- ⁴¹ Wright, A.; Hulme, R.; Grimley, D.; Sinclair, R.; Martin, S.; Price, D.; Galeener, F. The Structure of Some Simple Amorphous Network Solids Revisited. *J. Non-Cryst. Solids* **1991**, *129* (1-3), 213-232.
- ⁴² Ryu, C.; Dmowski, W.; Egami, T. Ideality of Liquid Structure: A Case Study for Metallic Alloy Liquids. *Phys. Rev. E* **2020**, *101* (3), 042615.
- ⁴³ Kim, H.; Jeffrey, G.; Rosenstein, R. The Crystal Structure of The K Form Of D-Mannitol. *Acta Crystallogr., Sect. B: Struct. Crystallogr. Cryst. Chem.* **1968**, *24* (11), 1449-1455.
- ⁴⁴ Fronczek, F.; Kamel, H.; Slattery, M. Three Polymorphs (A, B, And Δ) Of D-Mannitol At 100 K. *Acta Crystallogr., Sect. C: Cryst. Struct. Commun.* **2003**, *59* (10), o567-o570.
- ⁴⁵ Juhás, P.; Farrow, C.; Yang, X.; Knox, K.; Billinge, S. Complex Modeling: A Strategy and Software Program For Combining Multiple Information Sources To Solve Ill Posed Structure And Nanostructure Inverse Problems. *Acta Crystallogr., Sect. A: Found. Adv.* **2015**, *71* (6), 562-568.
- ⁴⁶ Skinner, L.; Huang, C.; Schlesinger, D.; Pettersson, L.; Nilsson, A.; Benmore, C. Benchmark Oxygen-Oxygen Pair-Distribution Function of Ambient Water from X-Ray Diffraction Measurements with A Wide Q-Range. *J. Chem. Phys.* **2013**, *138* (7), 074506.
- ⁴⁷ Takamuku, T.; Maruyama, H.; Kittaka, S.; Takahara, S.; Yamaguchi, T. Structure of Methanol Confined In MCM-41 Investigated by Large-Angle X-Ray Scattering Technique. *J. Phys. Chem. B* **2005**, *109* (2), 892-899.
- ⁴⁸ Hawkes, G.; Lewis, D. ¹H Nuclear Magnetic Resonance Spectra and Conformations of Alditols in Deuterium Oxide. *J. Chem. Soc., Perkin Trans. 2* **1984**, No. 12, 2073.
- ⁴⁹ Ocko, B.; Kortan, A.; Birgeneau, R.; Goodby, J. A High Resolution X-Ray Scattering Study of The Phases and Phase Transitions in N-(4-N-Butyloxybenzylidene)-4-N-Heptylaniline (40.7). *J. Phys.* **1984**, *45* (1), 113-128.
- ⁵⁰ Murata, K. I.; Tanaka, H. Liquid-liquid transition without macroscopic phase separation in a water-glycerol mixture. *Nature Mater.* **2012**, *11*(5), 436-443.

Chapter 8 Future work

8.1 New method for surface diffusion measurements.

In chapter 2 and chapter 3, we measured the surface grating decay of three different systems POS, ITZ and MTDATA. In the same amount of time, the grating of ITZ shows much less decay than the other two systems, and an accurate surface diffusion rate is hard to obtain due to the small amount of decay at low temperatures. As shown in eq. 2.1, the decay rate correlates with the grating wavelength in a reciprocal manner, meaning a grating with a smaller wavelength would decay faster. To shorten the experimental time, a promising way is to fabricate surface counters with sharper curvature. Below are shown two new methods for the fabrication, potentially useful for the measurement of slow-diffusing systems.

Anode aluminum oxide (AAO) template usually has well-controlled nanostructure and is commercially available. By manufacturing with a specific electrolyte solution and anodic voltage, the pore size can be tuned to as small as 100 nm. Single-pass AAO, with 100 nm interpore distance and 300 nm depth, was bought from ACS Material. Before thermal embossment, it was baked at 413 K for an hour and coated with 10 nm gold to prevent contamination. The treated template was used in the same way as those sinusoidal gratings in Chapter 2 and Chapter 3. Figure 8.1a shows the 2D gratings at the free surface of amorphous POS, fabricated by AAO embossment. The sample was kept at 318 K with N₂ purge, and the nanostructures decayed over time, achieved by the surface diffusion mechanism. By Fourier transforming the whole image and azimuthal integration, the amplitude of the gratings can be obtained. In Figure 8.1b, the amplitude of the surface grating is plotted against storage time and the decay constant can be obtained by fitting the decay with an exponential function.

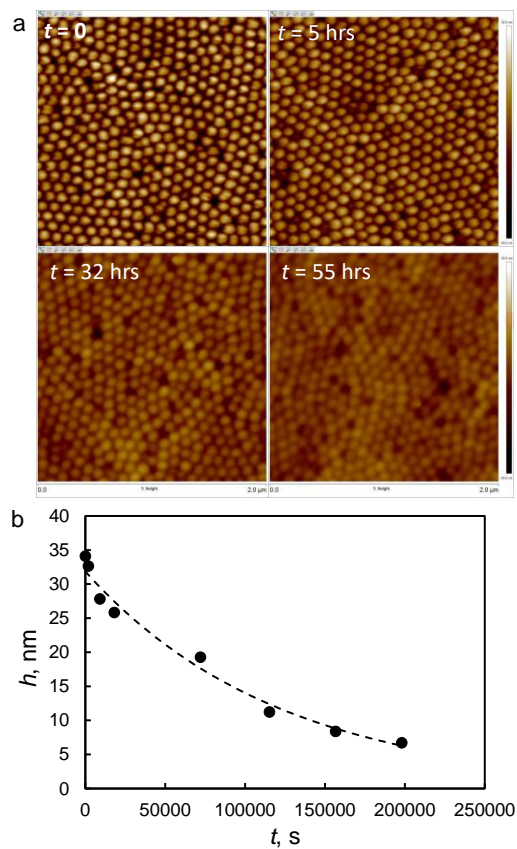


Figure 8.1. (a) 2D grating fabricated by AAO embossment and its decay overtime measured by AFM. The wavelength (peak-to-peak distance) is 100 nm, and the initial amplitude is 35 nm. (b) Decay kinetics of POS 2D grating at 318 K. The dashed line is the exponential fitting.

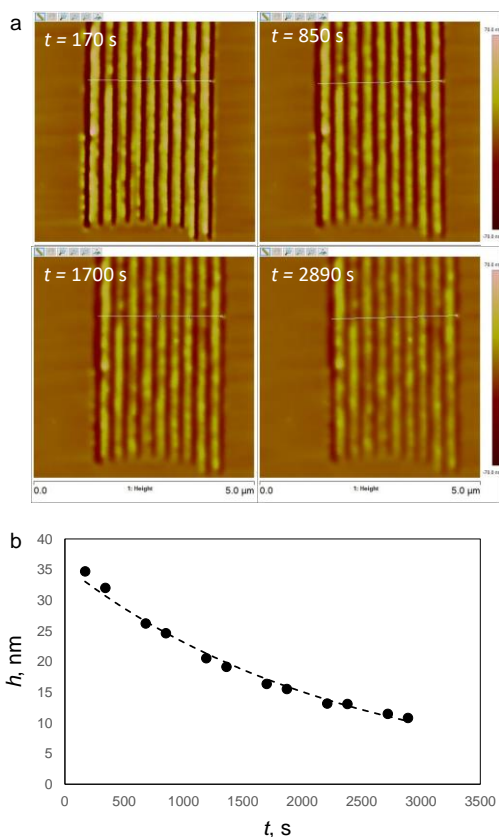


Figure 8.2. (a) Sinusoidal grating fabricated by AFM scratching at the surface of amorphous IMC and its decay overtime. (b) Decay kinetics of the grating at 299 K. The dashed line is the exponential fitting.

Another method for fabricating sharp nano-size surface counters is based on AFM. The technique of AFM based scratching has been successfully employed for various types of materials, and the structures can be well programmed by adjusting the applied force and scratching direction.^{1,2} The scratching was done at room temperature with Bruker BioScope Catalyst featured with nanolithography. During the scratching and the following measurement, the whole AFM stage was covered with plastic wrap and purged with N_2 to keep dry. In scratching experiments, the AFM was equipped with a diamond-coated pyramidal tip. The probes have a tip radius of curvature is range from 1 to 100 nm, a spring constant of 40 N/m and a resonant frequency of 300 kHz. In

scratching, the AFM tip was moved by a vector scan scheme that allows the planar XY moving velocity to be controlled in the range 10^{-6} to 10^3 $\mu\text{m/s}$. The vertical speed and distance in retracting from or pressing into the sample surface can be programmed in AFM software precisely. Figure 8.2a shows the morphology of the fabricated grating with 316 nm wavelength at the surface of amorphous IMC.). In figure 8.7b, the decay kinetics of the amplitude is shown to exhibit an exponential relationship with time. The decay rate for the grating is about $10^{-3.4}$ s^{-1} , very close to the reported value.³

Either AAO embossment or AFM scratch could produce sharper surface counters than that in Chapter 2 and 3, and help to shorten the experimental time. Both methods show promising decay kinetics and can be characterized easily by AFM. As mentioned in Chapter 4, the current knowledge of surface diffusion concentrates on the systems that diffuse fast. It is of interest to apply the above-mentioned methods to study the surface dynamics of slow-diffusing systems.

8.2 Growth of single-layer smectic structure.

In Chapter 2, the surface grating decay was tested on ITZ at low temperatures, while the surface diffusion rate is too slow to be confirmed and a new method is needed. When fabricating gratings by AFM scratching, it was found that the scratches initialized the growth of a new structure at the free surface of amorphous ITZ. This new surface structure is very thin. Figure 8.3 shows the growth of it overtime. While this new structure grows obviously in lateral directions, it never grows vertically and the thickness remains 3 nm, which is comparable to the molecular length of a ITZ molecule.

Because of its small size, the exact physical phase of this new structure is hard to be determined by traditional characterization methods. I rule out the possibility of a crystalline phase by the following three facts: 1. This new structure is only one-molecular thin, much smaller than the observed ITZ surface crystals. 2. When measured by AFM, this new structure has the same phase shifting as its surrounding amorphous parts in the phase mode, indicating very similar viscoelasticity. On the contrary, a big difference would be expected if the new structure is crystalline. 3. The same location was scanned before and after 373 K annealing. It was found that 3-second annealing would eliminate this new structure, while 373 K is much lower than the crystalline melting point but higher than the LC-to-isotropic temperature.

Based on the above-mentioned observations, this new phase is believed to be the smectic layer grown at the surface of amorphous ITZ. The growth rate of this smectic layer can be then obtained by figure 8.3, being 10^{-13} m/s at 323 K. It was previously studied that the surface crystal growth rate has a strong correlation with the surface diffusion rate, and a generic trend between has been observed in various systems (summarized in Ref. 4). Based on this trend, the surface diffusivity of

ITZ at 323 K can be estimated to be 10^{-19} m²/s, consistent with the estimation in Chapter 2, suggesting that the growth of the smectic layer is controlled by ITZ surface diffusion.

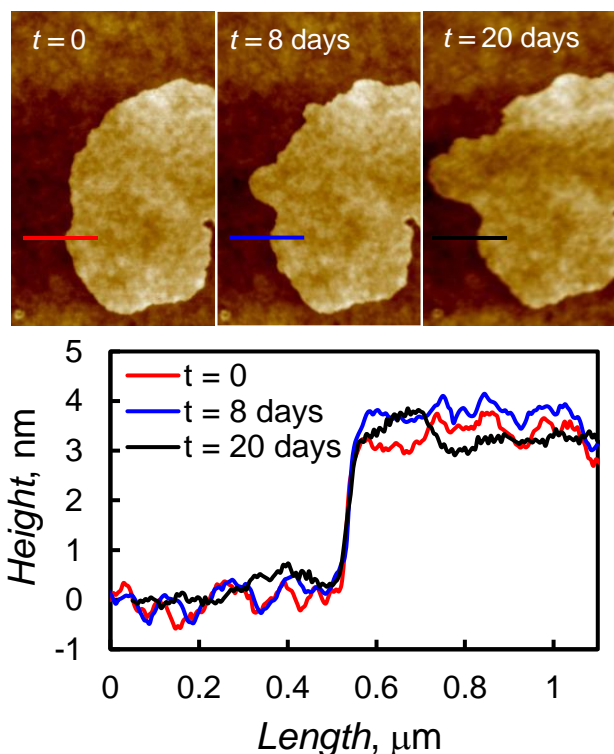


Figure 8.3. Top: Surface smectic layer measured by AFM. The same smectic layer was tracked overtime and it showed obvious lateral growth. Bottom: Height profile along the cross-section line at different time. The thickness of the smectic layer did not change overtime and is comparable to the length of a ITZ molecule along its long axis, indicating it is single-molecule layer.

This is an interesting observation of surface-assisted LC transition and there are multiple experiments that can be proposed based on this observation. So far, the observed smectic layers were initialized by surface scratching, meaning a result of heterogeneous nucleation. An interesting question would be: could these smectic layers nucleate from homogeneous nucleation? A systematic study on undisturbed ITZ surfaces would give the answer. It is also of interest to

study the temperature dependence of the growth rate of this smectic layer. As it is most likely achieved by the relatively fast surface diffusion of ITZ, the growth rate study would provide information on the surface diffusion rate of ITZ. Last but not least, this single-molecular smectic layer is certainly a 2D material and it is of interest to test its generality in other LC systems and to study if unique physical properties can be provided by this interesting geometry.

8.3 Drastic enhancement of crystal nucleation by polyamorphic transition

In Chapter 8, we discussed the structural change and the kinetic mechanism during the polyamorphic transition from HDA to LDA. The results from SWAXS indicate a significant rearrangement of the short-range order during the transition. As the crystallization of glasses is usually the major reason for material failure, a consequential question to be asked is: how does physical stability against crystallization react to such structural change? Kurita et al. studied such a question in the system of triphenyl phosphite (TPP).⁵ They observed a significant enhancement of nucleation rate at the temperature where the polyamorphic transition happens as shown in Figure 8.4a. Above the temperature of 225 K, the measured crystal nucleation rate is relatively slow and follows the trend predicted by classical nucleation theory (CNT, green curve). However, the nucleation rate below 225 K was dramatically enhanced by the appearance of polyamorphic transition. Such enhancement was attributed to the decrease of nucleus/liquid interfacial tension, which plays a vital role in determining the nucleation rate according to CNT.

We have measured the crystal growth rate and nucleation rate of D-mannitol at a serious temperature and the preliminary results are shown in Figure 8.4b and 8.4c. The crystal growth rate was measured by following the growth front of crystals under the microscope at different temperatures. And the nucleation rate was measured by observing the increase of nuclei density over time during the isothermal annealing of amorphous D-mannitol. We observed that the crystal

growth rate of alpha polymorph shows a smooth trend above and below the transformation temperature. However, a much higher nucleation rate was observed in the temperature range where LDA forms. As the interfacial tension is vital for nucleation rate but not necessary for crystal growth, it can be used to explain the different responses of nucleation and growth to the polyamorphic transition, consistent with that by Kurita et al.⁵ Currently, all the data shown here are collected by microscopy and other techniques should be dedicated to confirm the data. Considering the fast crystallization rate in the temperature range of interest, Flash Differential Scanning Calorimetry (FDSC) is capable to track the heat flow during crystallization and the obtained data can be analyzed by the Avrami equation to obtain the nucleation rate.

Kurita et al. argued that only one polymorph nucleated within the whole temperature range measured, which is, somehow, inconsistent with a recent report. Walton et al. found the two liquid structures of TPP mimic the molecular packing of two crystalline structures and two different polymorphs tend to nucleate at different temperatures.⁶ A similar is observed with D-mannitol: above the transition temperature, it was previously reported that LDA tends to nucleate δ polymorph,⁷ below the transition temperature, both X-ray diffraction pattern and Raman spectrum suggest α polymorph nucleated from HDA. This connection between polymorphism and polyamorphism would lead to a more fundamental understanding of the physical basis of the amorphous structures, and allow the control of the nucleation frequency and the obtained polymorph based on polyamorphic transition.

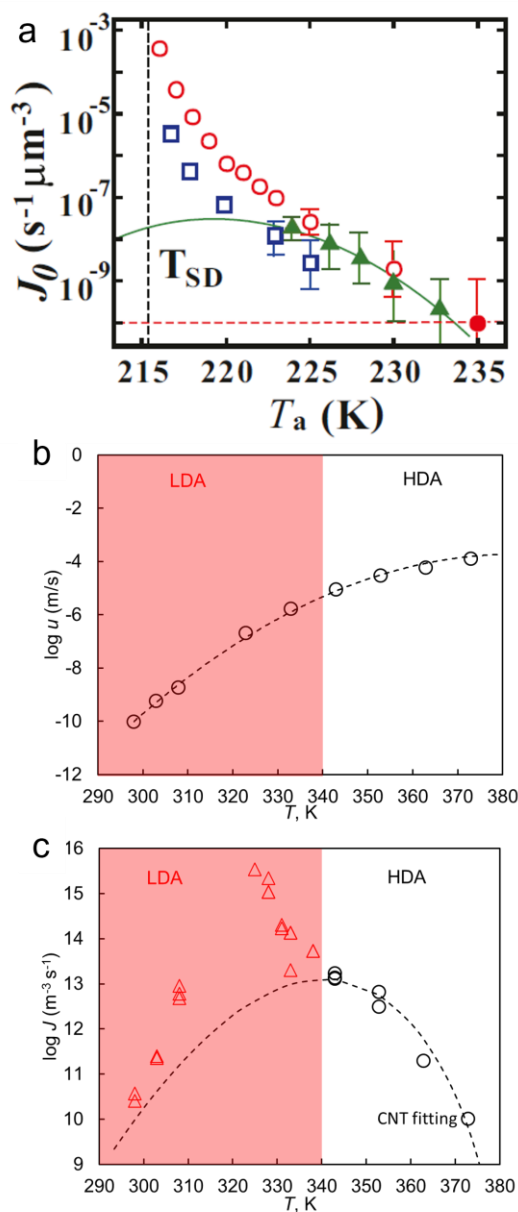


Figure 8.4. (a) The crystal nucleation rate of TPP as a function of temperature. Reproduced with the permission from Kurita, *Proc. Natl. Acad. Sci. U.S.A.*, **2019**, *116*, 24949-24955. Copyright 2019 National Academy of Science. (b) Crystal growth rate of α polymorph of D-mannitol as a function of temperature. A smooth trend is observed above and below the polyamorphic-transition temperature. (c) Crystal nucleation rate of D-mannitol as a function of temperature. A drastic enhancement of nucleation rate is observed when cooled to LDA phase.

¹ Tseng, A. A.; Notargiacomo, A.; Chen, T. P. Nanofabrication by scanning probe microscope lithography: A review. *J. Vac. Sci. Technol. B: Nanotechnol. Microelectron.* **2005**, *23*(3), 877-894.

² Tseng, A. A.; Kuo, C. F. J.; Jou, S.; Nishimura, S.; Shirakashi, J. I. Scratch direction and threshold force in nanoscale scratching using atomic force microscopes. *Appl. Surf. Sci.* **2011**, *257*(22), 9243-9250.

³ Zhu, L.; Brian, C. W.; Swallen, S. F.; Straus, P. T.; Ediger, M. D.; Yu, L. Surface self-diffusion of an organic glass. *Phys. Rev. Lett.*, **2011**, *106*, 256103

⁴ Huang, C.; Ruan, S.; Cai, T.; Yu, L. Fast surface diffusion and crystallization of amorphous griseofulvin. *J. Phys. Chem. B* **2017**, *121*, 9463.

⁵ Kurita, R.; Tanaka, H. Drastic enhancement of crystal nucleation in a molecular liquid by its liquid–liquid transition. *Proc. Natl. Acad. Sci. U.S.A.* **2019**, *116*(50), 24949-24955.

⁶ Walton, F.; Bolling, J.; Farrell, A.; MacEwen, J.; Syme, C. D.; Jiménez, M. G. et al. Polyamorphism mirrors polymorphism in the liquid–liquid transition of a molecular liquid. *J. Am. Chem. Soc.* **2020**, *142*(16), 7591-7597.

⁷ Yu, L. Nucleation of one polymorph by another. *J. Am. Chem. Soc.* **2003**, *125*(21), 6380-6381.